



UNIVERSITY OF LIEGE



FACULTY OF APPLIED
SCIENCES

Conception of a near-infrared spectrograph for the observation of massive stars

Thesis submitted in partial fulfillment of the requirements for the degree of Doctor in Applied Sciences by Kintziger Christian



JURY

Prof. Jérôme LOICQ

*Département d'aérospatiale et mécanique
Centre Spatial de Liège (CSL)
University of Liège (ULiège)
J.Loicq@uliege.be*

Prof. Serge HABRAKEN

*Département de physique/Optique - Hololab
Centre Spatial de Liège (CSL)
University of Liège (ULiège)
shabraken@uliege.be*

Prof. Eric GOSSET

*Groupe d'astrophysique des hautes énergies (GAPHE)
University of Liège (ULiège)
Eric.Gosset@uliege.be*

James Kent WALLACE

*Jet Propulsion Laboratory (JPL)
California Institute of Technology (Caltech)
James.K.Wallace@jpl.nasa.gov*

Prof. Jürgen SCHMITT

*Hamburger Sternwarte
Universität Hamburg
jschmitt@hs.uni-hamburg.de*

Prof. Pierre ROCHUS (Promoter)

*Département d'aérospatiale et mécanique
Centre Spatial de Liège (CSL)
University of Liège (ULiège)
prochus@uliege.be*

Prof. Grégor Rauw (Co-promoter)

*Groupe d'astrophysique des hautes énergies (GAPHE)
University of Liège (ULiège)
G.Rauw@uliege.be*

Table of Contents

List of acronyms.....	x
List of figures	xii
List of tables	xx
Abstract	xxii
Acknowledgement.....	xxiv
1. Introduction	1
1.1 ARC project: massive stars, key players in the evolution of the universe	1
1.2 Astrophysical background.....	2
1.2.1 Massive stars	2
1.2.2 The need of a near-infrared spectrograph.....	3
1.2.3 Scientific requirements.....	4
1.3 Considered telescopes	5
1.3.1 el TIGRE	5
1.3.2 3.6M DOT (ARIES)	6
1.3.3 Expected seeing and image size comparison.....	7
1.4 Near-infrared fiber-fed spectroscopy: from pioneers to nowadays innovators	8
1.4.1 ISIS IR	8
1.4.2 MOONS: the Multi-Object Optical and Near-infrared Spectrograph	11
1.5 Conclusion.....	15
Technical considerations related to ground-based spectroscopy.....	18
2. Technical considerations related to ground-based spectroscopy.....	19
2.1 Observation windows	19
2.2 Observation techniques	20
2.2.1 Noise sources.....	20
2.2.2 Telescope optimization and observing techniques	21
2.3 Atmospheric dispersion.....	22
2.4 A fiber-fed instrument.....	24
2.4.1 Use of fibers in astronomy.....	24
2.4.2 Properties of fibers.....	26
2.4.3 Fibers' configuration within the selected bundle.....	36
2.4.4 Optical couplers: micro-lenses	37
2.5 Suitable optical coating techniques	38
2.6 Filters.....	39
2.7 Glasses.....	40

2.8	Detector technologies	41
2.8.1	History	41
2.8.2	Generalities	43
2.8.3	Charge-coupled devices (CCD)	44
2.8.4	Photoconductive cells	46
2.8.5	Bolometers	46
2.8.6	Technologies under development	47
2.8.7	Identified manufacturers of detectors	48
2.8.8	Selected detector	51
2.9	Conclusion	52
3.	Theoretical background on spectroscopy	55
3.1	Introduction	55
3.2	The spectrograph figure of merit	55
3.3	Theory of diffraction grating spectrographs	57
3.4	Simple requirements on cameras and detectors	63
3.5	Conclusion	67
4.	Spectrograph optical design	69
4.1	Introduction	69
4.2	Basic considerations	69
4.3	From scientific requirements to instrument specifications	70
4.3.1	Basic equations	71
4.3.2	Figures of merit	72
4.3.3	General design procedure	72
4.3.4	The spectrometer-like specification	73
4.3.5	Investigations on Bingham's spectrometer-like methodology	78
4.3.6	Application to the instrument under study	81
4.3.7	Change of blaze wavelength with incident angle on grating	83
4.3.8	Implementation of micro-lenses	84
4.4	Optimization process	85
4.4.1	Configuration selection and associated techniques	85
4.4.2	Resolving power analysis	86
4.5	Tolerancing analysis	91
4.5.1	Sensitivity matrix	91
4.5.2	Coupling effects	96
4.5.3	Compensator selection	99
4.5.4	Overall budget	100

4.6	Alignment simulation.....	104
4.6.1	Simulation goal.....	104
4.6.2	Optimization scheme.....	104
4.6.3	Figure of merit.....	106
4.6.4	Mechanical considerations.....	106
4.6.5	Compensators.....	107
4.6.6	Simulation results.....	107
4.7	Calibration.....	118
4.7.1	Spectral calibration.....	118
4.7.2	Flat-field calibration.....	119
4.7.3	Practical implementation of the calibration box.....	119
4.7.4	HCL slit illumination system.....	121
4.7.5	Calibration stability vs. scrambling gain.....	122
4.8	Crosstalk.....	124
4.9	Straylight analysis.....	125
4.10	Conclusion.....	127
5.	Photometric budget.....	129
5.1	Introduction.....	129
5.1.1	Instrument requirements.....	129
5.2	Stellar radiometric budget.....	129
5.3	Interstellar absorption models.....	132
5.4	Atmospheric transmission.....	132
5.5	Instrumental throughput efficiency.....	133
5.5.1	Fiber Optics.....	134
5.5.2	Coatings and filters.....	135
5.5.3	Grating.....	135
5.5.4	Detectors.....	136
5.6	Noise sources.....	137
5.7	Signal-to-noise ratio.....	138
5.8	Signal saturation.....	139
5.9	Analyses.....	140
5.9.1	Required integration time.....	140
5.9.2	Reducing integration time.....	154
5.10	Conclusion.....	158
6.	Alignment and tests of the instrument.....	161
6.1	Fiber illuminating setup.....	161

6.2	Visible alignment of the spectrograph.....	162
6.2.1	Identification of fibers	162
6.2.2	Installation of the collimator and grating.....	163
6.2.3	Positioning of the focusing mirror.....	164
6.2.4	First spot verification with the toroidal lens	165
6.3	Going to the near-infrared.....	166
6.4	Polychromatic performances.....	168
6.4.1	<i>UNe</i> hollow cathode lamp spectra	168
6.4.2	Experimental resolving power assessment	174
6.5	Calibration box assembly and tests	177
6.5.1	Alignment of mechanical slits and beamsplitter.....	177
6.5.2	Calibration test.....	180
6.5.3	Verification of translation stage repeatability.....	183
6.6	Conclusion.....	184
7.	Star positioning system (SPS).....	187
7.1	Purpose of the instrument.....	187
7.2	Optical design.....	187
7.3	Atmospheric dispersion.....	188
7.4	Photometric budget	190
7.4.1	Methane filter	190
7.4.2	NIR Anti-reflective window	190
7.4.3	Visible camera characteristics	191
7.4.4	Stellar radiometric budget over the selected filter waveband.....	191
7.5	Assembly and alignment	196
7.6	Conclusion.....	198
8.	On sky observations from Liège	201
8.1	Introduction	201
8.2	Adapted photometric budget	201
8.3	First light in Liège	206
8.3.1	Preparation of spectrograph for observation.....	206
8.3.2	Coupling with the telescope and first tests	209
8.3.3	Advanced tracking device	212
8.3.4	Verification of performances.....	222
8.4	Conclusion.....	225
9.	Conclusion and perspectives	227
9.1	Overall conclusion on the conception of N3SIE.....	227

9.2 Perspectives and suggested improvements.....	229
Bibliography.....	234
A. Establishment of Bingham's equations.....	243
B. Control software overview.....	245
Introduction.....	245
Purpose of the software and devices under control.....	245
User interface presentation.....	246
Manual mode.....	246
Automatic mode.....	246
C. Associated scientific paper.....	248

List of acronyms

ARC	-	Action de Recherche Concertée
ULiège	-	University of Liège
GAPHE	-	Groupe d'Astrophysique des Hautes Energies
ASTA	-	Astrophysique Stellaire Théorique et Astérosismologie
CSL	-	Centre Spatial de Liège
IR	-	InfraRed
CCD	-	Charge-Coupled Device
NIR	-	Near-InfraRed
HRT	-	Hamburg Robotic Telescope
HEROS	-	Heidelberg Extended Range Optical Spectrograph
ARIES	-	Aryabhata Research Institute of Observational Sciences
CFHT	-	Canada-France-Hawaii Telescope
FRD	-	Focal Ratio Degradation
NICMOS	-	Near Infrared Camera and Multi-Object Spectrometer
HST	-	Hubble Space Telescope
MONICA	-	MONtréal Infrared Camera
ESO	-	European Southern Observatory
NTT	-	New Technology Telescope
IRSPEC	-	Infrared Spectrometer
MCT	-	Mercury cadmium telluride
MOONS	-	Multi-Object Optical and Near-infrared Spectrograph
VLT	-	Very Large telescope
ESA	-	European Space Agency
GAIA	-	Global Astrometric Interferometer for Astrophysics
MR	-	Medium Resolution

HR	-	High Resolution
FDR	-	Final Design Review
ATRAN	-	Atmospheric TRANsmission
FWHM	-	Full Width at Half Maximum
ADC	-	Atmospheric Dispersion Compensator
GMOS	-	Gemini Multi-Object Spectrograph
HARPS	-	High Accuracy Radial velocity Planet Searcher
TIR	-	Total Internal Reflection
KPNO	-	Kitt Peak National Observatory
JPL	-	Jet Propulsion Laboratory
TI	-	Texas Instruments
NASA	-	National Aeronautics and Space Administration
RCA	-	Radio Corporation of America
MIR	-	Mid-InfraRed
FIR	-	Far-InfraRed
IRAC	-	Infrared Array Camera
UCLA	-	University of California Los Angeles
PMT	-	PhotoMultiplier Tube
FPA	-	Focal Plane Array
SCA	-	Sensor Chip Assembly
ROIC	-	ReadOut-Integrated Circuit
EBCCD	-	Electron Bombarded CCD
ICCD	-	Intensified CCD
QWIP	-	Quantum Well Infrared Photodetectors
VISTA	-	Visible and Infrared Survey Telescope for Astronomy
TES	-	Transition Edge Sensors
STJ	-	Superconducting Tunnel Junction
RMS	-	Root-Mean-Square
FOM	-	Function Of Merit
HCL	-	Hollow Cathode Lamp
CRIRES	-	Cryogenic High-Resolution IR Echelle Spectrometer
KMOS	-	K-band Multi-Object Spectrograph
SNR	-	Signal-to-Noise Ratio
FWC	-	Full Well Capacity
Nd:YAG	-	Neodymium-doped Yttrium Aluminum Garnet
SPS	-	Star Positioning System
LED	-	Light-emitting diode
CMOS	-	Complementary metal-oxide-semiconductor
PSF	-	Point Spread Function
JATIS	-	Journal of Astronomical Telescopes, Instruments, and Systems
DOI	-	Digital Object Identifier

List of figures

Figure 1.1 - Observation of the near-IR spectrum of the Wolf-Rayet star <i>WR136</i> recorded with a CCD detector. The absorption features between 8900 \AA and $1 \mu\text{m}$ are due to the Earth's atmosphere. (Figure courtesy Jean-Marie Vreux).	4
Figure 1.2 - The TIGRE telescope at La Luz observatory site, Mexico [18].	6
Figure 1.3 - Geometrical star image size as a function of seeing for both considered telescopes. Typical (<i>left</i>) and best (<i>right</i>) seeing conditions are also depicted.	7
Figure 2.1 - Atmospheric opacity as a function of wavelength [30].	19
Figure 2.2 - Illustration of atmospheric windows around $1 \mu\text{m}$ for the Mauna Kea site (altitude $14\,000 \text{ ft}$) [30]	19
Figure 2.3 - Variation of near-infrared surface sky brightness in different bands as a function of the air mass for the night of the 31 st January 2008 [32].	21
Figure 2.4 - Illustration of chopping and nodding techniques [30]	21
Figure 2.5 - First multi-object spectrograph, Medusa [39].	25
Figure 2.6 - Fiber positioners of the Steward Observatory 2.3-m telescope [39].	26
Figure 2.7 - Different modes propagating into a step-index fiber. Lossy modes, that do not obey to TIR, leak to the cladding and vanish [43].	27
Figure 2.8 - Modal dispersion due to stress-induced micro-bending [44]. Light escapes at lower f-ratio or leaks through lossy modes which is in all cases a loss.	27
Figure 2.9 - FRD of a typical fiber vs. throughput of a circular aperture whose diameter equals the fiber core size [43].	28
Figure 2.10 - Focal ratio degradation of a 320 (<i>left</i>) and 100 (<i>right</i>) μm core fiber [43].	28
Figure 2.11 - Absolute transmission of fibers when output f-ratio is equal to input f-ratio [43]	29
Figure 2.12 - Intensity profile of the output beam of an unstressed (<i>dotted line</i>) and stressed (<i>solid line</i>) fiber [44].	29
Figure 2.13 - FRD properties of a $320 \mu\text{m}$ fiber for different input f-ratios (<i>left</i>) and throughput at equivalent f-ratio (<i>right</i>) [41]	30

Figure 2.14 - Required output f-ratio to collect 95% of the input f-ratio for different fibers [44].	30
Figure 2.15 - Fitting of the model (<i>solid line</i>) to Barden's results (<i>squares</i>) [46].	31
Figure 2.16 – Theoretical predictions of a fiber FRD properties compared to the experimental measures (<i>squares</i>) [46].	31
Figure 2.17 – Relative transmission with respect to the output f-ratio when injecting light at $f/8$ input f-ratios [46].	32
Figure 2.18 - Normalized (at 800 nm) transmission of a 30 meter wet fiber [44]. Circle points are manufacturer specifications, others are measures.	32
Figure 2.19 - Transmission of a 25 meter long "wet" (<i>up</i>) and "dry" (<i>bottom</i>) fiber [45].	33
Figure 2.20 - Azimuthal scrambling of fibers [43].	34
Figure 2.21 – Fraction of light radially scrambled as a function of input f-ratio [42].	35
Figure 2.22 - Fraction of unscrambled light as a function of input f-ratio [45].	35
Figure 2.23 - Output light pattern of a 200 (<i>left</i>) and 100 (<i>right</i>) μm fiber illuminated by a $f/8$ light cone [45].	35
Figure 2.24 - Fiber bundle configuration: input at telescope (<i>left</i>) and output to spectrograph (<i>right</i>).	37
Figure 2.25 – Reflectance of aluminum, silver and gold metallic coatings [50].	38
Figure 2.26 - Protected silver coating reflectivity for collimating and focusing mirrors.	39
Figure 2.27 - NIR longpass filter [51].	39
Figure 2.28 - Overview of several optical material properties [52].	40
Figure 2.29 – Quantum efficiency of several detectors including CCDs [30].	41
Figure 2.30 - A typical hybrid pattern of an infrared array device [30].	44
Figure 2.31 –Layout of a bolometer element [30].	47
Figure 2.32 - Quantum efficiency of Sofradir detectors [53].	48
Figure 2.33 - Dark noise levels of different IR detectors (Figure courtesy of AIM [54]).	48
Figure 2.34 - Quantum efficiencies of different CCDs [55].	49
Figure 2.35 - Typical dark current variation as a function of temperature [56].	50
Figure 2.36 - Typical variation of quantum efficiency with temperature [56].	50
Figure 2.37 - Quantum efficiency of the Photonic Science Snake camera.	51
Figure 3.1 - Schematic diagram of a spectrograph [39].	55
Figure 3.2 - Reflective grating [39].	58
Figure 3.3 - Diagram of a telescope followed by a spectrograph (adapted from [39]).	59
Figure 4.1 – Schematic view of the general procedure.	73
Figure 4.2 - Bingham's spectrometer-like method.	77
Figure 4.3 - Obtained specifications from the spectrometer-method for different values of α - β and $(\alpha+\beta)/2$.	79
Figure 4.4 - Variation of grating size (L) as a function of the blaze angle ($\theta B = \alpha + \beta/2$) for a given Littrow configuration.	80
Figure 4.5 – Collimator A_{coll} (a) and focuser A_{cam} (b) size as a function of Littrow angle α - β for a grating blaze angle.	80
Figure 4.6 - Grating first order efficiency curves.	83
Figure 4.7 - Obtained spectrograph instrument design featuring a toroidal lens.	86
Figure 4.8 - Resolving power assessment methodology illustration.	87
Figure 4.9 - Plot of exit slit spots from points located at the sides (red and blue) and center (green) of the entrance slit. The slit is elongated along the horizontal direction. The situation is depicted at three different wavelengths that are 1040 nm (a), 1050 nm (b) and 1060 nm (c).	87
Figure 4.10 - Plot of one sampled exit slit profile (a) and resolving power across focal plane for a given grating position (b).	88

Figure 4.11 - Variation of FWHM as a function of position through slit (all wavelengths plotted) (a) and wavelength (all positions through slit plotted) (b).....	88
Figure 4.12 - Plot of one sampled exit slit profile (a) and resolution across focal plane for a given grating position (b).	90
Figure 4.13 - Main channel of the spectrograph with local axes of the entrance slit indicated.....	91
Figure 4.14 - Alignment procedure block diagram view.....	105
Figure 4.15 - Axes implementation on optical surfaces	106
Figure 4.16 - Toroidal lens (blue), fold mirror (grey) and detector (red) with their respective local axes	107
Figure 4.17 - Compensators' evolution during alignment process	108
Figure 4.18 – Central slit spot evolution through the different paths investigated by the algorithm ..	108
Figure 4.19 - Slit images at three different wavelengths.....	109
Figure 4.20 - Zoom onto the slit image at one detector side	109
Figure 4.21 - Evolution of mean spot and during alignment process.....	110
Figure 4.22 - Compensators' evolution during alignment process	111
Figure 4.23 - Evolution of mean spot and standard deviation during alignment process	111
Figure 4.24 - Mean RMS spot evolution through the different paths investigated by the algorithm ..	112
Figure 4.25 - Evolution of MEAN RMS spots and standard deviation vs. focus ((a) and (b)), tilt ((c) and (d)) and tip ((e) and (f)) through focal plane at each step.....	114
Figure 4.26 – Evolution of RMS spots vs. focus ((a) and (b)), tilt ((c) and (d)) and tip ((e) and (f)) through focal plane at each step	115
Figure 4.27 - Induced piston at shorter and longer wavelengths after TILT movement.....	116
Figure 4.28 - Induced piston at bottom and up of the slit after TIP movement	117
Figure 4.29 - Resolving power through focal plane before (left) and after (right) alignment process	117
Figure 4.30 - Th-Ar spectrum [71] between 1060 and 1080 nm (a) and same part of the spectrum obtained from a U-Ne lamp [74] (b). Bottom parts of both figures are zooms from upper ones obtained when limiting the intensity y-axis.	119
Figure 4.31 - Calibration unit optical design. Light coming from the output end of the fiber reaches a moving fold mirror when positioned in its down position and is injected to the collimating mirror during observation (right to the fold mirror, not represented in the figure). When calibrating, the moving mirror moves upwards and light from the calibration lamps is gathered with a beamsplitter and eventually goes to the collimator.....	120
Figure 4.32 - Detected wavelength along the slit length when taking into account the error on the repeatability of the flipping mechanism (a) and of the translation stage (b). The horizontal red line represents the mean detected wavelength and the two green ones are located at plus and minus the calibrating requirement from the exact injected wavelength.....	121
Figure 4.33 - Optical design of the HCL slit illumination system	122
Figure 4.34 - Evolution of spectral shift with respect to scrambling gain.....	124
Figure 4.35 – Focal plane image of two central fibers (left) and profile of light intensity along imaging direction (right) with 25 μm pixels.....	124
Figure 4.36 - Focal plane image of two central fibers (left) and profile of light intensity along imaging direction (right) with 15 μm pixels.....	125
Figure 4.37 - Propagation of the rays from the grating zeroth diffraction order. Light is confined at the top left after hitting the walls of the calibration unit compartment and does not reach the detector...	126
Figure 5.1 – Star image footprint at a spectroscopic instrument’s focal plane.....	131
Figure 5.2 - Bolometric correction in J-band (left: cool stars [80], right: hot stars [81] [82]).....	132
Figure 5.3 - Atmospheric transmission in the range 1-1.1 μm [31].....	133

Figure 5.4 - Evolution of fiber core vignetting factor as a function of seeing for both identified telescopes. Sampled values for typical (<i>left</i>) and good (<i>right</i>) seeing conditions are also represented.	134
Figure 5.5 - FRD properties and transmission of dry fibers	135
Figure 5.6 - Protected silver coating reflectivity	135
Figure 5.7 – Selected grating efficiency curve [83]	136
Figure 5.8 - Selected InGaAs detector quantum efficiency	136
Figure 5.9 - Evolution of dark current (<i>left</i>) and quantum efficiency (<i>right</i>) with temperature (and wavelength) of a given cooled CCD detector	137
Figure 5.10 -Flux of photons received and detected for COOL stars	141
Figure 5.11 - Required integration time vs. T_{eff} for COOL stars	142
Figure 5.12 - Flux of photons received and detected for HOT stars	142
Figure 5.13 - Required integration time vs. T_{eff} for HOT stars	143
Figure 5.14 - Variation of integration time with AV (<i>left</i> : COOL stars, <i>right</i> : HOT stars)	144
Figure 5.15 - Flux of photons received and detected for COOL stars	145
Figure 5.16 - Required integration time vs. T_{eff} for COOL stars. Dashed lines in the right panel represent the saturation limit of the detector.	146
Figure 5.17- Optimal CCD temperature and integration time gain for COOL stars	146
Figure 5.18 - Evolution of integration time wrt. effective temperature for stars of magnitude 4 at different CCD temperatures (<i>left</i>) and integration time as a function of CCD temperature for a given cool star.	147
Figure 5.19 - Flux of photons received and detected for HOT stars	148
Figure 5.20 - Required integration time vs. T_{eff} for HOT stars	148
Figure 5.21- Optimal CCD temperature and integration time gain for HOT stars	149
Figure 5.22 - Evolution of integration time wrt. effective temperature for stars of magnitude 4 at different CCD temperatures (<i>left</i>) and integration time as a function of CCD temperature for a given HOT star	149
Figure 5.23 - Variation of integration time with AV (<i>left</i> : COOL stars, <i>right</i> : HOT stars)	151
Figure 5.24 – Relationship between dN_{tot} and dN_{foc} (<i>left</i>) and evolution of required integration time as dN_{foc} varies	152
Figure 5.25 – Evolution of integration time wrt. dN_{foc} as a function of CCD temperature (<i>left</i>) and optimum CCD temperature as a function of dN_{foc} .	153
Figure 5.26 – Relative integration time reduction by optimizing the CCD sensor temperature as a function of dN_{foc} (<i>left</i>) and normalized integration time as a function of CCD temperature for low, boundary and high photon fluxes (<i>right</i>).	153
Figure 5.27 – Required integration time under better seeing conditions for cool (<i>left</i>) and hot stars (<i>right</i>).	154
Figure 5.28 - Required integration time with lower FRD fibers for cool (<i>left</i>) and hot stars (<i>right</i>).	155
Figure 5.29 - Vignetting effect of fibers and instrument' collimator on integration time	156
Figure 5.30 – Evolution of integration time at optimal fiber core size (<i>left</i>) and when the collimator's f-ratio is equal to 4	156
Figure 5.31 - Required integration time when implementing micro-lenses (<i>left</i> : cool stars, <i>right</i> : hot stars)	157
Figure 6.1 - Fiber illuminating system	161
Figure 6.2 - Identification of relation between input and output fibers from the bundle	162
Figure 6.3 - Fiber bundle in auto-collimation with the diffraction grating. Light travels back and forth on the grating to focus at the bundle plane.	163
Figure 6.4 - Diffraction grating on top of its rotation stage	164

Figure 6.5 – Optical configuration that enables the alignment of the focusing mirror. The grating is positioned at the right inclination to enable the 2nd diffraction order to propagate through the system.	164
Figure 6.6 - Central fiber visible image through the imaging mirror	165
Figure 6.7 – Collimating (<i>left</i>) and focusing (<i>right</i>) mirrors	165
Figure 6.8 – Toroidal lens in its optical mount	166
Figure 6.9 – Simulated (<i>left</i>) and observed (<i>right</i>) images of the central fiber	166
Figure 6.10 - Full spectrograph main channel assembly	167
Figure 6.11 – Simulated (<i>left</i>) and measured (<i>right</i>) bundle images	167
Figure 6.12 - Adapted fiber illuminating system incorporating a UNe hollow cathode lamp	168
Figure 6.13 – Recorded spectrum of the Superlamp HCL centered at 1082.6898 nm.....	169
Figure 6.14 - Recorded spectrum of a UNe HCL by Redman et al. [74].....	169
Figure 6.15 - Recorded spectrum of the regular HCL centered at 1082.6898 nm	170
Figure 6.16 – Focal plane images (<i>left</i>) and reduced spectra (<i>right</i>) when observing the HCL spectrum centered at (a) 945.5 nm, (b) 994.9162 nm and (c) 1006.1 nm.....	171
Figure 6.17 - Focal plane images (<i>left</i>) and reduced spectra (<i>right</i>) when observing the HCL spectrum centered at (a) 1059.30 nm, (b) 1071.9 nm and (c) 1119.03 nm	172
Figure 6.18 - Focal plane image (<i>left</i>) and reduced spectrum (<i>right</i>) when observing the HCL spectrum centered at 1006.1 nm	173
Figure 6.19 - Rayleigh criterion on resolving power [52].....	173
Figure 6.20 - Reduced spectrum when observing the HCL spectrum centered at 1059.30 nm, red stars indicate spectral lines used for calibration	174
Figure 6.21 - Redman's atlas of a UNe HCL centered at 1059.30 nm. Red circles indicate spectral lines used for calibration.	174
Figure 6.22 – Dispersion relation: the red stars are the spectral lines selected for calibration and the blue line is the 2nd order fitting.	175
Figure 6.23 - Calibrated spectrum when observing the HCL spectrum centered at 1059.30 nm, red stars indicate spectral lines used for calibration.	176
Figure 6.24 – Redman's and calibrated recorded spectra superposed on top of each other.....	176
Figure 6.25 - Spectral profile of the U line centered at 1055.7822 nm and calculation of the associated resolving power.....	176
Figure 6.26 – Moving mirror (in home position), beamsplitter and scientific fiber (<i>left</i>) and mechanical slits (<i>right</i>).	177
Figure 6.27 – Superposition of both slit and bundle images.	178
Figure 6.28 – Profiles of bundle, spectral and flatfield slits' images	179
Figure 6.29 – Hollow cathode focal plane image as seen through the bundle (a) and the mechanical slit (b).	179
Figure 6.30 - Spectra of the UNe HCL as seen through the bundle (<i>red</i>) and the mechanical slit associated to the spectral calibration box (<i>blue</i>).....	180
Figure 6.31 – Spectral profile of a given fiber (<i>left</i>) and detected wavelength values along with their calculated average (<i>right</i>). The upper and lower limits to fulfill the requirement on calibration accuracy are depicted by red dashed lines.....	181
Figure 6.32 - Images of fibers (a), spectral calibration (b), identified lines (c), dispersion relation (d), calibrated and Redman's spectra (e) and fiber image along with the calibrated spectrum (f).....	182
Figure 6.33 - Horizontal component of the recorded centroids (<i>blue circles</i>). The mean value is indicated as a red dash-dotted line and the upper and lower limits of the tolerance interval are the red dashed lines.	183

Figure 7.1 - Star positioning system. The instrument intends to align the observed target image with the fiber core to maximize the transmitted flux from the telescope to the spectrograph.....	187
Figure 7.2 – Evolution of the differential refraction as a function of wavelength at different zeniths for two different guiding wavelengths.	189
Figure 7.3 - Transmission of the standard Methane filter from Custom Scientific [84].	190
Figure 7.4 - Reflection of the near-infrared AR window down to the visible region [85].	191
Figure 7.5 - Absolute quantum efficiency of the visible camera CCD [86].	191
Figure 7.6 - Photon flux per wavelength unit for arbitrary COOL (3000 K) and HOT (30 000 K) stars at $J\text{-mag} = 5$ and $AV = 0$	192
Figure 7.7 – Atmospheric transmission (a), Reflectivity of the window (b), transmission of the methane filter (c) and quantum efficiency of the detector (d).	193
Figure 7.8 – Detected star photon flux per wavelength unit $dN\lambda, det$	194
Figure 7.9 - Integration process of the detected star photon flux per wavelength unit $dN\lambda, det$	194
Figure 7.10 - Photometric budget results	195
Figure 7.11 – Alignment setup of the SPS: the <i>HeNe</i> laser is used to illuminate the SPS optical elements.	196
Figure 7.12 – Image of the fiber bundle onto the guiding camera.	196
Figure 7.13 - Complete SPS assembly with the coupling flange attached	197
Figure 8.1 – $J\text{-mag}$, bolometric corrections and effective temperatures of identified potential targets	201
Figure 8.2 – Bolometric corrections of identified targets sorted according to their temperature.	202
Figure 8.3 - Evolution of star image size and fiber core vignetting factor as a function of seeing with the selected small telescope. Sampled values for a typical seeing of 3 <i>arcsec</i> are also represented.	202
Figure 8.4 - Flux of photons received and detected at 1050 <i>nm</i> for the identified targets.....	203
Figure 8.5 - Required integration time at 1050 <i>nm</i> for the identified targets.....	203
Figure 8.6 - Required integration time for the identified targets when using a CCD at the central wavelength of 1050 <i>nm</i> (left) and 1100 <i>nm</i> (right).	204
Figure 8.7 - Optimal CCD temperature and integration time gain for the identified targets	204
Figure 8.8 - Evolution of integration time as a function of different CCD temperatures for the identified targets.....	205
Figure 8.9 - Evolution of integration time wrt. $dNfoc$ as a function of CCD temperature with targets depicted on top (left) and normalized integration time as a function of CCD temperature for Betelgeuse, Spica and the boundary flux (right).	205
Figure 8.10 - Final configuration of the instrument with black flocked paper.....	206
Figure 8.11 - Shutters that equip the spectral calibration mechanical slit and the fiber bundle.....	207
Figure 8.12 - Fiber back-illuminating system that incorporates the LED.....	207
Figure 8.13 – Observing control room (a) and final instrument configuration with removable cover plates (b).	208
Figure 8.14 - Telescope initialization and remote control computer.....	208
Figure 8.15 - Flipping mirror device: the upper flange connects to the telescope, the left connecting tube intends to hold an eyepiece and the lower hidden aperture incorporates a standard thread for cameras. The small turning button activates the flipping mechanism.....	209
Figure 8.16 - Connecting mechanical piece using the standard camera thread (a) and adapted fiber positioning system (b).....	209
Figure 8.17 - Focal plane image when pointing at Arcturus with the initial observing setup.....	210
Figure 8.18 - Arcturus spectrum centered at 1083 <i>nm</i> from our first observation on the 22 nd of June	211

Figure 8.19 - Advanced tracking device optical design. Light propagates from the telescope down to the bundle plane. The reflected beam onto the metallic ferrule then goes back to the beamsplitter along with the light from the fibers and reaches the camera.	212
Figure 8.20 - Beamsplitter mount (a) and modified flipping mirror box (b).	213
Figure 8.21 – Camera holder (a) and adapted tracking device (b).	213
Figure 8.22 - Observation setup installed on CSL facilities roof. A second display devoted to the tracking operation was added. The laptop was dedicated to the spectrograph control.....	214
Figure 8.23 - Internal reflections that occur within the beamsplitting glass plate.....	214
Figure 8.24 - Simulated behavior of the ghost generation associated with the fiber bundle light (b).	215
Figure 8.25 - Multiple image formation onto the bundle ferrule due to internal reflections within the beamsplitter during the transmission process of the star light.....	215
Figure 8.26 - Simulated behavior of the ghost generation issued from the star light (b).	216
Figure 8.27 - Focal plane image when pointing at Vega with the advanced tracking device.	217
Figure 8.28 - Quantum efficiency of the tracking visible camera [87].	217
Figure 8.29 - Live tracking acquisition. The star image lies at the left side of the picture and the fiber bundle right above. A zoom onto the bundle enabled to tick a mark onto a fiber to lock its position after having turned off the LED.	218
Figure 8.30 - Focal plane image when pointing at Vega with the first update version of the advanced tracking device.	219
Figure 8.31 - Focal plane image when pointing at Capella with the second update version of the advanced tracking device.	221
Figure 8.32 - Reduced spectrum of Capella centered at 10830 Å after combining the different observations from the last two nights.....	221
Figure 8.33 - NĒSIE spectrum of Capella (<i>black solid line</i>). The magenta spectrum corresponds to the atmospheric transmission tabulated by Hinkle et al. [93] and shifted for clarity by -1.0 . The red and blue tags indicate the expected wavelengths respectively of the most prominent primary and secondary spectral features.....	223
Figure 8.34 - Zoom on the spectral region around the <i>He</i> λ 10830 triplet. The atmospheric transmission is now overplotted on the NĒSIE spectrum. The other symbols are as in Figure 8.33. .	224
Figure B.1 – Overview of the control software manual (<i>top</i>) and automatic (<i>bottom</i>) modes.....	247

List of tables

Table 1.1 - Scientific requirements on the near-infrared spectrograph	5
Table 1.2 - Characteristics of the TIGRE telescope	6
Table 1.3 - Characteristics of the ARIES telescope	7
Table 1.4 - Technical requirements of the MOONS instrument	12
Table 2.1 - Identified detectors' characteristics	49
Table 2.2 - Main characteristics of the Photonic Science Snake camera	51
Table 4.1 - The 16 parameters describing a spectrograph instrument	71
Table 4.2 - Spectrograph's parameters after first and second runs	82
Table 4.3 - Comparison between spectrometer specifications obtained with both first resolution criterion and Bingham's spectrometer method to obtain a resolving power of 29 000	90
Table 4.4 - Sensitivity matrix assessing the individual effect on RMS spots of optical surfaces' alignment	94
Table 4.5 - Sensitivity matrix assessing the individual effect on RMS spots of optical surfaces' manufacturing	97
Table 4.6 - Typical tolerances for opto-mechanical constraints [69]	100
Table 4.7 - List of tolerances used when performing the overall budget of the instrument	102
Table 4.8 - Overall tolerancing budget results	103
Table 5.1 - Instrument requirements	129
Table 5.2 - Input parameters for the calculation of the atmospheric transmission with ATRAN	133
Table 5.3 - Photometric budget parameters summary	140
Table 5.4 - Upper wavelength limit for different <i>J-mag</i> for both cool and hot stars	150
Table 5.5 - Transmission factors of fibers	155
Table B.1 - List of devices controlled by the software	245

Abstract

This research contribution intends to introduce the conception of a new fiber-fed spectrograph, called NĒSIE, that operates in the near-infrared domain. This PhD thesis was part of a research project led by Prof. Rauw which focuses on massive stars. The final location of NĒSIE will be the TIGRE telescope located in La Luz, Mexico. The observational data provided by this instrument will help several research groups from the University of Liège to study massive stars. In particular, evolution models will be improved through the comparison of the collected spectra with theoretical models. This collaboration will therefore contribute to a better understanding of massive stars and the mechanisms that take place within these extraordinary objects.

The present manuscript will go through all the elementary steps of the design of the spectrograph: from the derivation of instrumental specifications to first light in Liège.

Key words: near-infrared spectroscopy, fiber-fed, massive stars, TIGRE telescope.

Ce travail de recherche a pour intention de présenter la conception d'un nouveau spectrographe, appelé NĒSIE, alimenté par fibres optiques qui opère dans le domaine proche-infrarouge. Cette thèse de doctorat faisait partie d'un projet de recherche mené par le Prof. Rauw centré sur les étoiles massives. La destination finale de NĒSIE sera le télescope TIGRE qui se trouve à La Luz au Mexique. Les données observationnelles fournies par cet instrument aideront plusieurs groupes de recherche de l'Université de Liège à étudier les étoiles massives. Plus particulièrement, des modèles d'évolution seront améliorés au travers de comparaisons entre les spectres collectés et les modèles théoriques. Cette collaboration contribuera dès lors à une meilleure compréhension des étoiles massives et des phénomènes qui se déroulent au sein de ces objets extraordinaires.

Le présent manuscrit parcourra l'ensemble des étapes élémentaires de la conception du spectrographe: depuis la dérivation des spécifications instrumentales jusqu'à sa première lumière à Liège.

Mots-clés: spectroscopie proche-infrarouge, fibres optiques, étoiles massives, télescope TIGRE.

Acknowledgement

I deeply acknowledge my co-Promoter Prof. Rauw for having offered me the opportunity to perform this PhD thesis within the frame of the ARC he supervised. The measureless amount of time he devoted me for any kind of advice, article and manuscript corrections, astrophysical and astronomical discussions was a precious help. Last but not least, I thank him for the several observations we carried out together at CSL facilities, which led to the instrument's first light.

I gratefully thank Prof. Rochus to have trusted me and proposed me as a proper candidate for this thesis. His vast instrumental knowledge was an extensive benefit during the thesis. The guidance he ensured as a Promoter during the last four years was particularly enlightening when I faced technical issues. Continuing the spatial adventure following my Master Thesis in his company at CSL was extremely fruitful.

Thanks to my entire committee for having supervised my thesis. The association of both scientific and technical knowledge within this committee was very productive to help facing the different issues I faced during the last four years.

Thanks to my colleague, and friend, Richard Desselte for having provided some hands-on help during the last four years. Our collaboration was a mutual rewarding experience which benefited to the development of both NIR and ultraviolet innovative instrumentation for the study of massive stars.

I acknowledge the team from the University of Hamburg for their support during this project. Their practical knowledge and experience in fiber-fed spectroscopy was very helpful during this thesis. I also thank them for their technical assistance to accommodate our instrument to the TIGRE telescope.

Many thanks to all CSL people who helped during the conception and tests of this instrument. A more specific attention goes to Jérôme who involved me in the ICON project and introduced me to

instrumental spectroscopy. His advice from conception to alignment helped in accomplishing these tasks. Thanks to Daniel, Michaël and Florian to have elaborated the fine control software of NĒSIE. Thanks to Nata for the numerous mechanical modifications he provided to the instrument enclosure. Thank you Marc to have offered me a laboratory to align and test the spectrograph. Eventually, thanks to the whole CSL staff for any involvement in my PhD thesis, from the first specifications to the first light in Liège.

Eventually, I heartily acknowledge all my family, my parents, my fiancée and my sisters without who I couldn't have led this thesis. Their support through the entire experience, and on a broader level during all my studies, was a key factor in accomplishing this task. The hardest aspect of the thesis was probably borne by those people and I apologize for any inconvenient it may have engendered. Thanks also to my sister for the great NĒSIE logo she provided to the project. Thanks to my father for the paint work of NĒSIE's enclosure and logo. Last but not least, thanks to my fiancée for her continuous kind presence and support particularly in the worst moments. I owe you all this successful story.

This research was funded through the ARC grant for Concerted Research Actions, financed by the Federation Wallonia-Brussels.

*Ir. Christian Kintziger
Faculty of Applied Sciences
University of Liège (ULiège)*

This page intentionally left blank.

Chapter 1

Introduction

1. Introduction

1.1 ARC project: massive stars, key players in the evolution of the universe

The global research project that involves the present PhD thesis aims at studying massive stars. This ARC (Action de Recherche Concertée) gathers three separate research groups from the University of Liège (ULiège): the Groupe d'Astrophysique des Hautes Energies (GAPHE), the Astrophysique Stellaire Théorique et Astérosismologie (ASTA) and the Centre Spatial de Liège (CSL). The GAPHE research group is in charge of the observation of massive stars at different wavelengths. These involve the TIGRE telescope (see Chapter 1.3.1) that will host the spectrographic instrument presented throughout this manuscript. The ASTA scientific unit on the other hand focuses on theoretical simulations which aim at studying the interior of massive stars and explain their evolution process. To do so, they use among other things the asteroseismology technique. The CSL eventually covers technical aspects and within this ARC, CSL is in charge of the conception of innovative scientific instruments to study massive stars.

The main question to which the research project intends to bring some enlightening answer elements is: *how do massive stars evolve?* Part of the answer may reside in the mutual influences that exist between the members of binary systems. The stellar rotation must also be considered to properly assess the induced effects on the evolution processes. The existence of a magnetic field and the mass loss experienced by such stars also need to be included in the stellar evolution models. The research project therefore intends to assess all these aspects by improving the associated models and collect useful data with the developed instruments. CSL is therefore in charge of the development of new dedicated instruments to provide scientific data to the other research units. These will be used to investigate the above hypotheses and improve the numerical models. A better understanding of massive stars will therefore result from this interaction between the groups involved in the ARC.

Today's instrumentation is largely dominated by oversubscribed telescopes which focus on a limited number of "fashionable" research topics [1]. The consequence is a lack of time for the study of massive stars, especially for long campaigns. The general actual opinion usually considers that large telescopes are better suited for spectroscopic astronomical purposes. This idea is correct when considering deep-sky observations that induce low-contrast imaging. For example, the observation of Quasars and Galaxies with small telescopes usually leads to low signal-to-noise ratio spectra and these small apertures do not actively participate to this research field [1].

The study of massive stars does not obey to this rule. Small telescopes can be used in association to low-cost instruments to conduct scientific research on stellar physics. The monitoring of the varying spectra of bright emission lines can for example be carried out with such observatories. Smaller telescopes are also naturally more numerous and easier to access than large observational platforms. This advantage therefore benefits to long-duration spectroscopic campaigns which can support other observations by larger platforms that focus on the determination of detailed spectroscopic parameters [1]. This interesting niche can therefore bring the light on poorly understood properties of massive stars and the present project intends to position our research group association as a key player in this field. This partnership intends to gather the individual expertise and give birth to a new instrument. This spectrograph will first be used on the TIGRE telescope that can be accessed by the University of Liège and is located in Mexico.

1.2 Astrophysical background

1.2.1 Massive stars

Massive stars exhibit large masses and extreme luminosities. These objects are usually the first ones we observe when targeting at galaxies [1]. However, these stars are also very rare: for one typical massive star in the Milky Way, there exist approximately a hundred thousand solar-type stars [2]. The enormous distance that separates us from the closest objects requires specific observing techniques. Indeed, standard imaging methods and even interferometric observations from combined telescopes are insufficient to provide enough resolving power. Most distance objects are therefore rather studied through spectroscopic analyses which are the key for understanding the cosmos [1]. The visibility of massive stars from large distances also enables probing the conditions of both their own environment and the intermediate space that separates us from those objects [3]. The observation of those rare objects may however be also problematic. Their visibility may indeed be threatened at early formation phases due to the surrounding dust. Some important evolution stages are also short in time and these objects usually appear in groups which complicates the understanding of evolution processes due to mutual interactions [4].

The spectroscopic analysis of bright massive stars does not require large telescopes as previously inferred. Indeed, the study of line profiles with the help of spectrographs can be performed with small telescopes when targeting massive stars. Moreover, the typical accessible time-scales for those objects range from a few minutes to several years. Their intense brightness also usually enables their observation from polluted areas close to urban centers. This benefits to amateur astronomy that can develop and supply useful complementary data to professional scientists. Long-term campaigns are usually also conducted with smaller telescopes as they are easier to access than oversubscribed large platforms.

Stars must exhibit an initial mass of approximately 8 solar masses to be qualified as massive [3]. These “cosmic engines” highly influence their environment. Indeed, during the major part of their life, they pour to the interstellar medium high quantities of ionizing photons. On the other hand, intense and fast stellar winds are generated due to their high luminosity and irradiate their surrounding medium. Massive stars are the major source of both ultraviolet ionizing radiation in galaxies and infrared-luminosity which originates from heated dust [2]. These stars also represent the major manufacturers of carbon, nitrogen and oxygen and enrich the interstellar medium. The turbulence induced by these exchanges with their environment strongly affects the formation of stars and planets and the structure of galaxies [4].

Their death generally occurs as a gigantic supernova. This final explosion ejects several components into the neighborhood. This violent event is indeed the source of the production of newly synthesized chemical elements [3]. The black hole formation that may follow when the star collapses is the source of gamma-ray bursts which is believed by many to be the most energetic phenomenon yet found [2].

The construction of accurate models of the evolution of massive stars is therefore of high importance to properly understand all these mechanisms. Internal mixing, mass loss and binarity are three elements that still need more accurate models [3]. This accomplishment cannot be achieved without the collection of observational data to compare with theoretical information. Indeed, defects of the models can only be highlighted by observations which in turn are used to improve the numerical simulations [2].

The ARC partnership therefore intends to shed new light onto these poorly understood processes. Modeling improvements are conducted by trying to include mechanisms such as stellar rotation, mass loss, magnetic field and binarity. On the other hand, new instrumentation is under study or development by the CSL to provide observational data and compare the results with theoretical predictions.

1.2.2 The need of a near-infrared spectrograph

The full understanding of astrophysical sources requires access to a rather wide wavelength range. Every wavelength domain provides another specific piece of information that is needed to solve the puzzle. However, some wavelength domains have been somewhat neglected in recent years, despite their enormous potential. This is the case for instance of the near-IR domain around 1-1.1 μm , notwithstanding the fact that this wavelength domain can be accessed from the ground. The main reasons for this situation are the decrease in sensitivity of conventional Charge-Coupled Device (CCD) detectors in this region and the fact that most instruments are designed for longer wavelength studies, e.g. to study the *J* (1.22 μm), *H* (1.63 μm) and *K* (2.19 μm) bands which are largely used in photometry.

The Near-IR (NIR) domain around 1 μm has an enormous diagnostic potential for stellar activity and stellar winds, prominent features of massive stars. Indeed, these stars are very hot and luminous. Their strong UV radiation fields drive energetic and dense stellar winds that have a strong impact on the surrounding interstellar medium. In this context, the wavelength domain near 1 μm is particularly interesting as it contains many spectral lines whose profiles provide useful information about stellar winds over almost the entire range of stellar masses. For example, this region contains the *He I* λ 10830 line, one of the few unblended *He I* lines. As it forms over almost the entire stellar wind, it has a huge diagnostic potential for models of stellar winds. Its morphology ranges from an absorption line in stars with low density winds to a broad P-Cygni profile in Wolf-Rayet stars [5] [6]. In some cases, the emission part of the P-Cygni profile is flat-topped, in other cases it is rounded or strongly peaked [7]. Whatever the morphology, it is related to the velocity law in the wind and can thus provide unique information. Moreover, this line is a good indicator of variability in the wind [7], especially for the so-called Luminous Blue Variables, which are in an intermediate evolutionary stage between *O* and Wolf-Rayet stars where important quantities of material are lost.

Last but not least, phase-resolved observations of the *He I* λ 10830 line in massive binary systems are a powerful diagnostic of wind-wind interactions in these binaries [8]. But *He I* λ 10830 is of course not the only interesting line in this spectral domain (see Figure 1.1). Other features include *He II* λ 10124, *Pa* δ and *Pa* γ , *C III* and *C IV* lines...

On the other hand, this spectral region is also of interest for studies of the activity of low mass stars. In cool *M* dwarf stars, chromospheric activity is a wide-spread phenomenon which manifests itself through quiescent line emission (*Ca II H & K*, *H α*) in the optical in addition to dramatic flaring events. Recently, it has been shown that emission in the higher order Paschen lines of hydrogen (*Pa* β , *Pa* γ , and *Pa* δ) as well as *He I* λ 10830 is a good proxy of a strong flaring activity [9] [10] [11]. Also, in the case of solar-type stars, *He I* λ 10830 and the Paschen lines are excellent indicators of chromospheric activity [12].

Moreover, this spectral range provides also key information on the circumstellar environment of cool giants. Indeed, in some cool giants such as Arcturus (*K2 III*), a highly variable *He I* λ 10830 emission has been observed and was attributed to shock waves in an otherwise elusive chromosphere [13]. Yet

in other objects such as *HD6833 (G9.5 III)* the line was found in absorption, but with a bluewards extension that reveals the existence of a stellar wind [14].

Finally, the *He I λ 10830* line is also of major interest for the study of accretion in classical T Tauri stars. T Tauri stars are low-mass pre-main sequence stars that are still accreting material from a circumstellar disk. The emission lines observed in the spectra of these stars form at the star-disk interface or in the inner disk region. These regions have a complex topology. The high opacity of *He I λ 10830* makes it a sensitive probe of both the accreting matter, in emission, and the outflowing gas via the frequently detected absorption features. Observations of this line in T Tauri stars can thus be used to constrain the wind geometry of such accreting objects [15] [16].

In summary, it is obvious that the spectral region around the *He I λ 10830* line has a huge potential for many topics in stellar astrophysics. This is the reason why several research groups from Liège University have joined their forces to develop a spectrograph that covers this wavelength domain with the goal to install it at the TIGRE telescope.

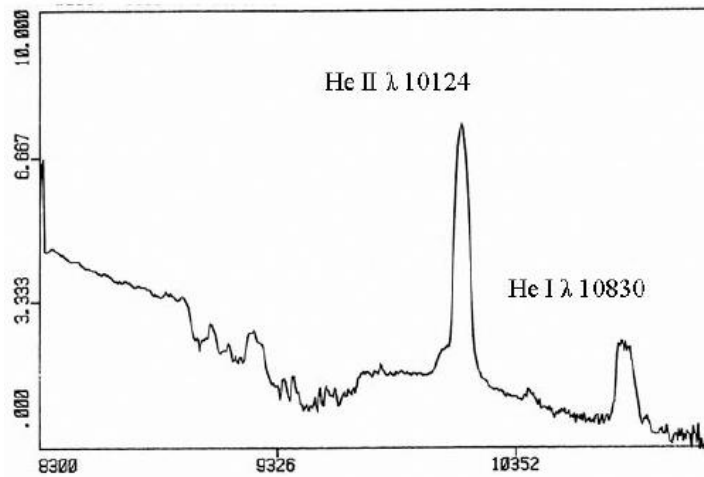


Figure 1.1 - Observation of the near-IR spectrum of the Wolf-Rayet star *WR136* recorded with a CCD detector. The absorption features between 8900 Å and 1 μ m are due to the Earth's atmosphere. (Figure courtesy Jean-Marie Vreux).

1.2.3 Scientific requirements

Scientific requirements were specified concerning the performances of the instrument under study (see Table 1.1). The conception of the spectrograph must be driven by these specifications in order to obtain an instrument which is able to do the intended science. This way, the quality of the obtained data will be high enough to tackle the scientific problems and answer open questions. Those specifications focus on spectral range, resolving power and photometric budget.

The required spectral range extends over 100 *nm* in the near-infrared *J*-band. The possibility to extend this latter from 940 to 1400 *nm* is considered as a goal performance. The associated resolving power must be at least equal to 10 000 but a value of 20 000 is preferred. The typical observation time cannot exceed half an hour when considering target magnitudes of 6 in *V*-band.

Eventually, a sky measurement must be carried out to properly enable its subtraction from the data as explained further in this chapter. The wavelength calibration accuracy must also be accounted for when designing the calibration box of the instrument.

Parameter	Requirement	Goal
<i>Spectral range</i>	1000 – 1100 nm	940 – 1400 nm
<i>Resolving power</i>	10 000	20 000
<i>Target magnitudes</i>	$V < 7$	$V < 9$
<i>Signal-to-noise ratio in continuum</i>	100 at $V = 6$	100 at $V = 7$
<i>Typical exposure time</i>	15 – 30 min	15 min
<i>Simultaneous sky measurements</i>	yes	yes
<i>Wavelength calibration accuracy</i>	$\delta\lambda/20 = 0.05 \text{ \AA}$	$\delta\lambda/20 = 0.025 \text{ \AA}$

Table 1.1 - Scientific requirements on the near-infrared spectrograph

1.3 Considered telescopes

1.3.1 el TIGRE

The TIGRE, formerly called Hamburg Robotic Telescope (HRT), is a fully robotic telescope located in La Luz, Mexico (see Figure 1.2) [17]. This private telescope is installed at an altitude of 2400 meters on a site operated by the University of Guanajuato. TIGRE is a collaboration between the universities of Hamburg (Germany), Guanajuato (Mexico) and Liège (Belgium). Currently, the only scientific instrument under operation on the TIGRE is the Heidelberg Extended Range Optical Spectrograph (HEROS), a double-channel spectrograph fed with the telescope's light through an optical fiber. First spectroscopic light in La Luz was achieved in April 2013 and regular automatic observations from Hamburg started on August 1st 2013.

The TIGRE is a $F/8$ Nasmyth telescope whose primary mirror has a diameter of 1.2 m. The typical seeing at the La Luz site amounts to 2 arcsec on average, approaching 1 arcsec for good nights. Therefore, this telescope is particularly well suited for the study of bright stars. Indeed, as previously noticed, this small telescope totally falls within the class of apertures that can enable intensive observations of (massive) stars.

The telescope benefits from a modern Alt-Az mount and concentrates light through a 3-mirror assembly to a Nasmyth focus. The spectrographic instrument that we present will be connected to the telescope through a fiber whose entrance will be placed at the currently vacant Nasmyth focus of the TIGRE telescope. The other end of this fiber will feed with light the instrument located in a separate building neighboring the telescope dome.

Figure 1.2 illustrates the TIGRE dome with the neighboring building which contains the HEROS spectrograph. Further modifications including another building are required to accommodate our NIR fiber-fed instrument. This separate room should be installed next to the HEROS enclosure and benefit from its own air conditioning system. Indeed, large temperature variations occur between day and night and this system will stabilize the instrument temperature during the day to avoid severe thermal perturbations.



Figure 1.2 - The TIGRE telescope at La Luz observatory site, Mexico [18].

The characteristics of the TIGRE telescope are summarized in the table below.

Parameter	Symbol	Value
<i>Diameter</i>	A_{tel}	1.2 m
<i>Focal length</i>	f_{tel}	9.6 m
<i>Typical seeing</i>	σ	2 arcsec
<i>Good seeing</i>	σ	1 arcsec

Table 1.2 - Characteristics of the TIGRE telescope

1.3.2 3.6M DOT (ARIES)

3.6M DOT is a 3.6 m Ritchey-Chrétien $F/9$ telescope installed at the Devasthal Observatory site, India. Equipped with one axial port and two side ports, this telescope belongs to the Aryabhata Research Institute of Observational Sciences (ARIES) and was first activated on March 31, 2016.

The Devasthal site is located far away from any urban development and benefits from about 210 spectroscopic nights a year [19]. A detailed survey which lasted several years led to the careful selection of this location featuring reduced temperature variations, low relative humidity outside the rainy season and low wind speeds. Eventually, the mean observed seeing amounts to 1.1 arcsec on the ground though a better value of 0.7 arcsec is estimated at the telescope height [20].

The first generation focal plane instruments consist in a faint object spectrograph and camera, a high-resolution fiber-fed optical spectrograph, an optical-near infrared spectrograph and imager and a CCD optical imager [20]. On the longer term, the spectrograph we designed may be a good candidate for visiting this telescope on one of its side ports through its fiber connection. Indeed, Belgium has a guaranteed access to 7% of the observing time on this telescope.

The versatile interface that represents the use of fibers enables to design an instrument that may be operated at several telescopes. Optical fibers facilitate this opportunity as they promote the separation of the spectrograph from the telescope focal plane. A disconnection occurs and adapting the fiber with suitable connectors enables to go from a telescope to another.

The characteristics of the ARIES telescope are summarized in the table below. The larger aperture of this telescope will benefit to the observation time. For exact photometric budget calculation, the longer focal length must also be accounted for as a larger star image may be induced depending on the local seeing.

Parameter	Symbol	Value
Diameter	A_{tel}	3.6 m
Focal length	f_{tel}	32.4 m
Typical seeing	σ	1.1 arcsec
Good seeing	σ	0.7 arcsec

Table 1.3 - Characteristics of the ARIES telescope

1.3.3 Expected seeing and image size comparison

When designing a fiber-fed instrument, a particular care to the telescope-fiber matching is required. Indeed, as much light as possible must be transmitted from the telescope to the fiber in order to minimize the required integration time. In order to collect the entire target light, the fiber core should therefore match the star image diameter, which depends on the seeing at the observation site. The typical seeing that is observed at the selected telescope location may therefore be considered in first approximation to assess the required fiber core size.

Figure 1.3 illustrates the predicted geometrical star image diameter as a function of the seeing for both identified telescopes. The observed target image size varies with the local seeing and selected telescope. Therefore, the maximum predicted star image should be considered in order to adapt to the worst observation case. However, instrumental limitations may appear due to manufacturing capabilities as will be noticed in Chapter 4.3.6. This may limit the entrance slit width of the spectrograph and the fiber core size as a direct consequence. An identified technique to overcome this issue will also be presented.

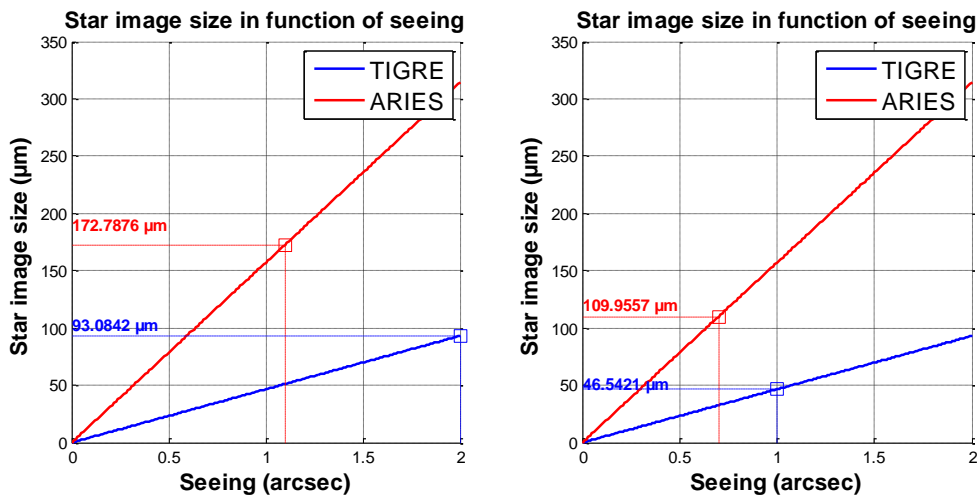


Figure 1.3 – Geometrical star image size as a function of seeing for both considered telescopes. Typical (left) and best (right) seeing conditions are also depicted.

1.4 Near-infrared fiber-fed spectroscopy: from pioneers to nowadays innovators

This chapter does not intend to list the full evolution story of NIR fiber-fed spectroscopy as it cannot be exhaustive and introducing all the elementary projects is beyond the scope of this work. The technology development of fiber-fed spectrographs in general is shortly summarized in Chapter 2.4.1. Chapter 1.4.1 on the other hand intends to illustrate the first NIR fiber-fed spectrograph ever built and the associated lessons to be learnt for our own project. The evolution of the technology is illustrated with a typical instrument that is employed nowadays in Chapter 1.4.2. The comparison between the two examples will clearly highlight the achieved improvements within a few decades. Each introduced project is presented in sub-chapters depicting the individual components of the optical chain assembly. This way, every element optimization can be understood and some heritage learnt for our own spectrograph. For further examples, reference [21] establishes a rather detailed list of all multi-object fiber-fed spectrographs and projects in 1997.

1.4.1 ISIS IR

Description

ISIS-IR is the first near-infrared fiber-fed spectrograph that was developed by Dallier et al. in the early nineties [22]. The target waveband initially included the *J*-, *H*- and *K*-bands (1-2.5 μm). This spectrograph was first tested at the 2 *m* telescope from the Pic du Midi in the south of France. Then, second tests occurred at the Mont Mégantic in Québec, Canada, with a 1.6 *m* telescope [23]. After these first assessments of the overall system performances, the spectrograph moved to the Canada-France-Hawaii Telescope (CFHT) for commissioning and observations [24].

The principal goal of this project was to mimic the already widespread visible techniques of multi-object spectroscopy to the NIR domain. Indeed, some parts of this wavelength range do not need spectrographic instruments to undergo severe modifications to properly operate in the NIR domain. The investigations of these pioneers are explained further below as they will be very useful for our own purpose.

Spectrograph

The first selected configuration for the spectrograph was the Czerny-Turner. Both the collimator and the camera were on-axis and several obstructions decreased the light transmission. These add to the one induced by the telescope because of another property of fibers: scrambling. The radial pattern of light that reaches the fiber core is mixed along the fiber length. The obstruction is thus not visible anymore at the spectrograph side of the fiber (see Chapter 2.4.2 for further explanations). The resolving power of this first setting was equal to 400 and 700 in *J*- and *K*-band respectively. The second run used other gratings and the available resolving powers were 350, 1400 and 3000 in *J*-band or 550 and 2300 in *H*-band. The third run implemented an Ebert-Fastie configuration with resolving powers of 400, 2000 and 10000 in both *J*- and *H*-bands.

According to the authors, the selected spectral range (1 to 2.5 μm), i.e. non-thermal IR, does not require the spectrograph to be cooled and the operation is similar to the visible waveband [22]. Only for the *K*-band is the cooling gain important as it averages between 1 and 2 magnitudes [23]. On the other hand, a cold interference filter in front of the camera that matches the observed spectral band already decreases the background level. This effect is almost negligible in the *J*- and *H*-bands.

Fibers

The use of silica fibers for spectroscopy was already common practice and for example employed to perform multi-object spectroscopic analyses. The transmittance of these light connectors from the telescope to the spectrograph is however limited in the K -band. On the other hand, J - and H -bands performances of dry, i.e. low OH content (see Chapter 2.4.2), silica fibers are perfectly acceptable [23]. Therefore, Dallier et al. first employed 20 m fluoride fibers instead because of their low spectral attenuation in the near-infrared and especially over 2 μm [22]. These had never been selected for that purpose before and were successfully tested for the first time at the Pic du Midi. The observed Focal Ratio Degradation (FRD), which characterizes the widening of light beam by the fiber, was worse than the one measured with typical silica fibers. The light injection with a fast ($f/5$) beam of light was however sufficient to minimize those losses. Since the telescope f-ratio was equal to 25, they used a focal reducer to adequately connect the telescope to the fiber. These fiber losses are deeply investigated in Chapter 2.4.2 but a first conclusion here is that the injection f-ratio is of major importance for the efficiency of fibers to transmit light from the telescope to the spectrograph.

The authors also pointed out that a proper light propagation occurs in a fiber when the cladding thickness equals several times the wavelength. This means packing several fibers into a bundle leads to light losses due to the absorption between the adjacent cores, especially at longer wavelengths such as the near-infrared domain. A solution already foreseen at that time was the use of a microlens array to properly sample the target flux and refocus the light only on fiber cores. The use of a fiber bundle was also seen as a suitable way for sky subtraction since the sky background is large in the J -, H - and K -bands. Eventually, their technique to align the star image onto the fiber was a drilled metallic mirror that incorporated the fiber. The reflected light was directed to a guiding camera. Minimizing the light on the edges of the hole therefore ensured a proper transmission through the fiber.

The second observation run featured an improved fiber bundle of 7 elements. The fibers exhibited a hexagonal pattern at the telescope side to be able to either sample the sky background with 6 surrounding fibers around the star-dedicated one or perform small area spectroscopy [22]. Unfortunately, this second run only used a satellite fiber because two others were broken on site.

The third update of the instrument implemented 15 m regular dry silica fibers. The K -band investigation was therefore limited as their transmission rapidly falls at 2 μm . In any case, the high background noise due to the “warm” spectrograph configuration did not enable its use far in the K -band. The hexagonal bundle packed 51 fibers to sample the object and 10 others to measure the surrounding sky background. As before, the bundle was reshaped at the spectrograph side to form a pseudo slit.

Detector

Another difference with the visible domain is the required use of a specific IR detector [22]. At that time, the availability of NIR cameras was growing up and enabled the development of NIR spectroscopy. As explained in Chapter 2.8.1, the early nineties correspond to an epoch where great progress was performed in the development of NIR detectors such as the NICMOS (Near Infrared Camera and Multi-Object Spectrometer) camera for the Hubble Space Telescope (HST). The first camera they used was a 32 by 32 $InSb$ CID (Charge Injection Device) cryogenic detector, a replica of the 128 by 128 CIRCUS camera under use at CFHT. While typical integration times of several minutes were provided by such cameras, they were initially limited to a few seconds due to an unknown leakage current.

The second run at Mont Mégantic benefited from an exceptional detector: the MONICA (MONtréal Infrared CAmera) that was based on a NICMOS chip. This was at the time one of the best available NIR detector in the world [23]. With that camera, the residual background level was about $80 e^-/s$ and $1500 e^-/s$ in J -band and H -band respectively. These were due to the removal of the cold optics within the camera assembly for specific purpose of the authors and limited the observation of faint objects. The last run featured an evolved NICMOS 3 chip, the RedEye camera of the CFHT. It was that time a 256 pixel height camera that enabled the imaging of the larger bundle manufactured for this observation.

Results

Their first observation led to the record of several spectra of M -type dwarfs whose magnitudes in H - and K -bands ranged between 4 and 5. Indeed, the large dark current of the first detector forced the observation of bright objects even in low resolution mode. Since the overall efficiency of the system was evaluated to 1.5 to 2%, the quality of the spectra was rather limited. However, these successful first tests motivated the second run with a better camera.

The second run successfully imaged the spectrum of a large sample of astronomic objects both at low and high resolving powers in the J - and H -bands. The camera did not enable observing in the K -band due to an insufficient full well capacity. The improved results inspired the use of this bench spectrograph with a third updated version at the CFHT [24].

The third observation tests were performed at the CFHT. The adapted system enabled the observation of a limiting magnitude in J -band of 17 to 18 within a one hour integration time [25]. A sample of 37 stars was studied and medium resolution spectra recorded. The subsequent evolutions of the setup therefore enabled to obtain quality spectra and compare them to those observed with the ESO NTT IRSPEC spectrograph.

Conclusion

Dallier et al. were pioneers in near-infrared fiber-fed spectroscopy. They investigated the required conditions to simply translate the knowledge acquired in the visible range to the near-infrared domain [26]. They benefited from the growing availability of specific NIR detectors and demonstrated that the J -band was accessible without a deep-cooling of the instrument. Indeed, the new detectors at that time exhibited narrower spectral sensitivity, i.e. the upper cutoff wavelength was shorter than before (typically $2 \mu m$ against $5 \mu m$). They demonstrated that a reasonable wavelength limit to perform warm NIR spectroscopy is between 1.4 and $1.8 \mu m$. The J -band thus fulfills the condition. The use of fluoride fibers also appears useless if concentrating onto the J -band. Fluoride was mandatory for the K -band and is the reason why Dallier et al. first employed such an exotic material. But the K -band appears as non-suitable for warm instruments and the fragility of this substrate is not sufficient for fiber bundles. Therefore, the authors suggest the use of dry silica fibers instead as they propagate light with high efficiency over long distances for wavelengths up to $1.8 \mu m$ [26].

The limit on “warm” NIR spectroscopy from Dallier et al. actually slightly differs from the most commonly known value of $2.2 \mu m$. This latter is indeed located at a turnoff in spectral energy distribution: the background is dominated by the OH airglow emission (see Chapter 2.2.1) at shorter wavelengths whereas thermal emission prevails further in the NIR [26]. The major reason is that the background level in a non-cooled spectrograph is not dispersed but rather integrated over the considered band. A typical value calculated by Dallier et al. for the background level observed by a

warm spectrograph in the J -band is equal to 0.3 ph/s/pixel at 273 K . They also propose a convenient way to decrease this value by a factor 10: implementing a relay lens that creates a pupil inside the camera Dewar to limit the viewing factor between the sensor and the instrument enclosure. This result shows that the J -band is not dominated by thermal noise but rather by the detector dark.

An important remark concerns the detector choice. If a warm spectrograph enables observing in the J -band the same way we proceed in the visible, this is not the case in K -band as previously mentioned. This also means that the chosen detector for operating in J -band must either be insensitive to the K -band or be equipped with a cold filter to both reject K -photons and not radiate any. For example, using an $InGaAs$ detector whose cutoff wavelength is equal to $1.7 \mu\text{m}$ does not require any cold filter but the $HgCdTe$ (MCT) technology, which is sensitive up to $2.5 \mu\text{m}$, does. Eventually, when using cold J - and H -filters, one must also pay much attention to their wing leakages in K -band and potentially install a second cold thermal filter (cutoff at $1.9 \mu\text{m}$ for example) [26].

Dallier et al. also propose proper conditions to effectively remove the background level from the observations. Recording dark frames naturally leads to a measure of this noise level. The location of the shutter is however important and impacts on the quality of these measurements. Indeed, this shutter should be set as far as possible from the detector to measure the overall instrument thermal noise. The best location would thus be before the fiber [26]. On the other hand, beam switching techniques (see Chapter 2.2.2) may be used to remove both the sky and thermal backgrounds in a single shot. A last remark concerns the recording frequency of those dark frames. Since the instrument temperature may highly vary during the night, they should not be taken only before and after the night but rather distributed over the entire observation session. If the beam switching occurs at a high enough frequency, it may lead to better results than dark frames [26].

1.4.2 MOONS: the Multi-Object Optical and Near-infrared Spectrograph

Description

MOONS is a new fiber-fed instrument under development for the Very Large telescope (VLT). This instrument intends to pave the entire 500 arcmin^2 Nasmyth focal plane of the VLT with 1024 fibers. The wavelength coverage extends from 0.8 to $1.8 \mu\text{m}$. The spectrograph will feature both medium and high resolution modes. The combination of the telescope grasp and the instrument features will provide observational data to study galaxy formation and evolution over the entire history of the universe. The high resolution mode will also enable the study of chemical abundances of stars and provide a follow-up to the ESA GAIA mission. This high multiplexed, i.e. which employs a large number of fibers, spectrograph will therefore cover the optical and near-infrared regions and meet the requirements of both extragalactic and galactic scientists [27].

Spectrograph

The instrument configuration of MOONS incorporates two identical cryogenic spectrographs which collect both 512 fibers. The individual spectrographs incorporate three channels that are separated by dichroics. These latter are located after the collimator so that three separate gratings are then used to disperse the light. The individual covered spectral regions by each channel are the I -band [$0.79 - 0.94 \mu\text{m}$], the YJ -band [$0.94 - 1.35 \mu\text{m}$] and the H -band [$1.45 - 1.81 \mu\text{m}$]. This configuration provides a medium resolving power over the complete required spectrum, more specifically: $R > 4000$ in the YJ -band, $R > 6000$ in the H -band and $R > 8000$ in the I -band. On the other hand, two spectral regions located within the YJ - and H -bands benefit from a high resolving

power greater than 20000. Eventually, the whole instrumental setup is installed inside a vacuum chamber that enables cryogenic cooling. The spectrograph requirements are summarized in Table 1.4 [28]. Additional capabilities are foreseen and under study, these intend to increase the resolving power within some spectral regions and extend the spectral coverage bluewards [29].

Parameter	Requirement
Total wavelength coverage	0.8 to 1.8 μm
Observing modes	Medium Resolution (MR) and High Resolution (HR)
Resolving power in High resolution mode	$\approx 4000 - 6000$
Resolving power in Medium resolution mode	≥ 7000 and ≥ 20000
Spectral coverage in Medium resolving power	0.8 to 1.8 μm
Spectral coverage in High resolving power	$[0.8 - 0.9 \mu\text{m}] + [1.17 - 1.26 \mu\text{m}] + [1.52 - 1.53 \mu\text{m}]$

Table 1.4 - Technical requirements of the MOONS instrument

Fibers

The multiplexing of the instrument therefore amounts to 1024 fused silica fibers. These are deployed over the total field of view of the VLT, which is approximately equal to 500 arcmin^2 (25 arcmin diameter). A field corrector, which consists of two 880 mm large and 110 mm thick lenses, is installed upon the fibers' location in order to improve the optical quality over the whole focal plane. Each fiber is equipped with a micro-lens to make the input f-ratio of the telescope faster. This technique was already foreseen by Dallier et al. and has been developed since then. This common practice intends to reduce the FRD losses of fibers (see Chapter 2.4.4 for detailed explanations). The telescope f-ratio of 15 is reduced to 3.65 which limits the fiber losses to only 2.5% at the $f/3.5$ collecting optics. Each micro-lens samples 1 to 1.2 arcsec on the sky (seeing-limited). The fibers are packed into bundles of 10 to 15 elements to form sub-slits and these latter are then co-aligned to compose the entrance slit of the spectrograph.

An automated fiber positioning system is foreseen. This technology has also been developed since Dallier et al. first investigated NIR fiber-fed spectroscopy. The 1024 fibers may actually be positioned individually or in pairs. This enables the near sky background to be sampled only a few arcsecs away from the target. The technique of cross-beam switching also advised by Dallier et al. is foreseen when observing faint targets. Two techniques were initially investigated to position the fibers: a micro-mechanical pick-off system and a "pick and place" spine positioner. The first system, which has been selected, consists in two rotating arms that position the fiber within a patrol field of $\sim 1 \text{arcmin}$. Some overlap between the sampled fields exists to avoid uncovered regions. The spine positioner on the other hand proposed to use another methodology: a dozen of radial arms pick and place the fibers at the target location. Eventually, the required time to reposition all the fibers should fall between 2 and 5 minutes.

The fibers were extensively tested in terms of cryogenic behavior, FRD properties and resistance to twisting. The results were extremely encouraging and it was shown for example that the fibers could undergo twisting of several rotations before their transmission changed by 2% [29]. This result shows that fibers are very robust light connectors between telescopes and spectrographs.

Detector

The selected detectors for both identical spectrographs are 2 specific NIR detectors and a CCD camera. The NIR sensors are the famous Hawaii-4RG-15 μm device from Teledyne Imaging, the same sensor (or an evolution of it) as the one presented in Chapter 2.8.7. These cryogenic sensors, certainly the best available up to date, are selected to capture photons from the *YJ*- and *H*-bands. On the other hand, a *4k* by *4k* optical CCD from e2v technologies is foreseen to image the *I*-band channel.

Status

MOONS has been selected by ESO as a third generation instrument for the VLT in 2013. The current project status has reached the Final Design Review (FDR) and the first operations are foreseen at the end of 2020.

Conclusion

Since the first NIR fiber-fed spectrograph was tested by Dallier et al., technology developments have improved all the elements of the telescope-spectrograph optical chain. This evolution enables now to perform highly-multiplexed fiber-fed spectroscopy with a high transmission efficiency. Thousands of targets are observed at the same time and a large data quantity is generated at each observation. Several sciences cases are also investigated with the same instrument thanks to ingenious optical designs and the versatility that precise actuators can provide nowadays.

Telescopes have grown in size and the associated spectrographs too. Typical optical elements of half a meter in diameter have become common practice. The optical manufacturing of large and complex, i.e. exotic shapes such as mirrors, lenses and gratings enables the optical engineer to provide designs that were several years ago impossible to manufacture (and sometimes impossible to simulate). The properties of these elements have also improved. For example, the typical overall throughput of the MOONS spectrograph amounts to 50% which is dramatically better than the few percent achieved by Dallier et al. [29]. The manufacturing, preparation and handling of fibers have also evolved and ultra-low OH content bundles now reach very high transmission in the NIR. FRD properties have also been largely studied and techniques have been developed to avoid such losses. Micro-lenses connectors are for example now available and enable the fibers to be properly connected with the telescope light beam.

Another technologic breakthrough was the development of high efficiency detectors for the NIR. These now propose high quantum efficiencies and low dark currents. Cryogenic solutions are employed to decrease this noise signal to a few $e^-/s/pix$ only while a few hundreds or thousands polluted the scientific signal at the time of Dallier. Their observation in *K*-band was for example unsuccessful and has now been enabled thanks to the development of technologies able to operate under deep cooling conditions. Both mechanical and optical design as well as electronics must indeed ensure their operation in this environment since not only the detector is located within a Dewar. In addition to the thermal aspect, the size of the detectors has increased as a typical format is *4k* by *4k* in order to support large multiplexed observations. Mosaics of detectors also now exist.

The automation of the fiber positioning system was mandatory with the growing number of fibers used to sample the telescope focal plane. Accurate positioners were therefore developed to locate the fibers onto the targets within a few microns only. This ensures both quick pavement of the focal plane and high transmission through the fibers. The device proposed for MOONS is for example able to position

more than a thousand of fibers within a few minutes only whereas hours or days of work were previously required to manufacture inflexible one-shot slit masks (see Chapter 2.4.1).

The evolution of fiber-fed spectroscopy has also been made possible thanks to the development of both high efficiency hardware and software solutions. Indeed, a large quantity of data is recorded every night due to the large multiplexing capabilities of new spectrographs. Their higher efficiency also leads to lower integration times and further increases the potential number of observations within a single night. Data treatment is therefore also an important point when developing new instruments on large telescopes. If recording a large amount of spectra becomes more and more frequent and widespread, it is mandatory that efficient recording hardware and algorithms are studied to treat these observations.

Eventually, such complicated and expensive instruments cannot be developed by small groups and involve a large consortium. For example the MOONS instrument brings together scientists from all over the world: Chile, France, Italy, Portugal, Switzerland and the United Kingdom are members of the scientific group for example. Both technical and astrophysical expertise is gathered within this collection to investigate the potential solutions to carry out the scientific experiments. This large scale spectroscopy slightly differs from the exploration of smaller groups but illustrates the most up-to-date technology developments that are employed and which scientific questions can be assessed by the scientists.

1.5 Conclusion

The global research project that involves the present PhD thesis was introduced. The focus of these studies is on the evolution of massive stars. Several research groups have joined their forces to clarify unanswered questions and reach a better understanding of the problem. In this context, CSL is in charge of developing a new spectrograph to obtain fine spectra of massive stars in the near-infrared domain. This instrument will indeed provide data within a spectral waveband that suffers from a lack of dedicated ground-based instruments at the moment. Moreover, massive stars are suitable targets to perform astronomy campaigns with the help of small telescopes. This niche was therefore selected for its high-potential scientific return by the elaborated partnership. The data provided by this instrument will also help astrophysicist partners to improve their evolution models by comparing both theoretical simulations and observations.

The scientific requirements elaborated by the scientists from GAPHE and ASTA were introduced. These must be fulfilled by the instrument under study to provide useful data to these research units. The target telescopes for which the University of Liège benefits from some observing time were then highlighted. These will be the first candidates to host the near-infrared spectrograph. In a first step, the instrument will be installed on the TIGRE telescope in Mexico.

Eventually, two near-infrared fiber-fed spectrographs were presented in order to illustrate the evolution of this technology over the years. Pioneers in NIR fiber-fed spectroscopy were Dallier et al when they developed the first prototypes of ISIS-IR. Their experience showed that accessing the J -band (and some of the H) with the same approach as for visible light was possible under some conditions. Other fruitful lessons can be learnt from their observations. The use of a proper detector, such as InGaAs, is advised to avoid the implementation of a cold filter which repels the environment thermal background. Dry silica fibers should be used if observing in the K -band is not foreseen. Then, appropriate dark subtraction is mandatory to isolate the scientific signal from the background level. All these considerations can be found in innovative instruments proposed nowadays to assess the scientific questions of astrophysicists such as MOONS. The techniques have evolved according to the technology developments that have been conducted over the years. The automation of the fiber positioning is now very efficient and covers the largest focal planes. The cryogenic solutions to cool the entire instrument reduced the dark noise to a few $e^-/s/pix$ at the detector level. The acquired knowledge on the fiber usage and manipulation enables a high transmission by avoiding the FRD losses for example. The combination of these progresses achieved at every level of the optical chain leads to efficient light gathering and the observation of very faint objects at high resolving powers.

Experience can be gained from both the investigations of pioneers and present-day state-of-the-art techniques. For example, the spectrograph instrument under study does not require any overall deep cooling if the proper solutions are selected. The specific cooled detector that is required to benefit from a high efficiency in the detection of infrared radiation should exhibit a short upper cutoff wavelength in a first step. Otherwise, a cold filter should be employed in front of the sensor. It is noticed that deep cooling systems are usually selected for those detectors as they are characterized by high dark currents at room temperature. A careful design is also mandatory to efficiently avoid and/or record the sky background. The optimization of the telescope pointing may also help in reducing this source of noise while dealing at the same time with the dark background. Suitable locations of shutters should also be identified.

Chapter 1

Chapter 2 focuses on the technical aspects related to the ground-based spectroscopic observation. As previously noticed, each element of the complete observation chain indeed requires specific considerations to optimize the photon flux transmission from the remote star down to the detector.

Introduction

Chapter 2

Technical considerations related to
ground-based spectroscopy

2. Technical considerations related to ground-based spectroscopy

2.1 Observation windows

Observing from the ground is not possible all the way through the electromagnetic spectrum due to absorption by the Earth's atmosphere. "Atmospheric windows" are wavelength intervals through which light can propagate down to the ground without being absorbed. Two major observation bands are located in the visible and near-infrared as well as in the radio band as shown in Figure 2.1 [30]. These regions of the spectrum enable the observation from the ground while others require going to space, or using balloons or sounding rockets for example.

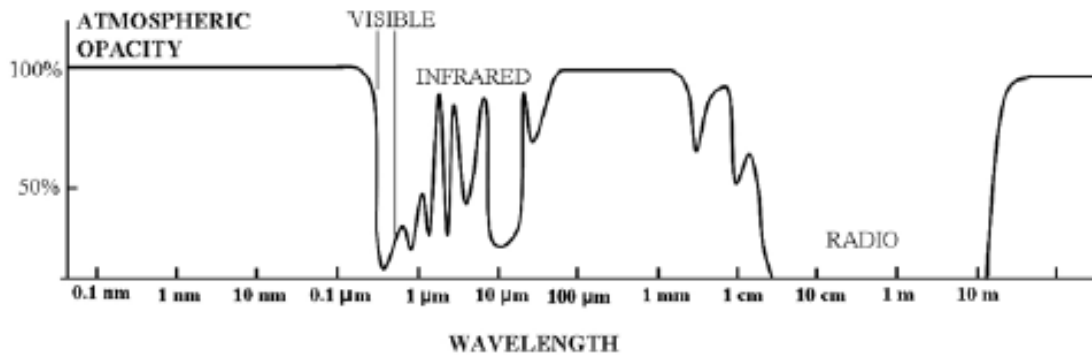


Figure 2.1 - Atmospheric opacity as a function of wavelength [30].

These limited spectral windows can be predicted with the help of models. ATRAN is one of them developed by Steve Lord and some results of the atmosphere transmission spectrum are presented below [31].

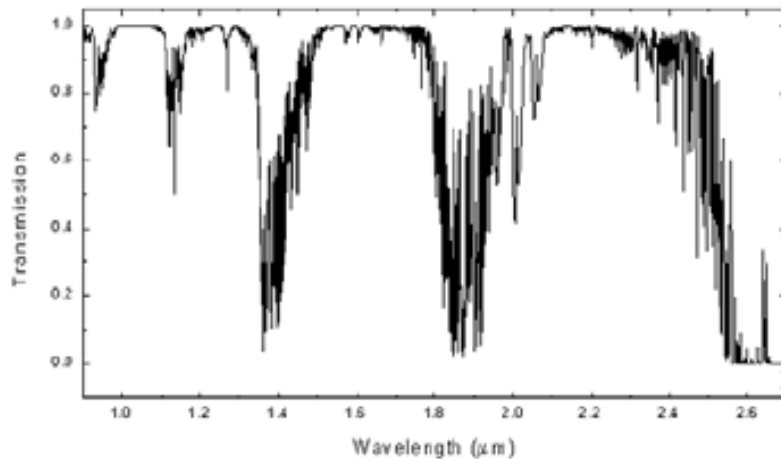


Figure 2.2 - Illustration of atmospheric windows around 1 μm for the Mauna Kea site (altitude 14 000 ft) [30]

The atmospheric opacity is due to water vapor and carbon dioxide and varies with altitude. Water vapor is an absorbing contributor that is highly variable with temperature and altitude in comparison with other gases whose concentrations are usually constant (except ozone). The amount of water along the line of sight is usually defined as "precipitable water" and measured in *mm* when considering a given observing site. This parameter defines the total amount of water that adds up along the optical path above the observatory and is therefore a characteristic of the local atmospheric absorption.

Within the spectral windows, astronomers use photometric filters with well-defined central wavelengths and bandpasses such as the J -, H - and K -bands in the infrared. Our scientific case focuses on the J -band which is centered at $1.25 \mu\text{m}$ and whose full width at half maximum (FWHM) is equal to $0.3 \mu\text{m}$. Interference filters are available for those wavebands to perform, for example, photometric observations [30].

Observing in one of those clear windows enables the study of (faint) celestial objects. Still, even though the opacity in these windows is low, the atmospheric transmission is a key parameter in the photometric budget of a given instrument. The ATRAN model will be used in Chapter 5.4 to predict the sky opacity as a function of wavelength at La Luz observatory.

2.2 Observation techniques

Observing in the infrared part of the spectrum raises some difficulties in terms of background noise. Both night sky and thermal black-body emissions interfere severely with the observed scientific signal and particular care must be taken accordingly. Noise sources and filtering techniques are briefly described in the following sections.

2.2.1 Noise sources

Thermal emission of a given optical component may be evaluated with the help of the Planck function and the object's emissivity. Common "visual" evaluation of one component's blackness should be set apart as its infrared behavior may be completely different. Every component of the telescope-spectrograph optical chain, dust included, adds its own emitted contribution to the target signal. The only solution to this issue is cooling the entire system, which means the telescope and the associated spectrograph. For instance, the low temperatures, ranging from $-13.6 \text{ }^\circ\text{C}$ to $-82.8 \text{ }^\circ\text{C}$, of the South Pole stimulated IR astronomy from Antarctica. Another solution consists in observing from the stratosphere onboard an airplane [30].

Sky background from OH emission lines is another source of pollution which adds to the scientific signal. An enlightening comparison is proposed by McLean to quantify this phenomenon by comparing the sky brightness at different wavelengths. Whilst this luminosity amounts to $m \approx 24$ in the blue when considering one square arcsecond, it levels up to $m \approx 13.5$ at $2.2 \mu\text{m}$ in the near-infrared and reaches $m \approx 0$ at $10 \mu\text{m}$ when combined to the telescope thermal noise [30]. This latter value motivated the development of the techniques presented in the next section to filter out those unwanted signals.

The sky surface brightness in the near-infrared was assessed by Sánchez et al. in 2008 at the Calar Alto observatory [32]. Figure 2.3 illustrates their results through different spectral bands. The sky surface brightness is plotted as a function of airmass and highlights the fact that there is a strong relation between both parameters [32]. In J -band, the average sky surface brightness is equal to 15.95, which confirms the previous values from McLean and proves that sky background must be taken into account when observing at these wavelengths [30]. This is why the chosen bundle geometry (see Figure 2.24) features satellite fibers that lie several *arcseconds* away from the star on the sky to enable precise measurements of this background component.

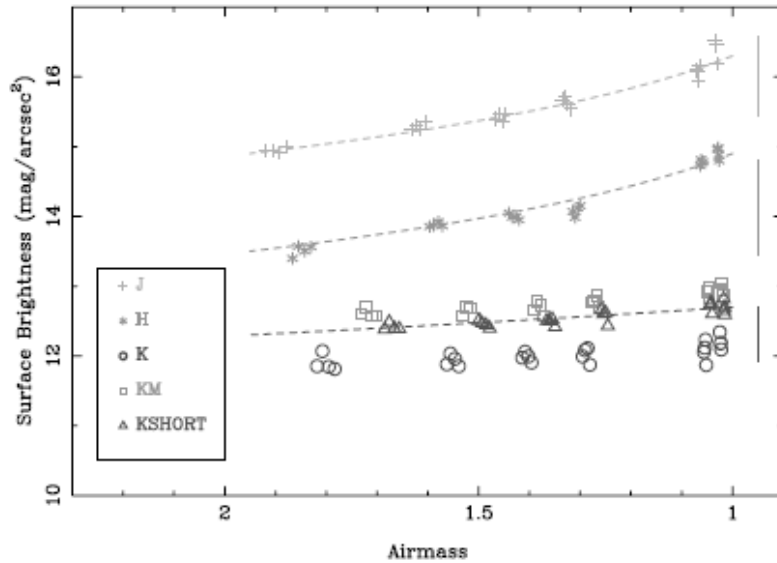


Figure 2.3 – Variation of near-infrared surface sky brightness in different bands as a function of the air mass for the night of the 31st January 2008 [32].

2.2.2 Telescope optimization and observing techniques

Chopping was developed by early infrared astronomers in order to overcome the background from infrared telescopes. This technique consists in switching the telescope observing position from the target to another nearby location in order to measure the underlying background. The target image is actually shifted through the telescope focal plane to observe a nearby sky location where there is no source. The difference between both measurements is free of any background radiation provided the background remained constant between both exposures.

Chopping is usually insufficient as the previous statements assume temporal but also spatial constancies. In order to overcome background non-uniformities, i.e. gradients, nodding is also carried out. In addition to quickly moving the telescope from chop positions 1 and 2 (see Figure 2.4), the whole telescope is moved from time to time (every minute or so) to sample the background at the opposite side of the object. This way, any systematic trend is also eliminated when the nod amplitude is the same as the “throw” of the chop for symmetry [30].

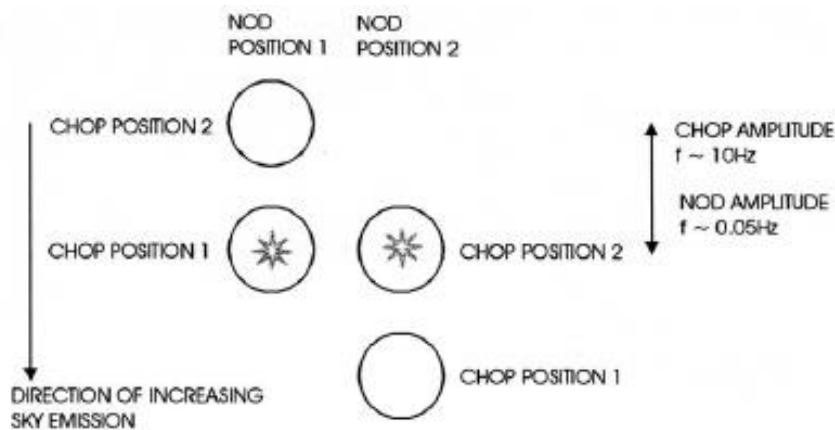


Figure 2.4 – Illustration of chopping and nodding techniques [30]

Mathematically, the difference between the two chopped signals at nod position 1 can be expressed as:

$$C_1(x) = S + B_{tel,1} - B_{tel,2} + \left(\frac{d}{dx}B_{sky}\right)\Delta x$$

where B_{tel} and B_{sky} stand for the telescope and sky backgrounds at the two chop positions separated by Δx and S is the source signal (which is usually much fainter). The same relation at the second nod position writes:

$$C_2(x) = S - B_{tel,1} + B_{tel,2} - \left(\frac{d}{dx}B_{sky}\right)\Delta x$$

and the addition of the two expressions gives

$$S = \frac{1}{2}(C_1(x) + C_2(x))$$

where any trace of background has disappeared. When observing beyond $3.5 \mu m$, chopping and nodding must be used, whereas nodding is required at least at shorter wavelengths for proper background subtraction [30].

The chopping mechanism is carried out by oscillating a wobbling secondary mirror at typical frequencies of ~ 10 to 20 Hz. Such moving secondary mirrors are usually made slow, i.e. with high f-ratios. This enables spreading the background on more pixels and therefore reducing the flux falling on each square millimeter [30]. On the other hand, secondary mirrors in such telescopes are undersized to enable chopping. They are thus overfilled by the light flux coming from the primary mirror and the entrance pupil is then defined by the secondary aperture rather than the primary one. Moreover, the secondary mirror of infrared telescopes does not exhibit a typical baffle to ensure that any subsequent image of this mirror inside the instrument is surrounded by sky [30]. Indeed, such a warm and black baffle would emit more background than the one due to sky. The coating applied to this mirror is usually made of gold, a better reflector than aluminum in the infrared part of the spectrum (see Chapter 2.5). Eventually, a small hole into the secondary mirror or a small deflector with access to the sky is usually set to eliminate thermal photons from the central Cassegrain hole. Telescopes which follow these prescriptions are said to be “infrared-optimized” [30].

2.3 Atmospheric dispersion

Due to atmospheric refraction, the near-infrared and visible images of a star at some distance from zenith¹ may not overlap exactly. This effect will have to be calibrated during the commissioning phase of the instrument. Actually, the star image already depicts a short spectrum at the telescope focal plane. In slit spectrographs, this dispersed image is usually aligned onto the slit to select the entire stellar light [33].

This problem affects all ground-based observatories and is usually tackled with an Atmospheric Dispersion Compensator (ADC). This system is made of two rotating prisms, the so-called Amici prisms, which enable the correction of atmospheric dispersion during observation. These doublet prisms are designed for a maximum airmass correction when aligned with their dispersion directions being parallel and in opposition to that of the atmosphere. When correcting for intermediate airmasses,

¹ The angular distance of the direction of observation from the local zenith is expressed by the *airmass* = $\sec z$ where z is the angle between the direction and the zenith.

those prisms are counter rotated while maintaining the bisector of their dispersion directions aligned with the atmospheric one. Such an instrument is foreseen as a future upgrade to the spectrograph and will be incorporated to the star positioning system located at the telescope focus (this device is discussed in Chapter 7). For this purpose, the aberration of such prisms in a converging beam is studied by Wynne and optimized powered prisms are studied to counterbalance the induced aberrations in this configuration [34]. For example, the Gemini Multi-Object Spectrograph (GMOS) at the Gemini North Observatory benefits from an ADC featuring an additional curved outer surface on its second prism doublet to compensate for the prismatic aberrations [35]. Novel designs were also studied and developed for the Magellan telescope. Several versions incorporating this time two triplets or even four doublets were optimized for compensating both primary and secondary chromatism effects [36].

The differential refraction between the reference targeting and scientific wavelengths of interest can be evaluated with the help of atmospheric dispersion models. According to Szokoly, the most up-to-date atmospheric determination formulae are those of Ciddor that we use hereafter [37] [38].

The atmospheric dispersion, i.e. the apparent displacement of the object, D_{atm} is defined as

$$D_{atm} = z_t - z_a$$

where z_t and z_a are the *true* and *apparent* zenith distances respectively.

Using Snell's law and making the assumption that the refraction index is only a function of altitude, we have

$$n(h) \sin(z(h)) = \text{const}$$

where h is the altitude and $z(h)$ the apparent zenith distance at altitude h . We thus obtain

$$n \sin(z_a) = \sin(z_t)$$

It follows that only the refraction index at the observatory influences the apparent zenith distance at the telescope. Assuming D_{atm} small, we have $\sin(D_{atm}) \approx D_{atm}$ and $\cos(D_{atm}) \approx 1$. Then,

$$D_{atm} \approx (n - 1) \tan(z_a)$$

If we consider that the telescope guiding is carried out with respect to a reference wavelength λ_0 , the differential refraction, which varies as a function of wavelength relatively to λ_0 , in radians is:

$$\Delta D_{atm}(\lambda) \equiv D_{atm}(\lambda) - D_{atm}(\lambda_0) = (n(\lambda) - n_0) \tan(z_a)$$

As can be seen in the above equation, the calculation of the differential refraction depends on the refractive index of air. This evaluation is crucial and old formulas are unfortunately still in use [37]. Szokoly uses the best up-to-date formula developed by Ciddor to continue the above calculations [38]. The complete development involves thermodynamic aspects and after several steps leads to a precise evaluation of the index of refraction which depends on pressure, temperature, relative humidity and CO_2 concentration. Neglecting the smallest effects such as water vapor and CO_2 concentration leads to a simplified formula which is sufficiently accurate for many applications [37]:

$$\Delta D_{atm}(\lambda) \approx \frac{p T_0}{p_0 T} (n_{as}(\lambda) - n_{as}(\lambda_0)) \tan(z_a)$$

where p is the pressure, p_0 the standard pressure of 101325 Pa , T the temperature (K), T_0 the standard temperature of 288.15 K ($t_0 = 15^\circ\text{C}$) and n_{as} the index of refraction of standard air (dry air at 15°C , 101325 Pa and 450 ppm CO_2 concentration). The formula to evaluate the standard air refraction index as a function of wavelength is

$$10^8(n_{as} - 1) = \frac{5792105}{238.0185 - \sigma^2} + \frac{167917}{57.362 - \sigma^2} \quad (1)$$

where σ is the wave number (reciprocal of the vacuum wavelength) in inverse micrometers.

This expression will be used further in Chapter 7.3 to develop an accurate strategy to align the star image onto the selected fiber.

2.4 A fiber-fed instrument

The fiber option to connect the spectrograph to the telescope opens up the possibility to use the instrument also at other telescopes in the future. A versatile interface was therefore required to enable such capabilities and the choice of using a fiber bundle was made.

2.4.1 Use of fibers in astronomy

The idea of using fibers to feed spectrographic instruments started as early as in the fifties. Narinder Kapany, a graduate student at Imperial College in London and widely known as the father of fiber optics, already proposed at that time to employ fibers as slicers to reformat a star image into a linear slit [39]. However, only during the seventies started the fibers to be tested on the sky when sufficient technology improvements reached to maturity.

At this time, low-loss fused silica fibers appeared and the first instrument concepts followed. Robert Angel, Hubbard and Gresham were the first pioneers to develop a fiber-fed spectrograph [39]. Angel also proposed the idea to combine several small telescopes with the help of fibers to simulate the observation of a larger one. This interest in fibers optics gave birth to several spectrographs to perform radial velocity measurements and multi-object spectroscopy. As will be seen in the following text, fibers revolutionized spectroscopy and dramatically increased the efficiency of a telescope [40].

Medusa is the first multi-object spectrograph and was developed at the University of Arizona by John Hill and his colleagues [39]. The dynamics of galaxies within a cluster were studied by imaging several spectra at a time. For that purpose, an aperture plate was used at the telescope focal plane. This consists in a plate within which holes are drilled and located at precise locations onto which stars would be imaged. Fibers were placed into these holes and fed a mechanical slit some 25 cm behind. This mask enabled sampling the spectra of the different objects within this scene of interest. Figure 2.5 illustrates a schematic view of the functioning of Medusa [39].

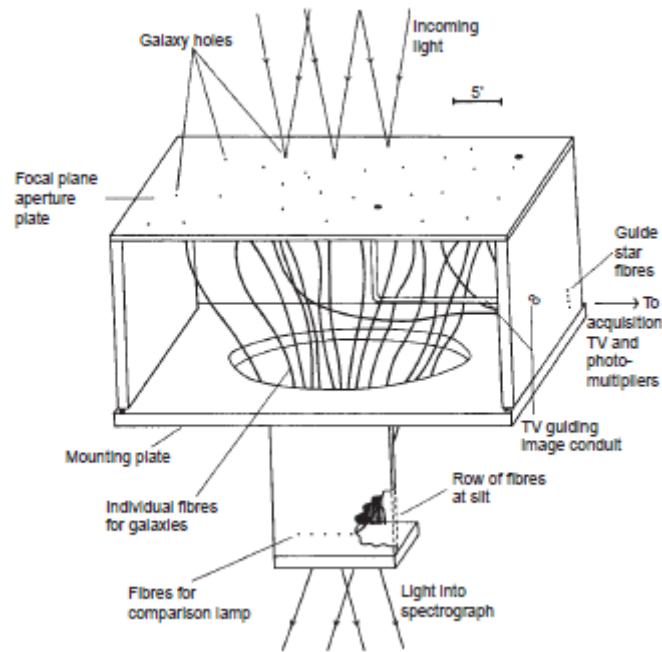


Figure 2.5 - First multi-object spectrograph, Medusa [39]

Medusa paved the way to new developments to overcome the painful use and need for precise manufacturing of aperture plates [21]. Automatic positioning of fibers onto focal plane targets was the step further. First tests of computer-controlled fiber alignment started as soon as in 1981 at the prime focus of the Hale 5-metre telescope [39]. John Hill then started working on an automatic positioner at Steward Observatory and named this Medusa successor the MX spectrometer for its multiplexing ability. MX was the first robotic fiber positioner [21]. Each probe of the system (see Figure 2.6) could be positioned with a precision of a few tenth of *arcsec* within the whole 45 arcmin focal plane of the telescope. The mapping of the fibers to the stellar arrangement in the focal plane only took 90 sec which is an invaluable benefit in comparison with the tedious inflexible aperture plates. Moreover, fiber positioning and orientation could be tuned to maximize throughput which could not be performed with the fixed, precision limited, stellar pattern of aperture plates [39].

Automatic positioners may be composed of simultaneous probes, going to their target position at the same time as for MX. On the other hand, some used a different approach that was first developed for Autofib, a fiber-fed spectrograph on the Anglo-Australian telescope. This one sequentially places a single fiber at a time under the falling light of a star to record multiple spectra. The employed technology usually relies on magnetic buttons that are picked up and then clinged on a metal back plate [33]. This new system allowed twice as much fibers to be used than with MX [21].

Integral field units are another application of multi-object spectroscopy. This technique uses packed fibers rather than specifically positioned probes as in the previous case. These are therefore used to sample different points closely located within an extended object [39]. Light losses appear when grouping fibers against each other due to cladding obstruction. To overcome this problem, microlenses were introduced to inject the light within fibers without losing any photon falling outside the cores. These are located closely behind the focal plane and are used to image the pupil of the telescope onto the input of the fibers [33].

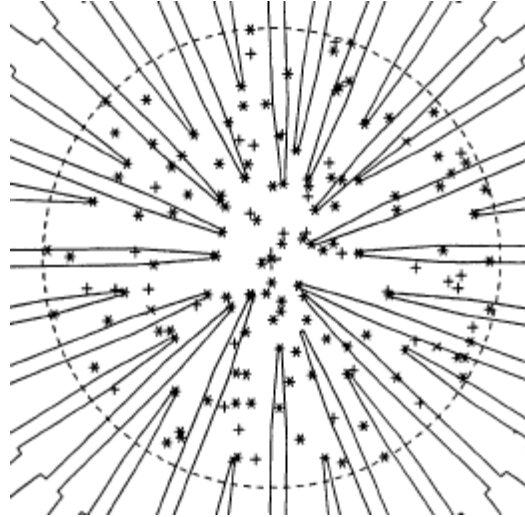


Figure 2.6 – Fiber positioners of the Steward Observatory 2.3-m telescope [39]

These are some examples of potential fiber applications in astronomy but many other advantages do exist. The use of fibers first enabled multi-object spectroscopy but also the physical separation of heavy scientific instruments from their observing telescope. Physical flexure is not encountered anymore and calibration highly benefits from this disconnection [41]. Indeed, the high enough throughput of fibers enables the relocation of the spectroscopic instruments in environmentally controlled rooms, which eliminates for example systematic radial velocity errors [42]. This novel idea emerged in the early eighties with Hubbard et al. and much of work has been performed until now to improve this way of transporting light [43]. For example, this also enables spectrographs to be located in vacuum chambers to record, for example, ultraviolet spectra [33]. Vacuum chambers may also be used for extreme stability conditions as this is the case for HARPS (High Accuracy Radial velocity Planet Searcher), the ESO's extra-solar planet finder. This instrument requires radial velocity precision down to ± 1 m/s and is for that purpose located 38 m away from the telescope in a temperature-controlled vacuum chamber.

The use of fibers for astronomical purposes leads to some adverse effects that cannot be set aside. These optical connectors facilitate the way scientific instruments are fed by telescopes but some considerations must be taken into account when dealing with fibers. Indeed, as any additional component introduced into an optical chain, optical fibers do suffer from attenuation when transporting light from one point to another. Moreover, fibers exhibit some effects that may be unforeseen at first glance. FRD losses are one example and are discussed further below.

2.4.2 Properties of fibers

Focal Ratio Degradation (FRD)

Focal ratio degradation arises from different causes but is characterized by a single effect: the reduction of the focal ratio of the transported light beam after having passed through the fiber. This issue cannot be avoided but particular care may limit the magnitude of this angular distribution change. A slight insight into this mechanism is required to understand the appropriate precautions when handling fibers to overcome, or at least lessen, this problematic behavior.

As explained by Ramsey [43], multi-mode fibers suffer from two types of light loss mechanisms. These can indeed be either mode independent or mode dependent. Modes are the several plane waves

that fall onto the fiber core entrance at different incident angles with respect to its optical axis. These then propagate if their inclination enables total internal reflection (TIR), which leads to the definition of a fiber's numerical aperture (see Figure 2.7) [43].

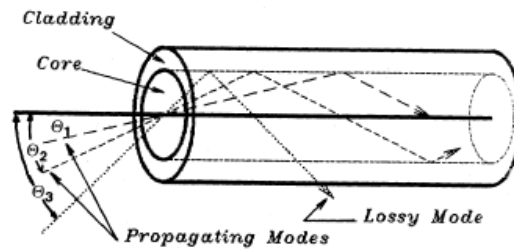


Figure 2.7 – Different modes propagating into a step-index fiber. Lossy modes, that do not obey to TIR, leak to the cladding and vanish [43].

Mode dependent light leakages originate in interactions between light and the fiber material. Light may be attenuated by molecular absorption and other impurities within the core. On the other hand, density fluctuations lead to light scattering and limit the transmission at lower wavelengths. These characteristics are usually well assessed by manufacturers.

FRD properties of fibers emanate from mode-dependent mechanisms and are rarely investigated by manufacturers [43] [41]. Mechanical deformations of a fiber, whether they occur on a macro- or micro-scale with respect to the core, initiate energy transfers between the different excited modes. This modal dispersion manifests itself as what is referred to FRD in astronomical purposes. It should be noticed that different studies highlighted the fact that macro-bending does not play a major role in FRD losses. These large deformations may however come into play since stress-induced micro-bending could appear and produce FRD [43]. Micro-bends tend to perturb the natural light path of a given mode, which then transforms into another one and this explains the modal dispersion (see Figure 2.8).

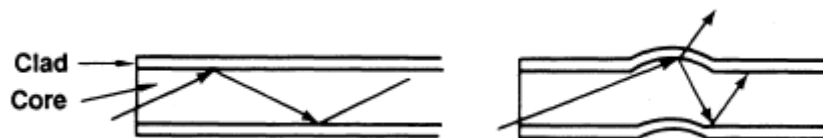


Figure 2.8 – Modal dispersion due to stress-induced micro-bending [44]. Light escapes at lower f-ratio or leaks through lossy modes which is in all cases a loss.

As pointed out by Ramsey and illustrated in Figure 2.9, FRD is always a loss when considering astronomical applications [43]. The solid line relates the output f-ratio of a circular aperture whose diameter is equal to the one of the fiber core. The slope of this line equals 1 as any well-designed spectrograph exhibits a collimator f-ratio equal to that of the telescope it is connected to. The dashed line highlights the behavior of a typical fiber which, in contrast with the previous results, widens the light beam it is swept through. A light loss then appears when the two curves diverge if the spectrograph collimator is matched to the telescope since some light fails at being collimated.

As noted by Ramsey, the overfilled collimator could be enlarged to entirely catch this wider light beam and avoid any lost photon. But, all following optics must then be larger than expected with no consequent increase in resolving power. The practical implementation of such a solution may have to face budget and manufacturing restrictions as will be noted in Chapter 4.3.6. In addition, short camera focal lengths are usually required to match the fiber core to the pixel pitch of the selected detector.

One may therefore quickly encounter very fast cameras [43]. In general, using a fiber can only decrease the function of merit of a given telescope-spectrograph association (see Eq. (3) of Chapter 3.2). However, as noted by Schroeder, this issue may be more than compensated if multiple fibers are used so that the spectra of several targets are simultaneously recorded [40].

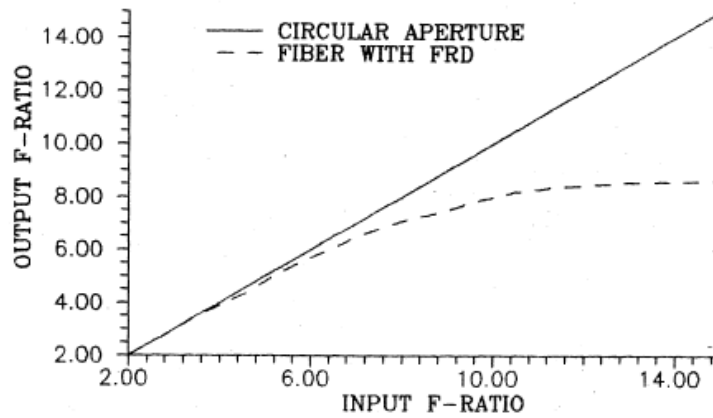


Figure 2.9 - FRD of a typical fiber vs. throughput of a circular aperture whose diameter equals the fiber core size [43].

As stated earlier, manufacturers rarely measure, and therefore specify, FRD properties of their optical fibers. During the eighties, many astronomers have therefore conducted their own experiments to get those measurements [43]. Ramsey is one of them and he characterized FRD properties of different fibers. The conclusions of this study, which are still relevant today, are summarized below.

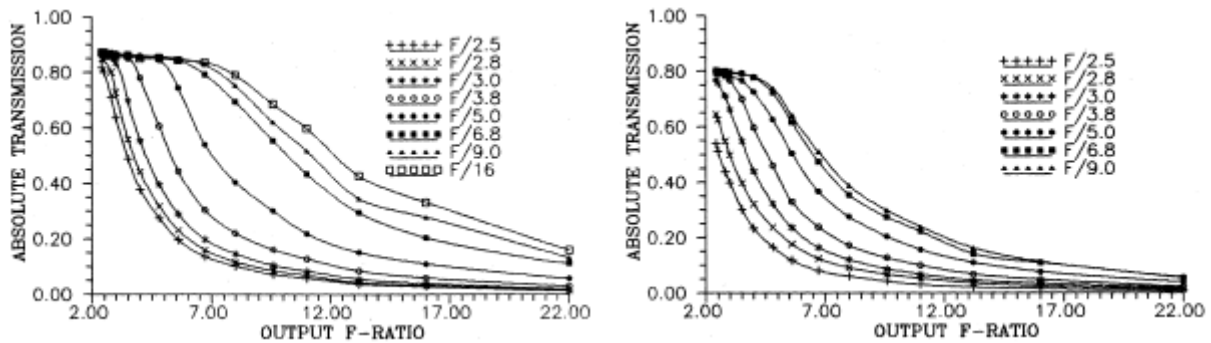


Figure 2.10 - Focal ratio degradation of a 320 (left) and 100 (right) μm core fiber [43].

Figure 2.10 illustrates the FRD Ramsey measured on two different core size fibers [43]. Several curves are shown, each representing the absolute transmission of the fiber when lit at different input f-ratios. The absolute transmission to a collecting surface is then measured for several output f-ratios. A direct conclusion when comparing left and right results is that the fiber core size matters. This parameter has indeed a large impact on the way the fiber will spread the input light beam at its end. Worse FRD properties of smaller core size fibers are explained as follows by Ramsey: since the accuracy of the absolute fiber diameter remains about the same in both cases, the relative change is larger for smaller cores. Therefore, waveguide scattering may have a larger impact in this case [43].

The FRD properties of both fibers in typical configurations where the output f-ratio, corresponding to that of the collimator, matches the f-ratio of the connected telescope are visualized in Figure 2.11. The light losses due to the overfilled collimator appear clearly, as well as their inversely proportional relation with fiber core size. This figure also highlights that the optimal f-ratios to minimize FRD are located around $F/3$ - $F/4$. Transmission tends to be optimal at $F/2$ - $F/3$ and is the reason why several

spectrographs are connected to the telescopes' prime focus [42]. The transmission drop at very small f-ratios is likely due to some modes propagating near the total reflection condition which become lossy due to microbends [43].

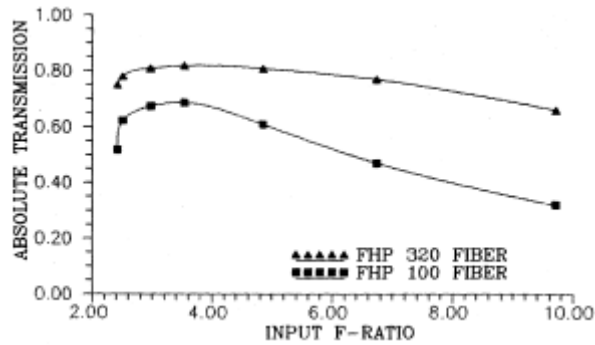


Figure 2.11 - Absolute transmission of fibers when output f-ratio is equal to input f-ratio [43]

Last but not least, the quality of the end termination of the selected fiber plays a major role in the FRD properties it will suffer from. The epoxy used to glue the optical fibers to the end ferrule induces shrinkage and therefore stresses. These lead to microbends and deteriorate the FRD properties of fibers [41]. The curing of this epoxy also matters as Ramsey and Craig et al. noticed different performances during later observations of the same fiber [43] [44]. The way fibers are mounted at their end also changes their behavior with respect to light transportation. Fibers should be installed in a manner that minimizes the stresses in order to obtain the best performances. Craig et al. noticed FRD was for example largely increased if the fibers were compressed by a sharp tool [44]. Figure 2.12 illustrates the output profile of a fiber that is first unstressed and then pressed against the edge of an optical table by the weight of a finger [44].

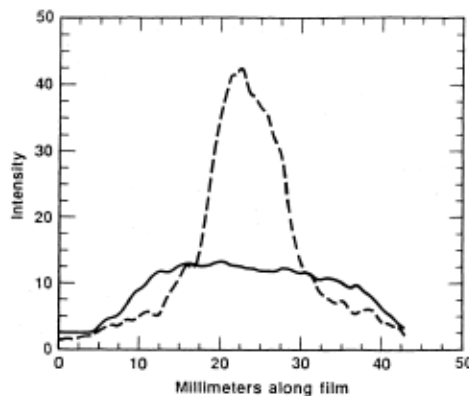


Figure 2.12 - Intensity profile of the output beam of an unstressed (dotted line) and stressed (solid line) fiber [44].

The end polishing of the fiber also affects their FRD efficiency and a particular care should be given to the surface quality of the fiber extremities. High roughness at the end of a fiber due to a lack of fine polishing may launch the light to extreme angles and therefore increase FRD. On the other hand, the junction of the fiber to another optical surface, such as the optical couplers addressed in a following section, may be eased and enhanced thanks to increased care in the polishing [44]. The fiber cabling and the stresses induced by the outer jacket may also lead to FRD degradation [45]. Eventually, cladding material selection and buffer softness seem to be of significance in FRD mitigation strategies [43] [41].

These observations are surely the reason why the authors observe results that may differ by a factor two while testing the same fibers [43]. The same models may behave in a totally different manner when settled within another mounting scheme, polished with less care to surface finish and glued with a poorer quality epoxy. Even more dramatic is the fact that fibers from batch to batch may differ in their ability to make the light beams faster [44].

For example, Barden also investigated the behavior of the same $320\ \mu\text{m}$ core fiber that Ramsey looked at and found better results (see Figure 2.13) [41]. One interesting point is that Barden's fiber was $32\ \text{m}$ long whereas Ramsey used $10\ \text{m}$ long fibers. This suggests that FRD properties of fibers do not strongly vary with their length [43]. A careful inspection of the left part of Figure 2.13 shows that the curves do not reach 100% transmission whereas those from the right do. This is because the first results account for reflection losses at the fiber ends [41].

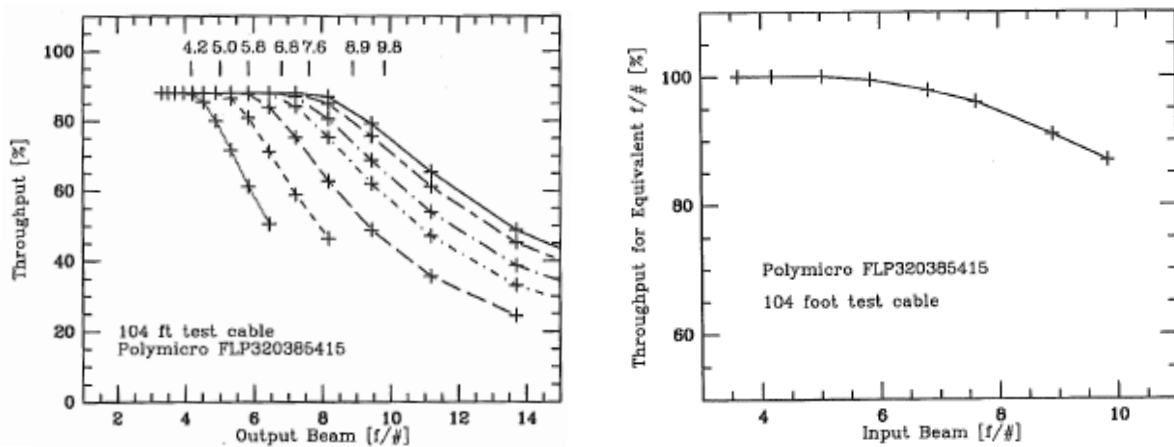


Figure 2.13 – FRD properties of a $320\ \mu\text{m}$ fiber for different input f-ratios (left) and throughput at equivalent f-ratio (right) [41]

Craig et al. also observed the same fiber model and obtained worse results, which they attribute to a stressed mounting scheme (see Figure 2.14) [44].

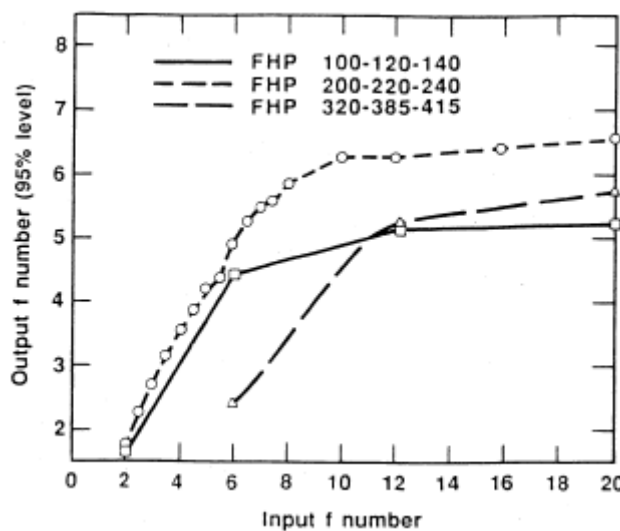


Figure 2.14 - Required output f-ratio to collect 95% of the input f-ratio for different fibers [44].

Those contradictions and discrepancies between different authors' results motivated researchers to identify standard fiber characterization procedures. For example, Carrasco and Parry elaborated an experimental method to measure FRD properties of a given fiber based on a theoretical model of microbending-induced beamspreading [46]. The main advantage of their approach lies in the fact that the overall FRD efficiency of the test fiber is summarized in a single parameter. Moreover, this one may be simply evaluated thanks to a fast experiment where the fiber is illuminated with the help of a collimated laser beam. Once this parameter is correctly evaluated, the fiber behavior with respect to any input beam may be predicted through the developed theoretical model [46]. Their model was tested on Barden's data and a rather proper fitting of his results appears when using a very good FRD response for the fiber (see Figure 2.15).

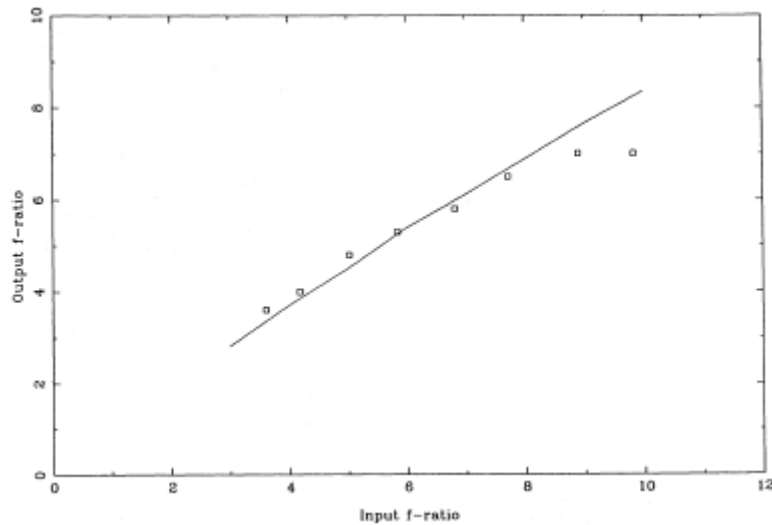


Figure 2.15 - Fitting of the model (solid line) to Barden's results (squares) [46]

Better results are obtained when using their own experimental measurements since Barden's ones were evaluated on his graphs and other data are simply missing. Figure 2.16 illustrates the results when assessing the behavior of a poor quality fiber with the theoretical model and comparing them to the measured data. The dashed line corresponds to tilt-corrected data that compensate for a misalignment inside the experimental setup.

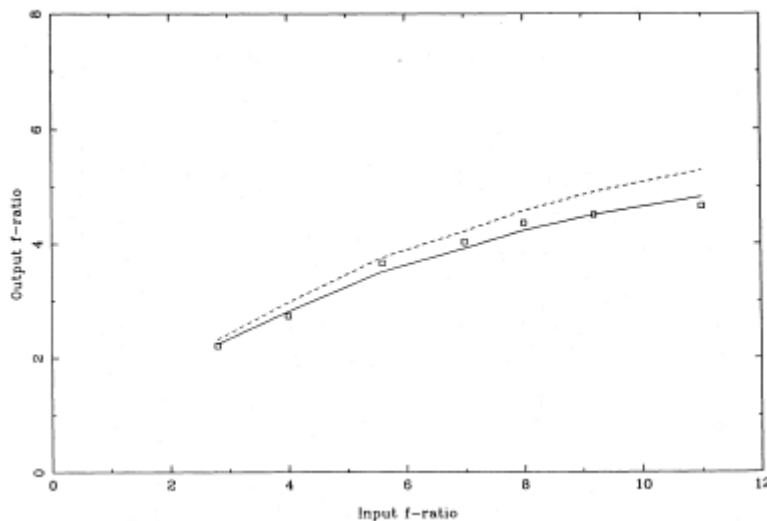


Figure 2.16 – Theoretical predictions of a fiber FRD properties compared to the experimental measures (squares) [46].

Figure 2.17 depicts the relative transmission of the poor-quality fiber when illuminated at $f/8$ input ratio. As can be seen from this figure, the dashed (model) and solid (experimental) lines are closely the same, attesting the validity of Carrasco's and Parry's model.

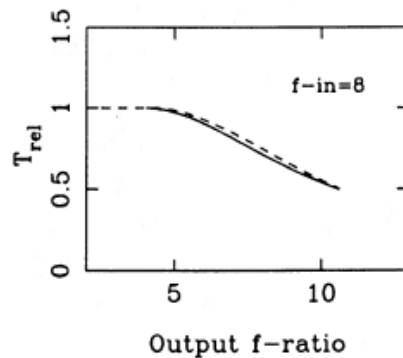


Figure 2.17 – Relative transmission with respect to the output f-ratio when injecting light at $f/8$ input f-ratios [46].

Wavelength-dependent fiber losses

As stated in the previous section, mode-dependent fiber loss mechanisms are usually properly characterized by manufacturers. These mainly involve material absorption and scattering, both varying as a function of wavelength. Material absorption in the near-infrared is dominated by the absorption bands of OH . On the other hand, metal ion impurities are the main absorption source at the blue side of the spectrum [43]. Variations in the density and composition of the fiber core result in scattering. Density fluctuations in fused silica fibers lead to Rayleigh scattering which sets the lower limit to fiber transmission [43].

Different fiber compositions exist to deal with these absorption features. “Dry” and “wet” fibers are for example two types that are commonly used in astronomy. Dry fibers are employed for high throughput from 4000 \AA to $1.9 \mu\text{m}$ and are thus preferred for our near-infrared application as advised by Dallier et al. Wet fibers, on the other hand, extend the observed spectrum down to 3200 \AA [41]. The fiber core density disruptions previously discussed are remedied by manufacturers with the help of a hydrogen treatment in the case of wet fibers. The scattering at lower wavelengths is therefore strongly reduced and a higher throughput enabled. However, those fibers should be avoided in case of any interest in observing the infrared part of the spectrum. Indeed, strong absorption bands occur at redder wavelengths due to OH vibrational transitions as can be seen in Figure 2.18 [44].

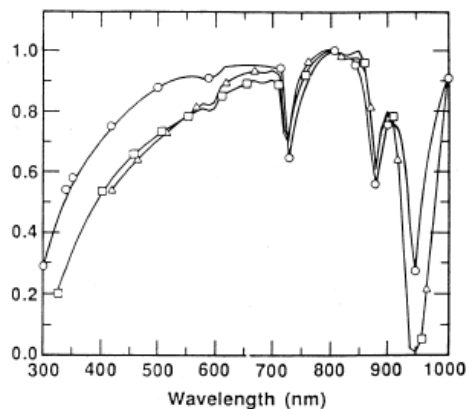


Figure 2.18 - Normalized (at 800 nm) transmission of a 30 meter wet fiber [44]. Circle points are manufacturer specifications, others are measures.

As can be seen in Figure 2.19, the transmission of dry fibers is high from optical to near-infrared waveband [45]. Their lack of efficiency at shorter wavelengths remains however a showstopper to observations in the blue and ultraviolet parts of the spectrum. Typical astronomical fiber lengths approach 20 m and their total transmittance, including 4% reflection at both ends, approach 90% at 1 μm in the case of dry fibers [40].

Some authors develop new technologies to face the fiber core inhomogeneities without any hydrogen treatment to enable wide-band observations. For example, Lu et al. manufactured a new silica core material which enables high throughput efficiency from 350 up to 2000 nm [47]. Although the obtained properties are not as good as those from high-OH fibers, this technology enables instruments to cover a larger waveband with a single fiber [45]. Ceramoptec, the selected manufacturer for our specific bundle, for example already proposed in the nineties a hybrid fiber which combined both low and high OH performances [21]. When going deeper in the infrared, specific materials such as zirconium fluoride may be used for example [33]. For example, fluoride was selected by Dallier et al. to be able to observe in K-band in their first two prototypes of ISIS-IR [23]. If the waveband of interest does not extend beyond 2 μm , the use of low-OH dry silica fibers is preferred as fluoride fibers are very fragile and expensive [21].

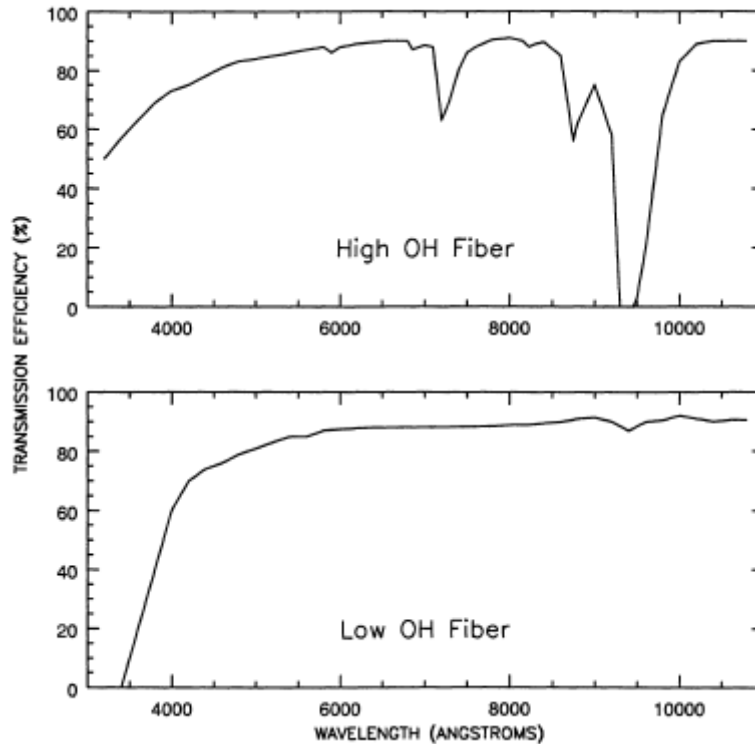


Figure 2.19 - Transmission of a 25 meter long "wet" (up) and "dry" (bottom) fiber [45].

Scrambling

Scrambling is another specific characteristic of fibers and is often referred to a “memory” effect. It is convenient to define two different scrambling mechanisms: an azimuthal scrambling and a radial scrambling. First one characterizes the trend of fibers to distribute the input light angular information into an output annulus of light.

This process is depicted in Figure 2.20 where an input collimated beam is transformed into an annulus whose thickness depends on the FRD properties of the test fiber [43]. The evaluation of the beam

output profile in this configuration is actually the way Carrasco and Parry characterize in a standard way the FRD properties of fibers [46]. Fibers are nearly perfect azimuthal scramblers, even over very short lengths and independently of the input f-ratio [42].

Radial scrambling on the other hand relates to the memory effect previously introduced. When a fiber is illuminated by a light spot centered onto its core, any lateral shift from this centered position will change the light pattern at the end side. This change in illumination of the spectrograph pupil is of importance when precise radial velocities are to be measured as for stellar seismology [43]. Such shifts in the star image positioning may be caused for example by seeing changes or pointing fluctuations and lead to radial variations in the light illumination of the instrument.

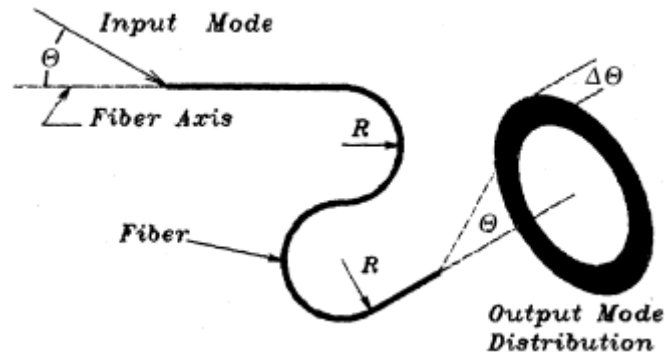


Figure 2.20 - Azimuthal scrambling of fibers [43].

As pointed out by Heacock, radial scrambling is substantial but still incomplete and must be taken into account in demanding applications where 1 *m/s* precision is required [48]. As noted by several authors, an important point is that fibers with best FRD properties are worse scramblers than others. A tradeoff between FRD attenuation and scrambling efficiency must therefore be found [43] [42] [45]. This can be seen in Figure 2.21 and Figure 2.22 where it is shown that FRD mitigation becomes worse as scrambling improves [42]. Indeed, FRD attenuation is best at input f-ratios of $f/2$ to $f/3$ but the unscrambled light percentage rises to 20 to 30% in this regime. High scrambling is only reached at higher f-ratios and becomes nearly optimal at f-ratios of 5 where FRD starts to dominate. As advised by Barden et al., input f-ratios should be located between $f/5$ and $f/7$ to benefit from high scrambling and moderated FRD losses [42].

Even though radial scrambling efficiency of fibers may not be perfect, using this light transmission method to feed spectroscopic instruments leads to better performances than regular mechanical slits [41] [42] [45]. One should however investigate if either FRD losses attenuation or radial scrambling is more important when selecting the input f-ratio feeding the fiber. Radial scrambling deficiency of some fibers may lead to some unexpected adverse effects.

For example, if the unscrambled light percentage is high, the memory effect of the fiber may be seen when observing its output light pattern when fed by an obstructed telescope. The obstruction of the secondary mirror may indeed be observed at the fiber output due to scrambling deficiencies as noted in the left part of Figure 2.23 [45]. This experiment was conducted with the help of two fibers: a 200 (left) and a 100 (left) μm core fiber. The attenuation of light in the centre of the left image comes from the secondary mirror obstruction, which is missing from the right part. However, FRD properties are worse in the case of the thinner fiber, as expected.

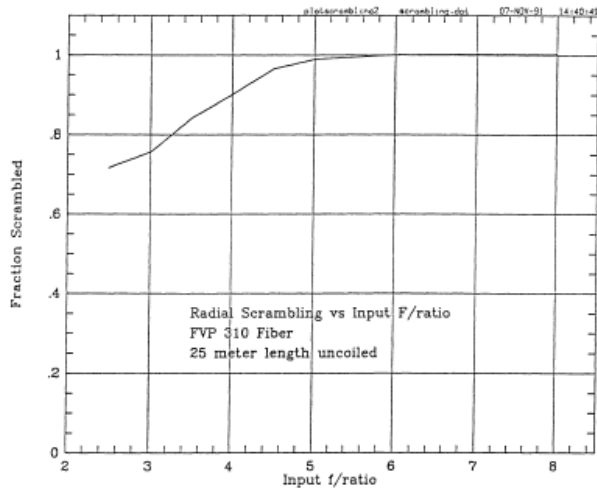


Figure 2.21 – Fraction of light radially scrambled as a function of input f-ratio [42].

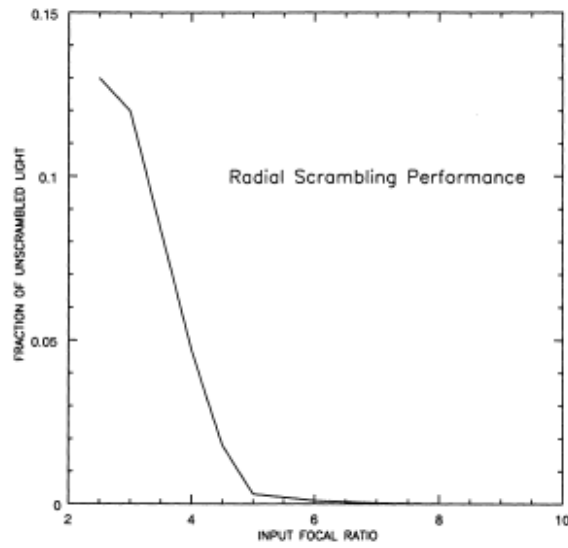


Figure 2.22 - Fraction of unscrambled light as a function of input f-ratio [45].

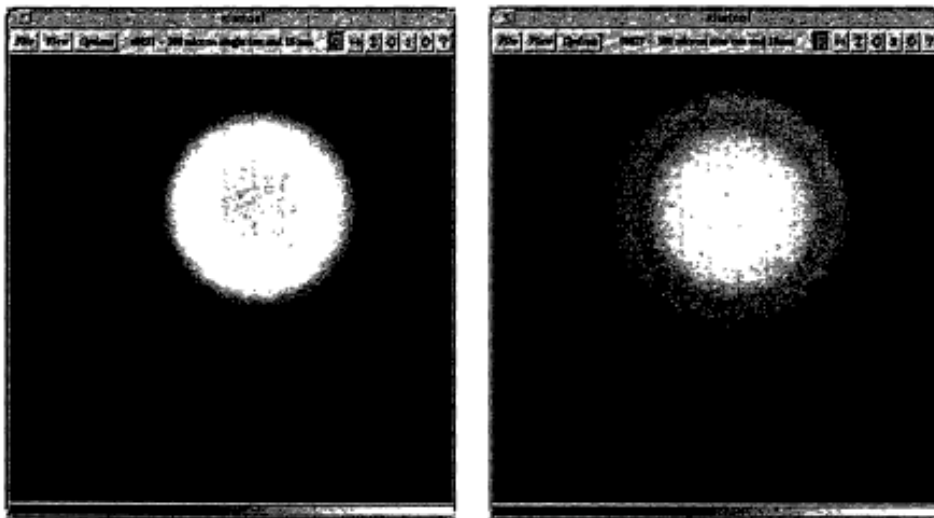


Figure 2.23 - Output light pattern of a 200 (left) and 100 (right) μm fiber illuminated by a f/8 light cone [45].

2.4.3 Fibers' configuration within the selected bundle

A bundle of 15 fibers is selected to link the telescope to the spectrograph, located in a separate room beside the dome. Figure 2.24 introduces the selected fiber configuration at each side of the bundle. The star light focused at the telescope focal plane is collected with the help of fibers located at the centre of the circular-shaped bundle input. These latter are set to form a square of 3 by 3 elements, which is reminiscent of the configuration Barden adopted at Kitt Peak National Observatory (KPNO) [41]. The great advantage of using a fiber bundle over masks to perform multi-object spectroscopy is the total freedom of fiber arrangement at both telescope and spectrograph sides [21]. The selected arrangement for our scientific case is explained below.

On the other hand, 6 other “satellite” fibers surround the “star” ones in order to sample the sky background. This way, the sky spectrum is recorded aside of the star signal and can thereafter be subtracted to obtain accurate target spectra. The satellite fibers lie on a circle of diameter 1 mm centered onto the star fibers. This 500 μm radius approximately corresponds to 10 *arcsec* on the sky (10.74 *arcsec* exactly) when considering the TIGRE telescope, which ensures measuring the sky background far enough from the star to avoid contamination by star light and close enough to collect representative measurements. On the other hand, this fiber distribution may allow for sky background gradients to be eliminated without performing any chopping or nodding (see Chapter 2.2.2).

It must be noted that sky background measurement and subtraction techniques are very important as noted by Parry [21]. In contrast with slit spectrographs, fiber-fed instruments must develop accurate subtraction methodologies because the sky signal is usually sampled some distance away from the source by a dedicated fiber. Moreover, the related spectrum is also imaged on a separate portion of the detector. Therefore, systematic errors may occur due to scattering or vignetting in the spectrograph for example [21].

At the spectrograph's side, the output of the bundle is reshaped into a linear arrangement to form the spectrograph's entrance slit. The star fibers lie at the center of the slit while the sky samplers are located some distance apart to avoid any crosstalk between the desired signal and its related noise. Three “dead” fibers separate the first sky fiber from the star ones to carry out this task. No light is transmitted by these elements. According to Kitchin's nomenclature, this multi-strand cable may be qualified as “coherent” since there exists a logical reshape between the input and output faces of the bundle [33].

Eventually, the total length of the bundle is 15 m to ensure a comfortable connection of the telescope to the spectrograph from its separate enclosure whatever movement the observer performs. Special gluing was used by the manufacturer to limit the stresses in the bundle and the FRD they would induce. A large cladding of 125 μm is advised by the manufacturer for better stability. The fiber core is 50 μm in diameter and the reason of this choice is explained in Chapter 4.3.6. The core material is made of pure fused silica and is optimized for high transmission in the near-infrared. Eventually, a stainless steel protection tube surrounds the bundle in order to prevent any unwanted damage that may be disastrous for throughput efficiency. All these considerations to fiber care and material selection are consistent with the notices provided in the previous section.

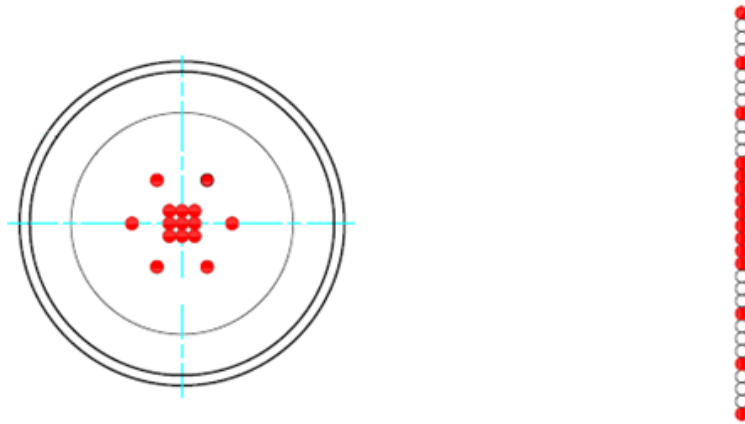


Figure 2.24 - Fiber bundle configuration: input at telescope (*left*) and output to spectrograph (*right*)

2.4.4 Optical couplers: micro-lenses

As we noted in Chapter 2.4.2, the coupling between the telescope and the fiber has an important impact on the spectrograph performances. The input f-ratio with which the light is injected into the fiber plays a major role especially. On the one hand, low f-ratios, namely fast beams, are suitable to minimize FRD losses of fibers. On the other hand, these will lead to poor scrambling of the input light beam and lower stability of the recorded spectrum with respect to seeing and pointing accuracy.

A tradeoff is therefore needed when trying to optimize the efficiency of the telescope-fiber-spectrograph chain coupling. One should identify which scientific requirement dominates the others to take the appropriate decision. Scientific requirements were specified in Table 1.1 concerning several performances of the instrument under study. Typically, resolving power, photometric budget and spectral calibration are involved in the tradeoff where FRD and scrambling compete against each other.

The FRD issue has also been identified by the fiber-fed spectroscopy pioneers and a solution using micro-lenses was already proposed by Dallier et al [23]. This consists of using very small size lenses at the front of the fibers to reshape the light beam before its injection into the core. A faster light cone then enters the fiber and FRD losses are minimized. This technology was for example installed on the Isaac Newton telescope on La Palma and the William Herschel telescope [39]. Due to conservation of etendue, a change in the input star image size inevitably occurs as explained below.

Optical devices such as micro-lenses are now commonly used to couple the telescope with the fiber in an efficient way. These are for example used at TIGRE to inject the star light with high throughput efficiency into the fiber core which feeds the optical echelle spectrograph HEROS [17]. Indeed, the typical seeing at La Luz amounts on average to 2 *arcsec* which corresponds to a star image diameter of approximately 93 μm . However, the selected fiber core by the Hamburg team is equal to 50 μm . Without any coupler, the light which falls onto the fiber cladding does not propagate to the spectrograph. The addition of micro-lenses tackles with this problem by resizing the star image down in order to transmit as much star light as possible.

These tapers are also, and more often, employed to reshape the input f-ratio reaching the fiber as explained earlier. This f-ratio adaptation also occurs for HEROS as the $f/8$ telescope beam transforms into $f/4$ under typical seeing, which is close to the $f/4.5$ value of the spectrograph collimator. A second microlens is also located at the spectrograph side of the fiber for better illumination of the instrument collimator [49].

As for HEROS, two micro-lenses are usually employed: one located at the telescope side to minimize FRD losses and a second one at the spectrograph input to match the fiber angular cone with the collimator's f-ratio. This last adaptation is not free of any disadvantage. Indeed, the change in angular width of the light beam comes with a modification of the spatial extent of the fiber core, namely the entrance slit width. Therefore, the resolving power of the considered spectrograph is decreased and another tradeoff appears where resolving power and photometric budget compete against each other.

In our case, direct feeding of the fiber with the telescope f-ratio of 8 leads to perfect scrambling of the star light and high stability. Spectral calibration will benefit from this light mixing since the spectrum will be less sensitive to seeing and telescope pointing accuracy. However, a large amount of light will be lost at the fiber entrance side under typical seeing conditions since the star image is not properly resized. Only during good nights will the entire target light fall into the fiber core. On the other hand, using micro-lenses will decrease the required integration time since this first downsizes the star image to properly fit the fiber core diameter and then limits the FRD losses. More photons are thus collected by the collimator and the required signal-to-noise ratio is reached in a shorter time period.

As a conclusion, adding micro-lenses to fibers thus improves the photometric budget of the instrument but deteriorates the scrambling of the star light as well as the resolving power of the connected instrument. Employing such connectors thus requires investigating whether photometric budget or resolving power and scrambling, namely calibration, issues are more important. Chapter 4.3.8 will investigate the effect of using micro-lenses on the resolving power during early stages of the spectrograph optical design. Chapter 4.7.5 will eventually evaluate the consequences of a poor scrambling on the spectral calibration.

2.5 Suitable optical coating techniques

Optical coatings with a high reflectivity must be identified in order to maximize the light throughput of the instrument. These ensure a maximum specular reflection percentage on each mirror of the spectrograph and avoid both transmission leaks and scattering. Suitable coatings for the selected near-infrared waveband are shown below.

Metallic coatings with a high reflectivity near $1 \mu\text{m}$ are usually made of silver or gold as shown in Figure 2.25 [50]. These coatings exhibit a typical reflectivity higher than 95% at the wavelengths of interest. Protected gold and silver coatings propose the highest reflectivity in this part of the spectrum but aluminum may be selected as a very good cheaper candidate. Indeed, its reflectivity is higher than 90% beyond $1 \mu\text{m}$, which is close to the performances of protected gold and silver. Moreover, these results extend to the visible and ultraviolet domain whereas those of silver and gold lead to poorer results in these wavelength ranges.

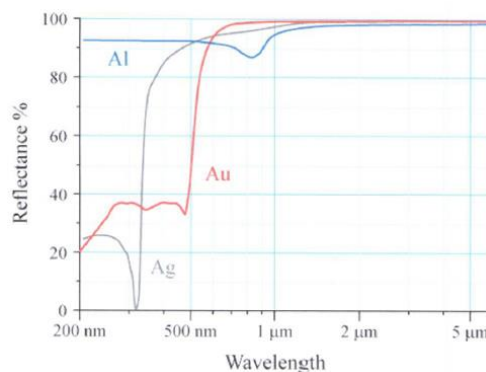


Figure 2.25 – Reflectance of aluminum, silver and gold metallic coatings [50]

A silver coating is selected for all reflecting optics of the instrument owing to the high reflectivity this material offers in the near-infrared region of the spectrum and down to 400 nm as well. This enables the instrument to be used in the visible region as well in the future. Figure 2.26 illustrates the reflectivity of the coating which is applied on the custom-made collimating and focusing mirrors of the spectrograph.

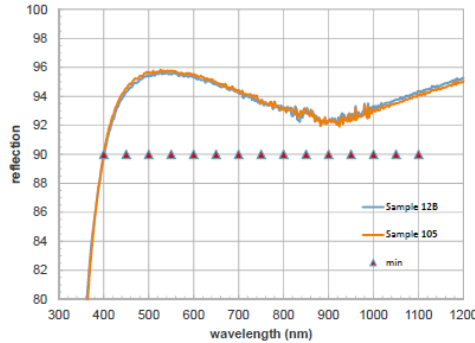


Figure 2.26 - Protected silver coating reflectivity for collimating and focusing mirrors

2.6 Filters

Filters should be used to block shorter wavelengths that could pollute the system through straylight or reach the detector following higher order paths of the grating. For example; shorter visible wavelengths follow exactly the same path as near-infrared ones through the second diffraction order of the grating. One may think these should not play a major role in the straylight generated on the detector since its quantum efficiency is very low in this spectral region but the incoming visible light from the star may be more intense than the one emitted in the near-infrared. A proper longpass filter should therefore be used to discard these wavelengths and avoid their propagation through the system.

A suitable filter curve is shown below. This edge longpass filter exhibits an average transmission of 90% through the NIR waveband under study. By inserting it into the spectrograph optical chain, a large contribution of the visible radiation is prevented from reaching the detector. When using typical CCD technologies in the near-infrared, this kind of filter is mandatory.

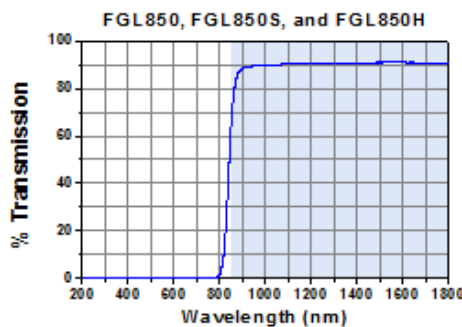


Figure 2.27 - NIR longpass filter [51]

On the other hand, as noted by Dallier et al., a cold filter should be used when selecting specific NIR detectors that are sensitive to the *K*-band. This cooled filter intends to prevent short-wavelength photons from reaching the detector while not emitting thermal emission that could reach the detector. If such a filter exhibits losses within the wings of its transmission curve, another low-pass thermal filter should be used. When selecting *InGaAs* technologies, this is not the case.

2.7 Glasses

Suitable glasses also need to be identified for the near-infrared domain if refractive elements are to be used within the spectrograph optical design. Figure 2.28 lists some of the optical properties of several typical glasses used for optical design [52]. The first one, *BK7*, is probably the most common glass selected for the design of lenses as it exhibits excellent transmission and mechanical characteristics. Its broadband transmission from ultraviolet to infrared wavelengths enables its selection within numerous different applications. More specific glasses may be more appropriate when dealing with far ultraviolet or infrared wavelengths. On the other hand, thermal issues may be of high importance and in this case sapphire may be the indicated solution. The glass selection process must therefore account for the instrument sensitivity.

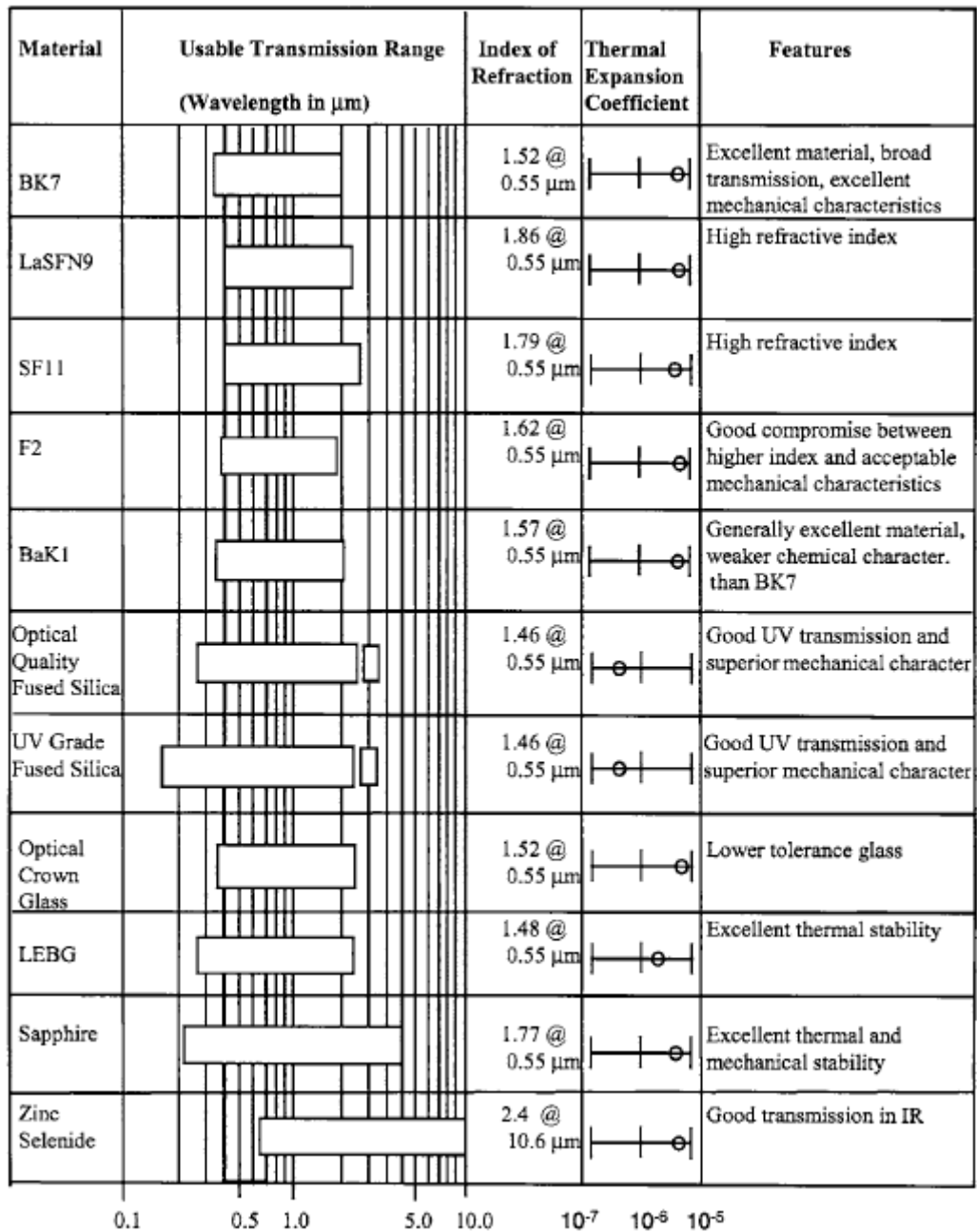


Figure 2.28 - Overview of several optical material properties [52]

2.8 Detector technologies

2.8.1 History

The CCD appeared in the late 1970's and kicked off a new era of astronomy with solid-state imaging. The idea of the CCD came to mind of Willard S. Boyle and George E. Smith from Bell Labs when they were working on the project of a Picturephone, a phone concept involving a tiny camera to enable callers to see each other [30]. While working on a silicon diode array camera, they got the idea of forming small metal plates where charge could be stored and passed from one to another. Within a few weeks, George E. Smith had manufactured a 9-element device and started the tests.

CCDs immediately appeared very promising as they proposed many advantages compared to other available technologies at that time. Their small size and high sensitivity over a wide wavelength range is a first point (see Figure 2.29) [30]. Moreover, their response to incoming light flux is linear and their power consumption is low. Eventually, the prospective of low-cost production was promising due to silicon manufacturing processes and mass production [30].

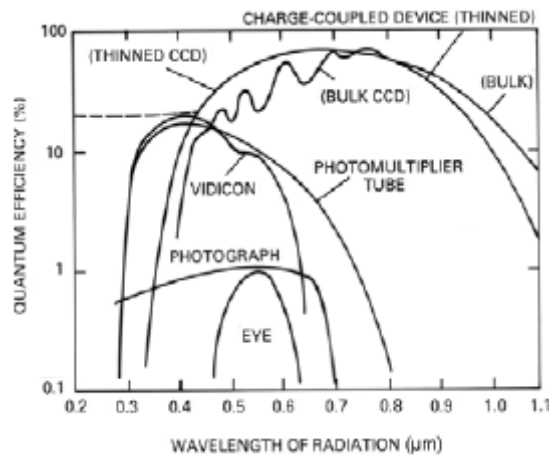


Figure 2.29 – Quantum efficiency of several detectors including CCDs [30]

For all those reasons, astronomers and space scientists quickly adopted CCDs and pushed their developments to prepare their involvement in missions such as Galileo or the HST. For that purpose, the Jet Propulsion Laboratory (JPL), Texas Instruments (TI) Incorporated and the National Aeronautics and Space Administration (NASA) joined their forces to develop large CCDs. Jim Janesick, a young engineer in charge of testing the CCDs at JPL, was also an amateur astronomer. He first imaged the moon successfully on its own small telescope and then performed the first capture of a CCD attached to a professional telescope with Dr. Bradford Smith, a planetary scientist at the University of Arizona. After having observed the giants Jupiter and Saturn, they switched to Uranus and discovered “limb-brightening” in the methane band, which manifests by shaping the planet into a donut [30].

Many people were attracted by those outstanding devices and left the old technologies they were working on to join the common effort developing further the CCD performances. Thinned, back-side illuminated devices then appeared during the late 70's. The first devices of that kind were developed by the Electro-optics Division of the Radio Corporation of America (RCA). The main advantage of that technology was their extremely good sensitivity in the blue [30]. TI CCDs then started to be available in the U.S.A. and their study and optimization had made great progress thanks to the work of Jim Janesick for example.

The Harvard-Smithsonian conference on solid-state imagers took place in June 1981. At that time, the number of observing groups using of CCDs had grown from 5 to 20 [30]. These scientists had deeply investigated the potential use of that technology. However, results were not satisfying yet when considering quantum efficiency and noise, leading to a situation where people started worrying about the readiness of this technology for the upcoming instruments.

Richard Aikens, founder and president of Photometrics Ltd., initiated a trend that finally led to an unprecedented success: he contracted directly with a silicon foundry to start the production of custom CCDs [30]. Nowadays, this trend is still running as astronomers directly work with a silicon foundry to customize their own CCDs. Photometrics then released a coating made of chemical phosphor to increase CCD sensitivity in the blue wavelength range. Several large-format detectors then appeared such as the 4000 by 4000 CCD with $15 \mu\text{m}$ pitch from Ford Aerospace (now Lockheed Martin) in the early 90's [30]. Nowadays, large sensors are packed together to form mosaics of up to some gigapixel focal planes [30].

CCDs quickly lose their sensitivity beyond $1.1 \mu\text{m}$ because of the intrinsic bandgap of silicon. Therefore, several other substrates are required to cover the infrared band up to at least $150 \mu\text{m}$. Approximately a decade after the CCDs revolutionized astronomy, the same tremendous event occurred for infrared arrays [30].

Infrared radiation was discovered by Sir William Herschel, who called it “colorific rays”, in 1800. However, the major breakthroughs did not happen before World War II since major developments in infrared detectors were accelerated by the military requirements [30]. Boosted by the military applications, several companies developed infrared sensors during the period 1974-1984. However, only a few of them were made available to astronomers as they were very often classified. Moreover, their size was at that time rather small (32 by 32 pixels or less).

Observing in the infrared enables probing star-forming regions full of clouds of gas and dust through which visible light does not penetrate. On the other hand, the most distant objects appear redder due to the cosmological redshift resulting from the expansion of the Universe and their spectrum effectively moves into the infrared. Observing deep into the centre of the galaxy, identifying cold interstellar material or performing chemistry analyses with the help of infrared spectroscopy are a few other applications infrared detectors offered to astronomers [30].

The boundary between optical and infrared regimes was in the past related to the lack of sensitivity of the human eye above 720 nm . CCDs then extended the “optical” observations up to $1.1 \mu\text{m}$ but a more sensible boundary appears close to 2.2 or $2.4 \mu\text{m}$. Indeed, a large change in the nature of the background light occurs at that point within the optical system (as stated in Chapter 1). Observing methods and instrumental designs therefore change accordingly. Below $2.2 \mu\text{m}$, background light essentially arises from *OH* emission from the Earth's atmosphere. Further in the spectrum, thermal emission from the atmosphere and the telescope optical parts dominate. The near-infrared region is usually defined as extending from 0.9 to $5.5 \mu\text{m}$. Available NIR detectors exhibit a sensitivity range that already overlaps with some CCDs at wavelengths shorter than $1.1 \mu\text{m}$ and will perform down to $0.5 \mu\text{m}$ [30]. Mid-infrared (MIR) is considered to extend from ~ 5 to $30 \mu\text{m}$ and far-infrared (FIR) from ~ 30 to $200 \mu\text{m}$.

The first generation of IR detectors suffered from a poor quantum efficiency, a high readout noise and a limited number of pixels. To overcome these limitations, budgets were allocated to research centers to conduct their own tests and develop new detectors. In the mid 80's, Ian McLean worked on the

definition of specifications for a future infrared sensor that would fit the astronomy requirements [30]. Driving factors then came from the wish for new instruments to be developed such as the Infrared Array Camera (IRAC) on Spitzer or NICMOS on the HST. Mercury-Cadmium-Telluride (*HgCdTe* or MCT) detectors, classified up to that time, were then considered for a wider use as they were very promising. They could indeed be customized to the shortest IR wavelengths and be run at 77 K while being controlled by CCD controllers [30].

Both space and ground astronomy programs stimulated the development of these infrared detectors and many laboratories were solicited in that goal. A key moment for infrared astronomy happened in March 1987 when a workshop occurred in Hilo, Hawaii. First images obtained with the latest detectors that were available were presented. The breakthrough that occurred at this time was similar to the one from 1981 with optical CCDs at the Harvard-Smithsonian meeting [30].

In 1993, when the meeting “Infrared Astronomy with arrays: the Next Generation” took place at the University of California, Los Angeles (UCLA), typical detectors had size of 256 by 256 pixels in the near-infrared and 128 by 128 in the mid-infrared. In 2008, typical available formats were in the NIR 2048 by 2048 and 1024 by 1024 in the MIR [30].

2.8.2 Generalities

This section focuses on the detector technologies that are suitable for near-infrared observation. Different possibilities exist and some of them are introduced in order to identify the most attractive sensor with respect to our instrument.

When considering the optical region extending from the ultraviolet to the near-infrared, the available detecting techniques may be separated into two groups: the thermal and the quantum detectors [33]. Both of them are said to be incoherent, i.e. they are sensitive to the light amplitude with no regard to its phase. Quantum detectors are sensitive to the incoming light flux through photon-electron interactions and individual detections may even be possible though longer integrations are more common. Their output signal then becomes analog as it is the case of thermal detectors. Light detection with thermal detectors occurs slightly differently: the incoming photon flux is measured through the increase of temperature induced by its absorption within the sensor material. Usually, they suffer from a reduced sensitivity and a slower response than quantum detectors but may be used through a much broader spectral waveband [33].

Two sub-groups may be considered within the quantum, or photon, detector category [30]. Photoemission sensors, such as photomultiplier tubes (PMT), are characterized by the ejection of a charge carrier (electron) following the external photoelectric effect which occurs when an incoming photon interacts with the sensor material. On the other hand, internal photoelectric effect occurs when a charge carrier is produced in a semiconductor substrate. These detectors are grouped within the photo-absorption category.

Two types of interactions may be considered in semiconductors: the photoconduction effect and the photovoltaic (or photodiode) effect. Photoconductors undergo a conductance change due to the creation of charge carriers within the material when illuminated. These are usually made of a single uniform semiconductor substrate [30]. On the other hand, junctions between several materials within photodiodes induce electric fields and potential barriers to which charge carriers then respond.

When the first infrared detectors were studied, it was initially considered to produce CCDs made from other semiconductors than silicon. Technical manufacturing problems were faced however and it

appeared that the knowledge accumulated in the silicon industry was not directly transposable to other substrates. Another approach, the “hybrid” array, was therefore followed. In this methodology, detecting and multiplexing tasks of the detector are separated and the infrared array adopts the morphology of a “sandwich” (see Figure 2.30) [30]. The upper slab of the array is made of the infrared sensitive material grid of pixels whereas the layer below is a silicon readout circuit. Indium “bump” connections are used to electrically link both parts of the array and an epoxy is injected between these to maintain the integrity of the sandwich. The assembly is usually called a focal plane array (FPA) or a sensor chip assembly (SCA). The silicon reading array is usually called a “readout-integrated circuit” or simply ROIC. This different sensor structure induces some differences with respect to typical CCDs. First, saturated pixels do not leak to their column neighbors and bad pixels do not totally obstruct their own column. Disadvantages are the fact that on-chip binning and charge-shifting are not allowed [30].

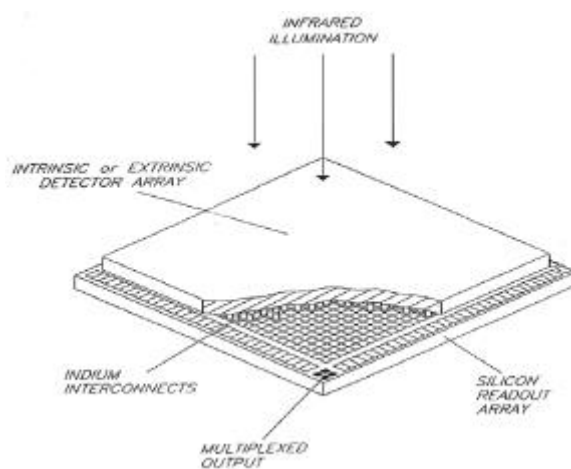


Figure 2.30 - A typical hybrid pattern of an infrared array device [30]

Last but not least, infrared arrays must be cooled down to temperatures way below those used for CCDs due to their smaller bandgaps. Most recent $HgCdTe$ arrays cooled at 77 K exhibit dark currents as low as $1\text{ e}^-/\text{min}/\text{pixel}$ and values around $0.1\text{ e}^-/\text{s}/\text{pixel}$ are reached at 30 K for $InSb$ detectors [30]. The maximum operating temperature T_{max} of a given detector whose cutoff wavelength is λ_c can be assessed with the rule of thumb from Hoffman, Love and Rosbeck [30]:

$$T_{max} = \frac{200\text{ K}}{\lambda_c (\mu\text{m})}$$

Examples from both technologies are presented in the next chapters and their related advantages and inconvenients are highlighted. Several manufacturers are identified and the selected detector will eventually be introduced.

2.8.3 Charge-coupled devices (CCD)

Since their first use in astronomy in the late 70's, CCDs rapidly became the dominant technology for professional observatories and amateur astronomers as well. Indeed, they benefit from attractive properties such as the possibility of long integrations and bi-dimensional imaging. On the other hand, their quantum efficiency and dynamic range largely surpass those obtained with the previously used photographic emulsions.

CCDs belong to the quantum detector category as they involve the photoelectric effect. Electron-pairs are produced as the photons impact the CCD semiconductor plane, which usually consist of silicon. The electrons are then accumulated with the help of electrodes which produce potential wells. Eventually, these are read out by a single electrode in order to evaluate their total number. Several developments appeared to improve this detection process such as electron bombarded CCD (EBCCD) or intensified CCD (ICCD). In both cases, many electron-pairs are created by accelerating a photoelectron before impacting the CCD.

Another detecting efficiency improvement involves the electrodes of the CCDs. Indeed, these can reflect part of the light impacting the detector, therefore decreasing the number of induced photoelectrons. Transparent polysilicon electrodes were first employed to replace the previous metallic ones and decrease these light losses. Then, back-illuminated CCDs were designed in order to completely overcome this issue since the incoming photons do not interact anymore with the electrodes. The risky required process of thinning the silicon substrate makes them rather expensive and fragile. However, they are less sensitive to cosmic rays than the standard versions and a quantum efficiency as high as 90% can be reached with a proper anti-reflective coating [33].

Typical CCDs exhibit a spectral sensitivity that ranges from 400 to 1100 nm, their efficiency dropping off in the near-infrared as the silicon substrate starts getting transparent [33]. Phosphor coatings may be used at shorter wavelengths to convert the incoming radiation back to the sensitive waveband of the detector. CCDs usually enable long integration times if the sensor is equipped with a cooling system to decrease its inherent dark signal. Amateur astronomy cameras usually implement Peltier coolers which enable a temperature difference of approximately 50° with the ambient one. Professional observatories rather use more sophisticated techniques such as liquid nitrogen to reach a typical operating temperature of -100°C .

One should however take into account the variation in quantum efficiency that these cooled conditions induce. Indeed, the sensor quantum efficiency typically decreases with temperature and a tradeoff appears between decreasing the detector noise and being able to detect photons. An optimum temperature must be identified to minimize the required integration time for a given signal-to-noise ratio. This phenomenon is presented in Chapter 2.8.7 when introducing a potential suitable CCD detector and deeply investigated in the analyses related to our instrument's photometric budget (Chapter 5).

Some disadvantages of CCDs should eventually be noted. Their strong interaction with cosmic rays induces spikes within the images as many ionizations are induced through these processes. One may average or interpolate the neighbors' information but the information originally contained in the pixels affected by the cosmic ray remains lost. Large variations as high as 10 to 20% in pixel sensitivity may also appear [33]. These may be overcome through a flatfield which consists of observing a uniform source and use this image as a normalizer.

“Hot” pixels, those suffering from a constant high background level, are the sources of additional issues. Indeed, these usually have a low charge transfer efficiency and a spurious line then appears since all the electrons coming from the preceding pixels follow the same charge transfer path [33]. No solution exists to solve this issue. Blooming or crosstalk also appears when some pixels approach their full well capacity and the following photo-electrons leak to adjacent pixels. This also happens in back-thinned CCDs as the electrons are formed away from the electrodes.

2.8.4 Photoconductive cells

Photoconductive cells are photon detectors which make use of their change in conductivity under illumination. Electrons from a semiconductor valence band are raised to the conduction band after their interaction with the incoming photon. The higher the incoming flux, the higher the conductivity, the latter being measured with the help of a small bias current [33]. Thanks to the large variety of semiconductors, detectors with a variety of characteristics such as cutoff wavelengths and operating temperatures can be found.

Two different categories of photoconductive cells are available: those implementing intrinsic semiconductors and the others using extrinsic semiconductors. Silicon, Germanium, mercury cadmium telluride (HgCdTe), lead sulphide (PbS) and indium antimonide (InSb) are examples of intrinsic semiconductors. Due to their large energy gap between the valence and conductive band, these materials are suitable for detection down to the near-infrared. In order to detect lower energy radiation, extrinsic semiconductors are manufactured by doping intrinsic ones. These doping atoms are introduced into the band gap in order to supply electrons or holes closer to the conduction band. One interesting feature of such detectors made from gallium doped germanium Ge(Ga) is their ability to tune their spectral sensitivity by applying a varying pressure on them. A spring is used for that purpose and their detectivity range can typically vary from $\sim[40-115] \mu\text{m}$ to $\sim[80-240] \mu\text{m}$ [33].

Quantum Well Infrared Photodetectors (QWIP) are made from the superposition of thin gallium arsenide (GaAs) and indium gallium arsenide phosphide (InGaAsP) or aluminum gallium arsenide (AlGaAs) layers so that electrons do not need to be excited all the way to the conduction band [33]. These electrons therefore need less energy to reach the conduction band and this makes these detectors sensitive from 1 to 12 μm . This sensitivity region remains rather narrow and can be modified thanks to different proportions between the constituents.

Typical $2k$ by $2k$ near-infrared-sensitive arrays can now be produced whereas $1k$ by $1k$ format is a more common limit in the MIR. Going further into the MIR domain, arrays are usually limited to a size of 256 by 256 pixels [33]. Although, some mosaic designs enable larger focal planes such as for the UK's 4 m infrared VISTA (Visible and Infrared Survey Telescope for Astronomy) telescope [33]. Some advantages of infrared arrays with respect to CCDs lie in the fact that their pixels are read-out individually. This enables non-destructive reading, the absence of cross-talk (blooming) and the fact that bad pixels do not corrupt the reading of their neighbors' information.

2.8.5 Bolometers

Bolometers are devices which undergo a change in their electrical resistivity when exposed to a radiation flux. The common practice is to introduce two strips of a selected material as arms of a Wheatstone bridge and measure its balance as one is illuminated. This way, slow environmental changes are filtered out as both elements are affected in the same way [33]. Rather difficult to construct, these sensors are usually used under very high background conditions [30]. Bolometers are essentially made of a large absorber associated with a thermometer through weak thermal links as depicted in Figure 2.31.

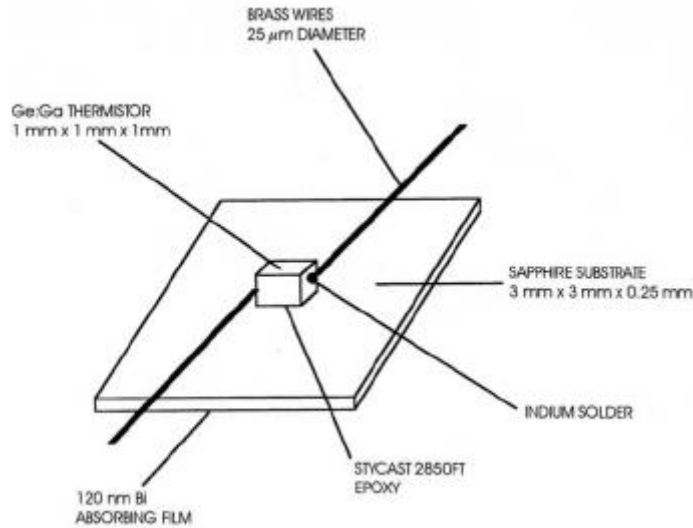


Figure 2.31 –Layout of a bolometer element [30]

Bolometers for astronomy purpose can be either used at room temperature or under deeply cooled conditions. Thanks to their simplicity and solidity, the first category, the thermistor bolometers, was selected in the past to be used in rockets and spacecraft. The others found their application over the entire infrared region but were replaced by photoconductive cells in the near- and mid-infrared regions. They are still in use in the far infrared and their typical operating temperature falls to 100 *mK* to reduce the thermal noise to its minimum. Typical materials used in such detectors are germanium doped with gallium, beryllium, silicon and silicon nitride [33].

Arrays up to 30 by 30 pixels can be produced but developments in thin films of superconductors could enable larger formats. These transition edge sensors (TES) are held at their transition temperature between superconduction and regular state. As a photon impacts on this material, the resistance changes due to the induced temperature increase and a bias current is employed to monitor this mechanism.

2.8.6 Technologies under development

A promising alternative technology may be found in superconducting tunnel junction detectors (STJ). These Josephson junctions offer a spectral response from the X-ray region to the longwave infrared and can detect individual photons. Moreover, they react at high speed to the incoming light flux and exhibit an inherent spectral resolution of perhaps 500 to 1000 in the visible [33]. The way they operate is based on the superposition of two superconducting layers between which is inserted an insulating material. Thanks to their wavelike behavior, electrons can flow between both superconducting layers as they form Cooper pairs at their lowest energy level. A magnetic field is applied to suppress this current.

These detectors are made from tantalum, hafnium or niobium Josephson junctions and cooled down to a tenth of the superconducting temperature (under 1 *K*). The absorption of an incident photon will split a Cooper pair if its energy approaches a milli-electron-volt. This energy amount is way lower than the required one for pair production within CCDs and enables the detection of radiation up to the millimeter scale. The spectral resolution of these sensors arises from the fact that multiple Cooper pairs will split as the incoming wavelength shortens.

2.8.7 Identified manufacturers of detectors

This section focuses on the identification of potential manufacturers of detectors which may be used within the considered instrument. As will be seen shortly, commonly used technologies in the near-infrared domain are proposed but CCDs are also investigated since the scientific waveband of interest drops off at the far end of their sensitivity range. Their potential use as a cheaper substitution option is studied in Chapter 5 in relation to the photometric budget.

Detectors specifically designed for near-infrared observations

Several detectors have been identified and some of them are listed below. Those are the most suitable ones with respect to the scientific goals of the project. Indeed, these highly sensitive NIR detectors offer the lowest intrinsic noise and therefore allow for shorter exposure times to reach the required SNR.

These detectors are the ActIR-1024 from AIM, the SATURN SW from Sofradir, the Cougar from Xenics and the Micro-Cam from Teledyne. They offer a high quantum efficiency in the considered near-infrared spectral band thanks to the use of *HgCdTe* or *InGaAs* focal planes (see Figure 2.32 for Sofradir detectors implementing a homemade anti-reflection coating). Moreover, their format ranges from 640 x 512 pixels to 4K by 4K and their pixel pitch can be either 15 μm or 30 μm in general.

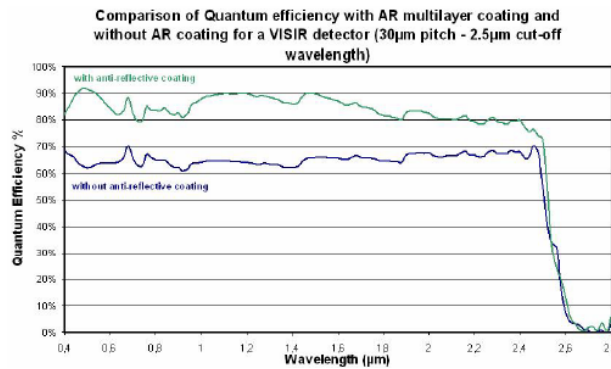


Figure 2.32 - Quantum efficiency of Sofradir detectors [53]

These detectors are equipped with an active cooling system which usually consists in a liquid nitrogen Dewar assembly. Their operational temperature therefore oscillates around 77 K which efficiently reduces the typical dark current affecting these detectors to less than 1 to a few e^-/sec .

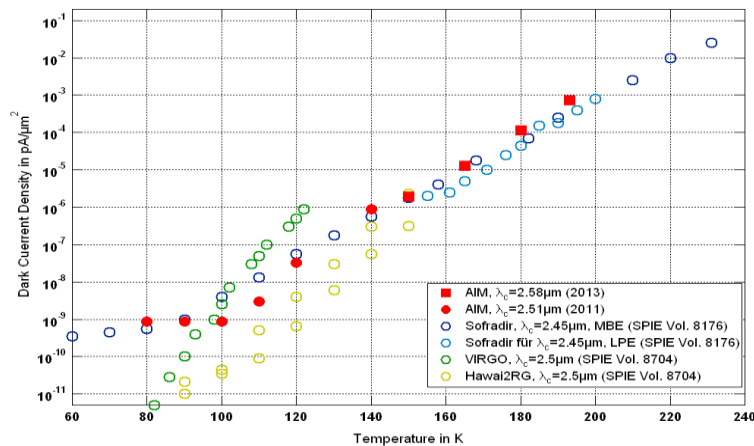


Figure 2.33 - Dark noise levels of different IR detectors (Figure courtesy of AIM [54])

The characteristics of these sensors, when available, are summarized in Table 2.1.

Dealer	Name	QE @ 1 μm	Readout noise	Dark current
Sofradir	Saturn SW	> 60% (80% with AR coating)	< 150 e^-	< 10 e^-/s (@ 80K)
AIM-IR	ActIR-1024	Not available	Not available	< 10 e^-/s (@ 80K)
Xenics	Cougar 640	Not available	15 e^-	< 10 e^-/s (@ 77K)
Teledyne	Micro-Cam	> 80% peak	< 20 e^-	< 2 e^-/s (@ 77 K)

Table 2.1 - Identified detectors' characteristics

CCD detectors with enhanced performances in the NIR domain

Specific NIR detectors have been mentioned in the previous section since those ones fit perfectly with our scientific goal. Indeed, they offer the highest quantum efficiency in the waveband of interest and reach low dark noise when cooled down to sufficiently low temperatures. However; those instruments are highly expensive (usually a few hundred k€) and other detectors, such as enhanced CCDs, may also be used in the near infrared even though their efficiency in this part of the spectrum sorely decreases. As an example, a potential candidate, the iDus 416 from Andor, is studied in Chapter 5 as a potential candidate by checking the required integration time when observing with such a detector. Its technical information are presented below.

The major issue with such silicon substrate materials is their extremely low sensitivity at 1 μm and beyond. Figure 2.34 below illustrates the varying quantum efficiency of several CCD technologies over the considered wavelength [55]. It can be seen from this figure that back-illuminated deep-depletion CCDs, which are near-infrared “optimized”, still have a low response around 1 μm and that this response steeply changes over a short wavelength range. Even though their peak photon-detection ability is shifted to redder wavelengths, their efficiency at 1 μm is not greatly increased.

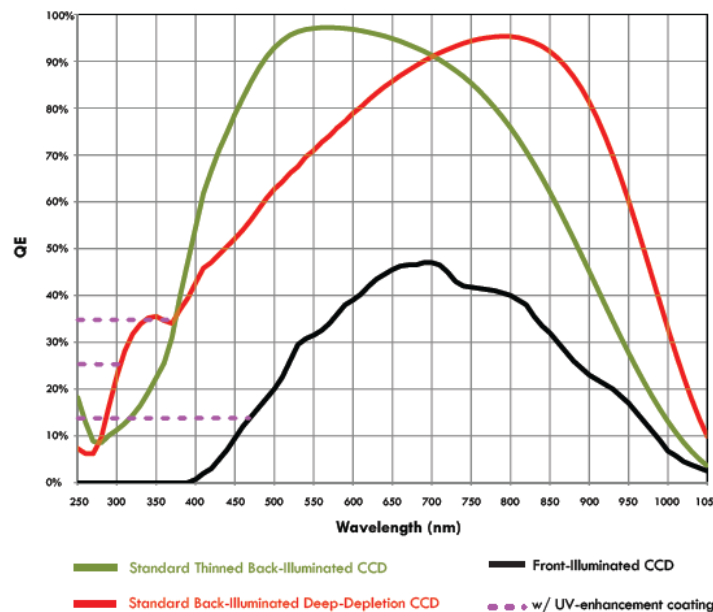


Figure 2.34 - Quantum efficiencies of different CCDs [55]

Usually, such detectors are used at low temperatures so that the dark current that pollutes the useful signal is as low as possible. The typical decrease in dark current with temperature is depicted in Figure 2.35 [56].

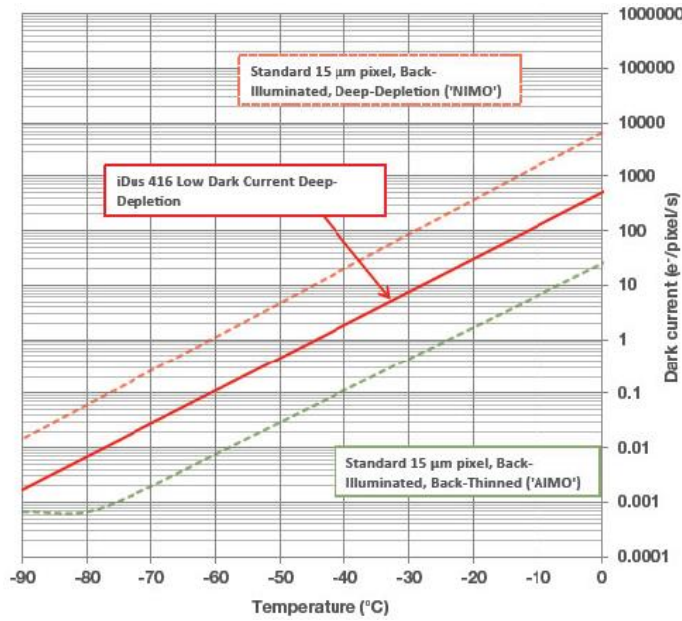


Figure 2.35 - Typical dark current variation as a function of temperature [56]

Decreasing the temperature is not free of any adverse effect however. Indeed, another important feature of those detectors that must be taken into account is the variation of their quantum efficiency with their operating temperature. Figure 2.36 highlights the typical decrease in quantum efficiency that occurs when cooling down these near-infrared optimized CCDs.

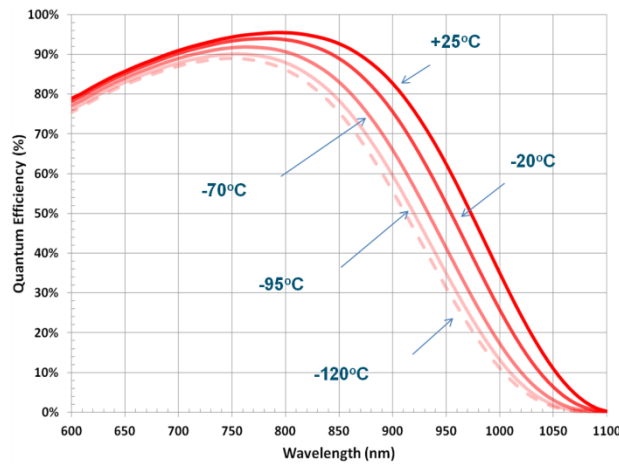


Figure 2.36 - Typical variation of quantum efficiency with temperature [56]

Even if reducing the temperature lowers the level of dark current, it may be more suitable to use such a detector at somewhat higher temperatures when considering its quantum efficiency decline. The decrease in dark noise may actually be compensated, and even overpassed, by the loss in quantum efficiency of the detector. Therefore, the photometric analyses related to CCDs, which intend to find the needed integration time to reach a given signal-to-noise ratio, must be conducted considering the entire range of operational temperatures of the detector and find the most suitable one to minimize the

required observation time. These conclusions will be confirmed and generalized in Chapter 5.9.1 under “Temperature control strategy”.

2.8.8 Selected detector

The selected detector is a 640 x 512 pixel *InGaAs* array from Photonic Science. The spectral sensitivity extends from 950 to 1700 nm and is depicted in Figure 2.37. The temperature of the sensor is decreased with the help of both a single-stage Peltier and a water-cooling system in order to decrease the thermally generated dark current. According to the manufacturer, the operating temperature of the chip is indeed lowered by approximately 55° with respect to the room temperature with this combination.

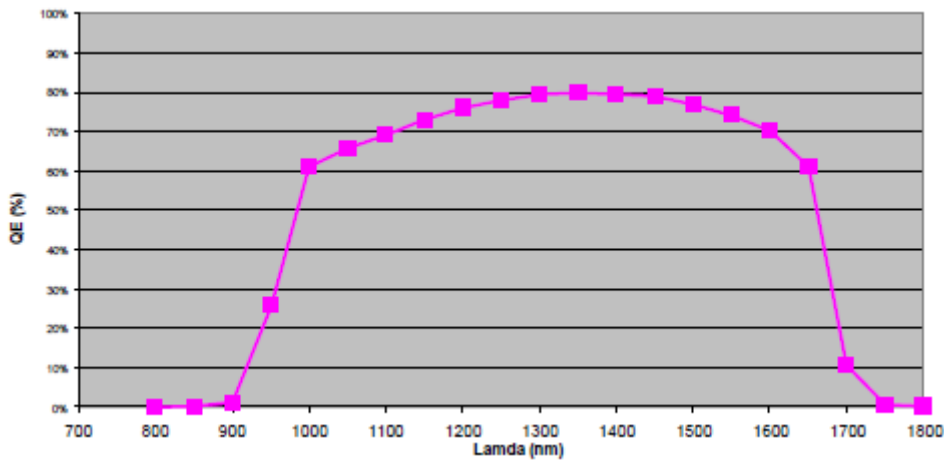


Figure 2.37 - Quantum efficiency of the Photonic Science Snake camera

The pixel pitch is 15 μm and the dark current is evaluated to $0.03 \text{ fA/pix} = 215.496 \text{ e}^-/\text{s/pix}$ when actively cooled. The table below summarizes the main features of this *InGaAs* detector according to the supplied Test Report from the manufacturer.

Parameter	Low gain mode	Medium gain mode	High gain mode
Full well capacity	1 384 000 e^-	103 959 e^-	23 762 e^-
Read out noise	400 e^-	47.9 e^-	25.3 e^-
Dark current	$0.03 \text{ fA/pix} = 215.496 \text{ e}^-/\text{sec/pix}$		
Non linearity	$< 2\%$		

Table 2.2 - Main characteristics of the Photonic Science Snake camera

Reasons for selecting this *InGaAs* detector are its high quantum efficiency in the *J*-band and its low cutoff wavelength around 1.8 μm . This avoids the use of a cold filter as explained by Dallier et al. and enables the spectrograph to be used at room temperature [26]. Moreover, this detector is equipped with a water-cooling system to decrease its inherent dark noise. Even if cryogenics should be selected instead, this cooling device does not require an intense care and refilling which is suitable for a robotic telescope such as TIGRE. The associated budget is also lower in terms of initial and continuous costs over the detector life. Chapter 5 eventually motivates the selection of a specific NIR detector over the classical CCD technology.

2.9 Conclusion

This technical chapter intended to discuss several aspects related to the ground-based spectroscopic astronomy. The whole optical chain was examined. Indeed, we started by reviewing the definition of observation windows and concluded with detector considerations.

Observing techniques and telescope optimization specific to the infrared domain were presented. These are mandatory at longer wavelengths in the infrared and may be required in our scientific case to increase the observation quality.

The atmospheric dispersion issue that occurs when performing astronomical observations from the ground was then introduced. Facing this problem cannot be avoided and large observatories use complex ADCs to overcome this obstacle. An alternate temporary strategy will be presented in Chapter 7.3.

Most suitable technologies were also studied for the optimization of instrument performances. This research concerned coatings, filters and glasses developed to perform in the near-infrared with a high efficiency. This maximization of the photon transmission through the system is required to minimize the required observing time. Indeed, even though bright sources are targeted, the TIGRE telescope has a limited collecting area.

Eventually, the potential detector technologies that could be used in the near-infrared were thoroughly explained. The selection of the most suitable detector is not a trivial point as it highly influences on many aspects of the instrument. Its characteristics for example intervene in the derivation of the instrumental requirements (see Chapter 4.3.6) and logically in the radiometric budget of the spectrograph (see Chapter 5). A careful attention was therefore dedicated to the selection of the detector.

Chapter 3 is devoted to the establishment of mathematical relations describing the behavior of spectroscopic instruments. Those will then be used in Chapter 4 to derive the instrumental specifications based on the scientific requirements.

Chapter 3

Theoretical background
on spectroscopy

3. Theoretical background on spectroscopy

3.1 Introduction

Spectrographs are instruments that analyse the wavelength dependence of the light emitted by a source. In astronomy, the emitted radiation is collected with the help of a telescope whose large aperture enables the observation of faint targets. Within the spectrograph, the collected photons are first collimated and then separated according to their wavelength, typically with the help of a grating or a prism. The dispersed image, called a *spectrum*, of the observed source is then recorded by a detector. The individual monochromatic components of the incoming light may finally be identified and provide useful information on the target properties.

The basic configuration of a spectrograph that is fed by a telescope is shown in Figure 3.1 [39]. It includes the different components cited above, that is a collimator, a dispersing element, a camera or focuser and a detector (a CCD for example). In this case, the spectrograph is equipped with a slit, i.e. a mechanical rectangular aperture which samples a portion of the object light through the telescope focal plane.

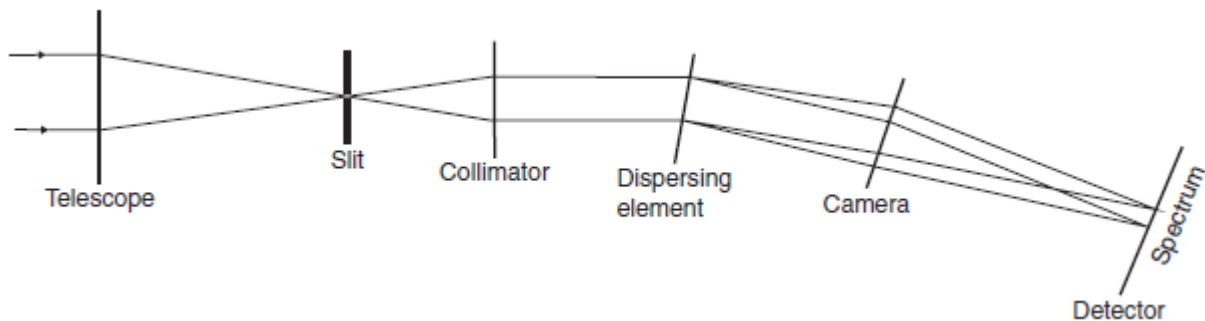


Figure 3.1 - Schematic diagram of a spectrograph [39]

3.2 The spectrograph figure of merit

The *figure of merit* of a spectrograph characterizes the rate at which spectral information is recorded. Both its radiometric and spectral efficiencies must therefore be involved in the calculation of this parameter. The throughput and the resolving power must first be defined in order to be able to evaluate the figure of merit.

The *throughput* of a spectrograph characterizes how many photons from the observed source effectively reach the instrument focal plane. Indeed, some of the telescope light grasp vanishes as the light travels from an optical surface to another. Photons may get lost or leave the regular light path due to absorption or scattering of optical components. Unwanted reflections and vignetting may also appear and decrease the light transmission efficiency. In other words, the throughput of a spectrograph defines the ability of this instrument to efficiently collect, transmit and use the telescope light and transform it into a spectrum. Of course, this parameter exhibits a chromatic behavior as the above mechanisms depend on wavelength.

The term *resolving power* should not be interchanged with *wavelength resolution*. The latter is the smallest separation $\delta\lambda$ of two spectral lines that a given spectrograph can resolve. An important point highlighted by Rayleigh is that the wavelength resolution value remains finite even when using an infinitesimally narrow slit due to diffraction effects [39]. Indeed, when considering an illuminated

rectangular aperture A , the intensity distribution $I(\theta)$ of the diffraction pattern that is induced follows the well-known *sinc* function:

$$I(\theta) \propto \left[\frac{\sin\left(\frac{\pi A \sin(\theta)}{\lambda}\right)}{\frac{\pi A \sin(\theta)}{\lambda}} \right]^2$$

The first minima of this function that appear next to the central peak occur at angles equal to $\theta \approx \sin \theta = \lambda/A$. Rayleigh's criterion on wavelength resolution then states that two spectral lines can be resolved until the principal maximum of the first wavelength λ just coincides with the first minimum of the second wavelength $\lambda + \delta\lambda$. This arbitrary choice depicts a situation that slightly underestimates the true limit at which two lines can be distinguished but is usually adopted [39].

The resolving power on the other hand is a dimensionless parameter equal to $\lambda/\delta\lambda$ where $\delta\lambda$ is the wavelength resolution. In order to establish an expression of the resolving power, we may use the Rayleigh criterion in first assessment. On the other hand, the dispersion relation of the selected optical element (whether a grating or a prism) must be accounted for. This latter relates the change in deviation angle θ as a function of incident wavelength λ and is equal to $\delta\theta = \frac{d\theta}{d\lambda} \delta\lambda$ at the separation limit. Hence, the expression of the resolving power R that follows is equal to:

$$R = A \frac{d\theta}{d\lambda} \quad (2)$$

The Rayleigh criterion is highly general. Indeed, neither the nature of the dispersing element nor the design parameters of the spectrograph are involved in Equation (2): only the horizontal aperture A and the angular dispersion $\frac{d\theta}{d\lambda}$ matter.

In practice, the resolving power of astronomical spectrographs is slit-limited. Indeed, a wider slit benefits for a higher throughput as more photons are collected. The final image detected at the focal plane of the spectrograph of a uniformly illuminated slit is simply the convolution of the above sinc^2 diffraction pattern and a box function. As the entrance slit width enlarges, the exit slit width depends essentially on the box function width and is less sensitive to diffraction.

Different disciplines can be distinguished depending on the value of R [57]. The value of 100 seems to be a common practice to separate photometry ($R < 100$) from spectroscopy ($R > 100$). Exceptions to that rule of course exist. For example, observing the Sun through a $H\alpha$ filter whose spectral resolution may be as high as 10 000 is considered to be related to photometry rather than spectroscopy. The study of astronomical objects with the help of an objective prism (located at the focal plane of the telescope) at $R = 50$ belongs on the other hand to spectroscopy.

Now that throughput and resolving power are defined, the figure of merit can be expressed. The figure of merit M of a spectrograph is the product of its resolving power R by the throughput:

$$M = R T \quad (3)$$

A rough approximation of one spectrograph's figure of merit can be quickly calculated. Let us consider the observation of a star of angular diameter θ_* under some seeing conditions. The associated mechanical slit is usually designed in such a way that its projected angular measure on the sky verifies $\theta_s = w/f_{tel} < \theta_*$ where w is the slit width and f_{tel} the telescope focal length. In this case, the throughput T is proportional to θ_s and the figure of merit can be approximated by the product $R \theta_s$.

Other factors can influence a spectrograph's figure of merit such as the total wavelength coverage $\Delta\lambda$. A second figure of merit derived by Bingham (see Chapter 0), can be defined to take into account this parameter. This latter is expressed by $\Delta\lambda R T$ and proportional to $N \theta_s$ where N is the number of wavelength resolution within the total image spectrum ($N = \frac{\Delta\lambda}{\delta\lambda}$). The relevance of this update version of the function of merit depends on the considered case. For example, one application may need to cover a large waveband whereas another would only focus on a specific line.

3.3 Theory of diffraction grating spectrographs

The successful use of diffraction gratings as dispersive elements in spectrographs started in the early 19th century on the Mt Wilson [39]. These optical surfaces were progressively preferred with respect to the previously selected prisms. Indeed, a first remark about diffraction gratings is that they outperform prisms at longer red wavelengths especially because of their higher angular dispersion. Moreover, diffraction gratings do not suffer from the large absorption prisms exhibit in the ultraviolet domain.

The grating equation and angular dispersion

The Fraunhofer's diffraction-grating equation is

$$m \lambda = d (\sin \alpha + \sin \beta) \quad (4)$$

where

- m is an integer, the grating order
- d is the spacing between the parallel grooves that pave the grating surface
- α is the incidence angle
- β is the diffraction angle

Usually, the grating is operated in collimated light so that α is constant whereas β varies as a function of wavelength. Both α and β are measured with respect to the grating normal and the sign convention states that both are positive if they lie on the same side of the grating normal (N). Figure 3.2 illustrates the case of a reflective grating where both α and β are positive [39].

In the previous grating equation, light is supposed to reach the grating in the normal plane, that is, the plane which is perpendicular to both the grating's surface and its grooves. If the light illuminates the grating at an incidence angle γ to the normal plane, the equation has to be rewritten as follows:

$$m \lambda = d \cos \gamma (\sin \alpha + \sin \beta)$$

Figure 3.2 also illustrates the notion of blaze angle θ_B which is the angle that can be conferred to the facets with respect to the grating normal. These tilted facets are used to concentrate much of the light in a single order and improve the grating efficiency. Blazed gratings are more commonly employed in what is called quasi-Littrow mode. The Littrow configuration refers to any spectrograph in which the dispersed beams come back close to the path of incident light, that is, $\alpha \simeq \beta$. Therefore, a system that approximately satisfies the Littrow condition is called a quasi-Littrow spectrograph.

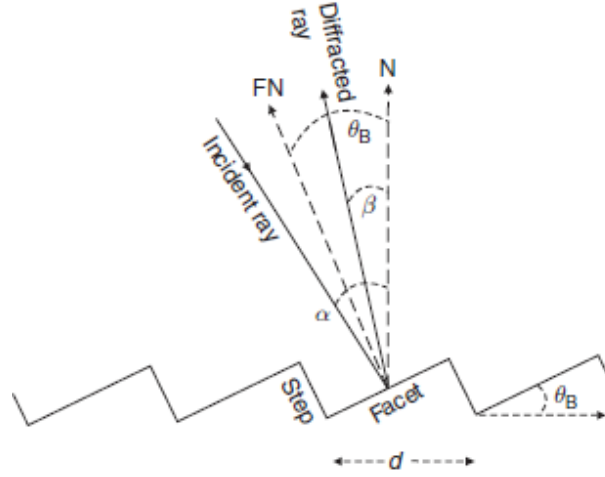


Figure 3.2 - Reflective grating [39]

The grating efficiency is actually greater when it is used in a quasi-Littrow configuration. Considering blazed gratings, we can write:

$$\alpha = \theta_B + \theta$$

and

$$\beta = \theta_B - \theta$$

where θ_B ($(\alpha + \beta)/2$) is the blaze angle and θ is called the Littrow angle ($(\alpha - \beta)/2$), which is a measure of the small departure from the Littrow configuration. By using these new notations, the grating equation can be rewritten this way:

$$m \lambda = 2 d \cos \gamma \sin \theta_B \cos \theta \quad (5)$$

Considering a quasi-Littrow configuration with incidence angle in the normal plane (θ small and γ zero), it follows:

$$m \lambda \simeq 2 d \sin \theta_B$$

The differentiation of the grating equation (4) leads to the evaluation of the grating *angular dispersion*:

$$\begin{aligned} m &= d \cos \beta \left(\frac{d\beta}{d\lambda} \right) \\ \Leftrightarrow \left(\frac{d\beta}{d\lambda} \right) &= \frac{m}{d \cos \beta} = \frac{\sin \alpha + \sin \beta}{\lambda \cos \beta} \simeq \frac{2 \tan \beta}{\lambda} \\ &\simeq \frac{2 \tan \theta_B}{\lambda} \end{aligned}$$

where the last approximation remains valid in a quasi-Littrow mode of operation.

Resolving power of a grating spectrograph: the diffraction-limited case

We previously introduced the Rayleigh criterion and noted its large application field as it does not infer any hypothesis on the dispersing element nature ($R = A d\theta/d\lambda$). In general, the larger the dispersing elements, the higher the resolving power. Considering a diffraction grating, the light beam leaving this element at β exhibits a width equal to $L \cos \beta$. Rayleigh's equation can therefore be rewritten as:

$$R_{diff} = L \cos \beta \frac{d\beta}{d\lambda} = L \cos \beta \left(\frac{m}{d \cos \beta} \right) = L \left(\frac{m}{d} \right)$$

$$= m N_{groove}$$

where N_{groove} is the total number of grooves engraved onto the grating surface. This shows the diffraction limited resolving power can be increased in using a high grating order or by increasing the number of illuminated grooves.

In a quasi-Littrow configuration, using the approximation $\frac{d\beta}{d\lambda} \simeq \frac{2 \tan \beta}{\lambda}$ leads to:

$$R_{diff} = L \cos \beta \left(\frac{2 \tan \beta}{\lambda} \right) = \frac{2 L \sin \beta}{\lambda}$$

$$\simeq \frac{2 L \sin \theta_B}{\lambda}$$

Otherwise, the exact solution can be rewritten as:

$$\frac{2 L \sin \theta_B \cos \theta}{\lambda}$$

Resolving power of a grating spectrograph: the slit-limited case

Figure 3.3 illustrates a schematic view of an astronomical grating spectrograph that is fed at its entrance slit by a telescope of aperture A_{tel} and focal length f_{tel} [39]. The entrance slit width at the telescope focal plane is equal to w whereas its corresponding image at the spectrograph focal plane is equal to w' . On the other hand, A_{coll} and A_{cam} designate the beam diameters respectively before and after the grating. The grating dimension perpendicular to the grooves is still denoted as L .

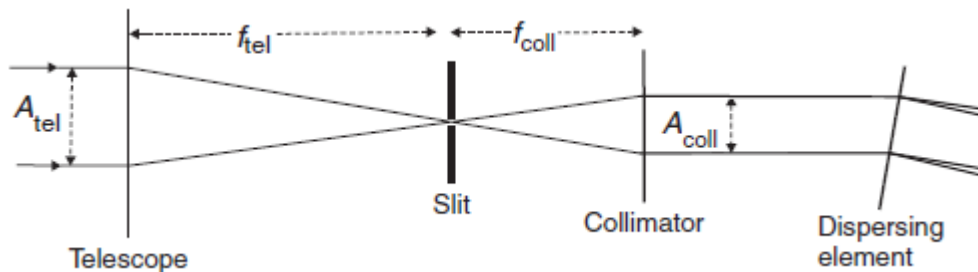


Figure 3.3 - Diagram of a telescope followed by a spectrograph (adapted from [39]).

The wavelength resolution is assumed to be dominated by the slit width. In other words, this will be the case if the angular spread $\delta\beta$ of a monochromatic beam leaving the grating due to the finite slit

size is much larger than λ/A_{cam} , the one induced by diffraction. The monochromatic angular spread of the entrance slit that impacts the grating is equal to:

$$\delta\alpha = \frac{w}{f_{coll}}$$

Previously, we derived the dispersion of a grating by differentiating the Fraunhofer equation with respect to the wavelength. This time, we perform the differentiation at constant wavelength to establish the connection between incident and diffracted angle variations. The obtained relation writes:

$$\cos\alpha \delta\alpha + \cos\beta \delta\beta = 0$$

or

$$|\delta\beta| = \frac{\cos\alpha}{\cos\beta} \delta\alpha = \frac{\cos\alpha}{\cos\beta} \frac{w}{f_{coll}}$$

where the term $\frac{\cos\alpha}{\cos\beta}$ is called the anamorphic magnification. Therefore, the slit-limited resolving power condition can be written as follows:

$$\frac{\cos\alpha}{\cos\beta} \frac{w}{f_{coll}} \gg \frac{\lambda}{A_{cam}}$$

Since $\frac{A_{cam}}{\cos\beta} = \frac{A_{coll}}{\cos\alpha}$, we obtain:

$$w \gg \frac{\lambda f_{coll}}{A_{coll}}$$

The wavelength resolution in slit-limited cases can now be calculated:

$$\begin{aligned} \delta\lambda &= \frac{1}{\frac{d\beta}{d\lambda}} \delta\beta = \frac{d\cos\beta}{m} \left(\frac{\cos\alpha}{\cos\beta} \right) \frac{w}{f_{coll}} \\ &= \frac{\lambda}{(\sin\alpha + \sin\beta)} \frac{w \cos\alpha}{f_{coll}} \end{aligned}$$

Eventually, the resolving power of slit-limited grating spectrographs can be expressed as:

$$\begin{aligned} R_{slit,1} &= \frac{\lambda}{\delta\lambda} = \frac{(\sin\alpha + \sin\beta) f_{coll}}{w \cos\alpha} \\ &= \frac{2 f_{coll}}{w} \frac{\tan\theta_B}{1 - \tan\theta_B \tan\theta} \end{aligned}$$

In the case of a quasi-Littrow configuration ($\alpha \simeq \beta$), the resolving power can be approximated by:

$$R_{slit,1,L} = \frac{2 f_{coll}}{w} \tan\theta_B$$

The general R_{slit} expression can also be expressed in terms of the collimator beam size, A_{coll} , by noting that $f_{coll}/f_{tel} = A_{coll}/A_{tel}$. Therefore, we obtain:

$$\begin{aligned}
 R_{slit,2} &= \frac{2 A_{coll} f_{tel}}{w A_{tel}} \frac{\tan \theta_B}{1 - \tan \theta_B \tan \theta} \\
 &= \frac{2 A_{coll}}{\theta_s A_{tel}} \frac{\tan \theta_B}{1 - \tan \theta_B \tan \theta} \quad (6)
 \end{aligned}$$

where $\theta_s = w/f_{tel}$ is the angular size of the slit projected back onto the sky. The expression can finally be approximated in a quasi-Littrow case by:

$$R_{slit,2,L} \simeq \frac{2 A_{coll} \tan \theta_B}{\theta_s A_{tel}}$$

The resolving power can finally be expressed in a third manner:

$$R_{slit,3} = \frac{2 L \sin \theta_B \cos \theta}{\theta_s A_{tel}}$$

which becomes in a quasi-Littrow configuration:

$$R_{slit,3,L} = \frac{2 L \sin \theta_B}{\theta_s A_{tel}}$$

All three expressions of the resolving power are fundamental to the design philosophy of astronomical spectrographs [39]. Indeed, in order to start the conception of a new instrument, the designer must account for the scientific requirements that were previously established. These expressions of the resolving power highlight which parameters impact on the instrument performances. A particular care is therefore required to optimize the performances of a spectrograph by playing on the right parameters. The size of the instrument is also a particular concern if the instrument must be portable. The above relations must also be used to identify how the resolving power may be maximized while keeping the size of the instrument as small as possible. These considerations will appear in particular in Chapter 4.3 when the instrumental requirements are derived with the help of Bingham's methodology [58].

Several useful conclusions can already be drawn when having a look at these equations.

- The expression $R_{slit,1,L}$ shows that long collimator focal lengths, narrow slits and high blaze angles contribute to increase the resolving power. Of course, the larger the focal length, the larger the beam size A_{coll} and consequently the grating could be overfilled. This must be considered as large elements may be required and manufacturing possibilities limited. Narrow slits naturally benefit to a higher spectral resolution since the associated monochromatic image reduces in size. One must still remember that diffraction establishes an upper limit on the resolving power. Higher blaze angles must be promoted and this will be taken into account in Bingham's methodology. The resolving power goes as $\tan \theta_B$. For a given focal length f_{coll} , larger blaze angles induce the need for gratings with larger dimension L . Otherwise, the grating may be overfilled and light leakages would reduce the throughput rapidly.
- The resolving power expression $R_{slit,1}$ emphasizes the fact that high resolving powers are promoted by long collimator focal lengths. Cassegrain spectrographs are not well suited for that purpose since flexure may quickly become an issue. This is the reason why Coudé spectrographs are preferred in that case since these spectrographs are stationary [39].

- By considering $R_{slit,2,L}$, we can see that large beam sizes A_{coll} also favour high resolving power. Once again, this does not depend on the fact whether or not the grating is overfilled. This is interesting and some spectrographs have been designed this way: promoting a large resolving power at the cost of vignetting losses because it may be more than compensated by a wider slit [39].
- $R_{slit,3,L}$ eventually indicates that R_{slit} is proportional to the size L of the grating normal to the grooves. This conclusion remains valid only if the grating is not overfilled, that is, $A_{coll} = L \cos \alpha$. If overfilled, the considered size must be the one that would fit the collimator beam to avoid any vignetting. This relation therefore highlights the fact that high resolving power either requires very large gratings or gratings with large blaze angles. This is why nowadays instruments exhibit optical elements whose diameters are much larger than before. Manufacturing limitations have changed from the time Dallier et al. first carried out NIR fiber-fed experiments. MOONS is an example of that trend as was emphasized in Chapter 1.4.2.

It might appear unsuitable to neglect the effects of diffraction in certain conditions. In this case, the overall resolving power that includes both slit- and diffraction-limits must be calculated. The use of small telescopes at long wavelengths is a typical example where those effects must be accounted for. The overall resolving power must therefore be expressed as follows:

$$\frac{1}{R} = \frac{1}{R_{slit}} + \frac{1}{R_{diff}} = \frac{1}{\frac{2 L \sin \theta_B \cos \theta}{\theta_s A_{tel}}} + \frac{1}{\frac{2 L \sin \theta_B \cos \theta}{\lambda}}$$

$$\Leftrightarrow R = \frac{2 L \sin \theta_B \cos \theta}{\theta_s A_{tel} + \lambda}$$

A last remark concerning resolving power is the comparison between the performances of prisms and grating spectrometers when using the same entrance slit. The prism instrument slit-limited resolving power is equal to:

$$R_{slit} = t \frac{dn}{d\lambda} \frac{\lambda}{\theta_s A_{tel}}$$

where t is the prism's base dimension, while the one of a Littrow grating instrument ($R_{slit,3,L}$) is:

$$R_{slit} = \frac{2 L \sin \theta_B}{\theta_s A_{tel}}$$

Therefore, the ratio between those expressions is:

$$\frac{R_{prism}}{R_{grating}} = \frac{\lambda t \frac{dn}{d\lambda}}{2 L \sin \theta_B}$$

When considering dispersing elements of the same size ($t \simeq L$), Jacquinot demonstrated that for all common glasses, wavelengths and a reasonable blaze angle, blazed gratings outperformed prisms. Eventually, the advantage was shown to be a factor of 50-100 in the near infrared and 5-10 times in the near ultraviolet and in the infrared [39]. At the time Jacquinot published his results, low-cost blazed gratings were becoming available and the combination led to the decline in the use of prisms as dispersers in spectrometers.

3.4 Simple requirements on cameras and detectors

The previous evaluations of the resolving power involved the wavelength and the dispersion relation of the grating. No hypothesis on the detector or the selected camera was stated. The purpose of the camera is to transform the angular distributions of photons into a linear one onto the detector. This transformation should occur while limiting the effect on the instrument resolving power, this means avoiding any degradation.

The further calculations involve an ideal camera, i.e. aberration free, of focal length f_{cam} which produces an exit slit of width w' , image of an entrance slit of width w . This camera is considered to exhibit a focal ratio of F_{cam} equal to f_{cam}/A_{cam} , where A_{cam} is as previously introduced the size of any monochromatic beam leaving the grating. The sensor lying in the camera's focal plane is supposed to be made of a number of pixels N_{pix} whose dimension in the dispersion direction is ΔS_{pix} . Thus, the overall size of the detector is equal to $\Delta S_{det} = \Delta S_{pix} N_{pix}$.

Reciprocal dispersion and free spectral range

In the previous section, we calculated the angular dispersion $\frac{d\beta}{d\lambda}$ which is equal to $\frac{m}{d \cos \beta} \simeq \frac{2 \tan \beta}{\lambda}$ for a grating instrument. On the other hand, the reciprocal dispersion on the detector, sometimes denoted as the *plate factor*, is defined as:

$$P = \frac{d\lambda}{dx} = \frac{1}{f_{cam} \frac{d\beta}{d\lambda}} = \frac{d \cos \beta}{m f_{cam}}$$

where x stands for the distance measured along the dispersion direction on the detector. The commonly used units for P are $\text{\AA}/mm$ or nm/mm .

Since the grating equation is satisfied for all wavelengths for which m is an integer, there are two wavelengths λ and λ' for which we have $m \lambda' = (m + 1)\lambda$ [57]. The difference $\Delta\lambda = \lambda' - \lambda$ is then called the free spectral range and is equal to:

$$\Delta\lambda_{FSR} = \Delta\lambda = \frac{\lambda}{m} = \frac{\lambda'}{m + 1}$$

The corresponding range of diffraction angles amounts to $\Delta\beta_{FWHM} = \lambda/(d \cos \beta)$. Further than this allowed spectral range, wavelengths from the two subsequent orders will overlap and the contained information will be mixed. Spectrographs operating at low orders of diffraction therefore enable a large waveband to be covered. Instruments working at higher diffraction orders must incorporate a second dispersive element whose axis is perpendicular to the first to split the different orders. This latter is called a cross-disperser [57].

The projected etendue of an order onto the sensor when accounting for the camera focal length is then equal to:

$$\begin{aligned} \Delta S_{order} &= f_{cam} \Delta\beta_{FWHM} = f_{cam} \frac{\lambda}{d \cos \beta} = \frac{\lambda}{m P} \\ &= \frac{\Delta\lambda_{FWHM}}{P} \end{aligned}$$

On the other hand, if the detector size ΔS_{det} is smaller than the order span ΔS_{order} , the actual recorded, and truncated, wavelength range will simply be equal to:

$$\Delta\lambda_{order} = P \Delta S_{det}$$

What has finally to be mentioned is that the actual intensity distribution over an order, or the efficiency function of a grating, is only roughly described by a *sinc*-squared function [39]. In reality, those curves are much more complex functions depending on the polarization, the blaze angle, the incidence angle as well as the groove profile. These are usually available from the manufacturer when selecting off-the-shelf gratings or may be tuned by specific techniques. These should be inspected before choosing any grating in order to check the efficiency over the scientific waveband of interest.

Resolution of a detector and Nyquist sampling theorem

The Nyquist theorem states a lower limit on the frequency at which a discretely sampled function must be evaluated to recover the entire information. This latter must be at least greater than twice the value of the highest frequency detected within the Fourier spectrum of the function. When considering spectroscopic applications, this theorem directly impacts the pixels density within the detector. In the case of slit-limited resolving power, the wavelength resolution element associated to the monochromatic slit image of width w' is given by:

$$\delta\lambda = w'P = \frac{\lambda}{R_{slit}}$$

Therefore, to satisfy the Nyquist theorem, each pixel must be of size:

$$\Delta S_{pix} \leq \frac{w'}{2}$$

or the pixel spatial density must be at least:

$$\rho_{pix} \geq \frac{2}{\delta\lambda/P} \text{ pix/mm} .$$

If the pixel size ΔS_{pix} overpasses this limit, the resolving power of the spectrograph then becomes detector limited. The distinction power of fine spectral features therefore decreases. The slit width may be increased to meet the requirement only if the observed spectrum does not exhibit such high frequencies. On the contrary, increasing the number of pixels and oversampling the spectrum leads to an increase of noise. The consequence is that a higher integration time is required to reach the same signal-to-noise ratio. In summary, any departure from the Nyquist condition leads to a degradation of the spectrograph efficiency. Usually, spectrograph instruments exhibit 2 or 3 pixels per wavelength resolution element [39]. The fulfillment of the Nyquist sampling requirement ($w' = 2\Delta S_{pix}$) enables to get a first approximation of the required focal length of the camera. Indeed, we already know that:

$$\frac{w'}{w} = \frac{f_{cam}}{f_{coll}} \left(\frac{\cos \alpha}{\cos \beta} \right)$$

and

$$w = \theta_s f_{tel}$$

and combining both relations to isolate the camera focal length, we obtain:

$$f_{cam} = \frac{2 \Delta s_{pix}}{\theta_s} \frac{\cos \beta}{f_{tel} \cos \alpha} f_{coll}$$

$$= \frac{2 \Delta s_{pix} L \cos \beta}{\theta_s A_{tel}}$$

Several conclusions may already be drawn by inspecting this last relation:

- As expected, the camera focal length depends on the pixels size of the selected detector,
- The larger the telescope, the smaller the focal length of the camera,
- The focal length of the camera is proportional to the grating illuminated height (perpendicular to the grooves direction),
- Observing spectra with a wide entrance slit to cover a large field of view requires the selection of a fast (short focal length) camera.

Using the expression of the resolving power $R_{slit,3,L}$, we get:

$$f_{cam} = \Delta s_{pix} R \cot \theta_B (1 + \tan \theta \tan \theta_B)$$

$$\simeq \Delta s_{pix} R \cot \theta_B$$

when θ is small (Littrow configuration). This latter relation shows in one equation that high resolving powers from narrow slits need longer focal length cameras. Eventually, the camera focal ratio can be calculated (when considering monochromatic light):

$$F_{cam} = \frac{f_{cam}}{A_{cam}} = \frac{f_{cam}}{L \cos \beta}$$

$$= \frac{2 \Delta s_{pix}}{\theta_s A_{tel}}$$

The latter relation is valid when the Nyquist theorem is fulfilled. This illustrates the fact that the camera focal ratio is a function of the angular slit width, the pixel size and the telescope aperture. On the other hand, this parameter is neither related to any characteristics of the grating, nor the focal ratio of the telescope and collimator.

The evaluation of the camera focal length was derived by ensuring the fulfillment of the Nyquist theorem. This does not certify the waveband of interest will entirely fall onto the selected detector. No consideration on total imaged spectral range was indeed involved in the calculation of the camera focal length. In reality, both conditions may not be met simultaneously. Usually, a reduction of the covered wavelength range is accepted in case the detector does not incorporate enough pixels to record the whole spectrum in one order [39].

The plate factor may also be evaluated in a convenient way when the Nyquist sampling condition is met:

$$P = \frac{d\lambda}{dx} = \frac{\lambda}{2 \Delta s_{pix} R_{slit}}$$

High resolving powers therefore means a low plate factor. This situation is commonly referred to as “high dispersion”. This term is not recommended as it may be ambiguous [39].

Number of detector pixels required

In order to assess the required number of pixels to image the entire order from a grating, we must calculate how many spectral resolution elements are included in the associated free spectral range. We previously obtained a relation to evaluate the subtended angle $\delta\beta$ by a resolution element $\delta\lambda$ which is $\delta\beta = \frac{\cos\alpha}{\cos\beta} \frac{w}{f_{coll}}$. The total angular range of the free spectral range was approximated by $\Delta\beta_{FWHM} = \frac{\lambda}{d \cos\beta}$. Dividing the whole angular range by the resolution element leads to the total number of resolution elements within an order:

$$\frac{\Delta\beta}{\delta\beta} = \frac{\theta_A N_{grooves}}{\theta_s}$$

The number of pixels needed to record all the information in an order can now be evaluated since it is just twice the number of resolution elements to verify the Nyquist theorem. Hence:

$$N_{pix} = 2 \frac{\theta_A}{\theta_s} N$$

We can conclude that the number of pixels in the detector is independent of order number and many other spectrograph parameters. A simple conclusion is that high frequency gratings require large detectors with a high number of pixels [39].

3.5 Conclusion

This chapter was devoted to the establishment of the basic mathematical relations governing a spectrograph instrument. The conception of a new instrument naturally requires the proper understanding of this instrumentation family. The establishment of these equations is therefore the starting point of any conception.

The spectrograph intrinsic configuration was first presented. The main optical elements involved in this kind of instrument were introduced and their related functions explained. The function of merit which maximizes both throughput and resolving power was studied. The grating equation was then deduced and the associated dispersing relation calculated. Several expressions of the resolving power were eventually derived.

Several conclusions could be drawn. The resolving power of spectrographs is influenced by several factors. We saw that large collimator focal lengths benefit to better spectral resolution. Narrow slits also naturally favor a high resolving power but throughput may suffer from this width reduction. Another parameter that can be modified to optimize a spectrograph's efficiency is the grating blaze angle. The higher the blaze angle, the larger the resolving power. This parameter is highly important as it benefits to the improvement of the spectral resolution while maintaining other mechanical parameters unchanged. In other words, the focal length of the collimator may be maintained at reduced values and the overall instrument size minimized. This is particularly important when the instrument size must be kept under certain limits. This may be the case for portable or Cassegrain instrument for which flexure matters. On the other hand, it was also shown that large optical beam apertures are suitable to maximize the slit-limited resolving power of spectrographs. For our purpose, it is therefore mandatory to select a high blaze grating in order to limit the size of the instrument. Even if the instrument is fiber-fed and located at a remote location from the telescope, its portability would be threatened if large optics are employed. On the other hand, the overall budget of the spectrograph has to be taken into account since the manufacturing cost of optics usually increases with size. Eventually, it was noticed that gratings outperform prisms in the considered near-infrared part of the spectrum for a similar illuminated aperture.

Investigations on the detector pixel size and number were also conducted. The Nyquist criterion was recalled and employed to answer these questions. Indeed, there exists a minimum number of sensor pixels to properly sample the spectrum and retrieve the entire information it includes. The required sensor size to image the entire spectrum from one order of the grating was also identified. Both conditions may not be fulfilled simultaneously and usually a reduced spectral range is accepted. For example, it might appear not sensible to adapt the spectrograph performances in accordance to the available technologies the actual budget offers. A better idea is to optimize the spectrograph figure of merit and then adapt the detector when additional funds are allocated. Moreover, the spectral waveband included within a single frame may not be of major importance. Indeed, some studies only focus onto specific spectral features and do not require a large waveband to be covered at each spectral record.

Chapter 4 concentrates on the optical design of the spectrograph which makes use of the developed mathematical relations from this Chapter 3. We'll see that the above statements will be employed in Bingham's methodology to derive the instrumental specifications. The associated optical analyses are also presented such as the resolving power verification with specific software solutions.

Chapter 4

Spectrograph optical
design

4. Spectrograph optical design

4.1 Introduction

This chapter focuses on the optical design of the instrument starting with the calculation of its parameters before optimization. One purpose here is to match the required instrument to the selected telescope to obtain optimal coupling efficiency. Then, the scientific requirements, such as the resolving power and the wavelength range, must be taken into account when deriving the instrumental parameters. The site location and its associated seeing quality also impact on the spectrograph design. Indeed, the overall throughput of the telescope-fiber-spectrograph chain also depends on the coupling efficiency between the star image and the fiber core. Eventually, the exit slit width has to match the pixel size of the detector in order to verify the Nyquist criterion.

All these considerations are treated in the next chapters, going from the early translation of the scientific requirements to specific spatial configurations of optics during optimization. General grating and spectrograph mathematical relations are used as a first step to calculate the instrument parameters and optical software are then used to optimize the design.

4.2 Basic considerations

The scientific requirements in Table 1.1 impose the spectrograph resolution to be at least 10 000, the ultimate goal being 20 000 over the spectral range 1-1.1 μm . Therefore, each resolved wavelength element has to be ideally equal to:

$$\begin{aligned}\delta\lambda &= \frac{\lambda_{mean}}{R} \\ &= 1.05 \text{ \AA} \quad \text{if } R = 10000 \\ &= 0.525 \text{ \AA} \quad \text{if } R = 20000\end{aligned}$$

Since the Nyquist theorem states that each wavelength resolution element has to be discretized by two pixels, the required number of pixels to cover the entire considered waveband of 100 nm is:

$$\begin{aligned}N_{pix} &= 2 \frac{100 \text{ nm}}{0.105 \text{ nm}} \approx 1905 \text{ pixels} \approx 2000 \text{ pixels} \quad \text{if } R = 10000 \\ &= 2 \frac{100 \text{ nm}}{0.0525 \text{ nm}} \approx 3810 \text{ pixels} \approx 4000 \text{ pixels} \quad \text{if } R = 20000\end{aligned}$$

Typical near-infrared detectors incorporating pixels that are 30 μm wide, a first assessment of the required detector size can be carried out. Indeed, considering a pixel size of 30 μm and the previously calculated number of pixels, the following detector size is obtained:

$$\begin{aligned}Det_{size} &= 2000 \times 30 \mu m = 60 \text{ mm} \quad \text{if } R = 10000 \\ &= 4000 \times 30 \mu m = 120 \text{ mm} \quad \text{if } R = 20000\end{aligned}$$

The results show that the required detector size is approximately equal to 12 cm and that the number of pixels approaches the maximum available detector sizes limited to approximately 4000 pixels. The direct consequence is that the total waveband of interest may not be covered in a single exposure unless an echelle spectrograph is considered. In our case, the imaging direction is used for sky

background measurements as well as potential other targets falling onto the bundle and therefore, the solution consisting in using a cross-disperser is currently not foreseen.

The reciprocal dispersion or plate factor may also be evaluated in first approximation. This parameter, as stated before, is usually expressed in nm/mm or $\text{\AA}/mm$ and depicts the variation in wavelength that is measured as the focal plane is swept through. Considering the required wavelength resolution element and the typical pixel size of near-infrared detectors, the reciprocal dispersion is equal to

$$P = \frac{1.05 \text{ \AA}}{2 \times 30 \text{ \mu m}} = \frac{0.105 \text{ nm}}{60e^{-3} \text{ mm}} = 1.75 \text{ nm/mm} \quad \text{if } R = 10000$$

$$= \frac{0.525 \text{ \AA}}{2 \times 30 \text{ \mu m}} = \frac{0.0525 \text{ nm}}{60e^{-3} \text{ mm}} = 0.875 \text{ nm/mm} \quad \text{if } R = 20000$$

Further calculations involving spectrograph relations must be performed to obtain accurate instrumental requirements. The next section intends to evaluate the optical elements needed to achieve the scientific requirements specified in Table 1.1.

4.3 From scientific requirements to instrument specifications

The first choice before starting any optical design or parameter calculation is to decide upon the nature of the dispersive element used inside the spectrograph, i.e. whether using a diffraction grating or a prism. As previously stated, according to Jacquinot analyses, gratings outperform similar size prisms by a factor of 50 to 100 in the near-infrared and a grating spectrograph is therefore selected [39].

When starting the conception of a new instrument from scratch, the first step is to translate the scientific requirements into technical specifications. This means obtaining rough estimates or relations between parameters involved in the optical design of a spectrometer. The complicated side of this problem lies in the fact that several parameters appear when considering a whole spectrograph. Some are given through the scientific requirements but others have to be deduced. The focal lengths of the collimating and focusing optics or the grating spatial frequency are some examples of variables that must be quantified.

The previous chapter established the basic relations that govern a spectrograph operation. Several considerations already enabled to derive good practice rules to limit the size of the instrument while maximizing the resolving power. Several equations were obtained but finding the starting point to enable the conception of the instrument is rather complicated. Some authors investigated this issue to help designers in making the best choices and reach the most appropriate configuration for their purpose.

A large number of variables has indeed to be fixed when designing an astronomical spectrograph. Bingham identified sixteen parameters for a grating spectrograph combined to a telescope and proposed a systematic approach to calculate them [58]. The method concerns plane reflection gratings but can be adapted to curved ones.

Those parameters are:

R	<i>Resolving power</i>
Dis	<i>Dispersion ($f_{cam} d\beta/d\lambda$)</i>
θ_s	<i>Angular slit size projected onto the sky</i>
$\alpha + \beta$	<i>Sum of incidence and diffraction angles</i>
$\alpha - \beta$	<i>Difference between incidence and diffraction angles</i>
m	<i>Grating order</i>
A_{tel}	<i>Diameter of telescope</i>
f_{tel}	<i>Focal length of telescope</i>
A_{coll}	<i>Collimator size</i>
f_{coll}	<i>Focal length of collimator</i>
A_{cam}	<i>Focuser/camera size</i>
f_{cam}	<i>Focal length of focuser/camera</i>
L	<i>Grating size (across grooves)</i>
w'	<i>Exit slit size</i>
λ	<i>Wavelength</i>
d	<i>Groove spacing</i>

Table 4.1 - The 16 parameters describing a spectrograph instrument

The method consists in maximizing figures of merit and fixing some basic parameters to obtain all the others in such a way that the derived instrument satisfies the scientific requirements properly. This method is employed here and briefly explained further below.

4.3.1 Basic equations

The basic equations used in the proposed method are the ones previously introduced in Chapter 3 or slightly modified versions of them. The complete development of these relations is available in Appendix A. They involve the principal notions previously introduced such as the resolving power, the linear dispersion or the magnification. Summarizing these results, we get the following 7 equations linking the 16 parameters describing a spectrometer. Bingham's methodology helps in fixing the right parameters first to then derive the others as a second step.

$$R \theta_s A_{tel} = R w' \frac{A_{cam}}{f_{cam}} = \lambda Dis \frac{A_{cam}}{f_{cam}} = 2 L \sin\left(\frac{\alpha + \beta}{2}\right) \cos\left(\frac{\alpha - \beta}{2}\right) = \frac{L m \lambda}{d} \quad (7)$$

$$\frac{A_{coll}}{\cos \alpha} = \frac{A_{cam}}{\cos \beta} = L \quad (8)$$

$$\frac{A_{coll}}{A_{tel}} = \frac{f_{coll}}{f_{tel}} \quad (9)$$

$$Mag = \frac{f_{cam}}{f_{coll}} \frac{\cos \alpha}{\cos \beta} = \frac{f_{cam}}{A_{cam}} \frac{A_{tel}}{f_{tel}} \quad (10)$$

4.3.2 Figures of merit

Figures of merit are used to compare different designs. The figures used in the method are mainly related to light-gathering and the aim is to increase the entrance slit width or the wavelength coverage.

The first considered figure of merit consists in the product of the resolving power by the entrance slit width $R \theta_s$. As previously stated in Chapter 3, the optimization of this function means maximizing both throughput and resolving power. In Eq. (7), we notice that gratings' illuminated width L and blaze angle $\frac{1}{2}(\alpha + \beta)$ determine $R \theta_s$ ($(\alpha - \beta)/2$ varies slowly). The availability of gratings and total instrument cost may therefore limit this figure of merit.

Then, the instantaneous wavelength coverage is chosen as a figure of merit. This parameter is equal to the number N of slit image widths (wavelength elements). This figure of merit can be expressed by:

$$N = \frac{F}{w'} = \frac{2 \theta f_{cam}}{w'}$$

where F is the full width of the camera field, measured along the focal surface and θ the angular half-width of the camera field. Note that this expression is an approximation since w' is taken as constant across the field. The parameter N alone is not very useful since it tends to promote large f_{cam} and therefore small θ_s . The proposed method rather considers N as part of the specification of an instrument rather than a figure of merit. A more useful figure is:

$$\begin{aligned} N \theta_s &= \frac{2 \theta f_{cam}}{w'} \frac{w'}{Mag f_{tel}} = \frac{2 \theta f_{cam}}{w'} \frac{w'}{\frac{f_{cam}}{A_{cam}} \frac{A_{tel}}{f_{tel}} f_{tel}} \\ &= 2 \theta \frac{A_{cam}}{A_{tel}} \end{aligned}$$

Since A_{cam}/A_{tel} appears in the same sense, maximizing both figures of merit simultaneously is consistent.

4.3.3 General design procedure

This section proposes a sequence to follow to derive the dimensions of a spectrometer using a prior specification, the figures of merit, the equations presented above and various limitations. Part of the specification is usually in terms of the required resolving power, wavelength coverage and/or entrance slit width. A sufficient number of other quantities must be fixed to define the instrument, usually involving the detector and the grating.

The first thing to consider is the number of variables to be fixed. Eq. (7) to (9) form a system of 7 independent equations involving 16 parameters. Therefore, 9 variables describe the spectrometer. The selection of those 9 variables is not arbitrary as some configurations are not appropriate. Indeed, if Dis , w' and λ , are assigned a value, R can be calculated and cannot be included as a free parameter anymore. Defining the exact conditions to establish the group of 9 free parameters is not trivial but the problem can be simplified. Indeed, 4 quantities are either fixed for a large number of instruments associated with a given telescope or can be ignored during the first steps of the conception. Therefore, only 5 free parameters must be constrained with the help of the scientific specifications, figures of merit and practical constraints which constitutes the essence of the method. These four fixed

parameters include the telescope diameter A_{tel} , the focal length of the telescope f_{tel} , the grating order m and the central wavelength λ . Fixing five other parameters enables calculating the dimensions of the spectrometer using Eq. (7) to (9). For example, one case below fixes R , θ_s , w' , $\alpha + \beta$ and $\alpha - \beta$ as the five initial parameters of the method.

A distinction between *spectrometers* and *spectrographs* is made by Bingham. “Spectrograph-like” instruments are characterized by a requirement on wavelength coverage or on a linear field which will be used to fix the camera focal length. On the other hand, the camera focal length of “spectrometer-like” instruments is determined as a result of the procedure without any concern about the total width of the camera field. The author suggests as a first attempt to run the spectrometer-like solution with no regard to wavelength coverage. In case the imaged spectrum by the camera does not suffice, the system may be adapted as a second step to increase the wavelength coverage. Indeed, one cannot always know in advance which specification applies. Eventually, the blaze angle is usually specified in the spectrometer-like option whereas it will be deduced, and reduced, in the spectrograph-like method. Below we depict a figure representing a schematic view of the general method.

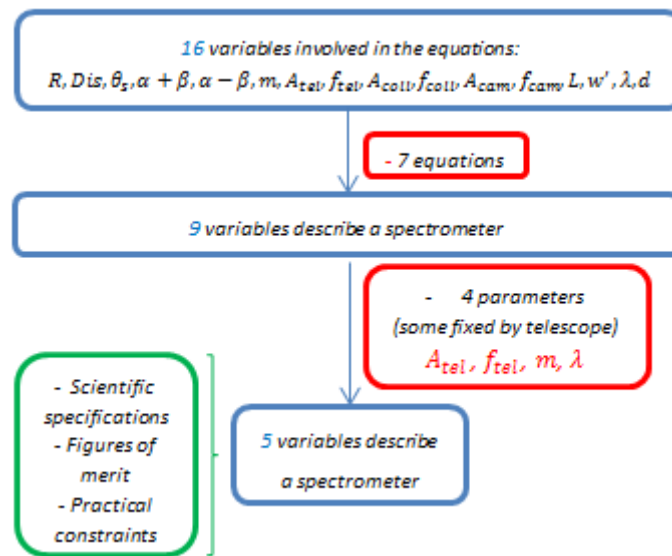


Figure 4.1 – Schematic view of the general procedure

4.3.4 The spectrometer-like specification

In the spectrometer-like specification, there usually exists a requirement on resolving power R and entrance slit width θ_s . The selection of a suitable detector should also occur early in the design. Therefore, R and w' can then be matched in accordance with the detector choice to ensure a proper sampling of the spectrum (see Chapter 3.4). The desired field size may be identified but nothing ensures it will be met at the end of the design procedure. In summary, these early considerations on the instrument provide numerical results for three of the five free parameters: R , θ_s and w' .

A first quantity can be derived at this point: the camera relative aperture $A_{cam}/f_{cam} = \theta_s A_{tel}/w'$. Indeed, Chapter 3 highlighted the fact that the camera focal ratio was only a function of the angular slit width, the pixel size and the telescope aperture which have all been attributed a value. Note that the magnification Mag is usually fixed by A_{cam}/f_{cam} (see Eq. (10)). The ratio f_{cam}/f_{coll} can vary through the following steps of the derivation but Mag will remain constant through changes in $\cos \alpha / \cos \beta$.

A fourth parameter is then introduced by making a preliminary choice of grating. This latter can either be the blaze angle $(\alpha + \beta)/2$ or $m\lambda/d$, each one concluding to an approximate value of the grating width as well as its blaze angle. Bingham advises to select the blaze angle because it avoids immediate involvement with m , λ and d [58]. Since it is often desired to maximize $R\theta_s$ with gratings as small as possible or limit the overall size of the spectrograph, large blaze angles must be preferred. Using Eq. (7), we can derive values for L and $m\lambda/d$:

$$L = \frac{R \theta_s A_{tel}}{2 \sin\left(\frac{\alpha + \beta}{2}\right) \cos\left(\frac{\alpha - \beta}{2}\right)}$$

Indeed, the cosine factor ranges between 0.92 and 1 for values of $\alpha - \beta$ up to 45° , we can thus take it as unity as a first approximation. It is important to note that L is evaluated this way because it may limit $R\alpha$.

Since estimates of L and $m\lambda/d$ are known, it is now useful to check if a suitable grating is available. One might notice that fixing the values of $m\lambda/d$ and $(\alpha + \beta)/2$ enables the calculation of $\alpha - \beta$ as a result. However, other constraints on $\alpha - \beta$ are usually overriding and $m\lambda/d$ is then found as a result. This requires the grating to exhibit the associated ruling frequency $1/d$ whether by searching for the appropriate off-the-shelf replica or manufacturing a custom item. Such constraints may be of mechanical concern for example since $\alpha - \beta$ is the angle between the collimator and the camera.

The blaze angle may be selected by carefully studying grating efficiency curves. Such diagrams are usually plotted against λ/d for a given groove profile and value of $\alpha - \beta$ but one can always transform the abscissa back in terms of α , β or $(\alpha + \beta)/2$ with the grating equation (right-hand part of Eq. (7)). Efficiency curves can be used in many ways. Practical groove profiles can for example be compared. Those curves can also be used in order to avoid Wood's anomalies². Polarization effects are also usually included. Eventually, several masters are usually available for off-the-shelf gratings and having a look at their efficiency curves may highlight the best element for the considered spectral range.

In order to image a wide spectral range in a single recorded frame; the first order of diffraction may be the best option. On the other hand, high-blazed gratings may not be suited for that purpose. Eq. (7) shows that large blaze angles require finer groove intervals d and manufacturing limitations may be encountered. If such a situation occurs, the blaze angle may need to be revised and given a lower value. On the other hand, this may also occur in order to fit the required spectrum to the camera angular field of view.

Eventually, the last parameter to be fixed from the five free ones is $\alpha - \beta$. Fixing this latter enables the calculation of α and β thus also A_{coll} , A_{cam} and f_{coll} . Therefore, the choice of $\alpha - \beta$ involves effects on the apertures and focal lengths.

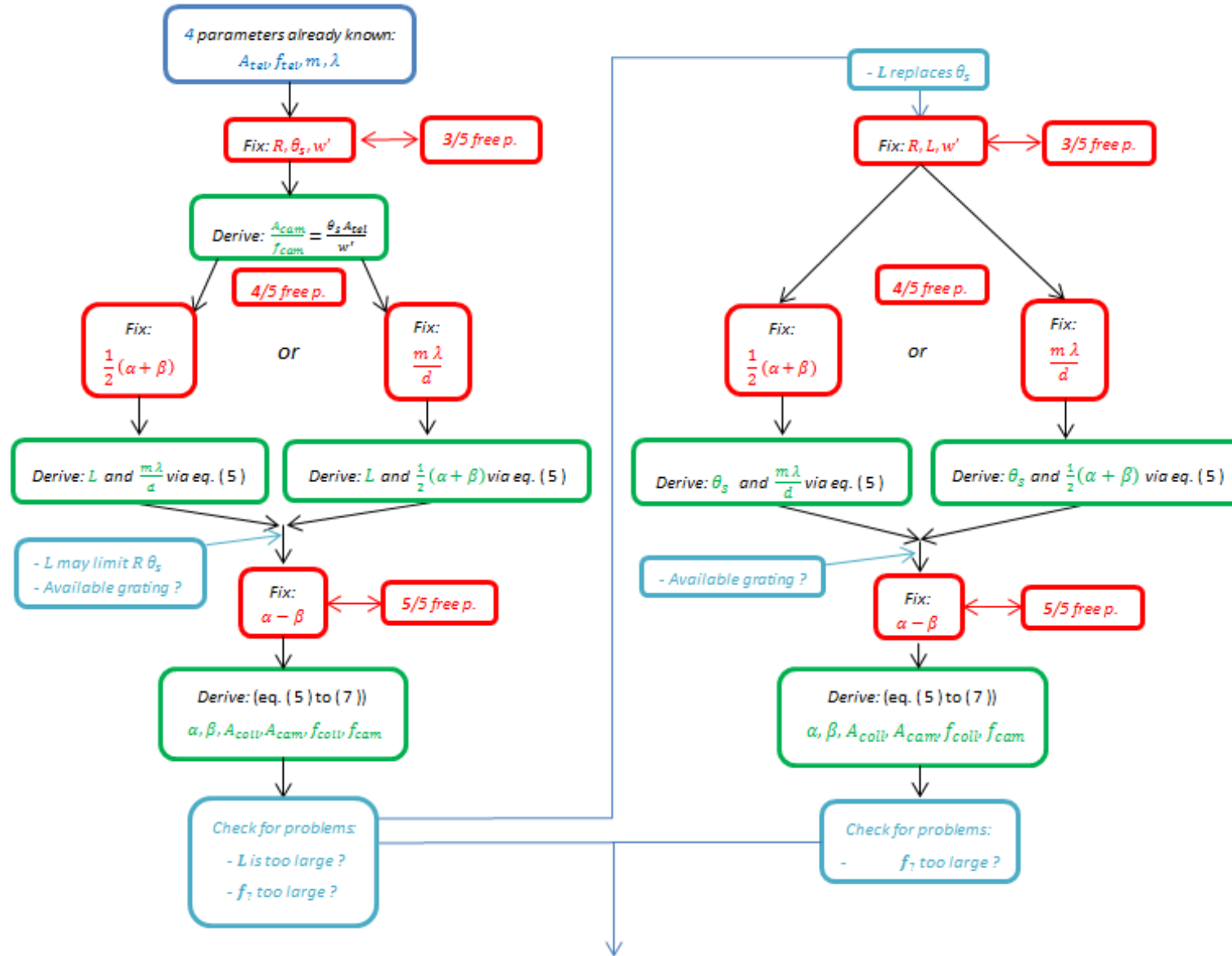
The five free parameters of this method are thus R , θ_s , w' , $\alpha + \beta$ and $\alpha - \beta$. It must be noted that physical limitations or special cases may be encountered during the following conception steps. The choice of five starting parameters or their values may therefore be changed accordingly. Several examples of such situations are listed below:

² Wood's anomalies are diffraction efficiency changes that are unexpectedly observed in continuous spectra. These originate from the formation of evanescent waves from tangentially diffracted orders. See [95] for more information.

- A narrow entrance slit may lead to diffraction effects and send the light outside the geometrical divergence of the beam. This leads to different illumination conditions of A_{coll} , including partial coherence. The collimator aperture may then also not be large enough to catch all the light.
- The obtained value of L may be too large considering manufacturing aspects. In such a case, one must select the grating exhibiting the highest value for $L \sin((\alpha + \beta)/2)$ should be chosen. The parameter L then becomes one of the five free parameters and replaces θ_s . A reduced value of θ_s is then deduced. The relative aperture of the camera will be lower as well. As mentioned before, Bingham thus recommends the use of the widest and highest blaze angle gratings.
- The focal lengths may be too large to accommodate within the available space. Also, it was previously inferred that large focal lengths may be inconsistent with the required mechanical stability, such as Cassegrain spectrographs where flexure matters. To overcome this issue, f_{coll} may be reduced by reducing f_{tel} . Otherwise, a probable consequence is the reduction of L and probably θ_s . In that case, the problematic focal length enters the basic parameters and L and/or θ_s are then calculated this time. This approach does not really follow Bingham's methodology purpose as the first goal was to derive the required specification of the instrument rather than taking into account several limitations [58].

Figure 4.2 summarizes the “spectrometer-like” method described by Bingham. The baseline methodology is depicted and potential secondary paths are investigated as well when limitations are encountered. No consideration on the camera field was involved in the methodology up to now. The obtained design must now be examined to see if a proper camera can be found. If so, the spectrometer-like methodology is confirmed as no compromise must be found. In contrast, basic parameters must be changed if no camera can be adapted to the specification, usually θ_s or L , w' , $\alpha + \beta$ and $\alpha - \beta$. The adjustment of other parameters refers to Bingham's “spectrograph-like specification”.

We invite the reader for further details to refer to Bingham's paper (reference [58]) because the “spectrograph-like” methodology is not considered here. Indeed, as previously stated, it is preferred to derive the specifications of a new instrument with no particular concern on the wavelength range as the requirement on wavelength coverage is usually sacrificed as stated in Chapter 3 [39].



Spectrograph optical design

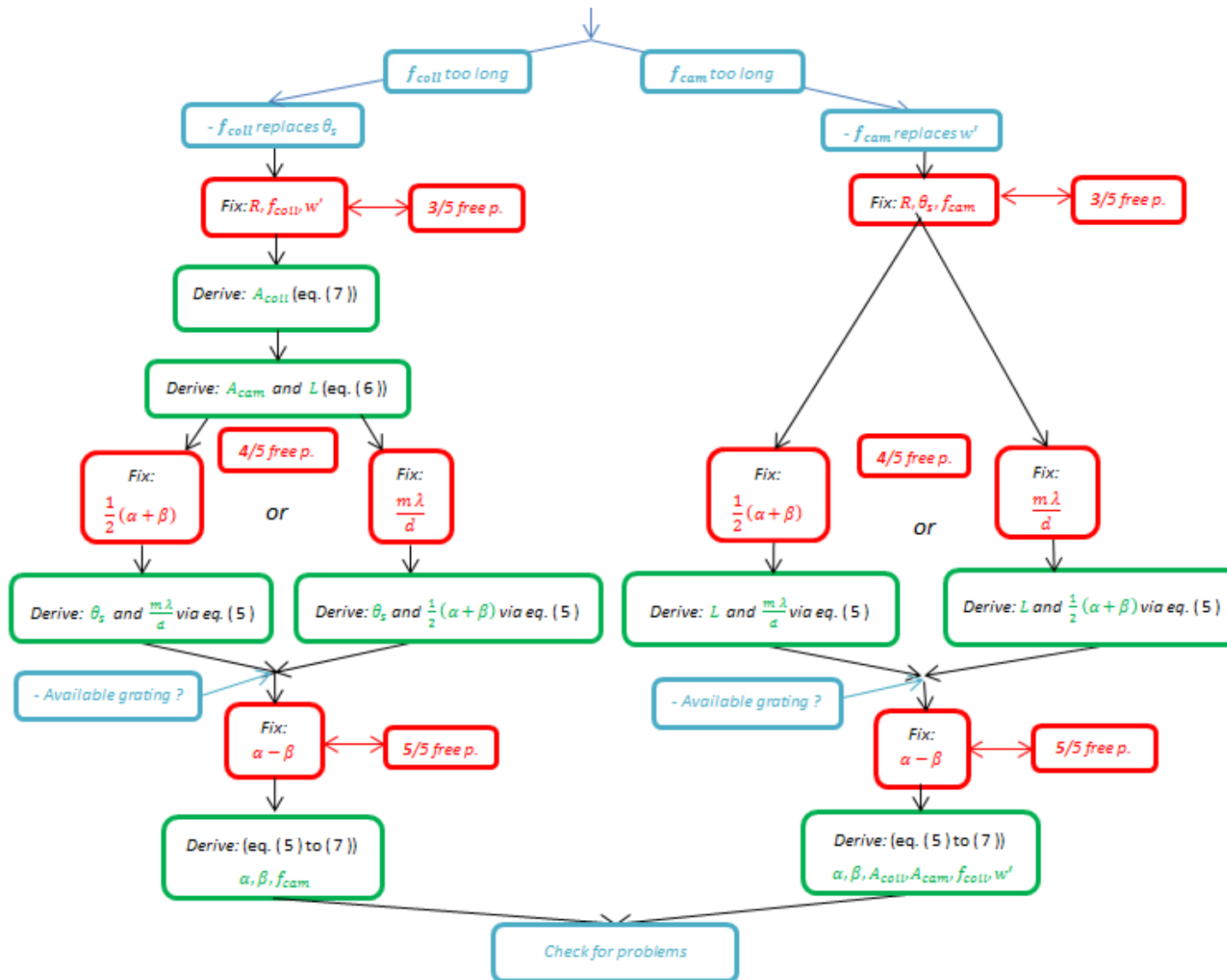


Figure 4.2 - Bingham's spectrometer-like method

4.3.5 Investigations on Bingham's spectrometer-like methodology

This section proposes to investigate Bingham's advice by implementing the methods into Matlab and derive the spectrograph's parameters for varying parameters such as the blaze angle or $\alpha-\beta$. The different schemes that the general procedure can get through have been implemented and the resulting design therefore reflects potential limitations that the user may have entered. For example, running the spectrometer-like method with a maximum grating size will first try to use the required angular slit size as an input parameter and replaces it by the maximum grating size if this limitation is exceeded. A reduced angular slit size will then be determined for the selected grating and its associated manufacturing possibilities. The spectrograph-like procedure can be followed as well if an instantaneous wavelength coverage has to be satisfied with regards to the chosen detector. This methodology was not considered however.

The spectrometer method calls for 5 initial parameters to be fixed to obtain the entire instrument specification. The initial group contains $R, \theta_s, w', (\alpha+\beta)/2$ and $\alpha-\beta$ as recommended by Bingham. The first three are usually specified by the scientific requirements, the selected telescope and detector. The grating blaze and Littrow angles must be fixed to initiate the calculation process implementing the Eq. (7) to (10). As stated by Bingham, one should use the highest blazed grating available to limit the whole size of the instrument. This will enable reaching high values of the figure of merit $R\theta_s$ while limiting the size of the grating and accordingly the dimensions of the instrument [58].

On the other hand, $\alpha-\beta$ can be associated with the angle formed by the collimator-grating-camera sequence of optical elements. The effect of this angle on the inferred parameters is deeply investigated by Bingham. As a brief conclusion, the choice of using a large or small $\alpha-\beta$ value depends on the specific application needs. For small spectrometers in which selectable gratings are used, a reduced value of $\alpha-\beta$ is advised. Moreover, a high value of this angle has simply no advantage in the increase of $R\theta_s$, it actually decreases it. The central wavelength can also be slightly tuned by changing the value of $\alpha-\beta$. One may also notice that the grating efficiency remains unchanged when reversing the sign of $\alpha-\beta$. Eventually, the variation of A_{coll} and A_{cam} are opposite in sign when considering an increase of $\alpha-\beta$ from zero with the same sign as $(\alpha+\beta)/2$: A_{cam} increases whereas A_{coll} decreases [58].

These behaviors can be observed in Figure 4.3 where the instrument parameters are depicted when the grating blaze angle and the Littrow angle vary. A first observation is the increase in the size of all optics when the blaze angle is low. The same behavior is observed when considering the focal lengths of the collimator and the focuser. It is therefore worth choosing a high-blazed grating to obtain compact instruments.

This tendency is confirmed by Figure 4.4 where the grating size is plotted with respect to the blaze angle when considering a standard Littrow configuration for instance ($\alpha-\beta = 0$). Indeed, the grating size sharply decreases when the blaze angle increases. The same conclusion can be drawn when looking at the other optics' dimensions but a careful attention must be paid to the grating specifications since manufacturing limitations may be rapidly encountered as pointed out by Bingham in the spectrometer-like methodology. One should therefore keep an eye on this instrument parameter to avoid future manufacturing issues.

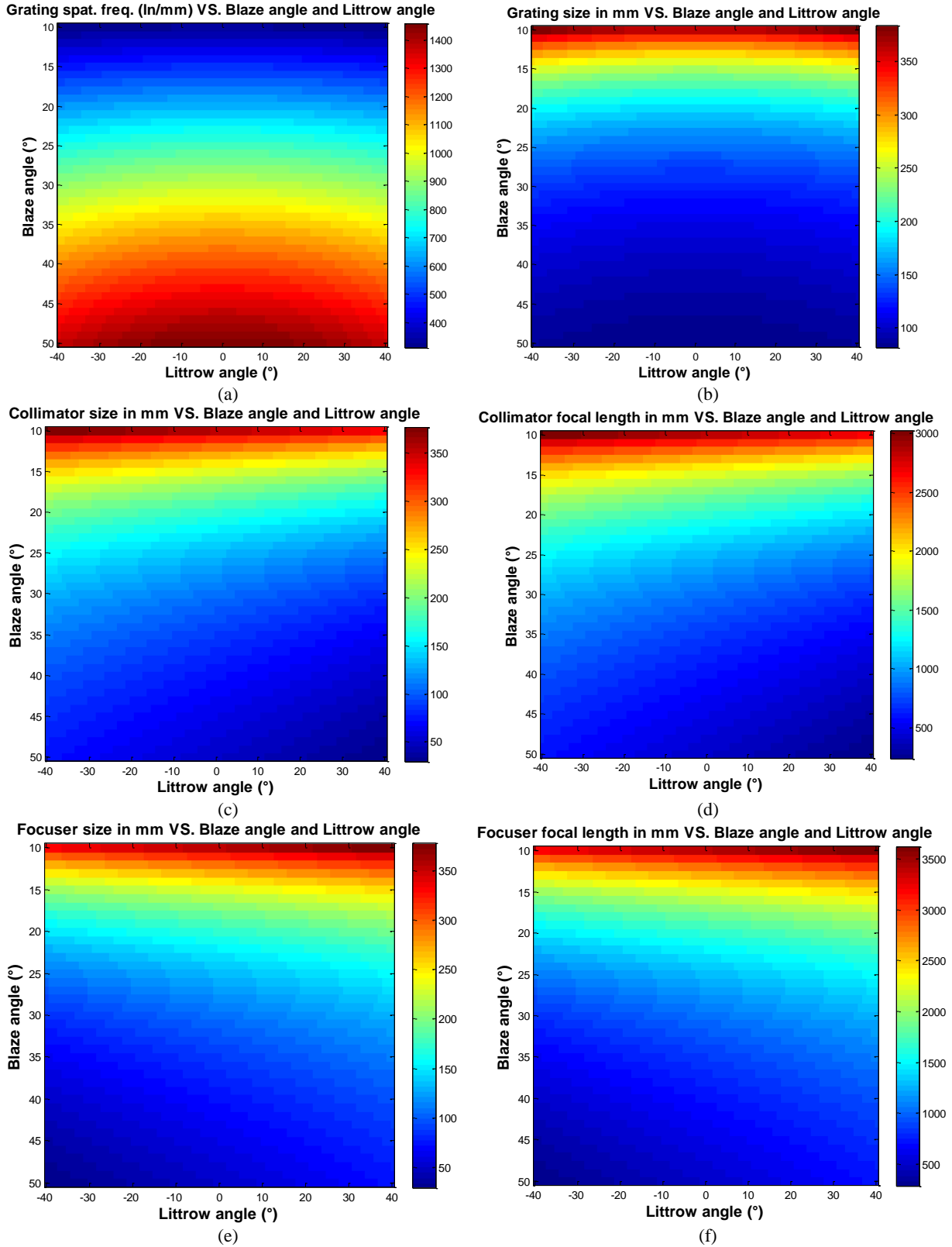


Figure 4.3 - Obtained specifications from the spectrometer-method for different values of $\alpha-\beta$ and $(\alpha+\beta)/2$.

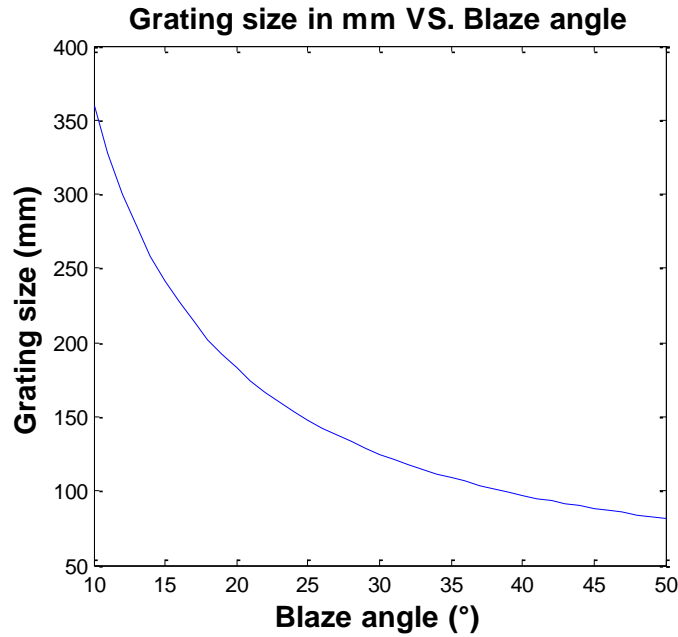


Figure 4.4 - Variation of grating size (L) as a function of the blaze angle ($\theta_B = (\alpha + \beta)/2$) for a given Littrow configuration.

Figure 4.5 (a) and (b) illustrate the effect of reversing the sign of $\alpha - \beta$ on the collimator and focuser sizes. As stated by Bingham, these variations are opposite in sign: the collimator size falls monotonically as $\alpha - \beta$ increases from zero with the same sign as $(\alpha + \beta)/2$ (positive here) whereas the focuser size increases. Departing from the Littrow configuration will therefore lead to opposite changes in size of the collimating and focusing optics. The implementation of non-Littrow configurations may lead to the use of large optics when separating the collimator from the focuser. The designer should therefore be aware of manufacturing limitations that he may encounter when building the instrument after this early design process. This section illustrates that optical and mechanical issues are tightly interconnected and one may limit the other, potentially impacting on the scientific requirements.

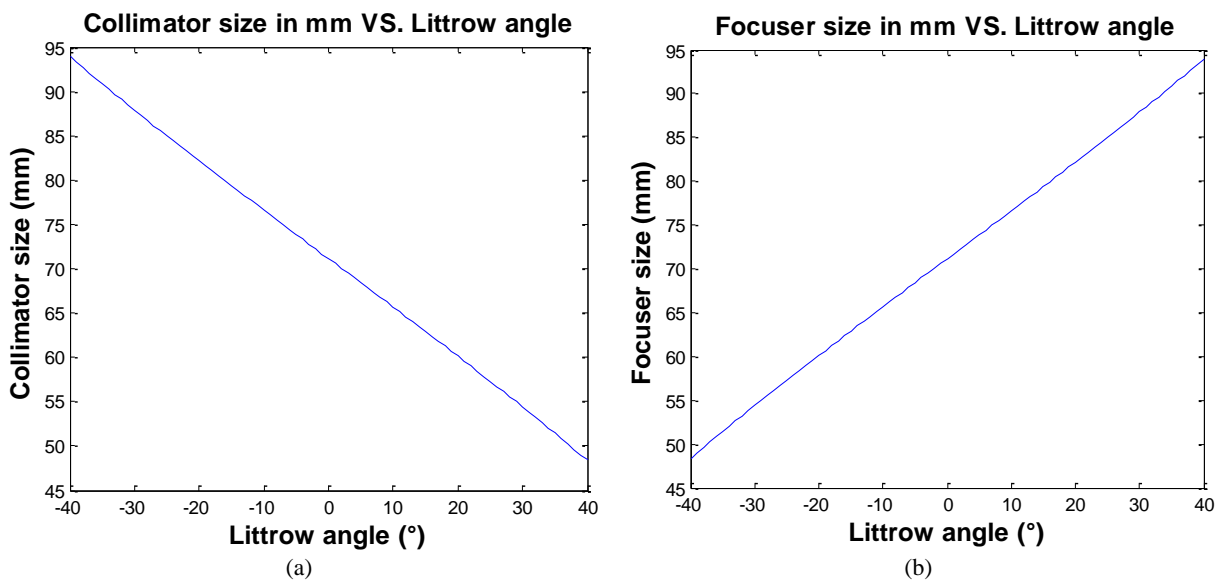


Figure 4.5 – Collimator A_{coll} (a) and focuser A_{cam} (b) size as a function of Littrow angle $\alpha - \beta$ for a grating blaze angle.

4.3.6 Application to the instrument under study

Bingham's spectrometer-like method is employed here to obtain a first glance onto the spectrograph's parameters. The scientific requirements paired to the telescope's characteristics as well as off-the-shelf gratings availability enable the definition of 6 from the 9 required parameters. Indeed, the telescope focal length and its diameter are specified in Table 1.2 while Table 1.1 specifies a goal resolution of 20 000 and a central wavelength of 1050 nm . On the other hand, a commercially off-the-shelf first order grating with a blaze angle of 41.3° , the maximum one found around $1 \mu m$ to follow Bingham's advice, is considered here.

The entrance slit angular size of the spectrograph should be matched to the maximum seeing of the telescope site. This way, the whole light beam from the target star will enter the spectrograph. On the other hand, in our case the spatial extent of the entrance slit is nothing else than the diameter of the fiber optic core which links the telescope to the spectrograph. Considering a maximum seeing of 2 arcsec , θ_s may be given this value in first approach. This leads to a fiber core of approximately $93 \mu m$ in diameter. Instead, a fiber core of $100 \mu m$ is chosen to respect manufacturing standards and θ_s is fixed to 2.15 arcsec .

When considering the choice of a suitable detector, we noted in Chapter 2 that the sensitivity of current generations of CCDs near $1 \mu m$ is extremely low, their quantum efficiency being of the order of a few percent at these wavelengths at most. Moreover, the quantum efficiency falls off steeply over this wavelength domain. Therefore, near-infrared detectors that are commonly used are rather *InGaAs* or *HgCdTe* sensors than CCD matrices. Their pixel pitch usually ranges from 15 to 30 microns with a majority exhibiting the latter. Therefore, w' is given a value of $60 \mu m$ as a first approximation.

The last parameter to be fixed to initiate the spectrometer-like method is $\alpha-\beta$. Following the analyses of Allemand [59], illuminating the grating in a given range of angles, between 0.6 and 0.9 radians , leads to a reduction of the coma aberration through the focal field of Czerny-Turner spectrographs (see [59] for exact assumptions and approximations). As a starting point, the grating incident angle is then fixed to 35° and therefore $\alpha-\beta$ is equal to -12.6° .

The results of a first iteration of the spectrometer-like method are shown in Table 4.2. The first 9 parameters are fixed through the above considerations whereas the remaining 7 are deduced with the help of Eq. (7) to (10). Having a look at those first results reveals that the collimator focal length should be a little bit longer than one meter while the camera's one should approach half a meter. This ratio agrees with the fact that the entrance slit is approximately twice as wide as the exit slit. The size of the optical elements ranges from 12.8 to 19 centimeters, the largest element being the grating. On the other hand, this latter should be ruled at a frequency of 1249.5 lp/mm . The high value of $\beta = 47.6^\circ$ promotes a large dispersion as advised by Hearnshaw (see Chapter 3.3). Since the manufacturing capabilities of such a grating specify a limited size of 154 mm , an adapted scheme to Bingham's spectrometer-like method must be followed.

When a limiting factor appears during the derivation of a spectrograph's specifications, this parameter is introduced into the starting group of 9 variables. This ceiled factor thus takes the place of another parameter that will this time be calculated with the Eq. (7) to (10). This process generally leads to a reduced value of the newly obtained specification [58]. In the present case, the maximum grating width is introduced into the initial conditions of the problem and a reduced value of entrance slit follows as a consequence.

A second run with the maximum value of 154 mm for L leads to an entrance slit whose spatial extent is equal to $80.82\ \mu\text{m}$. This represents the widest slit, and therefore the largest fiber core diameter, the system admits considering the manufacturing capabilities of the selected grating. The availability of optical fibers now restrains the possibility of using this width for the entrance slit of the spectrograph. Commercially available multimode fibers are mostly available with core diameters ranging from 25 to hundreds of microns, varying in size by a factor of two. Since finding a $80\ \mu\text{m}$ core fiber was simply unsuccessful and manufacturing a custom one an expensive option, the selection of a $50\ \mu\text{m}$ core standard fiber is therefore a reasonable new starting point for the next iteration of Bingham's spectrometer-like method. Of course, the potential use of micro-lenses already comes to mind at this point.

The results from the second iteration with a $50\ \mu\text{m}$ entrance slit are shown in Table 4.2. The changes that occurred with respect to the previous iteration are the variation by a factor two in the optics' sizes and the collimator focal length. The spectrograph's specification that is obtained constitutes a basic starting point for optimization with optical design software and is for sure subject to changes when considering, for example, aberrations and further optical analyses such as resolution calculations.

First run		Second run	
<i>Parameter</i>	<i>Value</i>	<i>Parameter</i>	<i>Value</i>
A_{tel}	1.2 m	A_{tel}	1.2 m
f_{tel}	9.6 m	f_{tel}	9.6 m
m	1	m	1
λ	1050 nm	λ	1050 nm
R	$20\ 000$	R	$20\ 000$
θ_s	2.149 arcsec	θ_s	1.074 arcsec
w'	$60\ \mu\text{m}$	w'	$60\ \mu\text{m}$
$(\alpha + \beta)/2$	41.3°	$(\alpha + \beta)/2$	41.3°
$\alpha - \beta$	-12.6°	$\alpha - \beta$	-12.6°
f_{coll}	1248.677 mm	f_{coll}	624.339 mm
A_{coll}	156.085 mm	A_{coll}	78.042 mm
f_{cam}	616.725 mm	f_{cam}	616.725 mm
A_{cam}	128.484 mm	A_{cam}	64.242 mm
$1/d$	1249.554 lp/mm	$1/d$	1249.554 lp/mm
L	190.544 mm	L	95.272 mm
D	0.875 nm/mm	D	0.875 nm/mm

Table 4.2 - Spectrograph's parameters after first and second runs

4.3.7 Change of blaze wavelength with incident angle on grating

When illuminating the grating at a different incident angle than the one fulfilling $\alpha = \beta$, i.e. leaving the Littrow conditions, the blaze wavelength does not remain unchanged and slightly decreases. If we denote λ_{θ_B} the blaze wavelength under Littrow conditions, the blaze wavelength λ_B when the grating is illuminated at an arbitrary angle α is equal to

$$\lambda_B = \lambda_{\theta_B} \cos(\alpha - \theta_B)$$

The selected off-the-shelf grating exhibits a ‘‘Littrow’’ blaze wavelength equal to $1.1 \mu\text{m}$. The selected geometrical configuration for the spectrograph features an incident angle equal to 35° and the blaze wavelength in that configuration therefore shifts to

$$\begin{aligned} \lambda_B &= 1100 \cos(35 - 41.3) \\ &= 1093.4 \text{ nm} \end{aligned}$$

This small deviation towards shorter wavelengths is an advantage as it leads to higher efficiency in the considered scientific spectral range of interest. Moreover, λ_B approaches the interesting *He I* λ 10830 line, which is a driving diagnostic feature of the spectrum for the study of massive stars.

One may be tempted to increase the incident angle until the *He I* λ 10830 lies within the grating blaze but this would first require the grating to be illuminated at an angle of approximately 51.39° and lead to only a tiny increase in performances when looking at the grating efficiency curves in Figure 4.6 (which is moreover subject to changes with such an incident angle). The wavelength drift due to the fact that the Littrow angle $\alpha - \beta$ is not equal to zero is not a conception driver but more a consequence of the design phase. However, playing on the Littrow angle remains one of Bingham’s suggestions to slightly tune the central wavelength of a given grating [58].

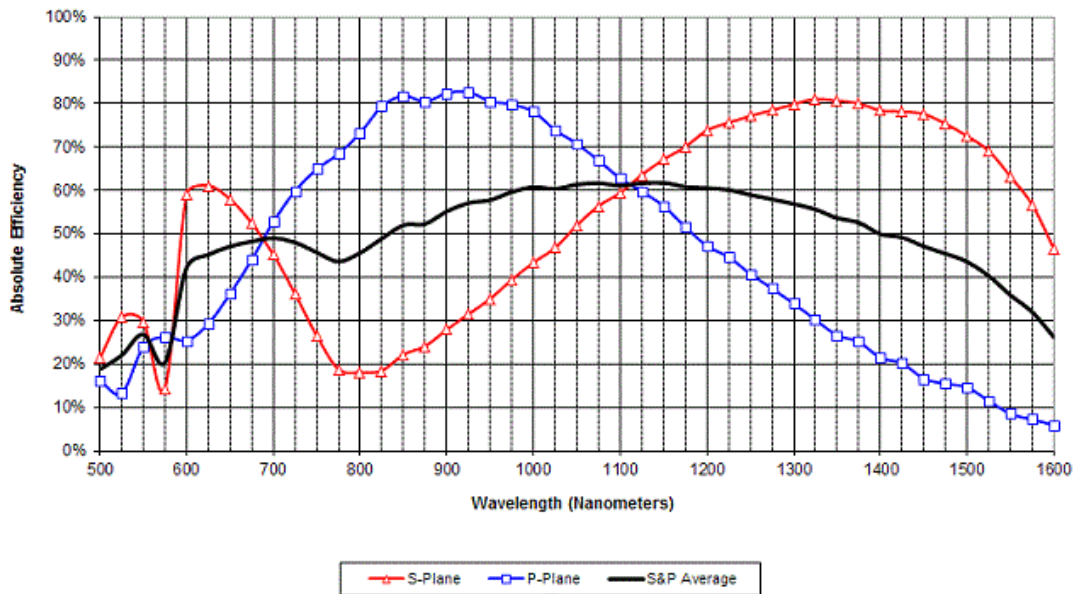


Figure 4.6 - Grating first order efficiency curves

4.3.8 Implementation of micro-lenses

The use of a smaller optical fiber than required to match the typical seeing leads to flux losses at the fiber entrance for typical seeing conditions at La Luz observatory. As explained earlier, the HEROS spectrograph currently under operation on the TIGRE telescope employs a $50\ \mu\text{m}$ core fiber optic associated with micro-lenses engraved at both ends within its own material to face this issue [17]. This way, the average star image of approximately a hundred microns under a typical 2 arcsec seeing entirely falls into the $50\ \mu\text{m}$ fiber core.

Moreover, this also adapts the focal ratio of the telescope to the fiber's one. This solution could also be adopted for the proposed spectrograph to avoid large light losses at the fiber entrance. This methodology is commonly used to minimize the FRD losses of fibers by feeding this latter with a light beam whose numerical aperture approaches the fiber's acceptance cone. The change in numerical aperture of light after transportation through the fiber is then minimized. Moreover, the micro-lens located at the spectrometer-side of the fiber contributes to reshaping the light beam back to its initial $F\#$ of 8.

The induced change in spatial extent due to conservation of etendue through the end micro-lens will however decrease the resolving power of the instrument. The implementation of such optical elements will therefore result in a compromise between higher photon flux and resolving power decrease. Another point of view is the calibration stability as scrambling vanishes when the input beam $F\#$ increases and requires inverse optimal conditions in comparison with FRD losses.

To optimize the photon flux transfer from the telescope to the instrument, i.e. minimizing FRD and collimator's losses, the optimal solution may consist in employing micro-lenses to adapt the telescope f-ratio of 8 to a lower value of 4.3, resizing the star image of approximately $93\ \mu\text{m}$ down to $46.5\ \mu\text{m}$. The entire star light would then enter the fiber core and FRD losses largely reduced.

Another micro-lens at the other end of the fiber would eventually do the inverse operation to adapt to the collimator's aperture of the spectrograph. The resolving power of the instrument would however suffer from such a modification due to the entrance slit enlargement due to the conservation of etendue. On the other hand, scrambling and therefore calibration stability would be badly impacted too.

An intermediate scheme may however be adopted. The selected grating exhibits a maximum manufacturing size of $154\ \text{mm}$, which corresponds to a entrance slit width of $80.82\ \mu\text{m}$. The micro-lens may then be manufactured in order to slightly adapt the star image to this reduced value. The input f-ratio would then be equal to 6.88 approximately and FRD losses would be reduced compared to the situation described above. Scrambling properties would eventually conserve its intense mixing properties. The resolving power of the instrument would be reduced by 37.5% but remain in the requirement range.

4.4 Optimization process

4.4.1 Configuration selection and associated techniques

A Czerny-Turner configuration is adopted from the various ones that exist. One of its advantages is the co-planarity between entrance and exit slits that is enabled through the separation of the collimating and focusing functions of the instrument. On the other hand, more degrees of freedom are made available to the designer thanks to the additional mirror element, which helps to tackle the optical aberrations [1] [60]. Moreover, the ability to cover a wide spectral range by, for example, rotating the grating makes it a suitable candidate to record the spectrum of the whole required waveband [61]. This is the reason why such spectrographs are often used as monochromators since the output wavelength can be finely tuned and selected [1]. Eventually, several studies identified techniques to deal with the inherent aberrations of this design.

Once the first technical specifications of the spectrograph are known, the optimization process can start. This consists in introducing the spectrograph model into a given optical design software and optimize its parameters in order to obtain the required imaging capabilities. These operations are performed with CODE V optical design software [62].

Starting from the previously obtained values for the spectrograph's specifications, the optimization is performed by varying the locations of the different optical elements as well as their orientations. The parameters obtained from the second run are adapted as well to obtain an ideal matching between optical elements' positioning and manufacturing. This procedure cannot be entirely left to the software but actually has to be driven by the user through appropriate initial conditions, specific constraints and careful choices of variable parameters. This avoids indeed going through meaningless situations where, for example, optical elements get into contact or leave the range of manufacturing limits.

Different approaches can be followed in order to guide the optimization process and obtain a rough location of the optical elements as a starting point. Many studies are available to optimize Czerny-Turner spectrographs, mostly focused onto techniques to face the astigmatism of such designs. They elaborate suitable guidelines concerning the use of specific elements to incorporate into the design to tackle with the inherent aberrations of Czerny-Turner spectrographs. Specific positioning of optical components is also advised to meet conditions that minimize the effects of aberrations that play a major role in the overall optical quality of the instrument.

The use of cylindrical and toroidal optical elements in Czerny-Turner spectrographs is explored by some authors to face the astigmatic behavior of those instruments. For example, Xue et al. propose using a toroidal focusing mirror instead of a spherical one to control both sagittal and tangential focal lengths separately and decrease the astigmatism [63]. Moreover, they find an adequate distance between the grating and the focusing mirror so that the aberrations are balanced over a wide spectral range. They eventually recall mathematical conditions to limit other aberrations such as the spherical and coma ones, the latter being known as "Shafer equation" [64]. Xue also suggests another possibility that consists in incorporating a wedged cylindrical lens into a Czerny-Turner spectrograph to achieve an astigmatism-correction for broadband spectral simultaneity [65]. Another solution, geometrical this time, is proposed by Austin to avoid astigmatic blurring effects: using divergent illumination of the grating instead of collimated light and an adapted positioning to obtain broadband performances [66]. Eventually, a cylindrical lens is used by Lee to correct for astigmatism over a wide spectral range with the help of low-cost optics [67]. The general methodology remains the same: incorporating into the design an asymmetry in order to be able to decrease the inherent astigmatism in such spectrometers.

The implemented method for the proposed spectrograph uses a toroidal lens that is located close to the focal plane. The difference between its tangential and sagittal focal lengths produces the required asymmetric parameter that enables the correction of astigmatism. A similar philosophy to Lee's methodology is followed in order to use smaller size low-cost optics. The asymmetric element is therefore placed near the focal plane where the converging beam is narrower. Indeed, this avoids the use of a large toroidal focusing mirror. Divergent illumination was also investigated but the required rotating grating avoided this opportunity. Indeed, divergent illumination only works for static spectrographs as the geometrical configuration remains valid for only one grating position.

Figure 3 illustrates the optical design where the typical collimator-grating-focuser optical chain is represented. The toroidal lens and a folding mirror are inserted close to the focal plane located at the bottom of Figure 3. The folding mirror utility consists in delivering some room for the detector and avoiding any interference with the optical beam.

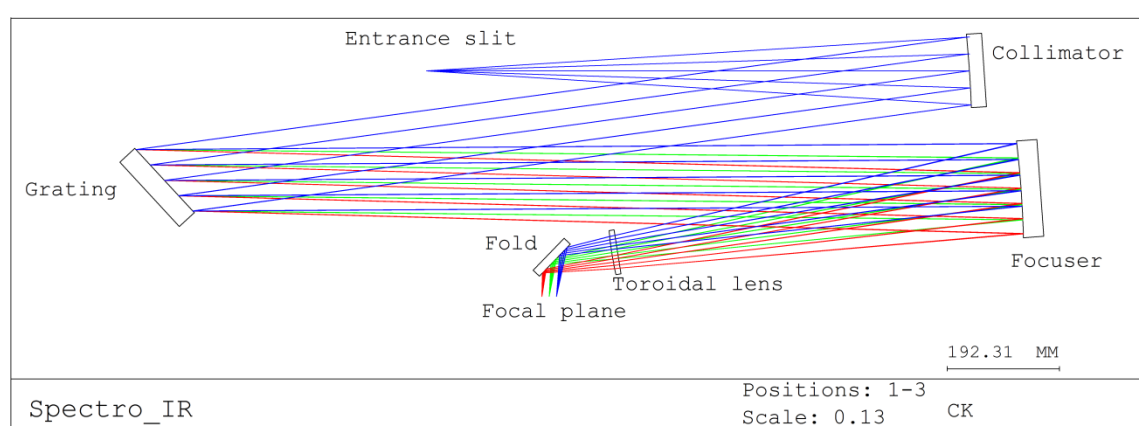


Figure 4.7 - Obtained spectrograph instrument design featuring a toroidal lens

4.4.2 Resolving power analysis

The optimization process consists in improving the quality of spots, i.e. images of point sources located at the object plane of the instrument. These point sources are located at different places through the entrance slit and their image diameter reflects the optical quality of the spectrograph. Indeed, the smaller the spot size, the better the imaging quality between the entrance and exit slits. As the exit slit blurs, it gets away from the required ideal size and the resolving power decreases. The resolution is then directly influenced by the spot sizes. The optimization process was therefore naturally driven by an evaluation of the resolution through the focal plane involving spot sizes.

The developed methodology to evaluate the resolution through the instrument focal plane during optimization consists in the calculation of the sampled waveband of each pixel. The entire bidirectional focal plane is scanned, this means probing the resolution changes with wavelength, along the spectral direction, and through the slit, along the imaging direction. Therefore, this two-dimensional analysis investigates the variation in resolution with wavelength and with the selected fiber as well.

The waveband that each pixel samples is obtained by computing the evolution of the inscribed area of the slit width into this pixel as the wavelength varies. The limiting footprint of the exit slit is approximated by the distance between the edges of the spots from points located at opposite sides of the entrance slit. The boundaries of these spots are geometrically determined by the optical software. This criterion considers 100% of the energy concentrated into the spot as uniformly distributed all

over this latter and thus does not take into account the typical Gaussian profile of a point spread function. The bidirectional evaluation of spots is depicted in Figure 4.8 where the entire focal plane of the instrument can be seen as well as some sampled spots. A zoom onto the center of the detector shows the three boundary spots that enable the slit profile calculation.

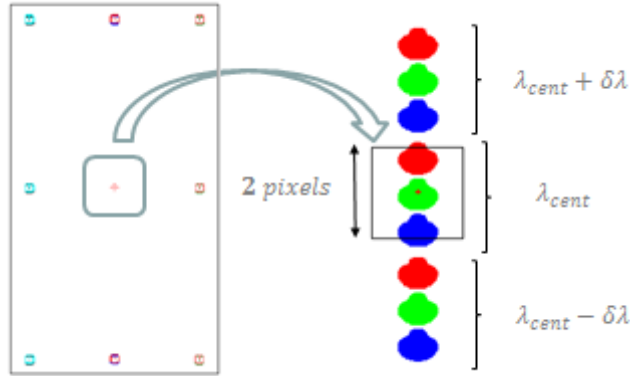


Figure 4.8 - Resolving power assessment methodology illustration

The evaluated exit slit width through this method is therefore slightly pessimistic since it tends to first enlarge its width and on the other hand consider its profile as a uniformly distributed rectangular function. Figure 4.9 (a) illustrates a step of the spectral profile calculation at 1040 nm where the local pixel, represented by a black rectangle, nearly encircles the full width of the exit slit approximated by the three spots. The obtained point of the spectral profile therefore lies close to its maximum. As the wavelength varies, the spots move upwards or downwards and start getting out of the considered pixel. The inscribed area then decreases and the obtained points lie further from the peak as the wavelength changes. When the spots are close to leave the pixel window, the inscribed area falls to zero and the wings of the final curve are obtained. Figure 4.10 (a) depicts the obtained profile at a given wavelength and position through entrance slit.

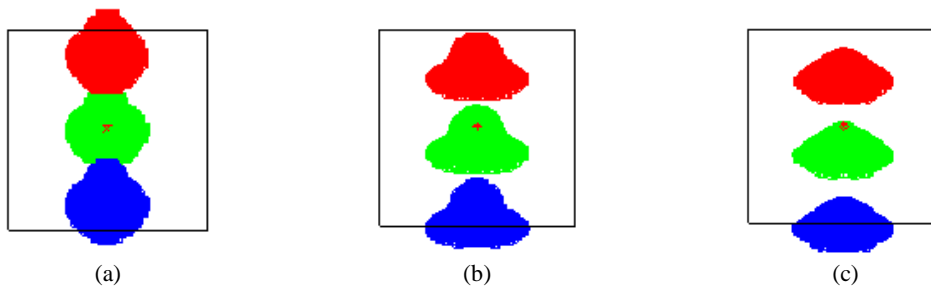


Figure 4.9 - Plot of exit slit spots from points located at the sides (red and blue) and center (green) of the entrance slit. The slit is elongated along the horizontal direction. The situation is depicted at three different wavelengths that are 1040 nm (a), 1050 nm (b) and 1060 nm (c).

The obtained triangular-shaped profile of one pixel's sampled waveband is nothing else than the convolution of two rectangular functions which are the pixel window and the approximated exit slit width (see Figure 4.10 (a)). The local resolution is then evaluated as the ratio between the central wavelength and FWHM of the spectral profile. The result of this analysis is a map of the resolution as a function of the local wavelength and the vertical position in slit, i.e. the selected fiber (see Figure 4.10 (b) for a selected grating position).

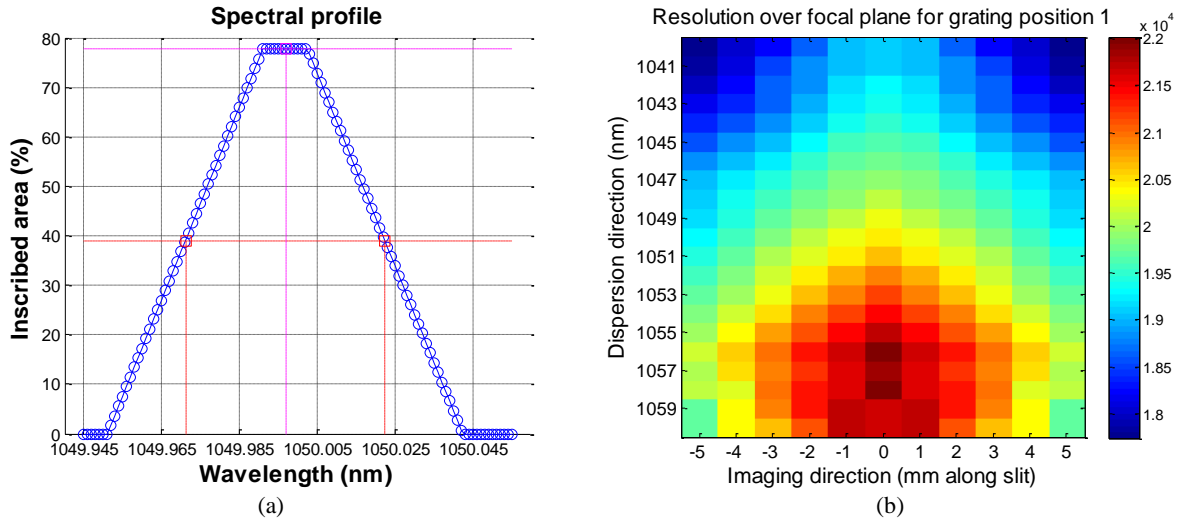


Figure 4.10 - Plot of one sampled exit slit profile (a) and resolving power across focal plane for a given grating position (b).

A symmetric variation of the resolution with respect to the slit center can be observed. This behavior comes from the change in spot sizes of the spectrometer with the position in slit. This variation of resolution also occurs with respect to wavelength as the spots actually change in shape rather than size. Indeed, since the 100% size of the spot is considered regardless of its actual energy distribution, a slight change in shape with no impact onto its RMS (root-mean-square) size leads to a variation in resolution with the employed methodology. This behavior can be observed in Figure 4.9 (a), (b) and (c) where the spots are depicted at different wavelengths, i.e. at different places along the dispersion axis. It can be observed that the spots' shapes vary as a function of wavelength and influence the calculated resolving power. Therefore, this 100% spot size does not suit accurate resolution calculation but rather allows assessing it in first approximation.

This behavior is confirmed in Figure 4.11 introducing the variation of the measured FWHM as a function of position through slit along the imaging axis (Figure 4.11 (a)) and wavelength along the dispersion axis (Figure 4.11 (b)). The symmetric evolution with respect to the selected fiber for all considered wavelengths is confirmed and the unexpected drift in resolving power as the wavelength increases is also observed for all positions through the slit.

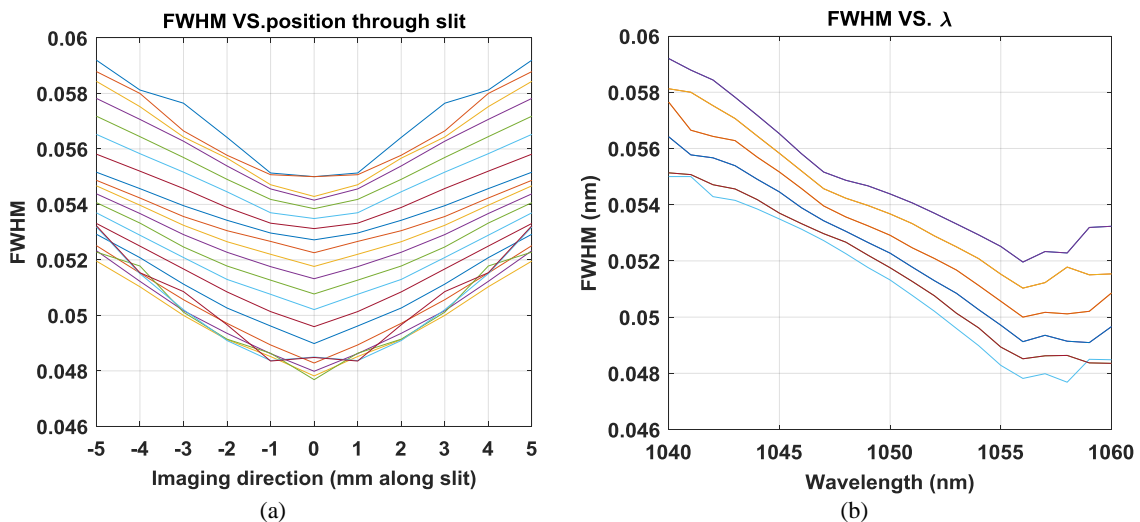


Figure 4.11 - Variation of FWHM as a function of position through slit (all wavelengths plotted) (a) and wavelength (all positions through slit plotted) (b)

An exit slit profile taking into account the energy distribution must be considered to obtain more accurate results. This first coarse estimate of the resolution is hence complemented by a second finer analysis presented below.

The second resolution analysis that is developed in ASAP optical software [68] consists in illuminating the overall entrance slit, considered as a rectangle of $50 \mu\text{m} \times 10 \text{mm}$, and observing its image at the focal plane of the instrument. By doing so, the exact slit profile can be examined and used in order to calculate the resolution in a proper way.

In order to investigate the evolution of the resolving power through the entire focal plane, the exit slit is observed at several wavelengths, i.e. at different locations along the dispersion axis. Its spectral profile is then calculated at multiple places along the imaging direction in order to evaluate the change of resolution with respect to the chosen fiber. In contrast with the previous method, the energy distribution over the exit slit is computed and used to evaluate the resolution.

The first step is to calibrate the focal plane in order to attribute to each pixel a specific wavelength. To do so, the entrance slit is lit with known wavelengths and the corresponding exits slits then fall on specific pixels that are separated along the dispersion axis. A polynomial fitting is eventually used to calculate the dispersion relation which associates each pixel of the focal plane with a specific wavelength.

The FWHM of the exit slit spectral profile can then be evaluated through the entire focal plane and the corresponding resolving power calculated as the ratio between the local central wavelength and the FWHM. Figure 4.12 (a) illustrates the sampling of the exit slit at a given height and wavelength. The obtained results produce a new bi-dimensional mapping of the resolution whose two directions remain the wavelength and the position through the exit slit (see Figure 4.12 (b)).

The values obtained are, as expected, higher than those found with the previous method since the uniform rectangular shape approximation is abandoned. The slit blurring due to changes in spot sizes is the only cause here for resolution degradation and the deformation of the spots does not impact the results anymore. As a consequence, the previously observed change in resolution with wavelength disappears. Indeed, the measured variation in this case amounts to approximately 2% whereas the previous change was 10%. The slight slope in resolution with wavelength is due here to the change in considered local wavelength in the calculation of $\lambda/\delta\lambda$.

In conclusion, the optimization process driving criterion underestimated the resolving power and leads to an average value of approximately 29 000, 45% above the scientific requirement. The obtained design therefore overfills the scientific requirements but the performed analyses neglect any alignment or manufacturing error. The final resolving power actually reached will then be lower and a tolerancing analysis is required to investigate the induced variation.

An interesting fact is running the Bingham's spectrometer-like method one more time to get the spectrometer specifications that are obtained when starting with the same basic parameters as for the second run from Table 4.2 except for the resolution that is now fixed to 29 000. These are compared to the spectrometer parameters reached when following the pessimistic resolution criterion in Table 4.3. A fine matching between both methods appears and confirms the validity of Bingham's spectrometer like methodology.

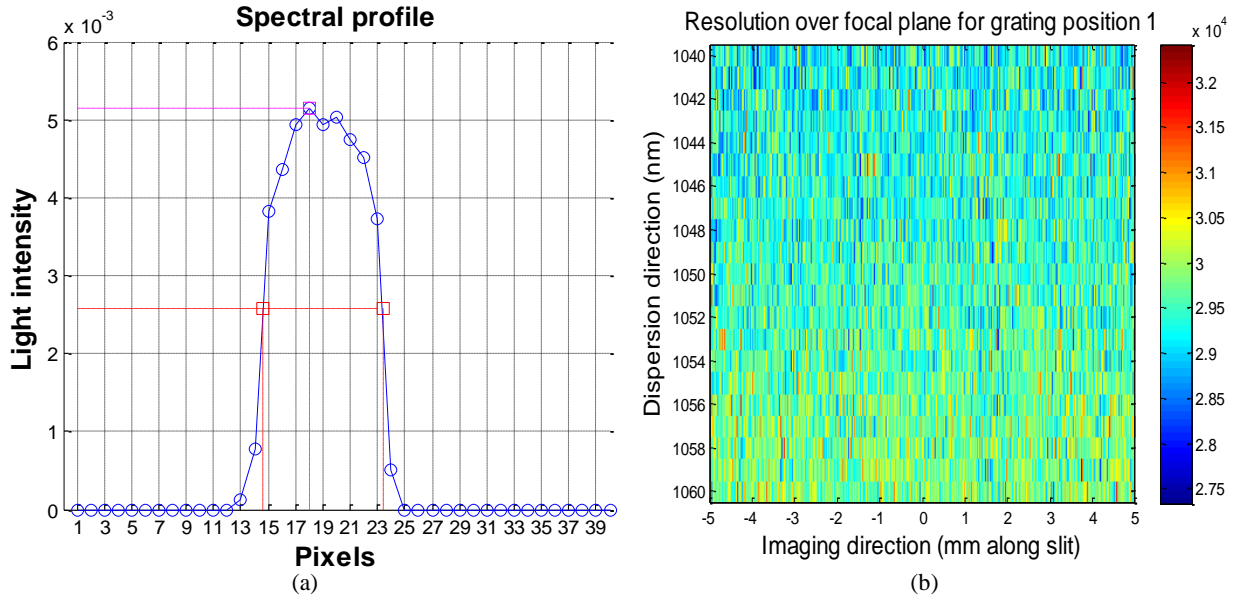


Figure 4.12 - Plot of one sampled exit slit profile (a) and resolution across focal plane for a given grating position (b).

First resolution criterion		Bingham's spectrometer method	
Parameter	Value	Parameter	Value
A_{tel}	1.2 m	A_{tel}	1.2 m
f_{tel}	9.6 m	f_{tel}	9.6 m
m	1	m	1
λ	1050 nm	λ	1050 nm
R	29 000	R	29 000
θ_s	1.074 arcsec	θ_s	1.074 arcsec
w'	60 μm	w'	60 μm
$\alpha + \beta$	41.3°	$\alpha + \beta$	41.3°
$\alpha - \beta$	-12.6°	$\alpha - \beta$	-12.6°
f_{coll}	938.136 mm	f_{coll}	905.291 mm
A_{coll}	120 mm	A_{coll}	113.161 mm
f_{cam}	888.395 mm	f_{cam}	894.251 mm
A_{cam}	100 mm	A_{cam}	93.151 mm
$1/d$	1200 lp/mm	$1/d$	1249.554 lp/mm
L	150 mm	L	138.145 mm
D	0.79 nm/mm	D	0.603 nm/mm

Table 4.3 - Comparison between spectrometer specifications obtained with both first resolution criterion and Bingham's spectrometer method to obtain a resolving power of 29 000.

4.5 Tolerancing analysis

The tolerancing analysis of the instrument intends to assess its performances variations due to perturbations. These may be manufacturing limitations arising from imperfect machining tools or alignment precision uncertainties for example. Accounting for these deviations with respect to the optimal baseline optical design is crucial during the conception of an instrument. Indeed, some parameters may be very sensitive and slight departures from their original value may lead to unsuspected severe effects. The designer responsibility is therefore to measure the sensitivity of the optimized system to confirm its potential future manufacture, alignment and use.

The first step in a tolerancing analysis consists in investigating the sensitivity of every constituent of the system. The compilation of those into a global table is called a sensitivity matrix. Coupling effects are then studied in order to evaluate the mutual interactions between all the considered parameters. A global budget involving all contributors is finally carried out and statistical performances of the instrument are evaluated. All these analyses are performed on the spectrograph main channel. Indeed, both calibration and observation propagate through this common light path and only differ by the location of the different images of the entrance slit.

4.5.1 Sensitivity matrix

The sensitivity matrix measures the variation of optical quality of an optical system with respect to individual variations in manufacturing precision or alignment positioning of a given optical surface. No interaction between the individual components of the instrument is taken into account. The coupling of these variations is investigated further in this chapter.

Alignment accuracy

This section focuses on the effect of alignment accuracy on the optical performances of the instrument. Every optical surface is slightly moved along its local X , Y and Z axes to assess the effects of linear movements. Rotations around these directions are also applied separately to study all 6 degrees of freedom and complete the analysis. The optical design of the spectrograph (only the main channel) is recalled in Figure 4.13 where the local axes of the entrance slit are depicted. The Z axis indicates the piston, or focus, direction while the X axis is perpendicular to the instrument plane and the Y direction is tangential to the plane of the optical surface. The optical surfaces of the instrument are therefore rotated around the X axis to obtain the Czerny-Turner configuration of Figure 4.13.

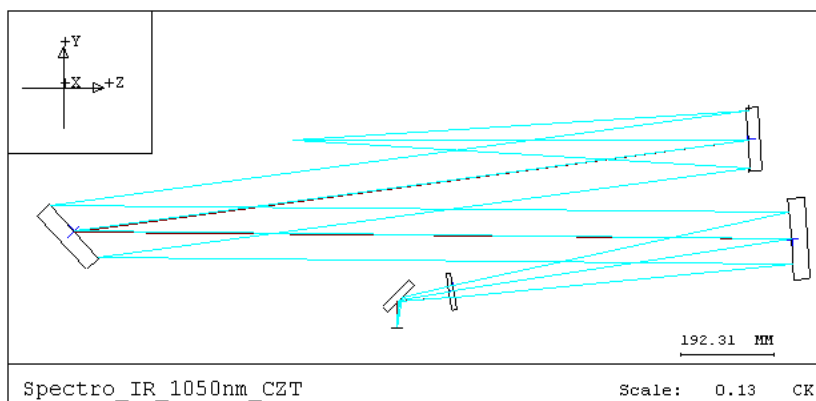


Figure 4.13 - Main channel of the spectrograph with local axes of the entrance slit indicated

In order to determine each surface sensitivity with respect to all 6 degrees of freedom, the optical element position is slightly changed until a given RMS spot value is reached through the exit slit. These limiting values range from $20\ \mu\text{m}$ to $50\ \mu\text{m}$ as the average initial spot size is equal to $15\ \mu\text{m}$. Chapter 4.4.2 conducted a resolving power analysis based on RMS spot size as it is a direct measure of the optical quality of the system. Any increase in spot size has a direct impact on resolving power and the sensitivity matrix is therefore a rapid tool to assess the variation of this parameter too. Indeed, this decrease in optical quality of the instrument has the same impact as widening the entrance slit of the instrument. For example, if the initial spot size enlarges up to $50\ \mu\text{m}$, the resolving power will approximately suffer from a division by a factor 2³. Assessing the sensitivity of the optical system with respect to such a spot size increase therefore investigates severe performance degradations. On the other hand, the first $20\ \mu\text{m}$ limit roughly depicts a 10% degradation of the resolving power.

Not all degrees of freedom must be tested since some of them may have no any influence. For example, Z rotations of rotationally symmetric surfaces, i.e. M_1 and M_2 , leave the optical system unchanged. Moreover, linear X and Y displacements of planar surfaces such as fold mirrors and the diffraction grating can be set aside. Both positive and negative tolerances are tested and their respective effect is recorded in Table 4.4 under “+ Tol” and “- Tol”. Some parts of the table may remain empty when the optical quality of the instrument is rather insensitive to the related perturbation and/or the ray trace becomes unfeasible. For example, large tilts of optical surfaces may lead some rays to escape from the system and miss subsequent optical surfaces, which is called vignetting. The conclusion in that eventuality is that the optical element is not that sensitive to alignment inaccuracies.

The analysis of Table 4.4 reveals interesting information about the optical system behavior. A comparison between M_1 and M_2 data reveals that both mirrors exhibit very close results. Their sensitivity to X and Y translation movements is minor on optical imaging quality and the major effect is a corresponding movement of the spot within the focal plane of the instrument. A focus movement of these surfaces has a direct impact on spot sizes. Indeed, the M_1 mirror intends to illuminate the grating with collimated light. The required condition for that purpose is the entrance slit being located at a distance equal to $f_{M_1} = R_{M_1}/2 * \cos \alpha_{M_1}$ away from the collimator. This distance is equal to the focal length of the M_1 mirror that is tilted by an angle α_{M_1} around the X axis. Going away from this condition therefore changes the imaging quality of the spectrograph. Indeed, α does not remain constant anymore in Equation (4) of Chapter 3.3. The divergence in incident angle $\delta\alpha$ induces a widening in diffracted angle $\delta\beta$ and the slit image of a wavelength element blurs. The same can be applied to a Z -movement of the M_2 mirror: any piston movement of this optical element changes its relative distance to the focal plane that must be optimized to $f_{M_2} = R_{M_2}/2 * \cos \alpha_{M_2}$. Angular perturbations applied on these two mirrors directly shift the optical spots within the detector plane. In addition, their focal length changes according to the cosine of the perturbation and the imaging quality is therefore impacted. The positioning of those two optical surfaces is therefore of major importance as it directly impacts the resolving power of the instrument. However, Table 4.4 reveals that a few hundred microns and $0.05^\circ = 180\ \text{arcsec}$ are required to reach the $20\ \mu\text{m}$ limit on RMS spot diameters. This accuracy of positioning can be largely achieved by typical off-the-shelf optical mounts equipped with setting screws and the alignment of these optical mirrors is not threatened.

The observation of the grating sensitivity indicates that this optical surface does not require tight tolerances to be respected. Indeed, this planar surface is first insensitive to X - and Y -translation

³ The slit spectral profile is sampled by three spots as depicted in Figure 4.9. If the spot sizes increase up to $50\ \mu\text{m}$, both sides of the slit will spread over an additional distance equal to half of this spot enlargement. The approximate exit slit width will then be equal to $100\ \mu\text{m}$ and the associated resolving power divided by two.

movements but also to defocus since it is illuminated by collimated light. Attention must however be paid in order to avoid any vignetting on subsequent surfaces. Indeed, the light beam may deviate from its optimal path and part of it may escape from the system. In this case, light losses may appear and the photometric budget is affected. Slight sensitivities to Y - and Z -rotations are identified. Y -rotations increase the vertical field of view imaged by the camera that is optimized for the entrance slit height and decrease the optical quality. On the other hand, Z -rotations tilt the grating grooves away from their vertical position and changes the effective dispersion of the grating. A tilt in the spectrum also appears and a minor effect on imaging quality appears. The major inconvenient of such a perturbation is the tilt in the spectrum which does not ease the data reduction process. Moreover, the different diffraction orders do not superpose on the detector but are rather vertically separated, which does not ease the visible alignment of the instrument.

Surface	Parameter	20 μm RMS spot		30 μm RMS spot		40 μm RMS spot		50 μm RMS spot	
		+ Tol	- Tol						
M₁	Dec X, Y (μm)	/							
	Dec Z (μm)	190	-150	360	-300	510	450	660	590
	Tilt X ($^\circ$)	0.05	-0.05	0.09	-0.1	0.13	-0.15	0.17	-0.18
	Tilt Y ($^\circ$)	0.12	-0.12	0.35	-0.35	/			
Grating	Dec Z (μm)	/							
	Tilt X ($^\circ$)	/							
	Tilt Y ($^\circ$)	0.25	-0.25	0.5	-0.5	/			
	Tilt Z ($^\circ$)	0.31	-0.31	0.61	-0.62	/			
M₂	Dec X, Y (μm)	/							
	Dec Z (μm)	180	-150	360	-300	500	-440	650	-580
	Tilt X ($^\circ$)	0.05	-0.04	0.08	-0.07	0.11	-0.1	0.14	-0.14
	Tilt Y ($^\circ$)	0.09	-0.09	0.2	-0.2	0.29	-0.29	0.36	-0.36
Toroidal lens	Dec X, Y (μm)	1800	-1900	/					
	Dec Z (μm)	390	-330	780	-680	1120	-1000	1440	-1320
	Tilt X ($^\circ$)	2.6	-1.4	/					
	Tilt Y ($^\circ$)	0.6	-0.6						
	Tilt Z ($^\circ$)	1.2	-1.2						
Fold	Dec Z (μm)	80	-90	150	-180	220	-250	290	-320
	Tilt X ($^\circ$)	0.5	-0.5	1	-0.9	1.7	-1.2	2.8	-1.5
	Tilt Y ($^\circ$)	1.1	-1.1	/					
Detector	Dec Z (μm)	120	-100	250	-210	350	-310	450	-400
	Tilt X ($^\circ$)	/							
	Tilt Y ($^\circ$)	1.6	-1.6	3.4	-3.4	/			

Table 4.4 – Sensitivity matrix assessing the individual effect on RMS spots of optical surfaces' alignment

According to Table 4.4, the toroidal lens alignment sensitivity is weak. Indeed, large translation and rotational perturbations are needed to affect the optical quality of the instrument. The piston position of the lens is naturally the most sensitive factor as it directly influences its conception purpose: the astigmatism correction. However, nearly half a millimeter is required for the spots to reach the $20 \mu m$ RMS limit which ensures an effortless control of this parameter.

The fold mirror is a planar surface and is insensitive to translation movements that are performed within its own plane. Piston movements decrease the imaging quality in a rather pronounced manner. The explanation comes from the fact that this element is very close to the focal plane of the instrument. The converging beam therefore goes rapidly out of focus when the fold mirror undergoes piston movements. Lateral shifts (along the dispersion axis) of the light beam are also induced after such displacements of the mirror. X - and Y -rotations do not directly impact on the performances of the spectrograph since the fold mirror has no other optical function except than folding the light beam.

The detector sensitivity with respect to X - and Y -shifts is naturally inexistent. The same conclusion applies concerning the focus movement along Z : any piston movement rapidly blurs the focal plane image as the detector is located at the focal point of a converging beam. Y -rotations of the detector bring out of focus the upper and lower parts of the slit in a light way. Rotations around the X -axis do not impact on the spot RMS diameter as the tolerancing analysis is monochromatic. This alignment of the detector requires observing polychromatic light and will be investigated further in this chapter.

Manufacturing precision

The evolution of the spectrograph imaging performances is now evaluated with respect to manufacturing tolerances. Each optical element parameter is slightly modified to assess its own effect on RMS spot diameters. The same limiting values as for alignment tolerances are used and the corresponding results are shown in Table 4.5.

The collimating mirror results show that slight modifications in the radius of curvature of this mirror quickly change the size of the spots in the focal plane of the spectrograph. This is no surprise as the alignment sensitivity matrix of this element previously highlighted pronounced spot size changes when this mirror was moved along the Z -axis. Indeed, the light source was therefore not located at the focal point of the mirror anymore. Since the focal length of a mirror is directly proportional to its radius of curvature ($f \approx R_{curv}/2$), any perturbation in this latter will modify the optimal location of the illuminating source. Similar results are in reality observed in this analysis, the limiting value of $20 \mu m$ is for example reached for a radius of curvature change equal to $370 \mu m$ and the associated change in focal distance is then equal to

$$\delta R_{curv} * \alpha_{M_1} = 370 * \cos 3.88^\circ \approx 185 \mu m$$

This value is very close to the one observed when changing the location of this mirror along the Z -axis as it was evaluated to $190 \mu m$ (the step value for scanning the piston movement was equal to $10 \mu m$). The conic constant of the mirror is then under study. The behavior of this manufacturing factor with respect to tolerances is very loose. Indeed, a 40 % degradation is necessary to decrease the spots' quality down to a $20 \mu m$ RMS diameter.

The grating flatness influence on imaging quality is then assessed. The flat element has an optimized radius of curvature equal to infinity. Departures from this situation will change the power of the element and illuminate the focusing mirror M_2 with non-collimated light and inevitably decrease the

resolving power of the spectrograph. For common practice (and technical reasons in CODE V), the flatness quality of this optical element is expressed with the help of a test plate fit⁴. The required grating flatness to avoid any blurring of the focal plane image is not tight as a single fringe is required to reach the $20\ \mu\text{m}$ limit. Commercially off-the-shelf flat surfaces exhibit typical available flatnesses of the order of $\lambda/10$ and the grating flatness sensitivity is therefore reduced.

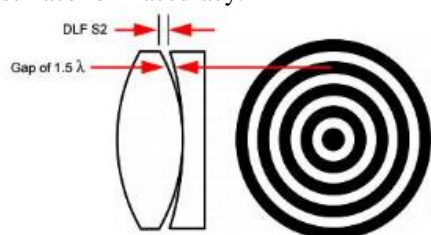
The behavior of the M_2 mirror is similar to the sensitivity observed for M_1 : the changes in its radius of curvature has the same impact as the associated Z -movement. The conic constant variations induce slightly more pronounced effects on the imaging quality but remain weak.

The overall conclusion for the toroidal lens is positive: both its radii of curvature, thickness and index of refraction variations do not largely impact on the optical performances. The manufacturing precision of this important custom element can therefore be relaxed for an easier fabrication and a lower cost. The analysis of the fold mirror sensitivity on flatness accuracy reveals that this parameter does not largely influence the optical quality of the spectrograph. Indeed, a large departure from a flat test plate is required to slightly alter the size of the optical spots. The purpose of this optical element is indeed to simply bend the optical light and it appears sensible that this element does not play a key role in the overall optical quality of the instrument.

4.5.2 Coupling effects

Investigating the individual sensitivity of all optical elements is necessary in order to identify the most constraining elements in terms of alignment and manufacturing. These will need tighter tolerances than others to be respected in order to reach the goal performances of the instrument. However, some parameters may be connected to others and their respective variation may counterbalance each other. Therefore, sensitive elements may not need as much precaution as foreseen by the sensitivity matrix if tuning some others attenuates their effect. This is the definition of compensators: these optical elements feature adjustable settings which intend to counterbalance alignment and manufacturing errors and recover the design performances as much as possible. This section intends to highlight the existing relations between the spectrographs parameters and identify suitable compensators that may be used for alignment purposes.

⁴ To characterize the radius of curvature of an optical surface, the optical element is usually held in contact with a test plate. This one is a highly calibrated optical piece that is either flat or characterized by a highly precisely known radius of curvature. The illumination of these with laser light then reveals any air gap with the help of light and dark bands whose spacing is equal to half the source wavelength (see figure below [62]). Counting the number of rings across the aperture, and the associated air gap in wavelength unit, is then a measure of the surface form accuracy.



Surface	Parameter	Tolerance to reach 20 μm RMS spot		Tolerance to reach 30 μm RMS spot		Tolerance to reach 40 μm RMS spot		Tolerance to reach 50 μm RMS spot	
		+ Tol	- Tol	+ Tol	- Tol	+ Tol	- Tol	+ Tol	- Tol
M1	<i>Radius of curvature</i>	0.02% = 0.37 mm	0.02% = 0.37 mm	0.04% = 0.75 mm	0.035% = 0.66 mm	0.055% = 1.03 mm	0.05% = 0.94 mm	0.07% = 1.31 mm	0.065% = 1.22 mm
	<i>Conic Constant</i>	49.87% = 0.6	41.56 % = 0.5	/					
Grating	<i>Test plate fit</i>	1 fringe		2 fringes		3 fringes		4 fringes	
M2	<i>Radius of curvature</i>	0.02 % = 0.35 mm	0.02 % = 0.35 mm	0.04% = 0.71mm	0.035% = 0.63 mm	0.055% = 0.98 mm	0.05% = 0.89 mm	0.07% = 1.24mm	0.065% = 1.15 mm
	<i>Conic Constant</i>	15% = 0.3	25 % = 0.5	/					
Toroidal lens	<i>Radius of curvature 1</i>	30 fringes		/					
	<i>Radius of curvature 2</i>	20 fringes		/					
	<i>Thickness</i>	200 μm	200 μm	450 μm	400 μm	650 μm	600 μm	850 μm	800 μm
	<i>Index of refraction</i>	0.003	0.002	0.005	0.004	0.007	0.006	0.009	0.008
Fold	<i>Test plate fit</i>	25 fringes		/					

Table 4.5 - Sensitivity matrix assessing the individual effect on RMS spots of optical surfaces' manufacturing

The previous section already highlighted the close relationship between the radii of curvature of the M_1 and M_2 mirrors and their respective piston alignment. The effect of changing either of these parameters was shown to be highly sensitive on imaging quality. The conclusion that follows is not however that the mirrors must be manufactured with an extremely high precision and located at their respective exact design location. Since these parameters are inter-dependent, a better interpretation that can be drawn is that one can compensate for the other. For example, if the entrance slit mount can be finely Z -adjustable, then the optimum location for collimating light with M_1 can be closely approached by correcting for any difference in its radius of curvature. The same applies for M_2 and the imaging quality is ensured if the detector can be moved along the piston direction to correct for any manufacturing error. A numerical simulation in CODE V for example shows that the required adjustment in the slit position is equal to 1.02 mm if the M_1 radius of curvature changes by $0.1\% = 1.87\text{ mm}$. This displacement is very close to the predicted one that is equal to $\delta R_{M_1}/2 * \cos \alpha_{M_1} = 1.87\text{ mm}/2 * \cos 3.88^\circ = 0.94\text{ mm}$.

The rotation angle of both M_1 and M_2 mirrors was identified as a sensitive parameter too. Tilting those mirrors enables bending light away from its incoming direction and creates some room for other optical components. The rotation of these mirrors directly changes their effective focal length as previously shown (the change in focal length is proportional to the cosine of the angle). More precisely, only their tangential (within the dispersion plane of the spectrograph) focal length is affected and their sagittal (perpendicular to the plane of the spectrograph) one remains unchanged. This mechanism was said earlier to be the source of the inherent astigmatism of Czerny-Turner spectrographs. Since the global contribution to astigmatism is made of the individual contribution of both mirrors, the misalignment of one can be partly recovered by modifying accordingly the alignment of the second. Therefore, after having set the collimating mirror onto the optical bench to its best position, any residual misalignment can then be recovered by a fine correction of the focusing mirror. This technique can only be used to correct for the additional astigmatism aberration induced by any departure from the optimal configuration. The toroidal lens was effectively designed to correct for a given initial astigmatism state of the design. Any change in this aberration makes this element less efficient and tuning the focusing mirror to recover this design amount is an efficient way to recover the best optical performances.

Once again, the high sensitivity of those optical elements does not involve tiny final tolerances on their manufacturing and alignment because adjustable settings can be used to compensate for such errors. Eventually, the effective focal lengths of both mirrors cannot however largely depart from their design value as they were previously calculated to fulfill the scientific requirements (the focusing mirror focal length directly drives for example the linear dispersion of the instrument). To illustrate the above considerations, a change in the M_1 mirror tilt and its associated M_2 correction is simulated in CODE V. For example, if the collimator angle is slightly modified by 0.1° , the focusing mirror tilt must be changed accordingly by 0.0821° after re-optimization of the system with CODE V. The factor between both values amounts to the ratio of the focal lengths of the mirrors.

The tolerancing of the toroidal lens is highly informative as it demonstrates that both alignment and manufacturing sensitivities of this optical element are moderate. This asymmetric lens is therefore able to finely correct for the astigmatism of the design while being quite insensitive to manufacturing and alignment tolerances. This small element, since it is close to the focal plane, eventually represents a handy alternate way to correct for the astigmatism aberration of Czerny-Turner spectrographs.

Finally, piston movements on the detector and the folding mirror induced noticeable spot changes at the focal plane. A change in the detector piston is however completely equivalent to a change in the fold mirror Z -position. A slight difference is due to the folding mirror tilt: the spot size will increase and a lateral shift along the dispersion axis will also occur. On the other hand, since the moved optical element is acting in reflection, the change in optical path length amounts to two times the mechanical perturbation. Nevertheless, any fold mirror piston movement can be easily balanced out by moving the detector by the appropriate distance (proportional to the sine of the fold angle with respect to the detector plane). Therefore, this identified coupling enables larger tolerances on the folding mirror positioning if the detector is enabled to finely set its position. For example; a $500\ \mu\text{m}$ shift of the flip mirror is compensated within CODE V by a $715\ \mu\text{m}$ focus movement of the detector. This result is very close to the foreseen value of $500 * 2 * \sin 46.03 = 719\ \mu\text{m}$.

4.5.3 Compensator selection

The alignment of an optical instrument needs to incorporate adjustable optical elements in order to compensate for both manufacturing and alignment errors of the all elements incorporated inside the optical design. These are the so-called compensators. This section intends to identify suitable compensators within the spectrograph with the help of the obtained sensitivity matrices and the identified coupling effects. These will then be used during the practical alignment to optimize the instrument performances with the manufactured elements positioned at their best positions.

The elaboration of the previous sensitivity matrices and the identification of several coupling effects enable to determine an appropriate alignment scheme of the instrument. On the first hand, the sensitivity matrix highlighted parameters that induced large imaging perturbations when altered from their design value. These therefore need a particular attention because of their strong impact on the instrument imaging capabilities. On the other hand, the identified coupling effects led to the conclusion that smartly located settings may compensate for those induced degradations. Indeed, a slight tuning of the position of another optical element may completely overcome the intense effect of these sensitive elements. The optical mounts of these items should therefore be fitted with suitable settings to accomplish these operations.

Therefore, the alignment scheme of the spectrograph is based on the positioning of the optical elements onto an optical breadboard in a successive manner, i.e. from the entrance slit (the fiber bundle) to the detector. At each elementary step, the optical quality of the instrument is optimized by finely repositioning an appropriately selected element. This latter should therefore feature the required setting screws to enable the compensation of the identified couplings. For example, the fiber bundle mount must be equipped with a piston setting screw to adapt to the collimator actual radius of curvature. On the other hand, the M_2 mirror requires to be tilt-adaptable to slightly compensate for the M_1 misalignment. Finally, the detector needs to be mounted on a translation stage to correct for the fold mirror misalignment. These intermediate alignment steps ensure the positioning of the selected optical element within a suitable tolerance range for an appropriate global alignment.

The alignment sequence therefore follows the natural light order starting from the fiber and ending at the detector. Each optical element is positioned at its best location and the remaining error corrected with the help of its coupled parameter. At the end, the detector focus can be modified to correct for the remaining alignment error and optimize the resolving power of the instrument. The detector focus is the unique global compensator of the overall system performances and is the last one to be updated after all others are installed on the optical bench.

4.5.4 Overall budget

Once the sensitivity matrix of the instrument is established and the main interactions between the components are identified, an overall error budget of the selected alignment scheme can be carried out. This process consists in randomly perturbing the elements within their range of tolerance and recording the associated spot sizes at the detector after having optimized the system with the selected compensator. The analysis is then run several times to obtain accurate statistics on the performances of the toleranced instrument. These can therefore be predicted with a high level of confidence if the number of trials is high enough.

The first step to conduct in such an analysis is to define for each optical surface an initial range of tolerance for both its manufacturing and positioning. This initial state of the element is based on the sensitivity matrix results, the identified coupling effects and the manufacturing limitations. Indeed, the overall budget of the instrument may reveal that very tight tolerances are required on the manufacturing of a given optical surface. The optical designer will then have trouble obtaining it from optical workshops. Table 4.6 illustrates typical tolerances for opto-mechanical mounting and manufacturing (from 2008). Departures from test plates are again expressed in fringes. The relation below directly links both fringes and variations of radius of curvature:

$$\delta R = \delta F \lambda \left(\frac{2R}{D} \right)^2 \quad (11)$$

where δF is the number of fringes, λ is the wavelength used to observe the fringes, R is the radius of curvature and D the clear aperture of the optical surface [62]. These should be compared to the required ones for the considered design in order to assess their validity in first order. If the required tolerances largely differ from Table 4.6, the conception of the instrument should be revised to identify the most sensitive elements and relax their manufacturing and/or alignment.

Parameter	Units	Tolerance		Approximate limiting value
		Loose	Tight	
Index of refraction	--	0.003	0.0003	0.00003 ^a
Radius departure from test plate	fringes ^b	10	3	1
Departure from spherical or flat	fringes ^c	4	1	0.1
Element diameter	mm	0.5	0.075	0.005
Element thickness	mm	0.25	0.025	0.005
Element wedge angle	arcmin	3	0.5	0.25
Air space thickness	mm	0.25	0.025	0.005
Decenter, mechanical	mm	0.1	0.010	0.005
Tilt, mechanical	arcsec	3	0.3	0.1
Dimensional errors of prisms	mm	0.25	0.01	0.005
Angle errors: prisms and windows	arcmin	5	0.5	0.1

Table 4.6 - Typical tolerances for opto-mechanical constraints [69]

The initial tolerance state of all considered parameters of the spectrograph is listed in Table 4.7. Both manufacturing and alignment errors are included into this analysis to investigate the overall performances of the spectrograph as precisely as possible. The perturbation of the instrument is then randomly performed based on these values and the spot analysis is carried out. Several runs are required to assess the instrument performances accurately and confirm its robustness. The larger the

considered tolerances, the more robust the instrument if the spot quality still fulfills the scientific requirements.

The tolerances from Table 4.7 are fairly large compared to the typical values from Table 4.6 or the sensitivity analysis previously conducted. The considered displacement uncertainties are fixed to $50\ \mu\text{m}$ which is rather loose when taking into account the foreseen alignment scheme. Indeed, at every step the optical quality is optimized with the help of micrometer setting screws located on the identified coupled parameters. Table 4.6 also specifies a tight value of $10\ \mu\text{m}$ for mechanical decenters and confirms the validity of this assumption. Angular decenters amount to $1\ \text{mrad}$, i.e. $206\ \text{arcsec}$, which totally exceeds the typical loose tolerance of $3\ \text{arcsec}$ in Table 4.6. Moreover, the alignment of the mirrors of the spectrograph is performed with the help of theodolites whose typical sensitivity and repeatability amount on average to a few arcsecond. The considered mechanical tolerances may therefore be reasonably characterized as loose.

Manufacturing tolerances on radius of curvature are fixed to $5\ \text{fringes}$ for planar surfaces and $R_{\text{curv}}/1000$ for M_1 and M_2 , i.e. $3.5\ \text{fringes}$ at the reference wavelength of $546\ \text{nm}$ according to Eq. (11). The other tolerances on index of refraction and element thickness for example confirm the previous assumption: loose tolerances are used within this analysis with respect to both alignment and manufacturing purposes.

The results of the tolerancing process are depicted in Table 4.8. Two different scenarii are presented to illustrate the importance of implementing compensators within an optical system. The left column of Table 4.8 concerns the evolution of spots when perturbing the system with the considered tolerances without any further correction with the help of a compensator. The right column on the other hand records the final spot values when the detector piston position is optimized for the best correction of aberrations⁵. The spot sizes of 9 different locations of the slit are sampled: at the extremities and in the middle of both its width ($50\ \mu\text{m}$) and height ($10\ \text{mm}$). The change in the detector focus position is also indicated. The X - and Y -coordinates are also changed only for centering purposes of the slit image as they do not influence the spot sizes.

The comparison between both scenarii highlights the importance of benefiting from a compensating element. Whereas spot sizes grow in size approximately by a factor 10 without any compensating action, changing the detector piston limits their RMS diameter to $20\ \mu\text{m}$. The decrease in resolving power of the instrument therefore falls to nearly 10% after this slight realignment. Enabling the detector to accomplish the Z -movement is therefore mandatory to reach the foreseen performances from conception. Eventually, the results from Table 4.8 confirm the robustness of the optical design with respect to alignment and manufacturing uncertainties. Even though loose tolerances were considered, the optical performances could be recovered by finely tuning the detector focus position. This compensator is therefore foreseen as essential to tackle with tolerance compensation during the practical alignment of the instrument.

⁵ The estimated RMS spot changes are based on the “3- σ rule”. This means 99.73% of all simulated systems exhibit spots size variations that are lower than or equal to the estimates listed in Table 4.8.

Surface	Parameter	Tolerance
M₁	<i>Radius of curvature</i>	$0.001 * R_{curv}$
	<i>Conic constant</i>	0.01
	<i>X-displacement</i>	50 μm
	<i>Y-displacement</i>	50 μm
	<i>Z-displacement</i>	50 μm
	<i>X-rotation</i>	1 mrad
	<i>Y-rotation</i>	1 mrad
Grating	<i>Z-displacement</i>	50 μm
	<i>X-rotation</i>	1 mrad
	<i>Y-rotation</i>	1 mrad
	<i>Z-rotation</i>	1 mrad
M₂	<i>Radius of curvature</i>	$0.001 * R_{curv}$
	<i>Conic constant</i>	0.01
	<i>X-displacement</i>	50 μm
	<i>Y-displacement</i>	50 μm
	<i>Z-displacement</i>	50 μm
	<i>X-rotation</i>	1 mrad
	<i>Y-rotation</i>	1 mrad
Toroidal lens	<i>Thickness</i>	50 μm
	<i>Index of refraction</i>	0.001
	<i>X-radius</i>	5 fringes
	<i>Y-radius</i>	5 fringes
	<i>X-displacement</i>	50 μm
	<i>Y-displacement</i>	50 μm
	<i>Z-displacement</i>	50 μm
	<i>X-rotation</i>	1 mrad
	<i>Y-rotation</i>	1 mrad
	<i>Z-rotation</i>	1 mrad
Fold mirror	<i>Test plate fit</i>	5 fringes
	<i>Z-displacement</i>	50 μm
	<i>X-rotation</i>	1 mrad
	<i>Y-rotation</i>	1 mrad
Detector	<i>Z-displacement</i>	50 μm
	<i>X-rotation</i>	1 mrad
	<i>Y-rotation</i>	1 mrad

Table 4.7 - List of tolerances used when performing the overall budget of the instrument

	No compensator	Detector X, Y, Z movements	
Compensator change (mm)	/	X-displacement	2.208194
		Y-displacement	2.323926
		Z-displacement	1.023726
Initial RMS spot (μm)			
(0 ; 0)	12.1180		12.1180
(0 ; 0.025)	12.2040		12.2040
(0 ; -0.025)	12.0340		12.0340
(5 ; 0)	13.4270		13.4270
(5 ; 0.025)	13.4410		13.4410
(5 ; -0.025)	13.4060		13.4060
(-5 ; 0)	13.4270		13.4270
(-5 ; 0.025)	13.4410		13.4410
(-5 ; -0.025)	13.4060		13.4060
Estimated RMS spot change			
(0 ; 0)	116.003		0.856
(0 ; 0.025)	115.948		0.624
(0 ; -0.025)	116.036		1.105
(5 ; 0)	110.359		7.868
(5 ; 0.025)	110.366		7.555
(5 ; -0.025)	110.352		8.18
(-5 ; 0)	110.331		7.818
(-5 ; 0.025)	110.339		7.483
(-5 ; -0.025)	110.324		8.131
Final estimated RMS spot			
(0 ; 0)	128.1210		12.9740
(0 ; 0.025)	128.1520		12.8280
(0 ; -0.025)	128.0700		13.1390
(5 ; 0)	123.7860		21.2950
(5 ; 0.025)	123.8070		20.9960
(5 ; -0.025)	123.7580		21.5860
(-5 ; 0)	123.7580		21.2450
(-5 ; 0.025)	123.7800		20.9240
(-5 ; -0.025)	123.7300		21.5370

Table 4.8 - Overall tolerancing budget results

4.6 Alignment simulation

4.6.1 Simulation goal

This simulation intends to investigate if the tolerances that were defined during the tolerancing analysis are sufficient to enable the practical alignment of the instrument. This analysis does not simulate an end-to-end alignment of the whole instrument, starting from a blank breadboard, but rather performs a fine realignment of the whole system when it stands within its tolerances range. This means a previous alignment of the system has been established and then a fine tuning is performed on selected compensators to achieve the best performances. The obtained resolving power is also calculated to check whether the system complies with the specified scientific requirements.

This process therefore goes hand in hand with the previously introduced tolerancing analysis and complements its results. Indeed, this section also runs an optimization process to investigate which compensator to apply and which order to follow. Several compensators are available for alignment and choosing the right one to achieve the optimal configuration remains a hard task, especially when several optics and their related movements are involved in the optical system. The sequence to follow is investigated and identified through a simple optimization process that is introduced further below.

4.6.2 Optimization scheme

The system starts from its designed configuration that is perturbed within the range of the identified allowable tolerances from Table 4.7 (see Figure 4.1). The system then suffers from misalignment and its performances are degraded. The associated spots sizes are larger and its resolving power is decreased. The alignment procedure naturally consists in optimizing the system through the reduction of these spots, which are images of entrance slit points. The change in spot size is obtained by modifying the position of the carefully selected compensators. The alignment is eventually complete when a minimum position is reached and further varying the compensators' values degrades the optical quality of the system.

The alignment loop the system runs trying to converge to a better optical system, ideally close to the design configuration, can be separated into three different steps:

- The algorithm scans all defined compensators' ranges, usually the focus, the tip and the tilt of a given optical surface. While scanning the whole compensator range, the system records all the different spots, the average spot over the slit, and their related standard deviation. It then finds and saves the best compensator value to apply in order to minimize the function of merit (FOM) that is selected. Starting back from the initial perturbed system, the algorithm then applies exactly the same sequence of operations with the second compensator. It thus scans all its mechanical range and records the best possible movement to apply. The algorithm then repeats this operation for all identified compensators in the system. The order the algorithm follows to try the different compensators does not matter here since they all start from the same initial position (the initial perturbed system).
- Once the algorithm knows all individual best compensators and their effect on the function of merit, it compares them and records the one that produces the major decreasing action on the function of merit. This means this procedure tends to follow the path that goes along the steepest descent to converge as fast as possible to a local minimum of the function of merit.

- The algorithm then applies the best compensator to position the system at the new local minimum with respect to the selected compensator.

This alignment loop is repeated a user-defined number of times. The stop-criterion could have involved a relative decrease in the function of merit but it is preferred here to ensure the end of the calculation. On the other hand, it is also interesting to investigate if a reduced number of steps may lead to an acceptable situation, i.e. where the scientific requirements are fulfilled. One may notice that all the compensators are tried in the alignment loop after the first iteration. For example, if the system applied a focus, it will investigate again the focus compensator at the next step. At first sight, one might think that it is a waste of time to try the focus again after having applied it at the first iteration, but in practice this is not the case. Indeed, when scanning the focus range at the first step, the algorithm may reach the situation where the function of merit is still decreasing at the maximum compensator value; this means the local minimum of the function of merit does not lie within this compensator range. In other words, the local minimum of the function of merit is not reachable within one focus step.

At the second step, the algorithm follows the same minimizing curve but starting closer to the unknown minimum and can potentially reach it this time. This in fact mimics the insertion of a shim or a global movement of the optical surface and its mount to be able to scan the focus again afterwards (since the travel of the actuators of the optical mounts is limited).

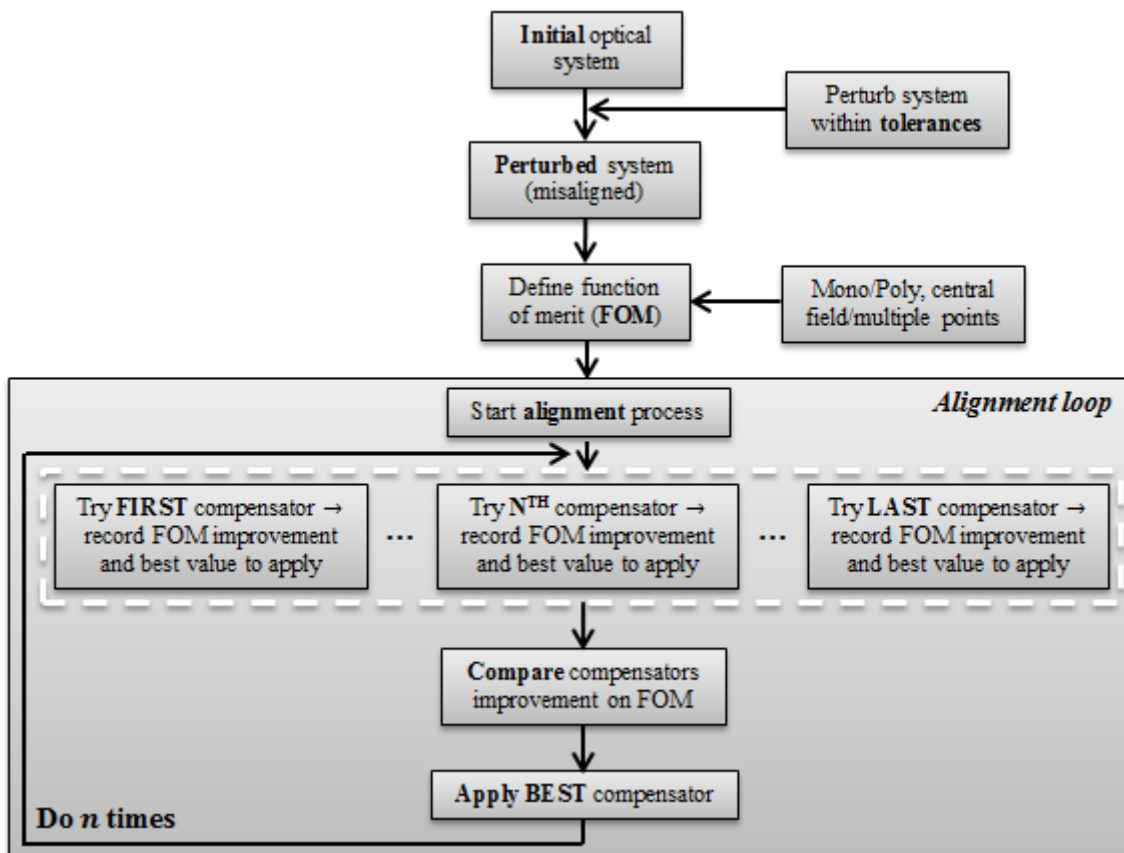


Figure 4.14 - Alignment procedure block diagram view

4.6.3 Figure of merit

This section focuses on the definition of a suitable function of merit to ensure a proper convergence of the alignment procedure. This is the quantity the algorithm will try to minimize/maximize to converge to an aligned system and optimize its optical performances. In this case, it will try to minimize the spot sizes at the focal plane of the instrument. These are reliable indicators of the imaging quality of the spectrograph.

However, the question of conducting a monochromatic or polychromatic analysis arises. On the other hand, the selection of points through the entrance slit is not trivial and one may wonder if the central point is sufficient to guide the optimization process. The selection of a suitable function of merit is thus not trivial and requires simulation tests to investigate if a given set of variables fits the application.

Two different functions of merit are implemented in the alignment simulation. The first one is the mean value of all the spot sizes resulting from the optimization fields that are located through the entire entrance slit. The second function of merit consists in the spot size of a single optimization field that can be selected from the 9 available ones.

4.6.4 Mechanical considerations

Movements of optical surfaces at initial perturbation and compensators during alignment must be performed around their respective local axes. These have been calculated for each surface with the help of rotation matrices and visually checked as can be seen in Figure 4.15. Focus, tip and tilt movements are thus executed with respect to those local axes, which differ from one optical surface to the other.

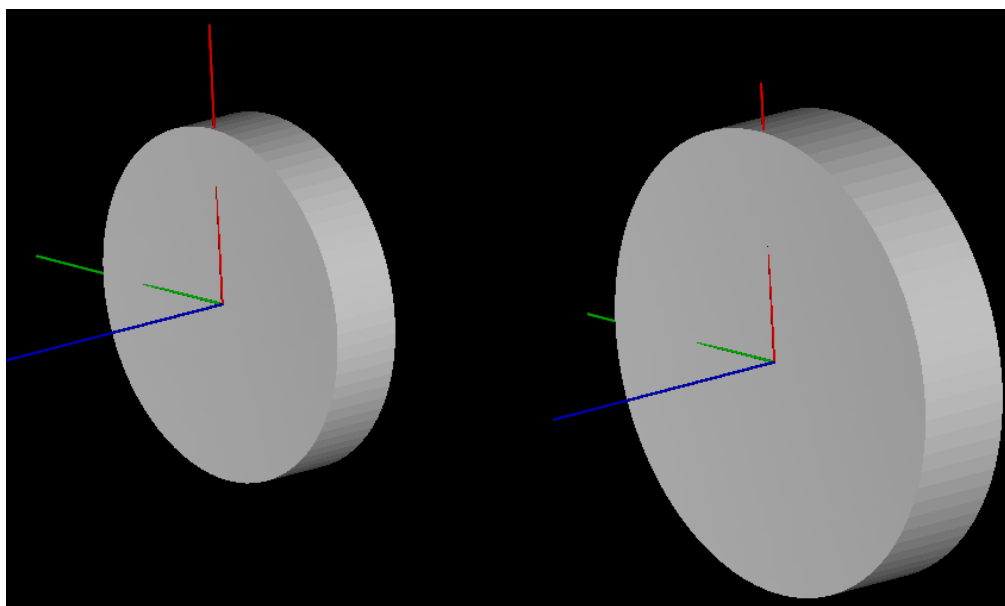


Figure 4.15 - Axes implementation on optical surfaces

4.6.5 Compensators

The compensators that are used for the optimization of the system during the alignment process are the focus (piston), tip and tilt of the detector (see Figure 4.16). Indeed, during the experimental alignment of the spectrograph, the detector is the last surface to be installed on the optical bench. All other surfaces are set up at previous steps when individual components are aligned, starting from the beginning of the optical train.

All optical elements are therefore supposed to be settled within their tolerance range when the installation of the detector takes place. The goal is therefore to adjust the piston of the detector and its angular position to recover as much as possible the design performances of the optical system. Local detector axes are represented in Figure 4.16 with the help of colored sticks which are respectively blue for the piston, green for the tip and red for the tilt.

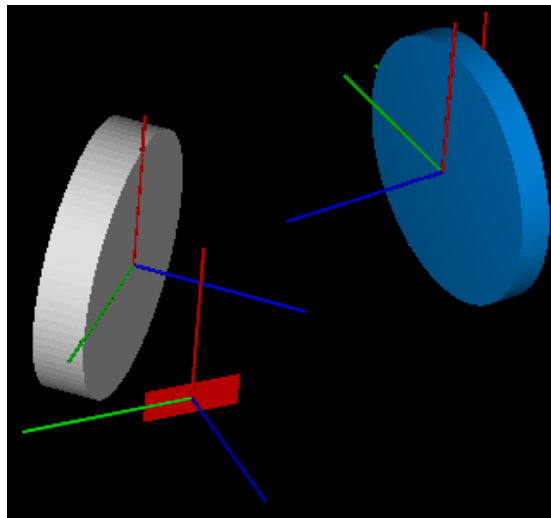


Figure 4.16 - Toroidal lens (*blue*), fold mirror (*grey*) and detector (*red*) with their respective local axes

4.6.6 Simulation results

Monochromatic single-point function of merit

The first function of merit that is selected is the spot size of the entrance slit center at the central wavelength for a given grating position. This location through the focal plane is both at the imaging and dispersion axes' origin, ensuring symmetry and no bias with respect to wavelength and location through slit during the optimization process.

Figure 4.17 illustrates the optimization path the algorithm followed: the actuator movement of a given step is represented by an arrow that is parallel to its related axis. The length of each arrow is directly proportional to the amount of movement that is required at each iteration of the alignment process. Eventually, each intermediate system state is depicted in this three-dimensional optimization space. For example, the presented case underwent a focus of $50 \mu\text{m}$ followed by a tilt rotation of 0.85° .

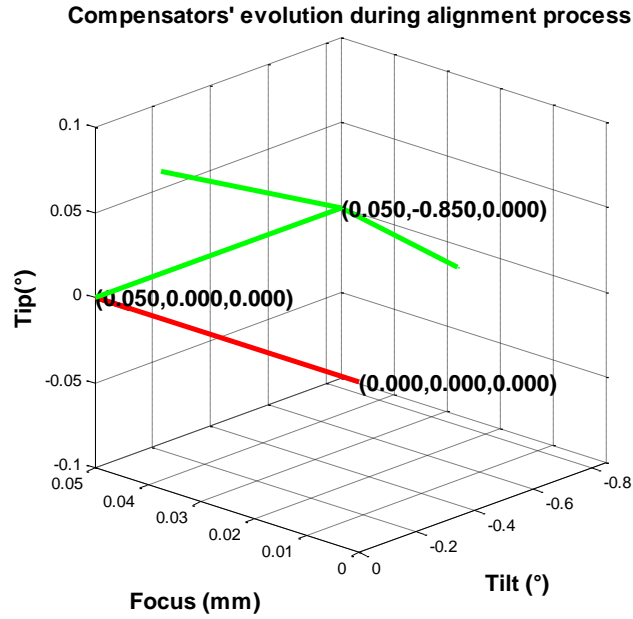


Figure 4.17 - Compensators' evolution during alignment process

The evolution of the function of merit during these movements can be seen in Figure 4.18. The focus, tilt and tip operations are represented in different colors and their corresponding effect on the function of merit can be observed. This confirms that the focus option was the most interesting one in terms of function of merit decrease at the first step. On the other hand, the tilt rotation is selected at the second step. The RMS spot sizes of the selected slit point before and after alignment are respectively $16.98 \mu m$ and $14.56 \mu m$.

The horizontal red dashed line between the first and second steps means that the system has reached an equilibrium point with respect to the focus compensator. The best movement to perform at first step was therefore within the range of focus that had been scanned and was not out of reach. If not, the algorithm would have identified the required additional amount of focus and this would simulate the use of a shim or a global movement of the detector assembly.

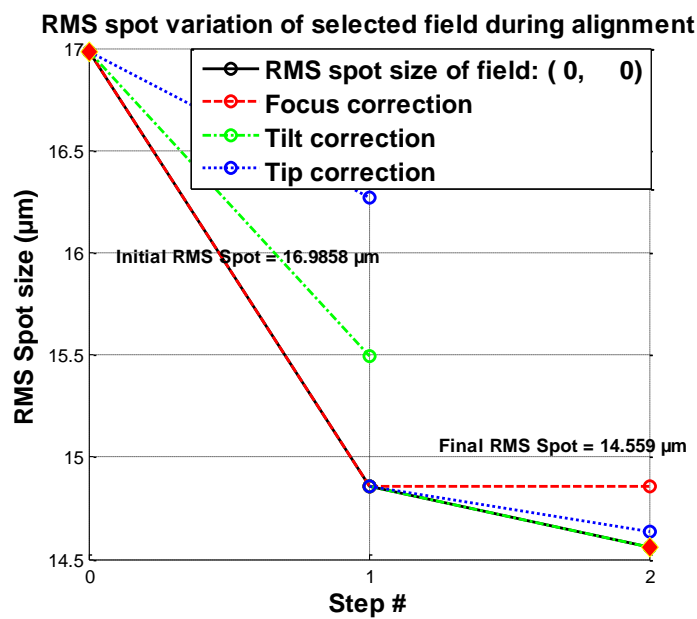


Figure 4.18 – Central slit spot evolution through the different paths investigated by the algorithm

To investigate if this function of merit is suitable to lead the optimization process, i.e. the alignment of the instrument, a resolving power analysis is carried out before and after running the algorithm. Figure 4.19 presents the images of the entrance slit at the focal plane at three different wavelengths. The resolving power is then calculated along the slit at each wavelength. The mean resolving power at initial and final configurations is respectively equal to 29 419 and 29 215. The average resolving power over the focal plane thus decreases during the alignment process.

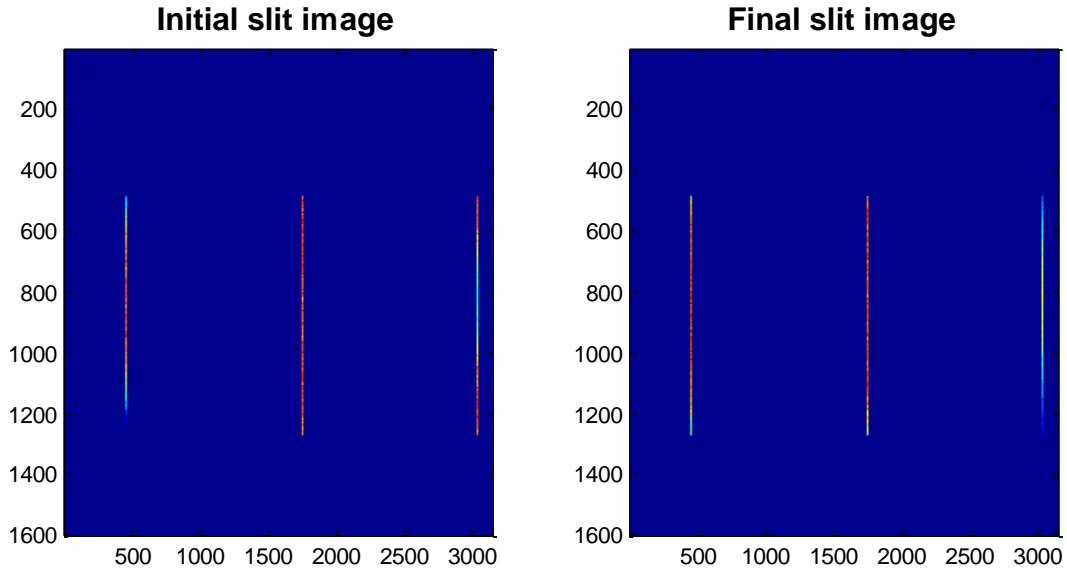


Figure 4.19 - Slit images at three different wavelengths

This “central slit-oriented” function of merit does not ensure the convergence to an equilibrium point where the resolving power increases over the entire focal plane of the instrument. Indeed, its value only takes into account the central location of the focal plane and the resolving power increase is only ensured at this place. Zooming onto the exit slit at another wavelength than the central one reveals that the imaging quality of the instrument has decreased (see Figure 4.20). Indeed, the initial slit image spreads over 6 pixels while the final one rather lies on 8. The full width at half maximum then increases and the resolving power decreases.

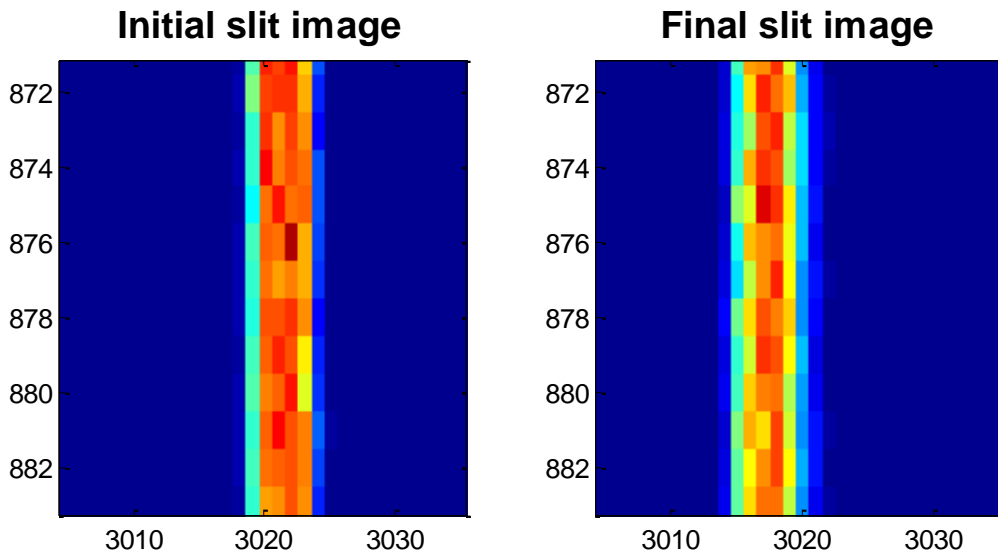


Figure 4.20 - Zoom onto the slit image at one detector side

When looking at the evolution of the mean RMS spot during the alignment simulation (see Figure 4.21), a large increase is noticeable between step 1 and 2. This means the optical quality of the instrument drops when the tilt movement is applied. As will be explained further in this section, this rotation movement affects wavelengths located at the sides of the detector with barely no effect at its center.

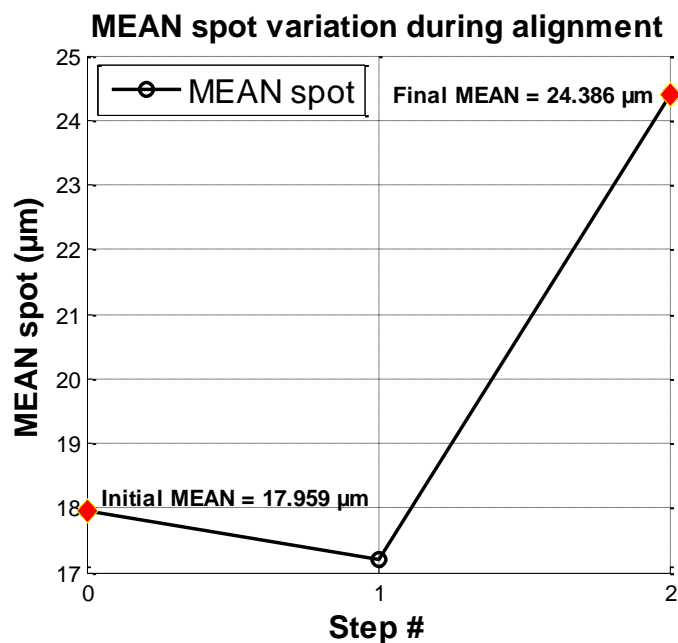


Figure 4.21 - Evolution of mean spot and during alignment process

The axis around which the rotation occurs is indeed located at the centre of the detector and oriented along the slit height (see Figure 4.16). All points lying at a given wavelength are thus affected the same way and those located onto this axis remain unperturbed (initially, at the central wavelength). The reason why the wavelength that is considered as being the detector central wavelength is sensitive to this movement is that the applied perturbations to the system induce slight wavelength shifts. After being perturbed, the central wavelength has therefore changed. The conclusion that arises is that another function of merit must be used, taking this time into consideration multiple wavelengths. Several points through the slit must also be investigated since the same conclusion applies to the tip movement.

Polychromatic multi-point function of merit

A second attempt is performed by trying this time to align the system while taking into account several wavelengths and points through the slit. The optimization process now tries to minimize the mean spot size over the entire slit, sampled with 9 different points (those used for the optimization process during optical design), evaluated at three different wavelengths. This way, the imaging quality is improved along both the imaging and dispersion axes at each alignment iteration, if any improvement is possible within the compensator step. This ensures that any compensator movement will therefore be performed only if it is of benefit to the resolving power increase all over the bidirectional focal plane of the instrument. The entire alignment process remains the same and only the function of merit changes from the first alignment approach.

Having a look at Figure 4.22 reveals that the algorithm first applied 0.4 mm piston movement of the detector followed by a tilt rotation of 0.1°.

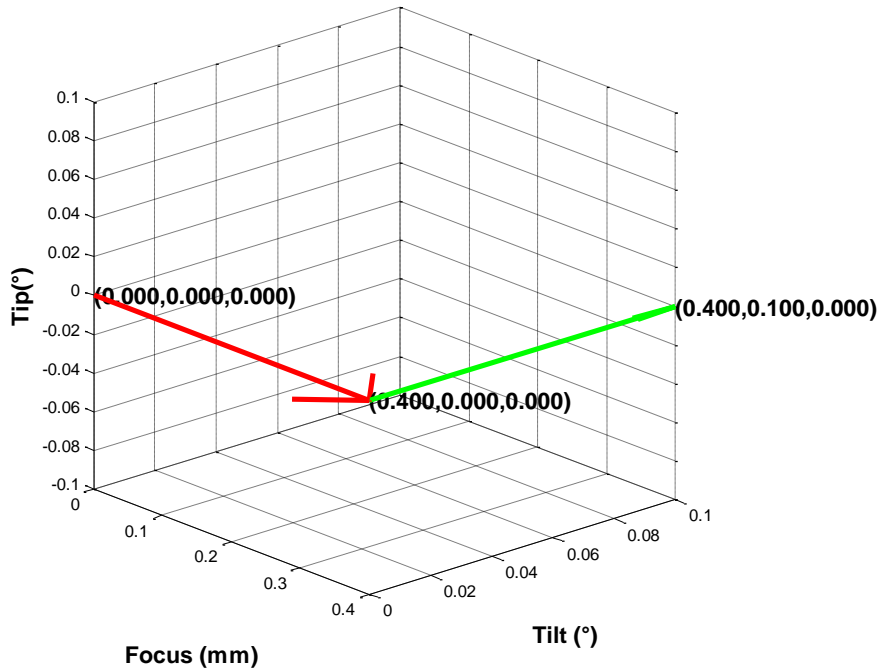


Figure 4.22 - Compensators' evolution during alignment process

The evolution of the mean RMS spot, the function of merit under use, and the standard deviation can be seen in Figure 4.23. As expected, the function of merit decreases monotonically from $53.63 \mu\text{m}$ to $27.17 \mu\text{m}$ in two steps, dividing the mean spot value by a factor 2. This induces an increase in the optical performances of the instrument all over the focal plane, i.e. through the considered waveband and along the entire slit.

The standard deviation falls at first step, during the detector piston movement and slightly increases afterwards. This is no surprise since no criterion is fixed on this parameter and it only testifies the tendency of the spots to group around a mean value. Of course, a large increase in the standard deviation certainly does not correspond to a proper movement to converge to the aligned system since the imaging quality does not remain constant over the focal plane.

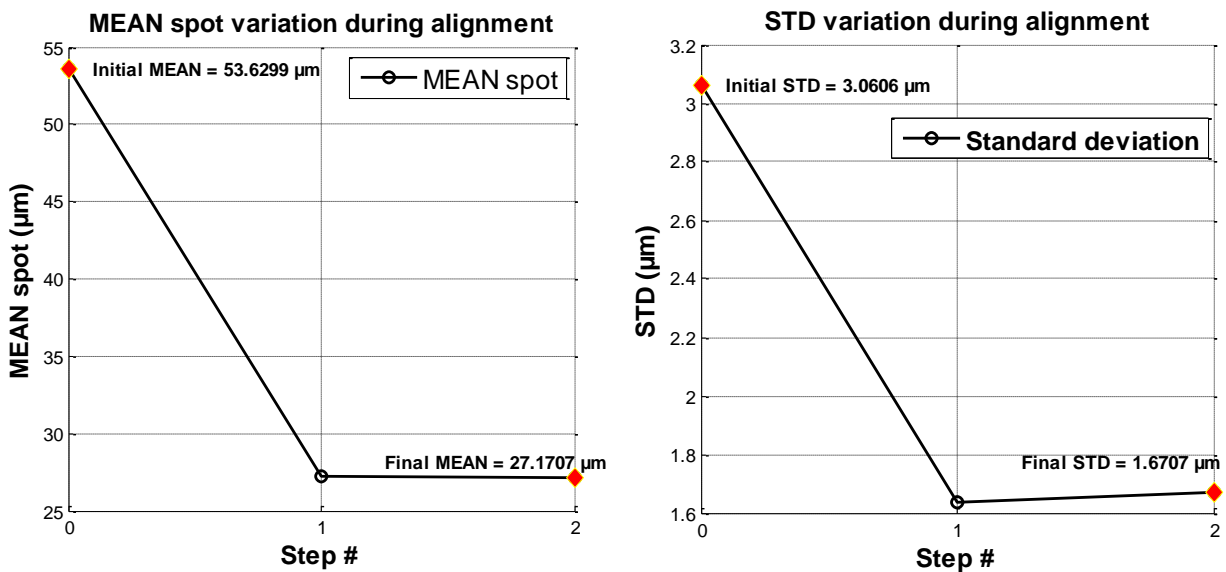


Figure 4.23 - Evolution of mean spot and standard deviation during alignment process

Figure 4.24 then introduces the different optimization paths the algorithm investigated to improve the function of merit. Focus (red), tilt (green) and tip (blue) movements are scanned and their related best improvement on the mean RMS spot is recorded. These are compared and the one that exhibits the steepest decrease in spot size is selected. Figure 4.24 confirms that the most suitable compensator in this case was the piston movement at first step and the tilt rotation as a second one.

The second step improvement only slightly changes the spot sizes over the focal plane, this confirms that the detector plane was mainly out of focus before compensation and did not need any further rotation. On the other hand, this figure highlights the fact that running the algorithm for two iterations is sufficient to reach an equilibrium situation where either any further improvement is of minor impact or the spots are worse than before.

Since the compensator step sizes are of finite value, increasing the number of optimization iterations will not lead for sure to an improvement in the function of merit value. Indeed, imaging quality increases will only happen if the step size is fine enough to approach the equilibrium point more precisely than the previous iteration did. As will be seen in the next figures, the step size under use samples the mean spot size evolution curve with high fidelity. Therefore, a “no-movement” decision surely testifies of having reached an equilibrium point rather than the need for a finer compensator step size.

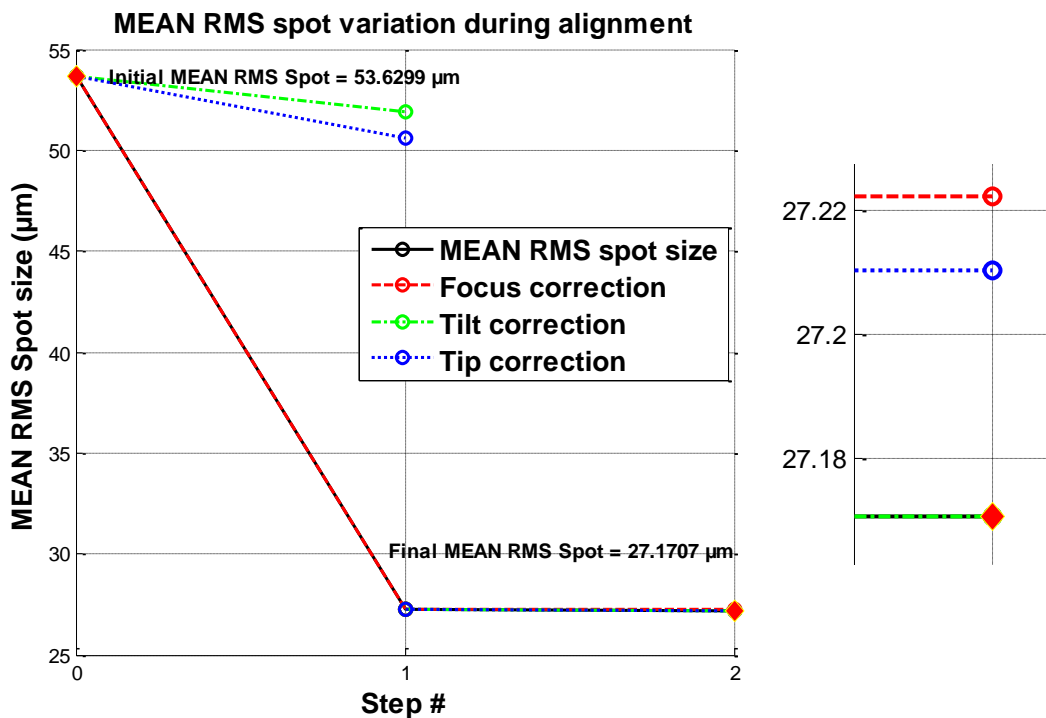


Figure 4.24 - Mean RMS spot evolution through the different paths investigated by the algorithm

Figure 4.25 introduces the evolution of both the mean RMS spot, i.e. the function of merit, and its related standard deviation at each step. The algorithm scans every available compensator at each iteration of the optimization process, obtaining the results depicted in the figures below.

Then, the minimum of the mean RMS spot curve is located for each compensator and a comparison between them is carried out to perform the most suitable movement. In this case, the piston movement is chosen and the next iteration scans start from this updated position of the detector. Since the detector moved along the optical axis by a distance of 0.4 mm, Figure 4.25 (b) is an exact copy of

Figure 4.25 (a), shifted by 0.4 mm along the axis of abscissa. Indeed, the same detector positions are tested except that the starting position has changed: it is now the optimal one with respect to the compensator under consideration. On the other hand, other compensators' curves do change with respect to the first iteration versions. The angular rotations that represent the tip and tilt are now carried out around newly calculated local axes. After each compensation, the detector axes must be recalculated in order to perform the next movements according to the instantaneous position of this component. In this case, all axes are shifted and repositioned at the actual detector centre, their orientation remaining the same. In the case of a rotation movement, the origin of the local axes remains unchanged and their orientation adapts to the selected angular movement.

The standard deviation evolution is also visible in Figure 4.25. Observing the green curve in Figure 4.25 reveals that its minimum does not occur for all compensators at the same location as the mean RMS spot one. However, this happens for the focus compensator at step 1, the compensator that is selected for its best decrease in the function of merit.

This highlights the fact that the standard deviation evolution can be usefully combined to the mean RMS spot to investigate whether it is recommended to perform a given movement. Indeed, thinking about the basic meaning of what the standard deviation stands for brings out some answer to this question. An increase in this parameter value means that the considered data set spreads around its mean value. The effect of the compensator therefore differs from field to field and wavelength to wavelength in this case since the different considered points are located through the entire focal plane.

In other words, one movement may improve the imaging quality at some location and degrade it somewhere else. This behavior must be excluded since a constant resolving power is aimed for over the entire bidirectional focal plane. Indeed, increasing the resolving power at shorter wavelengths to the detriment of longer ones is not sensible, the same holds when considering the upper and lower parts of the slit. This is why the focus movement was selected previously: this movement has a favorable effect over the entire focal plane rather than in a narrow location. Other compensators did not exhibit the same effect.

This conclusion is clarified and confirmed with the help of Figure 4.26 which depicts the evolution of all considered spots with respect to the tested compensators at each step of the optimization process. To ease the differentiation between different locations of the focal plane, a colored sorting with respect to wavelength is carried out. Blue, green and red respectively stand for the shorter, medium and longer wavelengths. Moreover, different symbols are used to distinguish between the upper (triangle pointed upwards), central (circle) and lower (triangle pointed downwards) parts of the entrance slit along the imaging direction.

Figure 4.26 (a) and (b) introduces the effect of a piston movement onto the spot sizes over the entire focal plane. These figures clearly confirm that this movement has a constant effect over the considered points and affect their spot variation in the same way. No distinction can be made with respect to wavelength or slit part, since all colored curves adopt the same behavior no matter the used symbol. The same conclusion cannot be drawn concerning the tip and tilt movements. Indeed, two different behaviors appear: a split between the curves with respect to colors in one case and with respect to the symbol in the other. This can be easily understood by thinking about the original meaning of those movements.

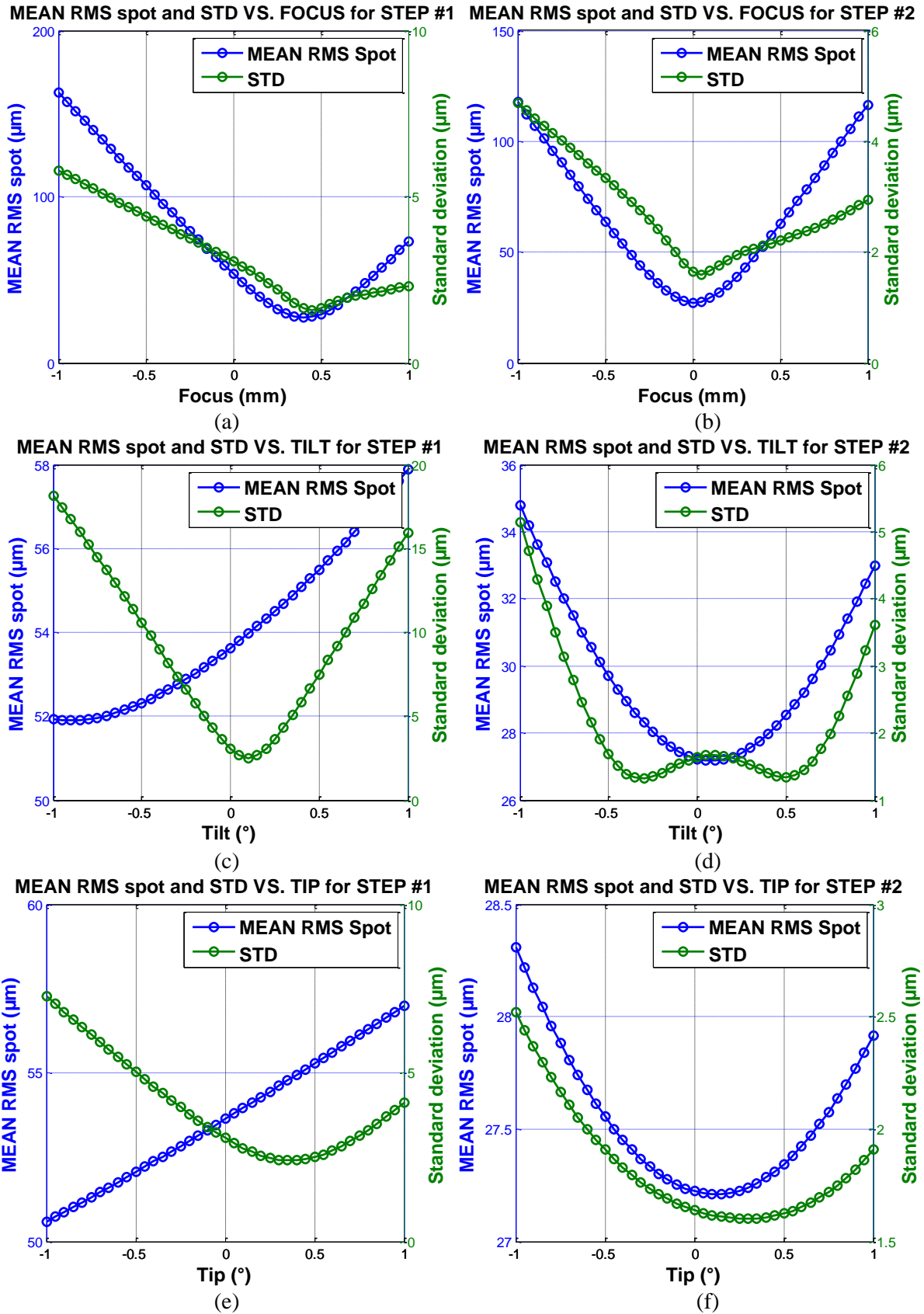


Figure 4.25 - Evolution of MEAN RMS spots and standard deviation vs. focus ((a) and (b)), tilt ((c) and (d)) and tip ((e) and (f)) through focal plane at each step

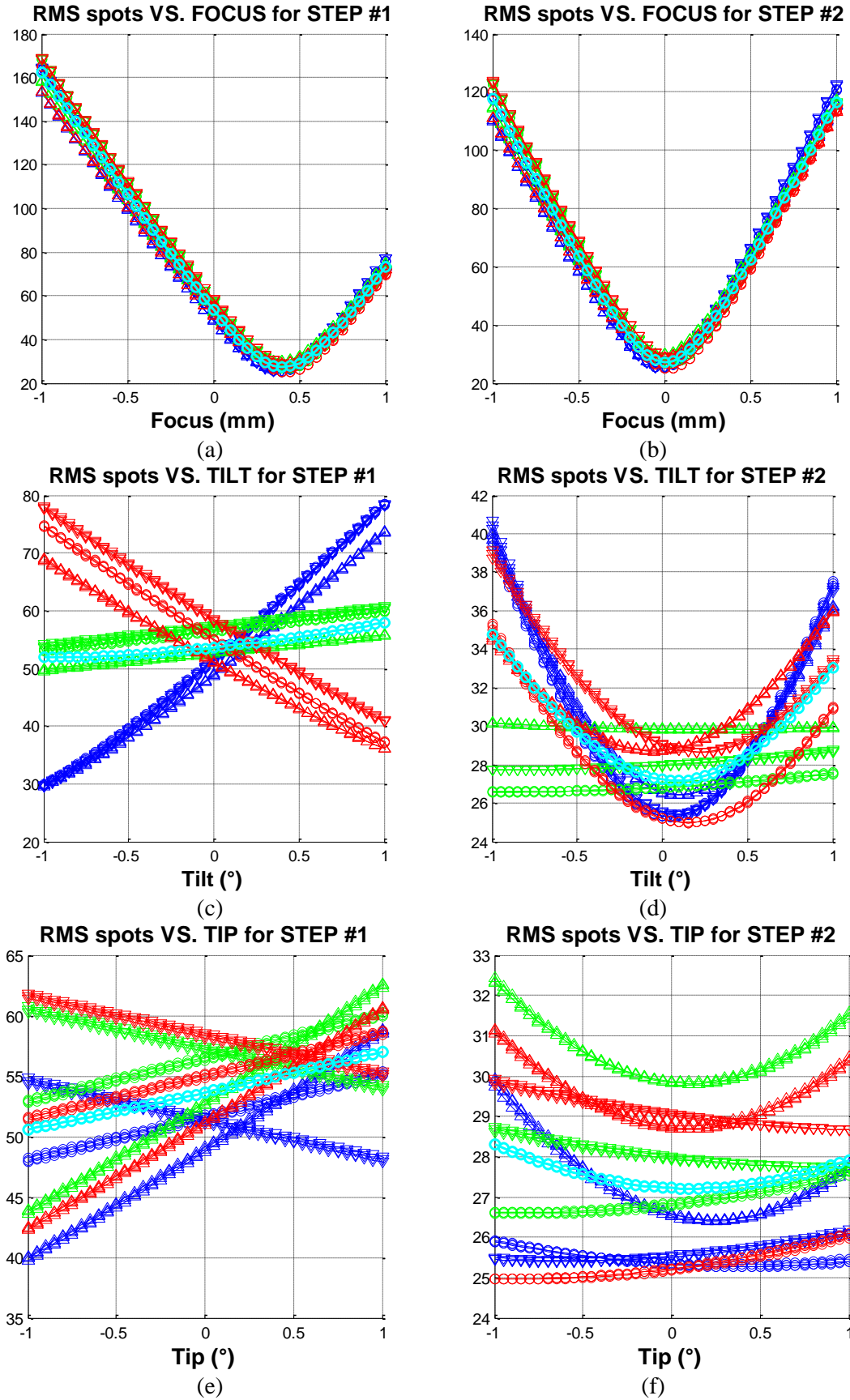


Figure 4.26 – Evolution of RMS spots vs. focus ((a) and (b)), tilt ((c) and (d)) and tip ((e) and (f)) through focal plane at each step

Figure 4.16 previously introduced the definition of the different movements: the tilt rotation is performed around the red local axis of the optical surface, while the tip movement is carried out around the green axis. A tilt movement, before any perturbation, is therefore performed along the length of the slit (its highest dimension) at the centered wavelength. Rotating the detector around this axis will not change the optical quality at this precise wavelength but will perturb it at the sides of the detector, i.e. at shorter and longer wavelengths. Indeed, at these locations, a piston movement is induced by the global rotation of the detector when considering the lever arm.

Figure 4.27 depicts this process; the initial (solid lines) and final (dashed lines) positions of the detector are represented from a “top” view (same view as in Figure 4.7), i.e. in the plane of dispersion, and the induced piston movements can be seen at both ends of this element. Figure 4.26 (c) and (d) confirm this analysis: the differentiation between the curves during step 1 is clearly with respect to wavelength. Since we know that a piston movement is the main reason for imaging quality degradation, it is now easier to understand the differences that exist between Figure 4.26 (c) and (d). In Figure 4.26 (c), the system is out of focus, at all wavelengths. A tilt movement therefore brings back a side of the detector in focus, i.e. a selected part of the imaged spectrum. Depending on the handedness of this rotation, either the shorter or longer wavelengths will come to focus, in this case shorter side benefits from this action. In Figure 4.26 (d), the detector has been put back to its optimal focus position and any tilt movement will equally degrade both longer and shorter wavelengths, as depicted in Figure 4.27. The reason why the central wavelengths is still slightly sensitive to the tilt movement, though it should not, is the fact that this wavelength after perturbation of the system does not remain at the center of the detector since it suffers from a certain amount of shift through its plane. A simple rotation of the grating before starting the initial optimization process would solve this issue.

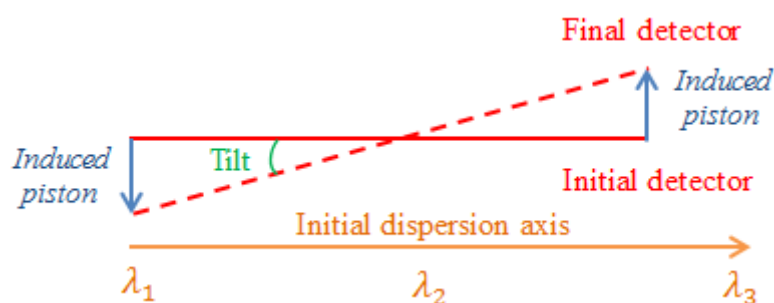


Figure 4.27 - Induced piston at shorter and longer wavelengths after TILT movement

Exactly the same conclusion can be drawn concerning the tip movement. This rotation is performed around an axis located in the plane of dispersion, i.e. the axis of rotation is along the dispersion axis whereas the tilt movement was performed around the imaging direction axis (respectively green and red axes in Figure 4.16). Figure 4.28 depicts the detector movement from a “side” view (oriented along the dispersion axis) onto the slit height. This time the split that occurs in Figure 4.26 (e) and (f) according to the location through the slit height. Therefore, curves with different symbols do not follow the same trend when the tip compensator is actuated. Triangles pointed up and down adopt different behaviors: some are going down whereas the others are going up. As before, the upper (lower) part of the slit comes back to focus when the lower (upper) part goes further away from the in focus position. All wavelengths do follow the same trend since the axis of rotation is the dispersion axis. The previous tilt analysis featured the opposite conclusion: the rotation was performed around the imaging axis along the slit height and all parts of the slit (up, center and bottom) followed the same trend in that case.

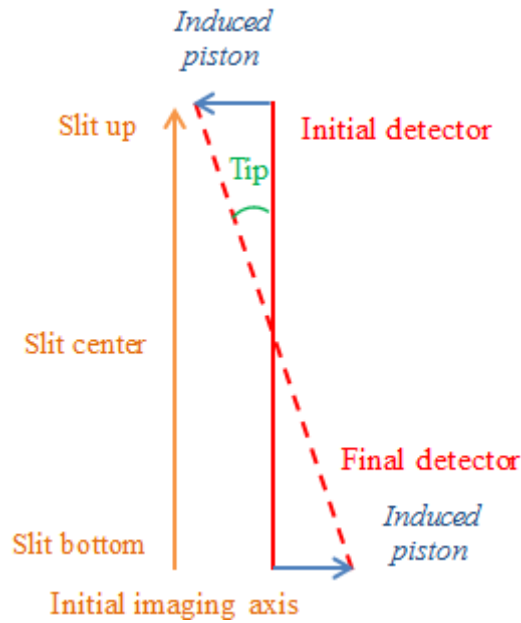


Figure 4.28 - Induced piston at bottom and up of the slit after TIP movement

Eventually, following this piston-tilt strategy leads to a change in resolving power through the focal plane represented in Figure 4.29. The resolving power clearly undergoes an increase in its average value with respect to wavelength and position in slit. The lowest value recorded after alignment approximately rises to 26 000 whereas it was only 18 000 initially. On the other hand, the average resolving power goes from 21 142 to 29 035 thanks to a proper alignment sequence. The alignment procedure clearly improved the imaging capabilities of the optical system.

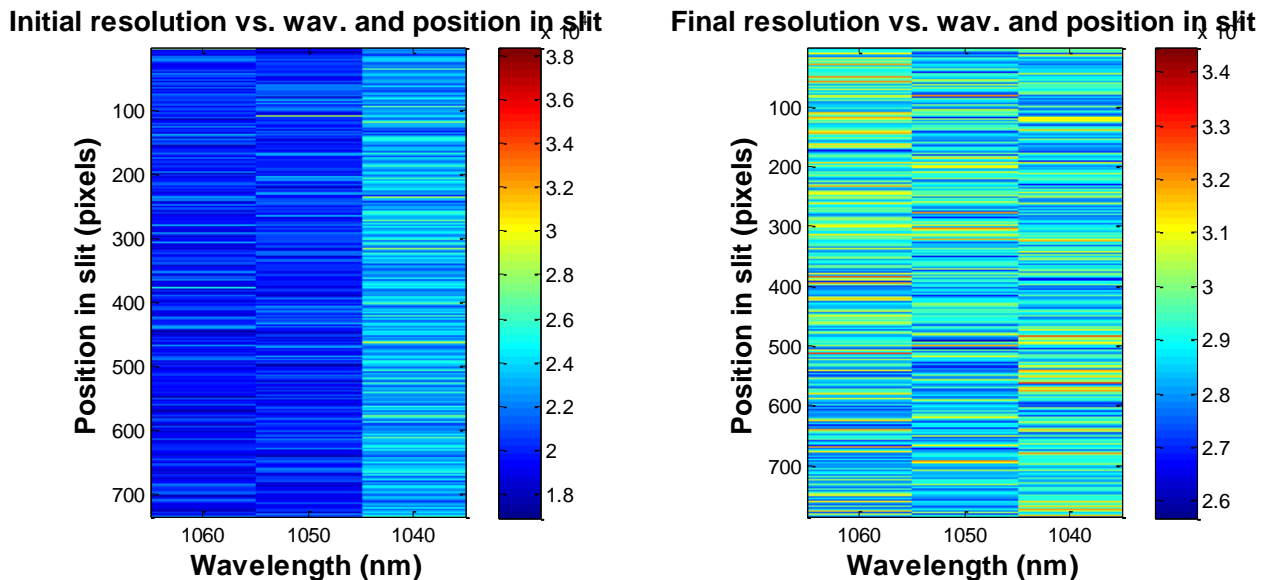


Figure 4.29 - Resolving power through focal plane before (left) and after (right) alignment process

The alignment simulation corroborates the outcomes from the tolerancing analysis and confirms the feasibility of the practical alignment of the instrument. Indeed, starting from a perturbed version of the optical design within defined tolerances, the optimization algorithm was able to reach an equilibrium point and recover its initial optical performances.

This analysis however highlighted the importance of accurately selecting the function of merit under use for optimization. Indeed, the bi-directional focal plane of the spectrograph instrument requires proper imaging quality all over this surface and not only at a specific location. Therefore, the practical alignment process must take into account several wavelengths and fibers while trying to compensate for tolerances. The applied movements must be performed only if they contribute to increasing the resolving power along both dispersing and imaging axes, if not they could lead to undesirable resolution gradients.

4.7 Calibration

4.7.1 Spectral calibration

The calibration of the instrument requires a repeatable source featuring precise spectral lines in order to attribute to each pixel of the detector the correct wavelength. The process consists in illuminating the spectrograph entrance slit with the light of a calibration lamp that features a sufficient number of easily identified spectral lines, with wavelengths that are precisely known. Then, the pixel to wavelength matching is performed with the help of a polynomial fitting yielding a dispersion relation that enables an accurate wavelength calibration of subsequent exposures of stellar spectra.

Typical lamps used for this calibration purpose are hollow cathode lamps (HCL). These lamps are generally made up of a glass tube which contains both an anode and a cathode surrounded by a buffer gas. This latter is ionized and turned into plasma by a large voltage applied between the anode and cathode and then accelerated to eventually extract some atoms from the cathode. Collisions between the plasma and both the buffer gas and the cathode atoms induce excited atoms that will emit light after their decay to lower states. The numerous metal lines that can be generated by such lamps make them highly suitable for precise spectral calibration of high resolution spectrographs while buffer gas lines should be avoided as they are less stable [70]. Indeed, they are usually subject to Doppler broadening and sensitive to the pressure inside the glass tube. Their popularity also arises from their easy handling, relative low-cost, long lifetime and their ability to cover large spectral wavebands by changing their chemical composition [70].

Hollow cathode lamps commonly used for astronomical applications incorporate a buffer gas composed of several atomic species. These are usually made of noble gases in order to avoid the creation of molecules and are characterized by a moderate atomic weight. Argon, Neon or Xenon are more common due to their relatively high ionization energies and operation ease [70]. Typical mixtures involve Thorium and Argon gases when spectral calibration is required for spectrographs operating from the visible to the infrared part of the spectrum. For example, an atlas reporting more than 2400 lines of a Th-Ar hollow cathode lamp is available for the wavelength calibration of the Cryogenic High-Resolution IR Echelle Spectrometer (CRIRES) at the Very Large Telescope [71]. Another atlas that covers the near-infrared spectrum from 1798 to 9180 cm^{-1} (i.e. from 1089 to 5561 nm) is provided by Engleman [72]. Other mixes of gases are also used such as Uranium-Neon when calibrating spectroscopic instruments in the near-infrared. Feasibility studies about using lamps which incorporate uranium as primary source in spectroscopic applications were realized as early as in the late sixties [73]. Atlases reporting spectral lines obtained with such hollow cathode lamps exist [74] [75] and are used as calibration sources for astronomical spectroscopy purposes [76].

Heavy elements such as Uranium or Thorium are usually preferred for the cathode composition. The advantages of those chemical elements in comparison with iron for example are the fact that only one isotope with high abundance exists, they do not exhibit any natural hyperfine splitting, are

characterized by a long half-life time and propose many energy levels to produce a spectrum with many narrow symmetric lines [70]. The choice of using a U-Ne hollow cathode lamp was made in order to calibrate our spectrograph. The selection between a Th-Ar or U-Ne hollow cathode lamp is motivated by the number of high intensity lines in the 1.0–1.1 μm waveband. When looking at Figure 4.30 where the spectra from a Th-Ar (Figure 4.30 (a) [71]) and a U-Ne (Figure 4.30 (b) [74]) hollow cathode lamps are plotted, it can be observed that very strong lines appear in the Th-Ar spectrum between 1060 and 1080 nm for example. These lines completely outshine many fainter ones, whose intensities are much lower, as can be seen when zooming onto the lower part of the intensity axis (see Figure 4.30 (a) bottom). This situation will likely lead to saturation of the detector for the strongest lines, while leaving the weaker ones badly underexposed. On the other hand, Figure 4.30 (b) reveals the same part of the spectrum that is produced by a U-Ne lamp this time. Though some strong lines are still present, their relative intensities compared to the weaker lines are much less extreme compared to the Th-Ar lamp. Another technical reason why Uranium is preferred is the lack of pure Thorium availability in today's market. Thorium oxide is more common nowadays and molecular lines can now be observed by high-resolution spectrographs while Uranium HCLs do not induce such artifacts [70].

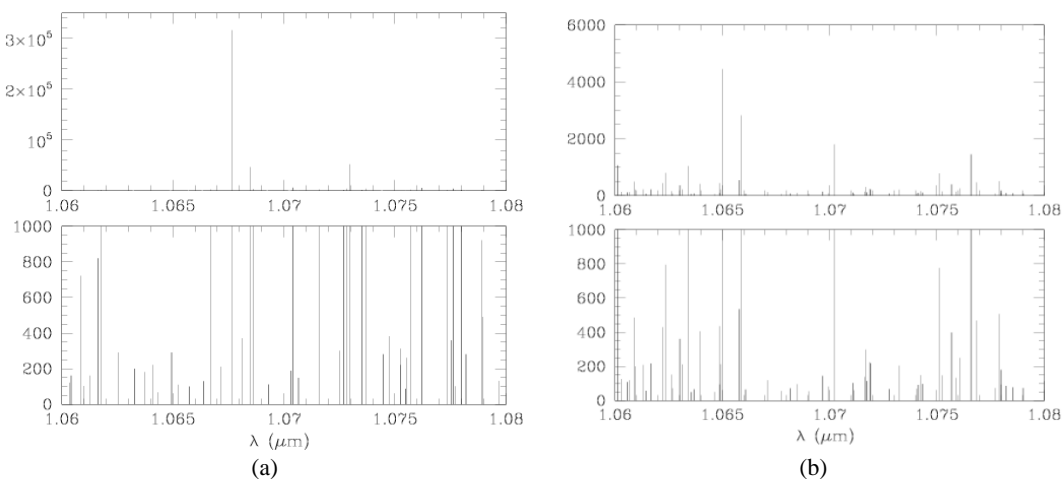


Figure 4.30 - Th-Ar spectrum [71] between 1060 and 1080 nm (a) and same part of the spectrum obtained from a U-Ne lamp [74] (b). Bottom parts of both figures are zooms from upper ones obtained when limiting the intensity y-axis.

4.7.2 Flat-field calibration

Flatfield calibration consists in correcting astronomical images for the pixel to pixel variation in sensitivity. Illuminating the spectrograph with a known continuum source enables measuring those fluctuations and leads to the so-called flat-field image.

The required lamp to perform such a calibration must therefore exhibit a continuous spectrum over the considered waveband of interest, i.e. from 1 to 1.1 μm . Typical halogen lamps are used to flat-field near-infrared spectrographs as it is the case for the K-band multi-field spectrograph (KMOS) currently installed at the VLT [77]. A halogen lamp is therefore selected as a flat-field calibrator for the proposed spectrograph instrument.

4.7.3 Practical implementation of the calibration box

The calibration unit of the instrument is located near the fiber entrance and features two illuminated mechanical entrance slits positioned at symmetrical places with respect to a beamsplitter (see Figure 4.30). A moving folding mirror is employed to enable light selection either from the calibration box or the observed target. The folded path of light connects the output end of the fiber to

the collimator when the mirror stands in its down position. When calibrating, the moving mirror moves upwards and the light from the calibration box illuminates the collimator. The beamsplitting element is used to collect light from both lamps and inject it to the collimating mirror and performs either the spectral or flat-field calibrations.

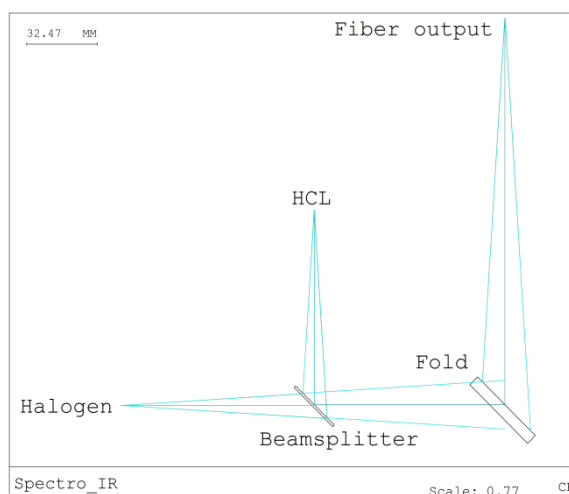


Figure 4.31 - Calibration unit optical design. Light coming from the output end of the fiber reaches a moving fold mirror when positioned in its down position and is injected to the collimating mirror during observation (right to the fold mirror, not represented in the figure). When calibrating, the moving mirror moves upwards and light from the calibration lamps is gathered with a beamsplitter and eventually goes to the collimator.

To move the folding mirror in and out of the calibration light beam we first considered a flipping mechanism. The mechanical repeatability of this component is however not sufficient to achieve the calibration accuracy needed to fulfill the scientific requirements (see Table 1.1). Indeed, a rough repositioning of the mirror after calibration induces a shift in wavelength measurement that must be avoided for precise calibration of stellar spectra. The comparison of the two components is represented in Figure 4.32.

Light is first injected through the fiber channel when the moving mirror is settled within its maximum positioning error. Calibration is then performed through the HCL path and the detected wavelength is measured along the entire slit length with the help of the polynomial dispersion relation. The measured wavelength profile over the exit slit height is altered since the HCL and fiber channels are not perfectly superposed. Typically, the entire profile shifts vertically, which induces a wavelength offset in measurements. Figure 4.32 (a) [respectively (b)] illustrates the simulation results when taking into account the accuracy of the flipping mechanism (respectively the translation stage).

The calibration precision specified in the scientific requirements states a value of $\delta\lambda/20$. Figure 4.32 (a) immediately proves that the mechanical repeatability of the flipping component cannot reach such a precision. Indeed, the measured shift in wavelength amounts to 2.25 times the requirement and thus the mean detected wavelength does not fall inside the acceptance zone defined by the two horizontal green lines. On the other hand, the translation stage precision leads to a wavelength error of 0.1 times the specified maximum value and the mean detected wavelength, represented by a red line, is located in the tolerated error interval (see Figure 4.32 (b)).

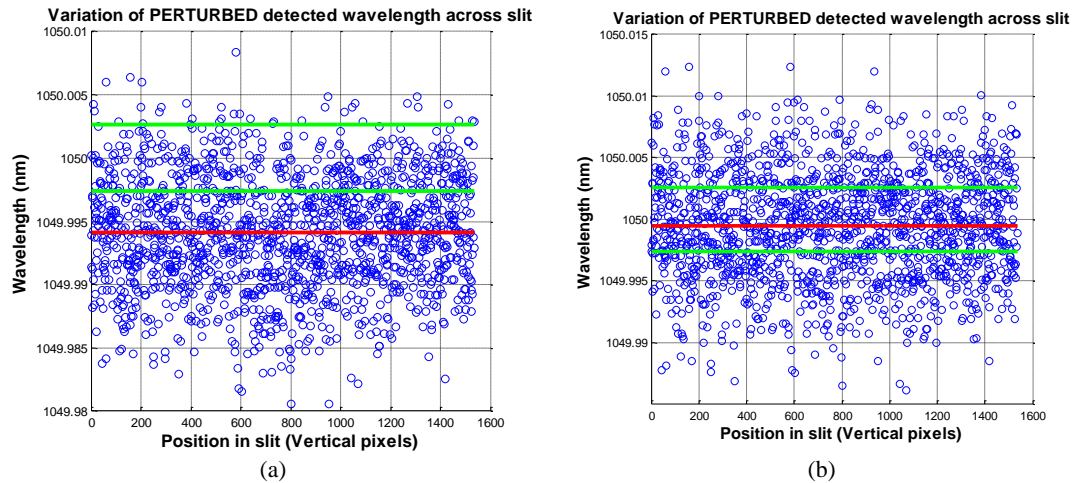


Figure 4.32 - Detected wavelength along the slit length when taking into account the error on the repeatability of the flipping mechanism (a) and of the translation stage (b). The horizontal red line represents the mean detected wavelength and the two green ones are located at plus and minus the calibrating requirement from the exact injected wavelength.

4.7.4 HCL slit illumination system

As noticed by Huke et al., the light distribution within an HCL is pretty complex as many different paths coexist. Indeed, light is emitted from different regions between the cathode and the anode with their own spectral characteristics [70]. These light beams show different angular characteristics as well as flux disparities which complicate the coupling efficiency of an HCL with a mechanical slit or a fiber. Huke et al. deeply studied off-the-shelf HCLs and developed an optical scheme which maximizes the metal-to-gas line-strength ratio to benefit from as much metal lines as possible. The goal is to collect the light from regions where metallic atoms, emitting stable and usable spectral lines, are excited. This optical setup therefore tends to avoid the usually high intensity buffer gas lines that pollute and may saturate the calibration spectra.

The light-emitting region from HCL's cannot be considered as a point source but is rather spread in all three dimensions, which makes its emitted pattern quite complex [70]. The optimal setup they developed consists in using a collimating lens close to the front window of the HCL to collect the central beam emitted by the cathode. This light portion of the whole pattern is in majority made of metal lines and of high importance for accurate spectral calibration of spectrographs. Wider beams originate from other regions between the cathode and the anode and contain a high amount of gas lines. These ones need to be filtered out as they do not favorably contribute to the spectrograph calibration. A second lens is then employed to focus the filtered light beam onto the spectrograph entrance port.

In our case, since the calibration box is located within the spectrograph enclosure, the calibration aperture that must be lit is a mechanical slit whose dimensions are $0.5 \times 10 \text{ mm}$. This elongated format asks for an asymmetric illuminating element instead of the original achromatic lens. For a more efficient illumination of the entrance slit, a cylindrical mirror is thus selected. The coupling efficiency increases since the original circular spot becomes rectangular and more light is transmitted through the slit (see Figure 4.33).

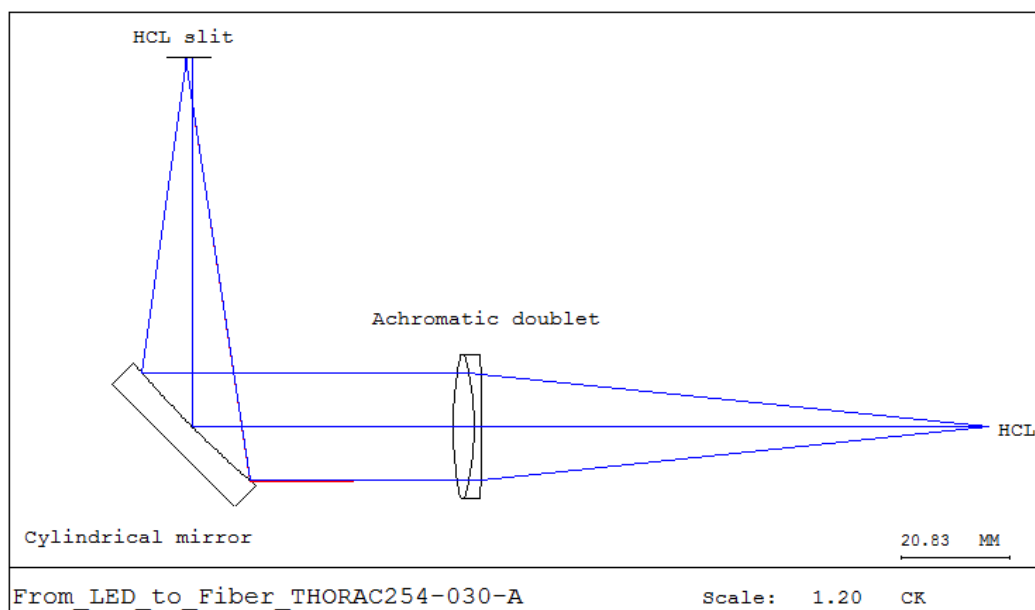


Figure 4.33 - Optical design of the HCL slit illumination system

One important point underlined by Huke et al. is that this optical scheme maximizes the metal-to-gas line-strength ratio with no particular attention on flux transmission. This geometrical configuration optimizes the metal line affluence and does not ensure the maximum photon flux transmission from the HCL to the mechanical slit [70]. Indeed, the goal of the study is to propagate as much useful photons as possible and mitigate the pollution from others by filtering unwanted light paths.

4.7.5 Calibration stability vs. scrambling gain

The scrambling properties of fibers were introduced in Chapter 2.4.2. As a reminder, the scrambling behavior of a fiber develops both azimuthally and radially. The focus is on the radial component of this mechanism in this section. Light propagating within the fiber through several modes loses, to some extent, its memory concerning its original impacting point on the fiber entrance plane. The output light pattern becomes then independent of any input beam movement.

Experimental results however show that radial scrambling is not complete [42] [43] [45] [48] [1]. Demanding applications with respect to calibration precision may therefore suffer from varying seeing and telescopes' lack of pointing stability. Even though radial scrambling of fibers is imperfect, using a mechanical slit is a worse option. Fibers represent a proper way to isolate with high efficiency the spectrograph from several perturbations which negatively affect the calibration accuracy.

Improving the radial scrambling of fibers may also be an easy task. Slightly bending a fiber, which inevitably increases its FRD losses, decreases its radial memory. Scrambling is also affected by stress: the behavior of a given fiber differs at rest and under stress [1]. Therefore, perturbing a fiber may lead to non-negligible advantages with respect to calibration stability at the detriment of light transmission. Indeed, the trade-off between FRD and scrambling was already approached in Chapter 2.4.2 where the conclusion was that optimal conditions for better calibration accuracy or photometric budget are opposite.

The scrambling gain of an optical fiber measures the sensitivity of its emitted pattern with respect to perturbations applied to its illumination conditions. More precisely, it is a measure of the stability of a spectral resolution element in relation to the geometric alterations of the star image falling onto the fiber entrance [1]. It is expressed as follows

$$G = \frac{d/D}{s/FWHM} \quad (12)$$

where

- d is the displacement of the star image,
- D the aperture of the fiber optic,
- s the shift of the spectral resolution element,
- $FWHM$ the full width at half maximum of this spectral resolution element.

Typical scrambling gain values of 120 are reached by 3 m long 60 μm fibers when they are at rest and illuminated by a light beam at $F/2.5$. This value increases up to 500 when bending is applied while FRD losses rise by 20%. On the other hand, larger core fibers (600 μm) see their scrambling gain affected by a factor 20 under moderate stress conditions [1]. Avila et al. actually showed that the scrambling gain grows proportionally with the fiber diameter and its numerical aperture [78].

In order to assess the impact from scrambling properties on the calibration of the instrument under study, the evaluation of the required scrambling gain is carried out. In first assessment, the seeing is considered as constant all over the duration of the observation as these will last several minutes and seeing predictions are complex. The tracking accuracy is on the other hand considered here as a contributor to fiber illumination alterations. The specified tracking accuracy of the TIGRE telescope is said to be better than 0.2"/min, which equals to a drift through the focal plane of approximately 9.31 $\mu m/min$ [18]. In order to fulfill the requirements on calibration accuracy, the maximal spectral shift of the resolution element s should be less than $\delta\lambda/20$ (see Table 1.1). The required scrambling gain to fulfill these requirements can then be calculated since the displacement of the star image d is known ($d = drift_{tel} \cdot t_{int}$), the fiber aperture is 50 μm and the FWHM of the instrument is approximately equal to 0.036 nm according to the resolution analysis.

The evolution of the spectral shift s with respect to the scrambling gain G is calculated using Eq. (12) and depicted in Figure 4.34. Integration times of 1 min, 10 min and 30 min are simulated and the maximum spectral shift is depicted (dotted line). As can be seen, the required scrambling gain ranges from 2.74 for a 1 min-integration time to 82.28 when observing the target half an hour. The required scrambling gain is therefore rather limited when comparing to typical values that were presented before. However, the selected fiber has a rather small core (50 μm) and reduced numerical aperture (0.12) which does not participate to scrambling gain increase. Its moderate length of 15 m should however be sufficient to produce the required light mixing and enable accurate calibration measurements.

The considered integration times may be higher than those permitted in reality since the fiber core is only 50 μm in diameter. A repositioning of the star image onto the fiber will be required if the drift in tracking accuracy reaches the considered value for these calculations.

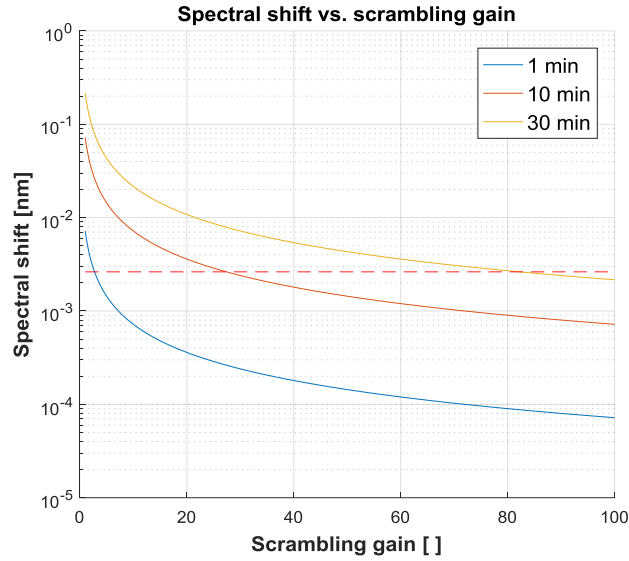


Figure 4.34 - Evolution of spectral shift with respect to scrambling gain

4.8 Crosstalk

The crosstalk analysis intends to investigate the maximum number of fibers the bundle can incorporate without threatening any mixing of spectra at the focal plane of the spectrograph. This leads to the specification of a minimum spacing between fibers to also enable a proper sky subtraction. The image of two adjacent fibers is studied to identify the minimum jacket diameter that fibers should exhibit to avoid insufficient spacing.

A first ray tracing is carried out with a focal plane paved by $25 \mu\text{m}$ pixels, the average size of typical NIR detectors. The results are shown in Figure 4.35 where the left panel is the focal plane image of the two adjacent fibers and the profile over the imaging direction is plotted in the right panel. These data are obtained with a fiber inter-distance of $140 \mu\text{m}$, which is the minimum one that enables dark pixels to be located between the fiber signals. This way, fiber spectra do not mix up and a proper spectrum extraction can be performed. The maximum number of fibers than can be allocated through the 10 mm long entrance slit is then equal to 71.

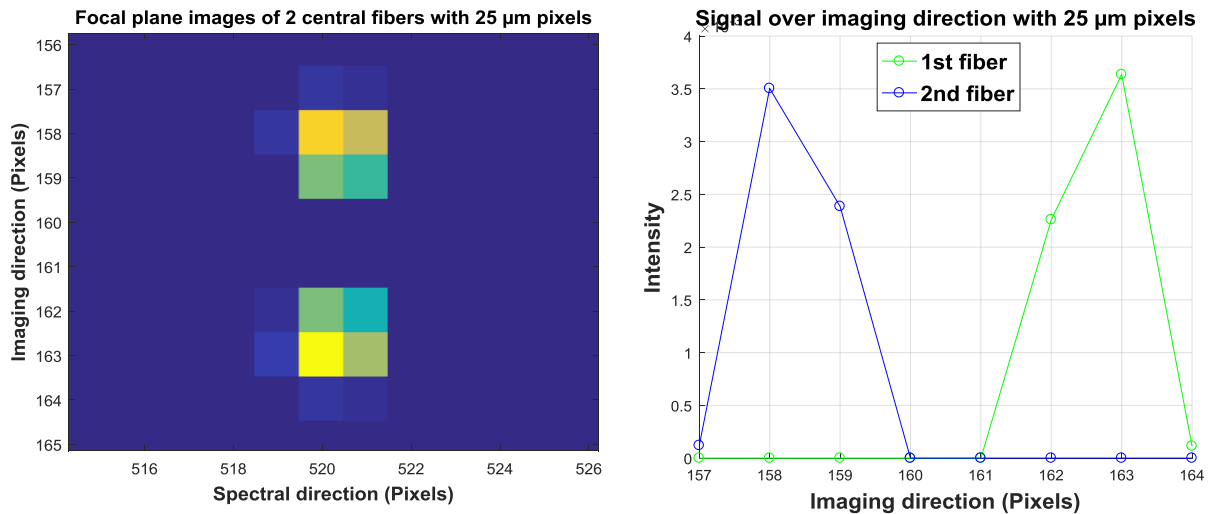


Figure 4.35 – Focal plane image of two central fibers (left) and profile of light intensity along imaging direction (right) with $25 \mu\text{m}$ pixels

The same analysis is carried out when using $15\ \mu\text{m}$ pixels, the same size as those in the selected detector. The results obtained are presented in Figure 4.36 with a jacket diameter of $100\ \mu\text{m}$ which is the minimum distance fiber cores must be apart from each other to avoid any signal mixing. With this jacket diameter, 100 fibers can be distributed over the entrance slit without any risk of the star spectrum to be polluted by other sources. An important remark is that the jacket diameter is usually fixed by manufacturing limitations. Fiber strength is an important factor that may set a lower limit on this parameter and the number of fibers may therefore be affected for such reasons.

The selected bundle of Figure 2.24 contains 15 fibers whose total diameter is equal to $140\ \mu\text{m}$ (core, cladding and jacket included) which is the minimum one allowed when using $25\ \mu\text{m}$ pixels. This bundle may therefore be used in combination with pixels of $25\ \mu\text{m}$ that are very common in near-infrared scientific cameras.

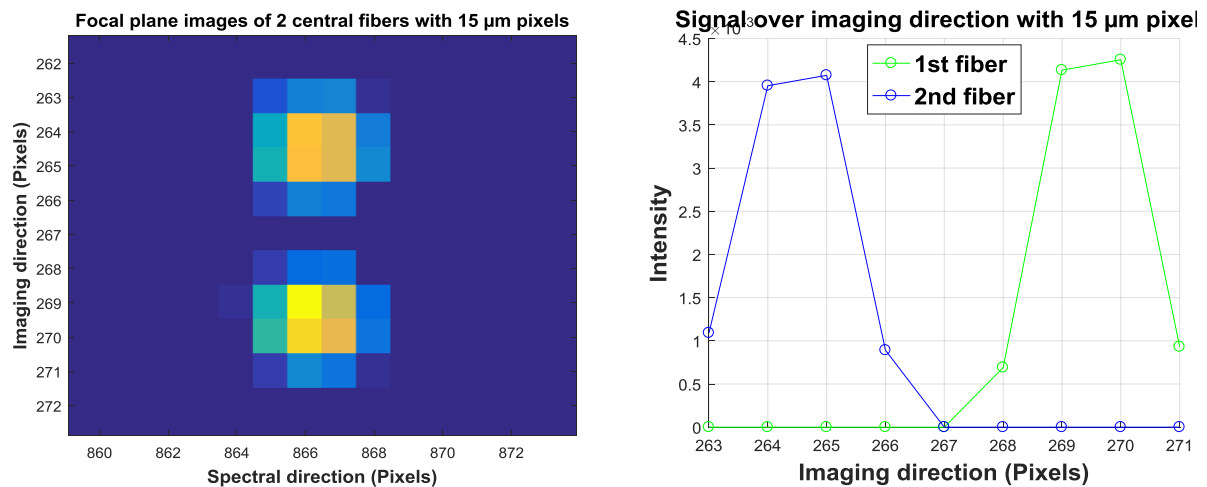


Figure 4.36 - Focal plane image of two central fibers (left) and profile of light intensity along imaging direction (right) with $15\ \mu\text{m}$ pixels

4.9 Straylight analysis

The straylight analysis intends to identify and mitigate potential unwanted paths of light reaching the detector that may cause blurred images or decrease the signal-to-noise ratio for example. The interaction between the optical design and its surrounding instrument walls is considered here to account for any multiple reflection paths. Eventually, this analysis leads to the design of suitable internal panels that aim at blocking these straylight sources.

A particular care is given to the out-of-band wavelengths, i.e. the ones that vignette and reach the detector after a few reflections onto the instrument walls. Their propagation through the system is stopped with the help of a specific enclosure around the detector which selects the waveband of interest.

Direct paths from the calibration lamps are also prohibited and an accurate shielding is required to cope with the wide opening angle of the light cone emitted through the entrance slits. The design of the internal calibration unit thus includes many separation walls in order to discard as much unwanted light as possible and prevent it from escaping from this part of the instrument. Specifically sized apertures also limit the angular size of the emitted calibrating beam of light.

On the other hand, the zeroth diffraction order from the grating may also lead to problems. This polychromatic reflected path of light may be of high intensity and reach the detector after several interactions with the instrument walls. In our design, the rays from this straylight source follow trajectories that impact to the left side of the calibration unit where an internal panel is added to form a light trap (see Figure 4.37).

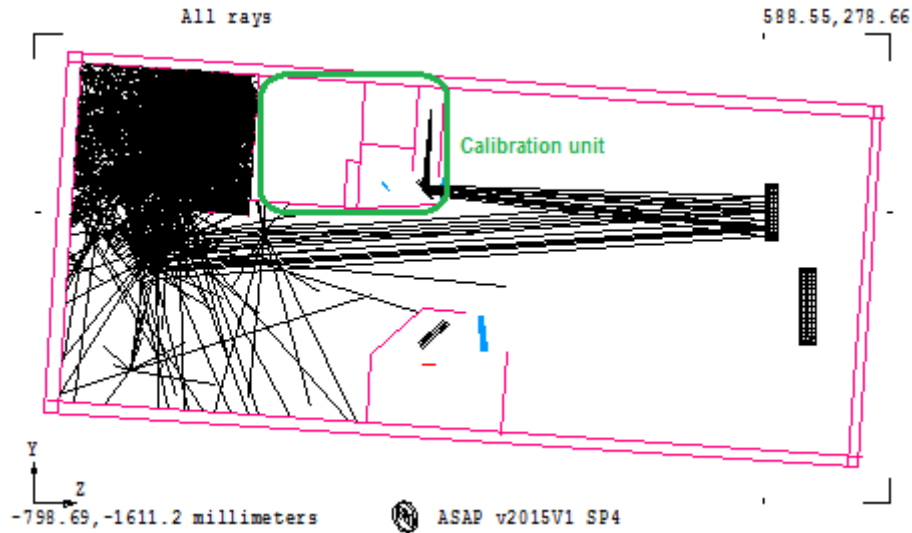


Figure 4.37 - Propagation of the rays from the grating zeroth diffraction order. Light is confined at the top left after hitting the walls of the calibration unit compartment and does not reach the detector.

The ghost generated from the toroidal lens imperfect transmissivity is also studied. This second order ghost image is formed between the folding mirror and the toroidal lens. This therefore induces a divergent beam onto the detector after being reflected onto the folding mirror. Considering that an anti-reflective coating is applied on both sides of the lens, only a negligible pale veil spreads over the detector due to the internal reflections that occur through the lens.

Those considerations lead to the instrument mechanical enclosure that is shown in Figure 4.37. This latter features a rectangular shape into which several internal panels are included to isolate the calibration unit and the detector from multiple reflection paths. A light trap is also located next to the calibration unit to attenuate the reflected light from the grating. Eventually, grazing incidence is avoided as much as possible since this configuration may lead to the collection of photons escaping from an imperfectly collimated beam for example.

4.10 Conclusion

The optical design of the instrument started from a blank sheet. Scientific requirements were available to drive its conception. Basic considerations on these specifications enabled to derive several first-order parameters such as the required dispersion and number of detector pixels. The entire derivation of the spectrograph parameters required further investigations. Indeed, Bingham highlighted the fact that a spectrograph can be fully described by 16 parameters [58]. Their evaluation is therefore not trivial. However, some may be fixed by external constraints or evaluated in first order. The problem can then be simplified to the resolution of a system of 7 equations involving 7 parameters. This methodology was used to formulate more precise guidelines on the spectrograph characteristics. Practical limitations were faced and alternative resolving paths were consequently investigated.

Once the overall description of the instrument finalized, the optimization process of the design started. This conception step required selecting an optical configuration for the spectrograph. The associated possibilities for the aberration mitigation were also identified. After having selected the most suitable option for the present research project, the optimization of the instrument optical quality could be initiated. Analyses were developed to assess the resolving power of the instrument and the optimization function of merit was based on these evaluations.

After having obtained satisfying optical imaging performances, the robustness of the obtained design had to be checked. Alignment and manufacturing perturbations were therefore applied and their respective consequences on the imaging quality recorded. The so-called sensitivity matrix summarized these degradations. Several coupling effects were then identified to illustrate potential parameters that could be tuned to compensate for sensitive elements. The detector focus was also proposed as the final compensator to optimize the instrument performances. Eventually, an overall budget incorporating all tolerances was carried out to statistically evaluate the potential imaging quality of the spectrograph.

The next optical analysis focused on the alignment simulation. The proposed alignment loop was introduced. The figures of merit that constitute the driving criterion to complete the alignment scheme were presented. The results highlighted the importance of evaluating the performances through the whole detector plane. This means verifying that the performed alignment actions benefit to the spot size reduction along both imaging and dispersion axes. Otherwise, resolving power gradients may appear and the spectrum quality would vary as a function of the selected detector region. In order to avoid such issues, the polychromatic behavior of the instrument must be assessed while trying to improve its performances.

The conception of the calibration unit was then illustrated. Both spectral and flatfield operations were explained. The lamp selection was also justified such as the composition of the hollow cathode lamp that maximizes the line abundance in the near-infrared region. The stability of the translation stage was also investigated.

The crosstalk analysis intended to identify the maximum number of fibers the system could accommodate. This latter is indeed limited since a minimum distance between two subsequent fibers is required to avoid any inter-pollution.

The straylight analysis eventually highlighted the need for a proper mitigation of unwanted signals within the instrument. These originate from light leakages outside the nominal photon path and contribute to degrading the instrument signal-to-noise ratio. Moreover, they may create second order images and interfere with the scientific signal. Solutions were found to either attenuate the intensity or isolate those photons and prevent them from reaching the detector plane.

Chapter 5

Photometric budget

5. Photometric budget

5.1 Introduction

When designing an optical instrument, a photometric budget is needed to investigate whether enough flux reaches the detector. Indeed, the scientific requirements ask for a given signal-to-noise ratio (SNR) within typical observation times. This calculation has to take into account several factors such as, for example, the incoming flux from the observed star, vignetting of the instrument and quantum efficiency of the detector. The resulting photon flux on the detector is then compared to the level of noise to evaluate the signal-to-noise ratio and check whether the optical design fulfills the requirements.

5.1.1 Instrument requirements

Scientific requirements concerning the performances of the spectrograph have been formulated and they were previously used to derive instrument specifications for the optical design. Other specifications are also stated concerning the signal-to-noise ratio that the instrument has to fulfill. Table 5.1 summarizes the scientific requirements that have been stated for the spectrograph.

	Requirement	Goal
Target magnitudes	$J < 7$	$J < 9$
SNR in continuum (30 min exposure @ TIGRE telescope)	100 @ $J = 6$	100 @ $J = 7$
Typical exposure time	30 min	15 min

Table 5.1 - Instrument requirements

5.2 Stellar radiometric budget

Establishing the overall radiometric budget requires first to evaluate the star's photon flux in the waveband of interest. To do so, a few reminders are first necessary. Let us start by defining the *absolute magnitude* of a star in a given filter W as:

$$M_W = m_W - DM - A_W \quad [mag]$$

where $DM = 5 \log d - 5$ is the *distance modulus* and d the actual distance of the star (in *parsec*). Within this expression are also involved A_W , the interstellar extinction as equivalent magnitudes, and the *apparent magnitude* of the star, all in filter W . Knowing those parameters, one can then assess the *bolometric magnitude* of a star, i.e. its energy output over the entire electromagnetic spectrum, by means of bolometric corrections evaluated with the help of model atmosphere codes:

$$M_{bol} = M_W + BC_W \quad [mag]$$

Once the bolometric magnitude is known, one can calculate the *bolometric luminosity* of a star by using:

$$\begin{aligned} L_{bol} &= 3.03 \cdot 10^{35} \cdot 10^{-0.4 M_{bol}} = 3.03 \cdot 10^{35} \cdot 10^{-0.4 (m_W - DM - A_W + BC_W)} \\ &= 3.03 \cdot 10^{35} \cdot 10^{-0.4 (m_W - A_W + BC_W)} \cdot 10^{0.4 (5 \log d - 5)} \\ &= 3.03 \cdot 10^{35} \cdot 10^{-0.4 (m_W - A_W + BC_W)} \cdot 10^{\log d^2} \cdot 10^{-2} \end{aligned}$$

$$= 3.03 \cdot 10^{33} \cdot 10^{-0.4(m_W - A_W + BC_W)} d^2 \quad [erg \ s^{-1}]$$

Then, if the stellar spectra can be approximated as a black body, Planck's function can be used to describe its spectral energy distribution:

$$B_\lambda(T_{eff}) = \frac{2 h c^2}{\lambda^5} \frac{1}{\exp\left(\frac{h c}{\lambda k T_{eff}}\right) - 1} \quad [erg \ s^{-1} \ cm^{-2} \ sr^{-1} \ \text{\AA}^{-1}]$$

A small waveband $d\lambda$ then emits an amount of energy equal to $d\epsilon = B_\lambda d\lambda$ and the integral of this quantity over the full electromagnetic spectrum is equal to $\sigma T_{eff}^4/\pi$. Considering a star of bolometric luminosity L_{bol} , one can evaluate the emitted flux over a small wavelength range at a distance d with zero interstellar absorption:

$$\begin{aligned} d\mathcal{F} &= \frac{L_{bol} B_\lambda d\lambda \pi}{4 \pi d^2 \sigma T_{eff}^4} \\ &= L_{bol} \frac{2 h c^2 d\lambda \pi}{\lambda^5 4 \pi d^2 \sigma T_{eff}^4} \frac{1}{\exp\left(\frac{h c}{\lambda k T_{eff}}\right) - 1} \\ &= L_{bol} \frac{h c^2 d\lambda}{2 \lambda^5 d^2 \sigma T_{eff}^4} \frac{1}{\exp\left(\frac{h c}{\lambda k T_{eff}}\right) - 1} \quad [erg \ s^{-1} \ cm^{-2}] \end{aligned}$$

Therefore, the number of incident photons amounts to

$$\begin{aligned} dN &= \frac{d\mathcal{F} \lambda}{h c} \\ &= L_{bol} \frac{h c^2 \lambda d\lambda}{h c 2 \lambda^5 d^2 \sigma T_{eff}^4} \frac{1}{\exp\left(\frac{h c}{\lambda k T_{eff}}\right) - 1} \\ &= \frac{c L_{bol} d\lambda}{2 d^2 \sigma T_{eff}^4 \lambda^4} \frac{1}{\exp\left(\frac{h c}{\lambda k T_{eff}}\right) - 1} \\ &= \frac{3.03 \cdot 10^{33} \cdot 10^{-0.4(m_W - A_W + BC_W)} d^2 c d\lambda}{2 d^2 \sigma T_{eff}^4 \lambda^4} \frac{1}{\exp\left(\frac{h c}{\lambda k T_{eff}}\right) - 1} \\ &= \frac{3.03 \cdot 10^{33} c}{2 \sigma} \frac{10^{-0.4(m_W - A_W + BC_W)} d\lambda}{T_{eff}^4 \lambda^4} \frac{1}{\exp\left(\frac{h c}{\lambda k T_{eff}}\right) - 1} \quad [ph \ s^{-1} \ cm^{-2}] \end{aligned}$$

The photon flux, expressed in *photons* $s^{-1} \ cm^{-2}$, is then calculated with

$$dN = \frac{8.412 \cdot 10^{34} \cdot 10^{-0.4(m_W - A_W + BC_W)} d\lambda}{T_{eff}^4 \lambda^4 \left(\exp\left(\frac{1.439 \cdot 10^8}{\lambda T_{eff}}\right) - 1\right)} \quad [ph \ s^{-1} \ cm^{-2}]$$

when expressing the wavelength in \AA .

Eventually, this relation has to be corrected for the interstellar absorption at the considered wavelength as follows

$$dN = \frac{8.412 \cdot 10^{34} \cdot 10^{-0.4(m_W - A_W + BC_W + A_\lambda)} d\lambda}{T_{eff}^4 \lambda^4 \left(\exp\left(\frac{1.439 \cdot 10^8}{\lambda T_{eff}}\right) - 1 \right)} \quad [ph \ s^{-1} \ cm^{-2}] \quad (13)$$

The photon flux per wavelength unit dN_λ will rather be used in the following calculation:

$$dN_\lambda = \frac{8.412 \cdot 10^{34} \cdot 10^{-0.4(m_W - A_W + BC_W + A_\lambda)}}{T_{eff}^4 \lambda^4 \left(\exp\left(\frac{1.439 \cdot 10^8}{\lambda T_{eff}}\right) - 1 \right)} \quad [ph \ s^{-1} \ cm^{-2} \ \text{\AA}^{-1}] \quad (14)$$

Finally, the number of photons detected per second at the focal plane is equal to

$$dN_{tot} = dN_\lambda d\lambda T_{atm} A_{tel} \eta_\lambda f_\lambda \epsilon \quad [ph/sec]$$

where

- $d\lambda$ is the wavelength sampling of a pixel at the spectrograph focal plane [\AA]
- T_{atm} is the atmospheric transmission at the considered wavelength
- A_{tel} is the effective collecting area of the telescope (accounting for secondary obstruction) [cm^2],
- η_λ is the total throughput efficiency of the instrument,
- f_λ is the factor of binning in the detector realized during read-out along the axis of dispersion. We consider here $f_\lambda = 1$, i.e. no binning in this direction,
- ϵ is the fraction of the total signal of the star taken into account at the time of the numerical binning in the spatial direction to build the spectral profile (binning along the direction perpendicular to dispersion). We consider here that the binning is sufficiently broad to integrate all stellar flux, therefore $\epsilon = 1$. Otherwise, $\epsilon = p/N_{pix}$ where N_{pix} is the number of pixels onto which the star image lies and p the amount of binned pixels (see Figure 5.1).

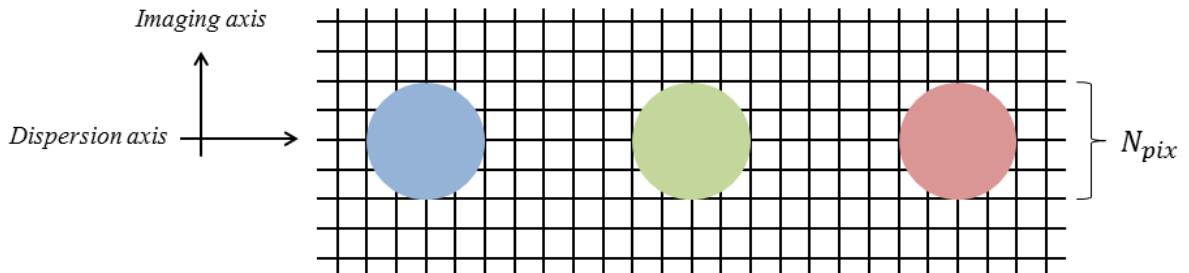


Figure 5.1 – Star image footprint at a spectroscopic instrument's focal plane

5.3 Interstellar absorption models

The requirements ask for a given signal-to-noise ratio at a selected magnitude in the J-band. Therefore, a suitable model for the extinction A_λ should be used. This parameter has to be expressed in terms of an extinction value. For example, we can use the relationship presented below [79]:

$$A_\lambda = 2.4 \lambda^{-1.75} E(J-K) \quad (\lambda \text{ in } \mu\text{m})$$

where $E(J-K)$ is the color excess of the color index $J-K$. Then, the color excess $E(J-K)$ is linked to the interstellar extinction in the V band A_V through the following relation:

$$E(J-K) = 0.172 A_V$$

On the other hand, Eq. (14) also involves the interstellar absorption in the J band. This parameter can be expressed in terms of A_V through the following relation:

$$A_J = 0.29 A_V$$

Fixing the parameter A_V is therefore sufficient to evaluate $E(J-K)$, A_λ and A_J . Different values of A_V are scanned through in the following analyses to investigate different absorption scenarii.

Eventually, the bolometric correction in J-band can be correlated to the effective temperature through the law that is depicted in the figure below (cool stars on the left [80] and hot stars on the right [81] [82]).

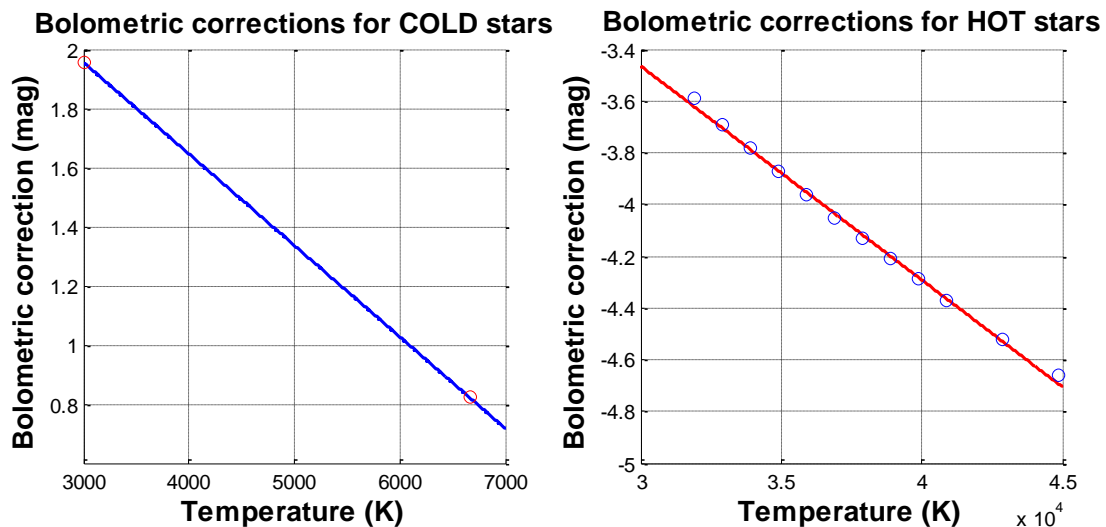


Figure 5.2 - Bolometric correction in J-band (*left*: cool stars [80], *right*: hot stars [81] [82])

5.4 Atmospheric transmission

The atmospheric transmission in the range $1-1.1 \mu\text{m}$ is calculated with the help of ATRAN [31]. This software uses a model of the Earth atmosphere to compute the spectrum of atmospheric transmission that one should observe at a given observatory. Input data are the observatory altitude and latitude as well as the zenith angle of observations and the wavelength range under investigation.

The results for the input parameters below are shown in Figure 5.3 [31].

Parameter	Value
Observatory altitude	7873 feet
Observatory latitude	30° (nearest value)
Zenith angle	0°

Table 5.2 – Input parameters for the calculation of the atmospheric transmission with ATRAN

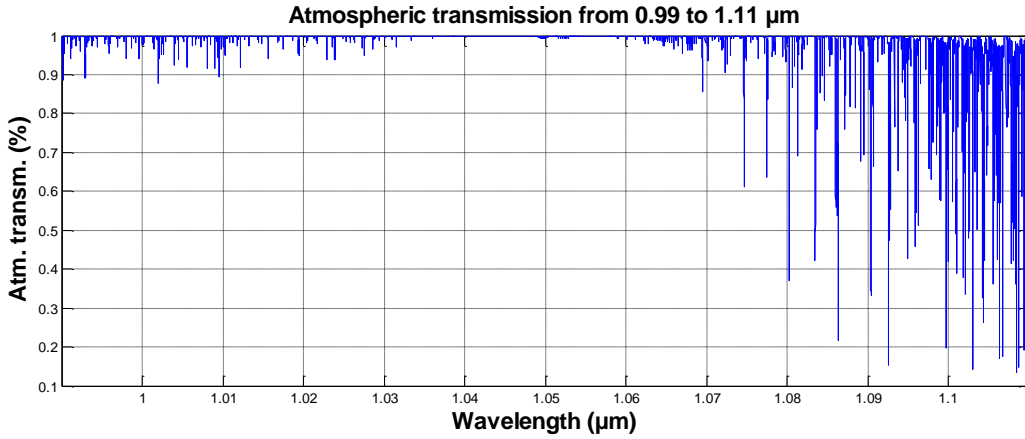


Figure 5.3 - Atmospheric transmission in the range 1-1.1 μm [31]

5.5 Instrumental throughput efficiency

The instrumental throughput efficiency is evaluated by considering the entire optical chain performances, including its variation with wavelength. In the case of the studied spectrograph, the optical chain starts from the telescope and reaches the spectrograph through the selected fiber to finally reach the detector through the multiple reflections inside the instrument. The instrumental throughput efficiency may therefore be evaluated as follows:

$$\eta_{\lambda} = \alpha_{fiber} V_{fiber\ core} (FRD)_{fiber} T_{filt} R^x T^y E_{grat} Q_{det}$$

where

- α_{fiber} is the attenuation factor of the fibers used to feed the instrument from the telescope,
- $V_{fiber\ core}$ is the vignetting factor due to the fiber core being smaller than the source image (depends on the seeing),
- $(FRD)_{fiber}$ is the Focal Ratio Degradation of the selected fibers,
- T_{filt} is the transmission of the selected filter,
- R^x is the cumulative reflectivity of the x mirrors used,
- T^y is the cumulative transmission of the y refractive surfaces used,
- E_{grat} is the efficiency of the grating in the selected order,
- Q_{det} is the quantum efficiency of the detector.

5.5.1 Fiber Optics

Fiber optics are used to feed the instrument with light collected by the telescope. Their core diameter has therefore to match the typical image size of the observed star. The typical seeing at TIGRE and ARIES sites induces spots that were presented in Figure 1.3. To collect all the flux in the focal plane, the fiber cores should naturally match the maximum predicted star image size. However, the actual design of the spectrograph allows an entrance slit size of $50 \mu\text{m}$ and some vignetting is therefore induced.

The actual amount of this fiber vignetting depends on the seeing during the observation. We will refer here to vignetting factor as the relative amount of light that is injected through the fiber core at its entrance, the remaining part being discarded as it falls onto the cladding. The relation below relates the approximated vignetting factor to the observation seeing.

$$V_{fiber\ core} = \left(\frac{D_{fiber\ core}}{D_{star}} \right)^2 = \left(\frac{D_{fiber\ core}}{f_{tel} \tan(seeing)} \right)^2$$

The vignetting factor evolution as a function of seeing is depicted in Figure 5.4. Two different regimes can be observed: a complete transportation of star light and an attenuation varying with seeing. Indeed, the incoming stellar photon flux from the telescope entirely propagates through the fiber as long as the seeing induces a star image that is smaller than the fiber core diameter. Once the target image exceeds this limit, light leakage occurs and increases proportionally to the square of the seeing, as stated in the above equation. Eventually, typical and good seeing vignetting factors are highlighted in the graphs on the left and right of Figure 5.4 respectively.

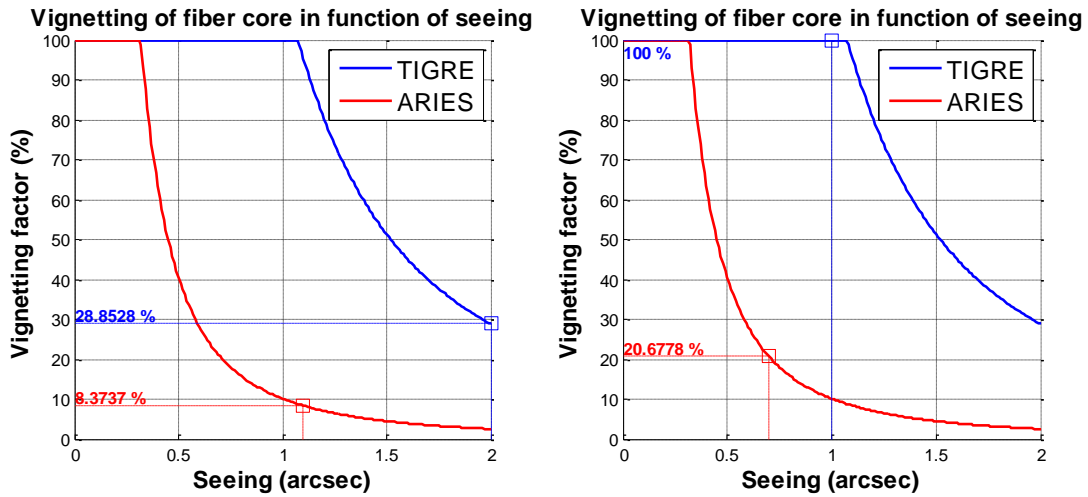


Figure 5.4 - Evolution of fiber core vignetting factor as a function of seeing for both identified telescopes. Sampled values for typical (*left*) and good (*right*) seeing conditions are also represented.

On the other hand, FRD properties of fibers studied by Carrasco et al. [46] and Barden [41] are used to simulate this photon flux attenuation. Their data on both poor and high quality fibers are employed to account for the induced mismatch between the degraded telescope and collimator focal ratios. Eventually, the typical transmission of dry fibers is included within the calculation [45]. Carrasco's results on FRD properties and typical transmission of dry fibers measured by Barden are plotted in Figure 5.5.

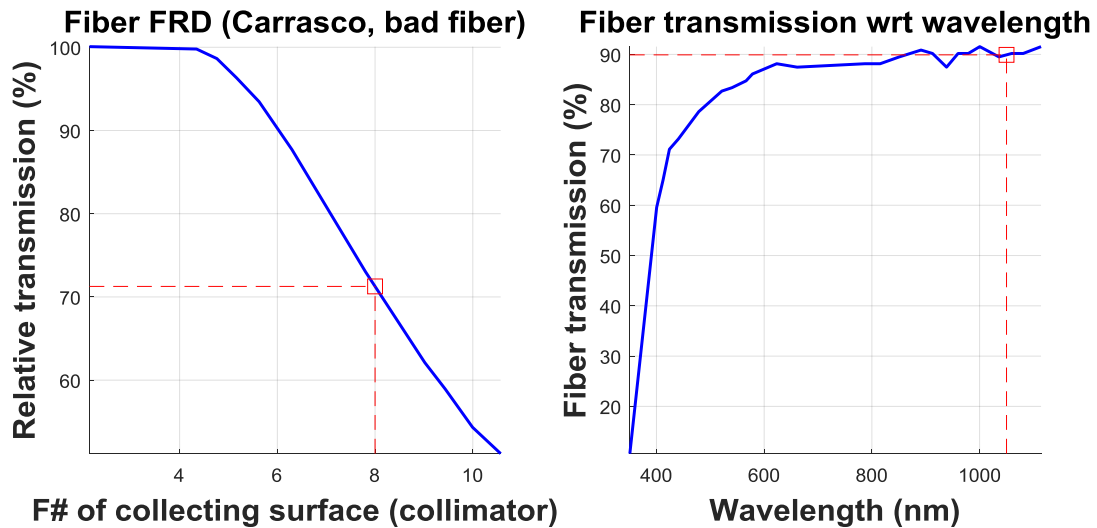


Figure 5.5 - FRD properties and transmission of dry fibers

5.5.2 Coatings and filters

As pointed out in Chapter 2.5, silver coatings are well-suited to maximize the mirrors' reflectance from the visible to the near-infrared part of the spectrum. The manufactured collimating and focusing mirrors exhibit a protected silver coating with a minimum measured reflectance of 90% from 400 to 1100 nm (see Figure 5.6). Other plane reflection mirrors benefit from higher reflection properties and this coating is therefore used as a worst case reference.

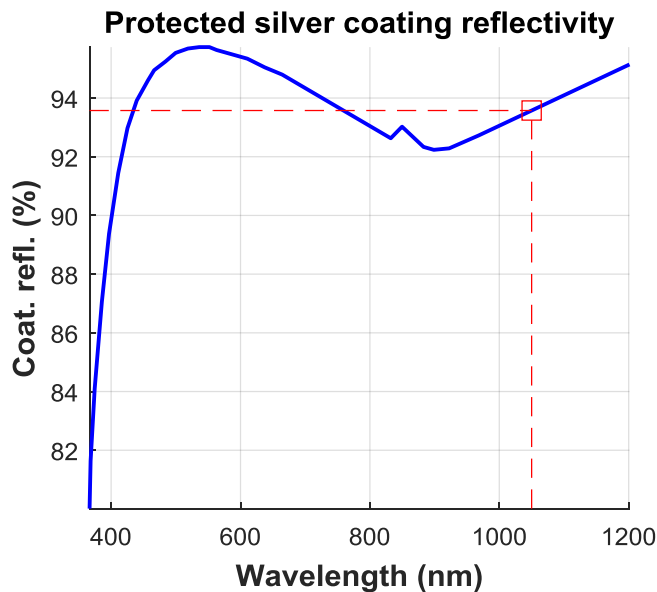


Figure 5.6 - Protected silver coating reflectivity

5.5.3 Grating

The characteristics of the selected grating are also included in this photometric analysis. The typical mean efficiency of the first order in Littrow configuration exceeds 60% in the scientific waveband of interest [83]. As can be seen in Figure 5.7, the near-infrared part of the spectrum between 1 and 1.1 μm lies in the efficiency peak of the grating.

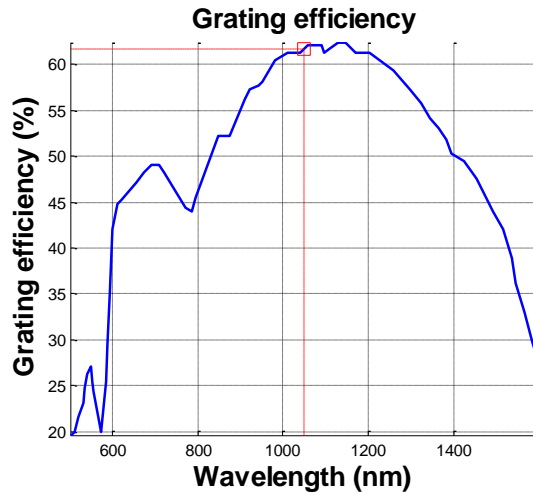


Figure 5.7 – Selected grating efficiency curve [83]

5.5.4 Detectors

Chapter 2.3 investigated which detector technologies are suitable for the near-infrared observation of astronomical objects. Standard InGaAs detectors were identified as the most adequate sensors due to their high quantum efficiency in the waveband of interest. Their high dark current requires however low operational temperatures in order to decrease the amount of thermally-induced electrons since they may lead to an early saturation of the detector. Common CCD detectors suffer from a lack of sensitivity over $1 \mu\text{m}$ and, therefore, they are not foreseen as convenient candidates regarding the scientific case under study. Nonetheless, near-enhanced technologies exist to spread further the quantum efficiency to redder wavelengths. Yet, the induced change in photon detection ability does not usually tremendously impact the wavelength regime over $1 \mu\text{m}$ but is more centered around 800-900 nm. Eventually, the uncertainty on the behavior of those detectors at these wavelengths makes them a risky option that may lead to unexpected results. Both InGaAs and CCD technologies are studied here even though the first option was selected.

The identified InGaAs detector that is used in the spectrograph assembly benefits from a high quantum efficiency from $1 \mu\text{m}$ to $1.7 \mu\text{m}$ approximately, falling to a minimum of 60.91% at $1 \mu\text{m}$ (see Figure 5.8). Eventually, the measured dark current of this camera rises to $0.03 \text{ fA} = 215.496 \text{ e}^-/\text{s}/\text{pix}$ at its operating temperature when water cooling is active.

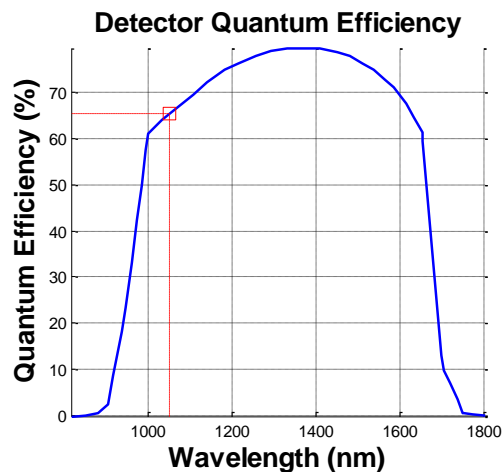


Figure 5.8 - Selected InGaAs detector quantum efficiency

When considering common near-IR enhanced Silicon-based CCD detectors, the operating temperature of the selected device must be considered, as explained in Chapter 2.8.3. Indeed, both the quantum efficiency and the dark current are highly-dependent on this parameter, inducing opposite effects on the required integration time. Indeed, lowering the temperature will decrease the noisy dark signal but at the same time it will reduce the quantum efficiency thereby reducing the scientific signal (see Figure 5.9). A compromise must therefore be found between both actions through the adoption of an optimal working temperature. The photometric budget must therefore be computed at different sensor temperatures and highlight the one that minimizes the observation time.

Figure 5.9 below illustrates the variation of dark current and quantum efficiency of the CCD under study. To establish the photometric budget and hence the optimal operating temperature, the dark noise and quantum efficiency, which is a function of wavelength, are finely sampled from 0 to -90°C . Those intermediate values are represented in red in both figures below.

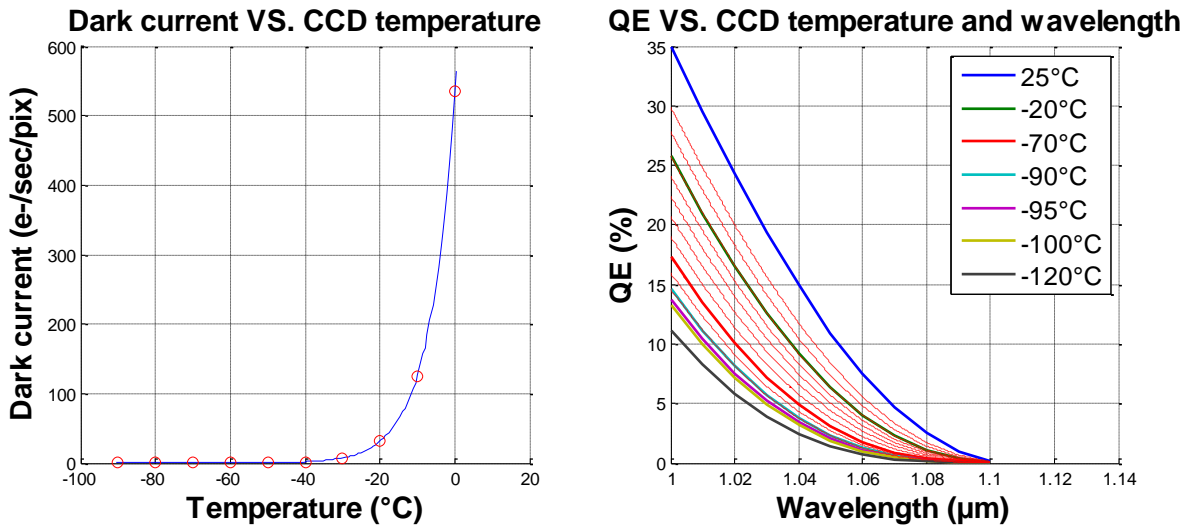


Figure 5.9 - Evolution of dark current (*left*) and quantum efficiency (*right*) with temperature (and wavelength) of a given cooled CCD detector

5.6 Noise sources

Many sources of noise affect an instrument. Photon shot noise acts as the square root of the incoming photon flux while other noises depend on the detector's characteristics. Dark noise is the signal recorded by the detector when the latter is exposed to no radiation for a given integration time. On the other hand, readout noise is the one measured during a null integration time without any incoming light flux. The different expressions of those perturbing sources are listed below:

- Shot noise: $\sigma_{shot}^2 = dN_{tot} t_{int}$ where t_{int} is the total integration time,
- Dark noise: $\sigma_{dark}^2 = D t_{int} p$ where D is the dark factor [$e^{-pixel^{-1} s^{-1}}$],
- Readout noise: $\sigma_{read}^2 = R^2 N_{expo} \frac{p}{f_s}$ where R is the RMS quantity of electrons per pixel at readout and f_s the amount of pixels that are binned along the imaging axis at readout within the CCD.

Dark and readout noises involve the parameter p , the number of pixels along the imaging direction on which numerical binning occurs. Indeed, the star image pitch spreads over more than a pixel and binning in this direction, which does not degrade the spectral resolution, leads to an increase in the total noise that has to be considered. On the other hand, a hardware binning in this direction at readout at the CCD level (f_s) will decrease the readout noise since the electrons are gathered to a same pixel before a single readout.

The combination of those noise sources can be expressed as follows to give the total noise that pollutes the instrument measurements:

$$\sigma_{tot} = \sqrt{\sigma_{shot}^2 + \sigma_{dark}^2 + \sigma_{read}^2} \quad [e^-]$$

It can be noticed that both thermal and sky backgrounds are neglected. As a reminder of Chapter 1.5, this is due to the fact that the observed J -band is not dominated by those sources of noise if several conditions are fulfilled. For example, the selected NIR detector is an InGaAs technology whose cutoff wavelength does not extend into the K -band. No cold filter is therefore required [26]. The major source of noise however comes from the high dark current of the selected detector since it does not benefit from any cryogenic cooling, which is usually required for NIR spectroscopy.

5.7 Signal-to-noise ratio

Now the incoming flux from the target star and the noise are known, we can evaluate the total amount of photons reaching the focal plane after a given integration time

$$N_{tot} = dN_{tot} t_{int} \quad [ph]$$

where

- $t_{int} = N_{expo} d_{int}$ is the total integration time [s],
- d_{int} is the integration time of a single exposure [s],
- N_{expo} is the number of exposures [].

Eventually, the signal-to-noise ratio that is observed at the detector is equal to

$$\begin{aligned} (SNR)_J &= \left(\frac{N_{tot}}{\sigma_{tot}} \right)_J = \frac{dN_{tot} t_{int}}{\sqrt{dN_{tot} t_{int} + D t_{int} p + R^2 N_{expo} \frac{p}{f_s}}} \\ &= \frac{(dN_\lambda)_J d\lambda T_{atm} A_{tel} \eta_\lambda f_\lambda \in N_{expo} d_{int}}{\sqrt{(dN_\lambda)_J d\lambda T_{atm} A_{tel} \eta_\lambda f_\lambda \in N_{expo} d_{int} + D N_{expo} d_{int} p + R^2 N_{expo} \frac{p}{f_s}}} \\ &= \sqrt{N_{expo}} \frac{(dN_\lambda)_J d\lambda T_{atm} A_{tel} \eta_\lambda f_\lambda \in d_{int}}{\sqrt{(dN_\lambda)_J d\lambda T_{atm} A_{tel} \eta_\lambda f_\lambda \in d_{int} + D d_{int} p + R^2 \frac{p}{f_s}}} \end{aligned} \quad (15)$$

5.8 Signal saturation

Integrating a signal over a long time may lead to the saturation of the detector. Indeed, each pixel is characterized by its own *full well capacity* (FWC), that is the amount of charge an individual pixel can hold before saturating. In other words, there is an upper limit in the number of photons a pixel can detect before becoming inefficient. Oversaturating a pixel can lead to electron leakages between adjacent pixels and keeping the detector illuminated will not increase the signal-to-noise ratio. Given the full well capacity of a detector's pixel, one can evaluate the maximum integration time that this detector can sustain through the formula:

$$p \text{ FWC} = dN_{tot} d_{int sat} + D d_{int sat} p + R^2 \frac{p}{f_s}$$

$$\Leftrightarrow d_{int sat} = p \frac{\text{FWC} - \frac{R^2}{f_s}}{dN_{tot} + D p}$$

5.9 Analyses

5.9.1 Required integration time

The analysis performed below aims at evaluating the approximately needed integration time to reach the required signal-to-noise ratio. The free parameters during those analyses are the effective temperature, the magnitude in *J*-band and the interstellar absorption in the *V*-band A_V . Different values of A_V are thus scanned to investigate the variation of the needed integration time with respect to this parameter. The selected models and all instrument characteristics are summarized in the table below. Those parameters are chosen in a "worst case" manner when found in the literature rather than available from the manufacturer. Moreover, typical and nice seeing conditions are simulated and the use of micro-lenses is also examined.

Parameter		NIR detector	CCD detector
Scientific requirements	Required SNR	100	
	Resolving power	20000	
	Wavelength	10500 Å	
	# of pixels per $\delta\lambda$	3	
Star	Magnitude in <i>J</i> -band	4 to 6	
	Effective T°	3000 K to 7000 K and 30000 K to 45000 K	
Space and sky	Interstellar absorption A_V	0, 0.5, 1, 1.5, 2	
	Atmospheric transmission	ATRAN model (see Figure 5.3)	
	Seeing	2 arcsec	
Fiber	Fiber FRD model	Carrasco's data (see Figure 2.16)	
	Fiber transmission	See Figure 5.5	
Telescope	Telescope	TIGRE	
	Primary diameter	120 cm	
	Secondary diameter	45 cm	
	F# telescope	8	
Spectrograph	F# collimator	8	
	Grating diffraction efficiency	See Figure 5.7	
	Detector quantum efficiency	See Figure 5.8	See Figure 5.9
	Detector readout noise	400 e^-/pix	5 e^-/pix
	Detector dark noise	215.496 $e^-/\text{s}/\text{pix}$	See Figure 5.9
	Full well capacity	1200000	300000 e^-
	Hardware binning factor along dispersion direction	1	
	Hardware binning factor along imaging direction	1	
	Numerical binning factor along imaging direction	3	
Optical chain	Number of reflecting surfaces	3 (TIGRE) + 5 (Spectro) = 8	
	Reflectivity of coating	See Figure 5.6	
	Number of refractive surfaces	1 (SPS) + 1 (Spectro) = 2	
	Trans. of refractive surfaces	0.95	

Table 5.3 - Photometric budget parameters summary

By reversing Eq. (15), we obtain the following relation which enables the calculation of the needed integration time to reach the signal-to-noise ratio stated in the requirements:

$$d_{int} = \frac{(dN_{tot} + D p) + \sqrt{(dN_{tot} + D p)^2 + 4 \frac{N_{expo} p}{f_s} \left(\frac{dN_{tot} R}{SNR}\right)^2}}{2 N_{expo} \left(\frac{dN_{tot}}{SNR}\right)^2}$$

The purpose of the following analyses is to evaluate the integration time needed to reach the required signal-to-noise ratio when considering different types of stars and interstellar absorption values.

NIR detectors

The photometric analyses are first performed by considering the use of a typical NIR detector. Both cool and hot stars are simulated as well as several absorption cases. A central wavelength of 1050 nm is considered as the detector quantum efficiency does not exhibit a highly wavelength-dependent behavior. Moreover, it is naturally supposed that the observation does not occur within an absorption band but well in a observation window.

First case: $A_V = 0$

Cool stars

In this section, we focus on cool stars, that is, stars whose effective temperatures are located between 3000 and 7000 K. The figures below illustrate the results from the photometric budget considering the selected detector characteristics.

First, the flux of the star per wavelength unit as one would see it from a distance d is presented in the left panel below (dN_λ). On the right side of this illustration we present the number of photons that are detected in the focal plane per unit of time considering the entire observation chain efficiency ($dN_{tot} = dN_\lambda d\lambda T_{atm} A_{tel} \eta_\lambda f_\lambda \epsilon$).

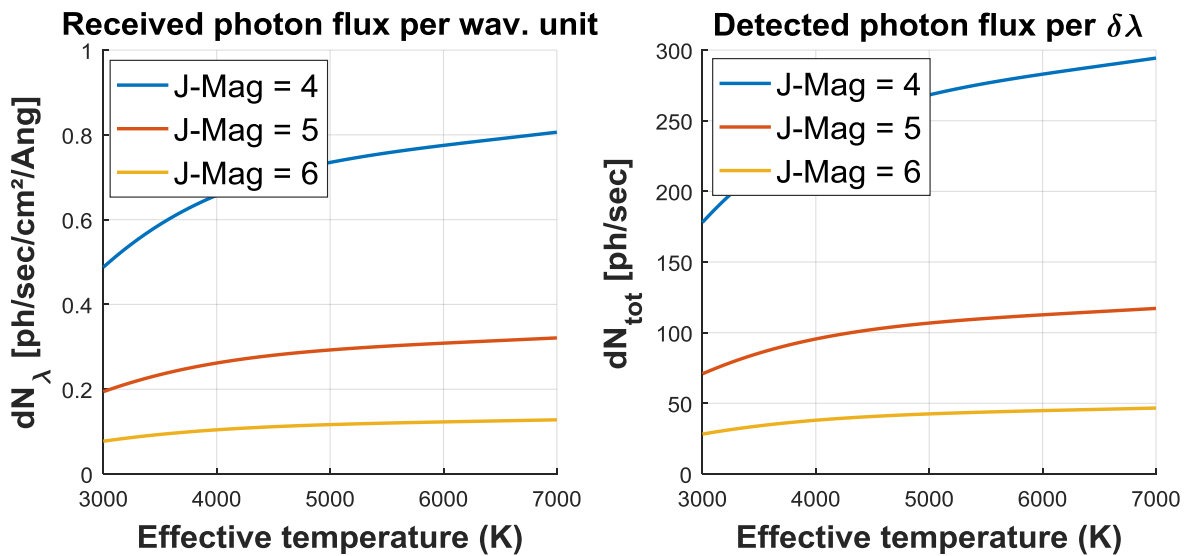


Figure 5.10 -Flux of photons received and detected for COOL stars

Then, the following graphs highlight the needed integration time to reach a signal-to-noise ratio of 100 when considering different J -magnitudes.

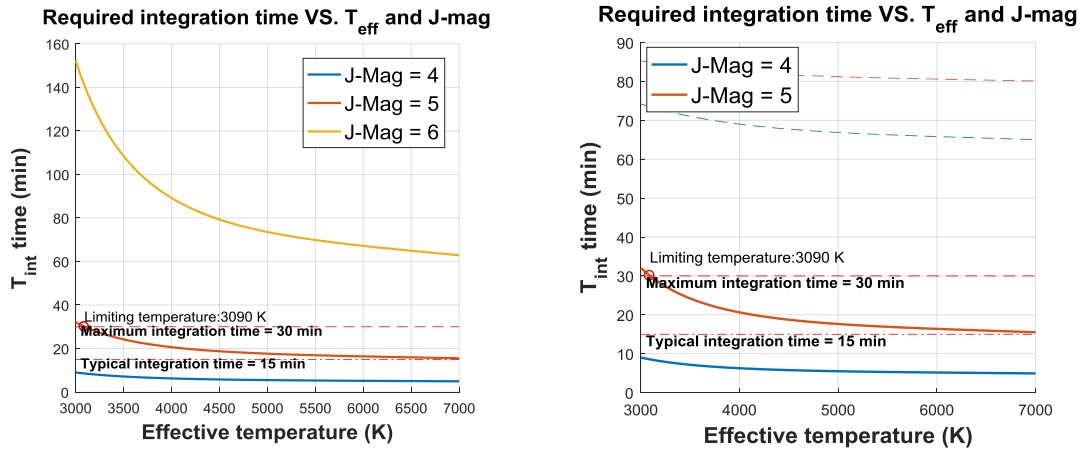


Figure 5.11 - Required integration time vs. T_{eff} for COOL stars

We can clearly see in the left picture that the required observing time is far too large to reach a signal-to-noise ratio of 100 when considering stars of magnitudes larger than 5 in J -band. Therefore, the right panel only focuses on stars of J -magnitude equal to 4 or 5 to investigate if the actual optical design fulfills the requirement on signal-to-noise ratio stated at these magnitudes. Saturation curves are also presented on this panel (dashed curves, one for each magnitude). As we can see, the required integration time for the considered effective temperatures and stars of J -magnitude equal to 4 is totally located below the maximum allowed observation time equal to 30 minutes. On the other hand, an effective temperature limit of 3090 K appears when considering stars of magnitude 5. In conclusion, cool stars of magnitude 4 belonging to the considered range of temperature can be observed with a SNR of 100 within the typical observation time specified in the requirements when $A_V = 0$. Stars of magnitude 5 and whose effective temperatures are higher than 3090 K also fulfill the requirement. Eventually, no saturation will occur in this range of temperatures.

Hot stars

Hotter stars than in the previous case are considered now whereas all other parameters during the calculation remain the same. The left panel of Figure 5.12 illustrates the number of photons that are reaching the telescope collecting surface whereas the number of detected photons per second is depicted in the right panel.

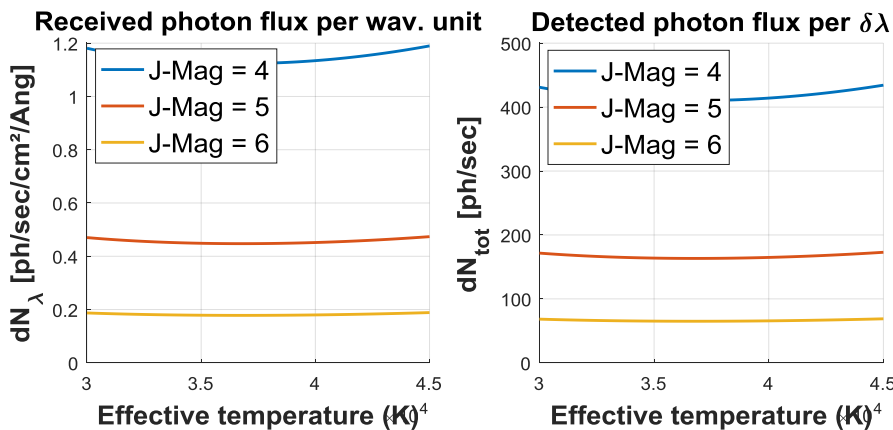


Figure 5.12 - Flux of photons received and detected for HOT stars

Figure 5.13 then illustrates the integration time that is needed to fulfill the scientific requirements when considering hot stars of different magnitudes.

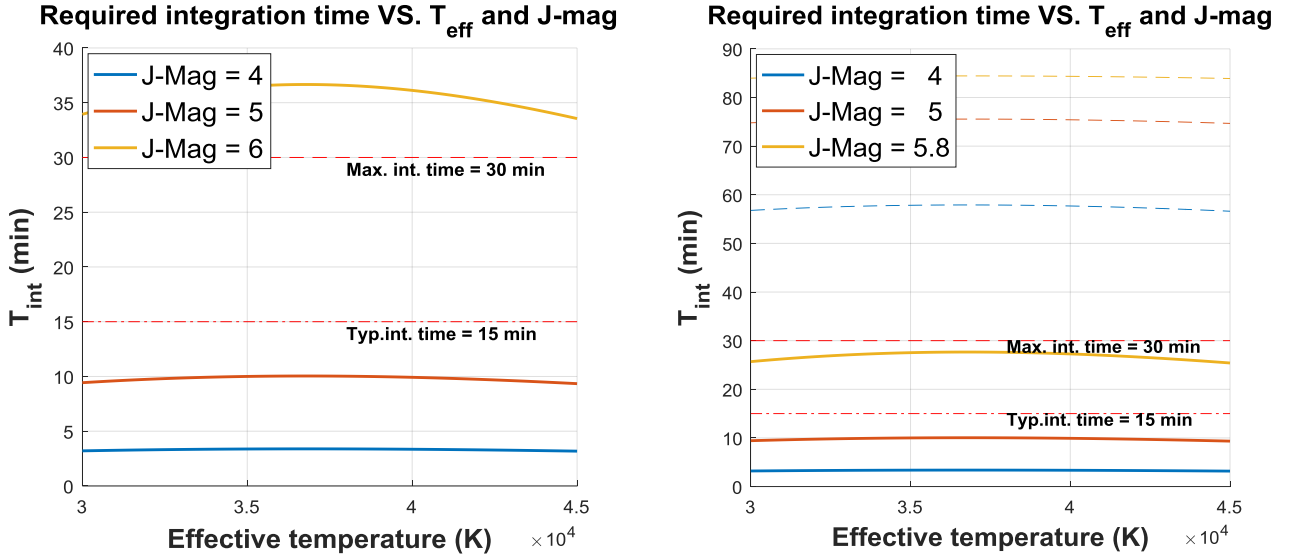


Figure 5.13 - Required integration time vs. T_{eff} for HOT stars

Stars of magnitude equal to 6 in J -band are not observable within the allowed time duration with the considered parameters from Table 5.3. The right panel of Figure 5.13 shows however that slightly brighter stars are observable without any saturation from the detector.

Second case: effect of A_V

This section intends to examine the effect of the parameter A_V on the integration time. Values ranging from 0.5 to 2 are scanned to find if any limiting magnitude or temperature appears when this parameter varies. The figures below (see next page) illustrate the required integration time for cool and hot stars for every scanned value of A_V .

From those figures, we can confirm that the global effect of A_V is an increase in the interstellar absorption A_λ and therefore a reduction in the incoming flux of photons. The integration time required to reach a constant signal-to-noise ratio of 100 then becomes longer. The variation is however rather weak because variations in A_λ due to a change in A_V are nearly compensated by the induced change in A_J .

As a result, limiting temperatures for cool stars become hotter with the increase of A_V . For example, a 30 minute observation is sufficient to reach a SNR equal to 100 for stars of magnitude 5 whose effective temperatures exceed 3190 K when A_V is equal to 0.5. Then, when A_V reaches the value of 2, this temperature limit rises to 3570 K. The conclusion for hot stars remains the same: the higher A_V , the longer the observation time. Eventually, hot stars of magnitude 5 are not observable anymore within a duration of 30 min when A_V reaches 1.5.

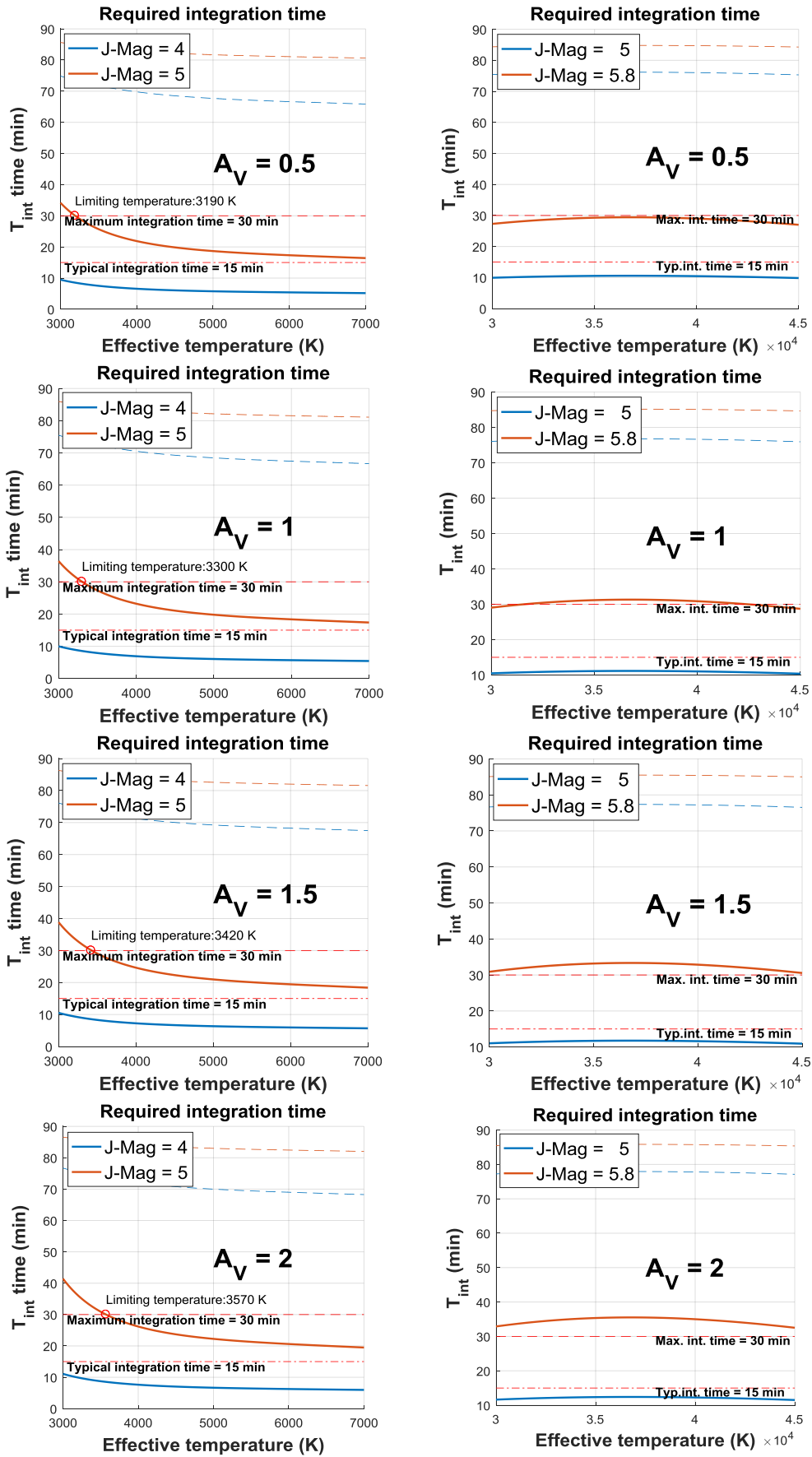


Figure 5.14 - Variation of integration time with A_V (left: COOL stars, right: HOT stars)

CCD detectors

The same analyses as conducted above for specific NIR detectors are now performed for CCD sensors. As explained in Chapter 2, since the quantum efficiency and the dark noise of the CCDs sorely vary with their temperature, these analyses have to be performed considering the whole detector's operating temperature range. The optimum working temperature is naturally the one that minimizes the required observation time to reach a given signal-to-noise ratio.

Eventually, it will be shown that this optimal temperature usually differs from the lowest one the detector cooling unit is able to achieve. The induced observing time reduction percentage in this configuration will also be illustrated. The following analyses are also performed at the central wavelength of 1050 nm in a first step and the wavelength-dependent behavior of the results is then investigated. Indeed, the hypothesis of nearly constant quantum efficiency does not hold anymore for CCDs as will be shown.

First case: $A_V = 0$

Cool stars

The photometric budget analysis when using CCDs is first performed considering cool stars. The evaluated photon flux per wavelength unit and the one detected at the instrument focal plane are depicted in Figure 5.15. The observed jump in the detected photon flux for stars of magnitude 5 originates from a change in optimal detector operating temperature and the optimization of this parameter leads to discontinuous curves.

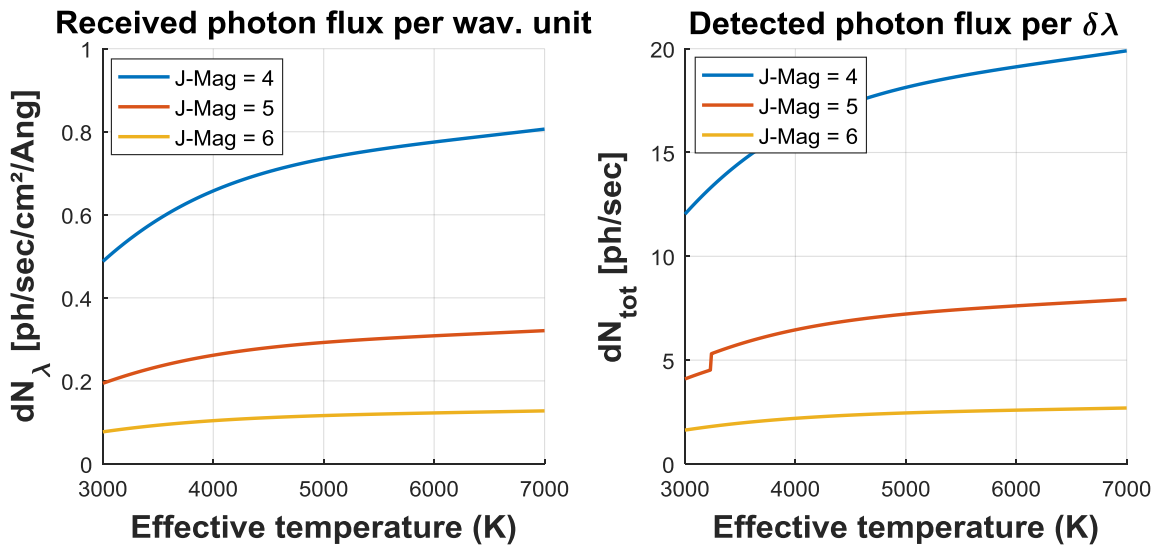


Figure 5.15 - Flux of photons received and detected for COOL stars

The required integration time can then be assessed by using the detected flux values of Figure 5.15.

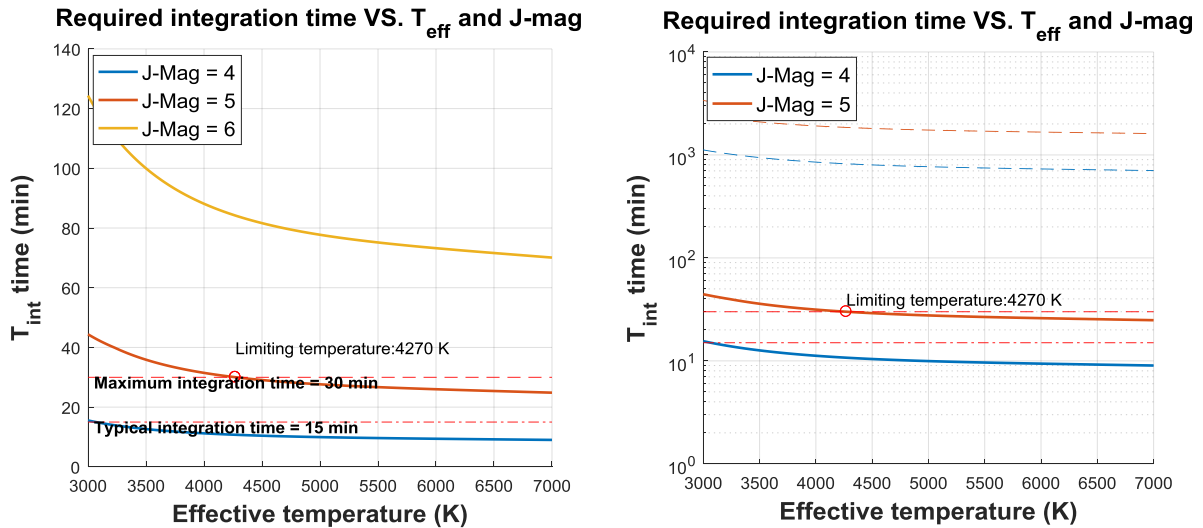


Figure 5.16 - Required integration time vs. T_{eff} for COOL stars. Dashed lines in the right panel represent the saturation limit of the detector.

We can clearly see in the left panel that the required observing time is far too large to reach a signal-to-noise ratio of 100 when considering stars of magnitudes larger than 5 in J -band. On the other hand, the requirements are fulfilled when considering stars of magnitude 5 whose effective temperatures are greater than 4270 K. The right panel focuses on stars of J -magnitude less than or equal to 5 to illustrate on a logarithmic scale that the saturation time of such detectors is much higher than the required integration time.

As mentioned before, the analyses that are conducted to find the required observation time to reach a given signal-to-noise ratio also involve finding the best CCD temperature, that is the one that minimizes the integration time. Figure 5.17 illustrates the results of this optimization by showing the most suitable detector temperature as well as the integration time gain that is obtained when observing at this specific temperature. The integration time gain is calculated as the relative decrease in observation time compared to the situation where the CCD is cooled down to its lowest operational temperature. Both results are plotted with respect to the effective temperature of the observed star and considering different J -magnitudes.

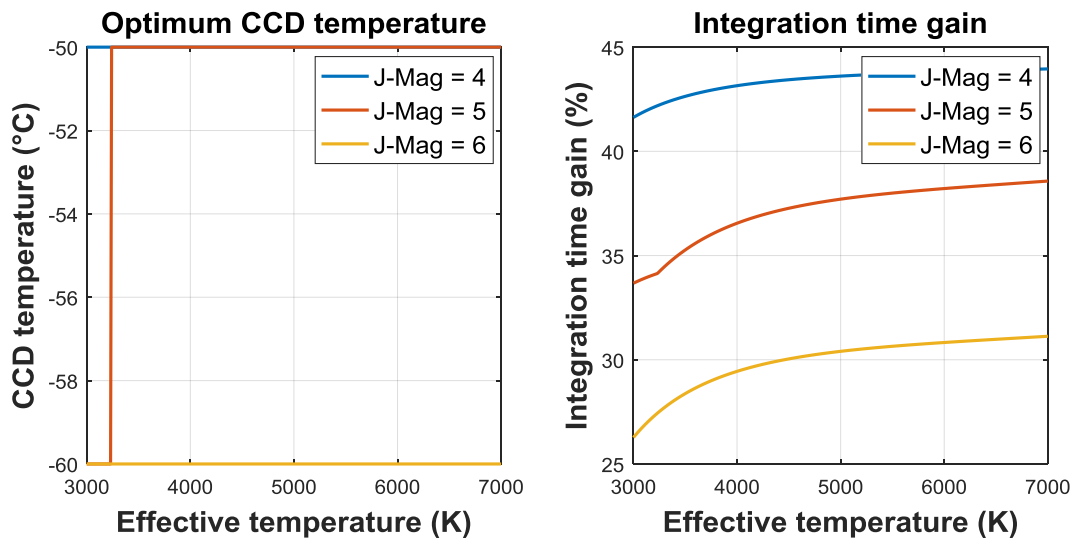


Figure 5.17- Optimal CCD temperature and integration time gain for COOL stars

A first conclusion from the above pictures is that the best operating temperature is not the lowest operational one of the detector. Indeed, whereas the CCD detector can be operated at -90°C , the most suitable one is located between -50°C and -60°C when observing targets of magnitude less than or equal to 6. We can also observe in the right panel of Figure 5.17 that integration time savings up to nearly 45% are reached through a well-chosen temperature setting.

Then, it can also be observed that the optimal CCD temperature actually varies as a function of the target, that is with the incoming flux intensity. Indeed, the ideal temperature setting is different from one effective temperature to another and also depends on the considered magnitude.

The global tendency is that the best operating temperature decreases when the incoming flux does, that is when the effective temperature is lower or the magnitude higher. When considering lower fluxes entering the instrument, it appears that it is more efficient to decrease the temperature and therefore the dark current to obtain the shortest integration time. On the other hand, when the stellar flux increases, the most efficient way to shorten the integration time is obtained through high quantum efficiency rather than a low dark current. Eventually, the integration time gain decreases as the observed flux does since the required operational temperature approaches the lowest one the CCD can be operated at.

The left panel of Figure 5.18 eventually illustrates the previous conclusion stating that the optimal operating temperature differs from the lowest operating one. One can see that decreasing the CCD working temperature first leads to a shorter integration time. Then after a minimum, the integration time increases again as the CCD temperature decreases. The existence of an optimal temperature is illustrated in the right panel of Figure 5.18 when considering a specific cool star.

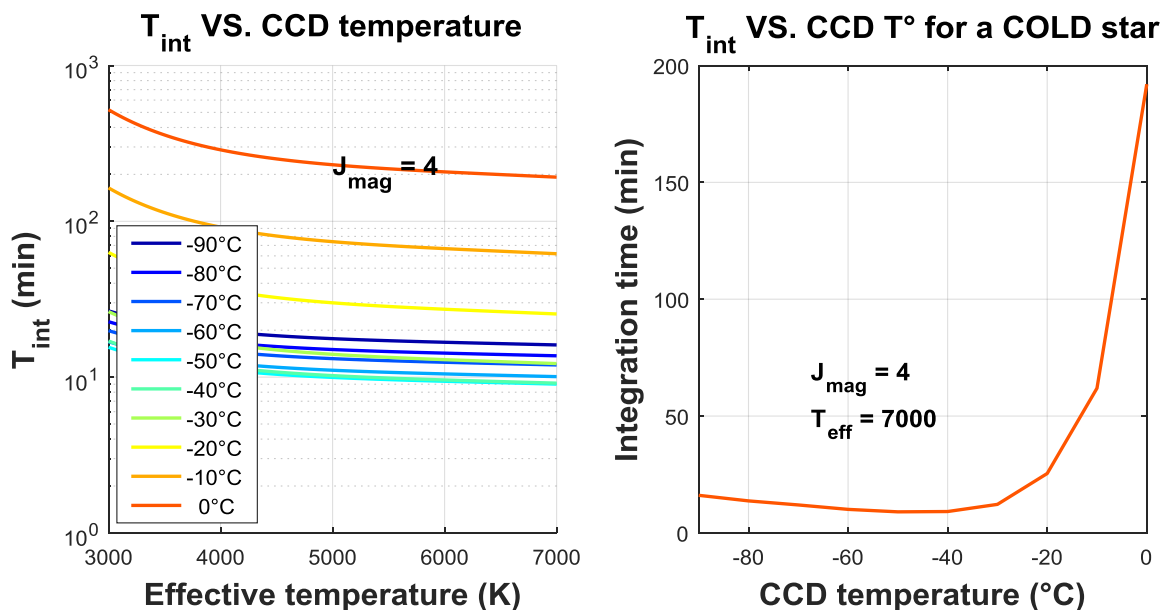


Figure 5.18 - Evolution of integration time wrt. effective temperature for stars of magnitude 4 at different CCD temperatures (*left*) and integration time as a function of CCD temperature for a given cool star.

Hot stars

The analysis focuses this time on hot stars, that is, stars whose effective temperatures range between 30000 and 45000 K. The figures below introduce the calculated fluxes for those objects.

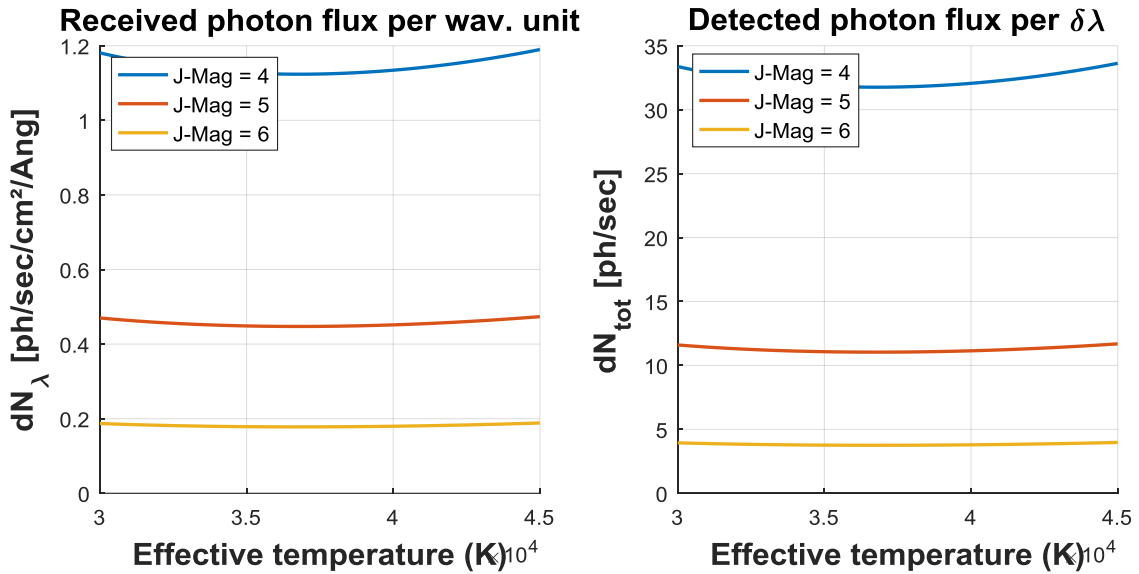


Figure 5.19 - Flux of photons received and detected for HOT stars

The estimated integration time is then presented in Figure 5.20. The obtained results show that stars of magnitude 6 are not observable within a 30 min observation time but those slightly brighter whose J -mag are equal to 5.5 fulfill the requirements. Saturation of the detector does not appear as an issue as this phenomenon occurs at very long integration times.

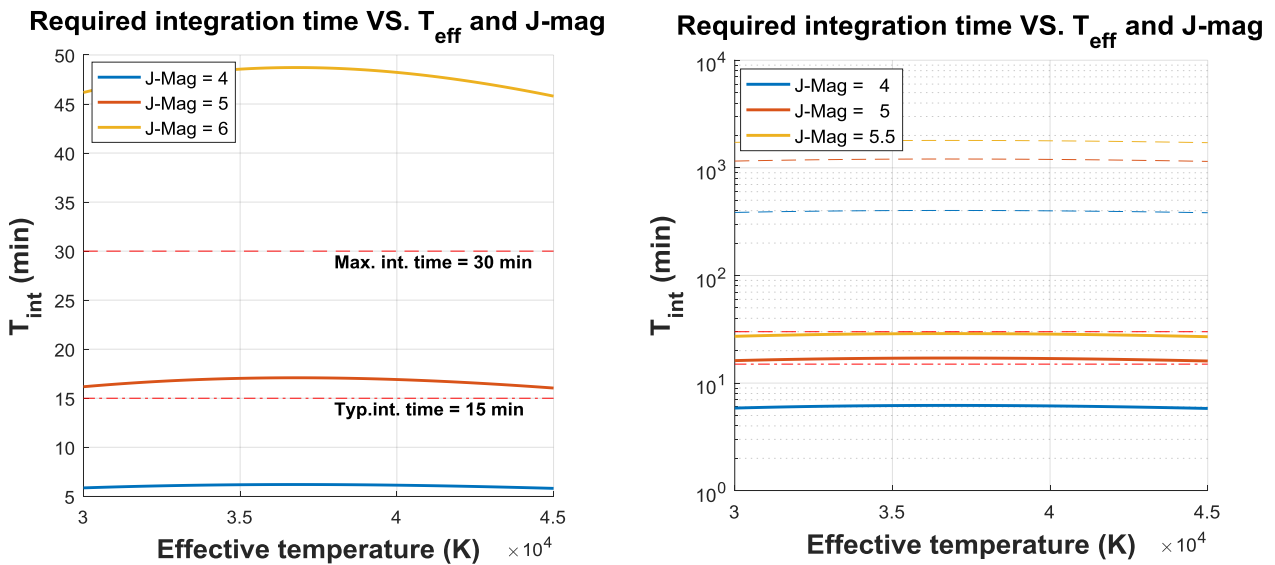


Figure 5.20 - Required integration time vs. T_{eff} for HOT stars

The figures below illustrate the calculated optimal temperature at which the CCD has to be operated to minimize the integration time and the observation time saving that may be obtained by doing so.

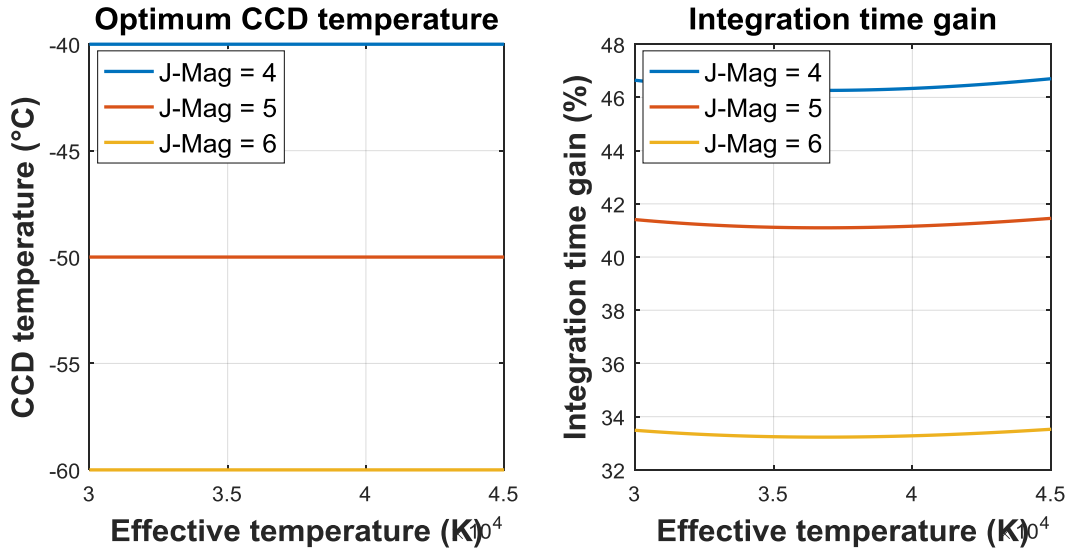


Figure 5.21- Optimal CCD temperature and integration time gain for HOT stars

The same conclusions as for the cool stars can be drawn. The most suitable CCD temperature decreases as the target star flux does too. The required operational temperatures in this case are located between -40°C and -60°C depending on the observed star. The reduction in observing time varies between 33 % and 47% according the considered target. Once again, using the CCD detector under warmer conditions than its lowest affordable one leads to a large gain in integration time.

Eventually, the evolution of the integration time with the CCD temperature is depicted in Figure 5.22. The different temperature curves are represented in the left panel. This confirms the previous conclusion which stated the existence of an optimal temperature that sorely differs from the lowest operating one. The optimization process is finally illustrated for a given hot star in the right panel.

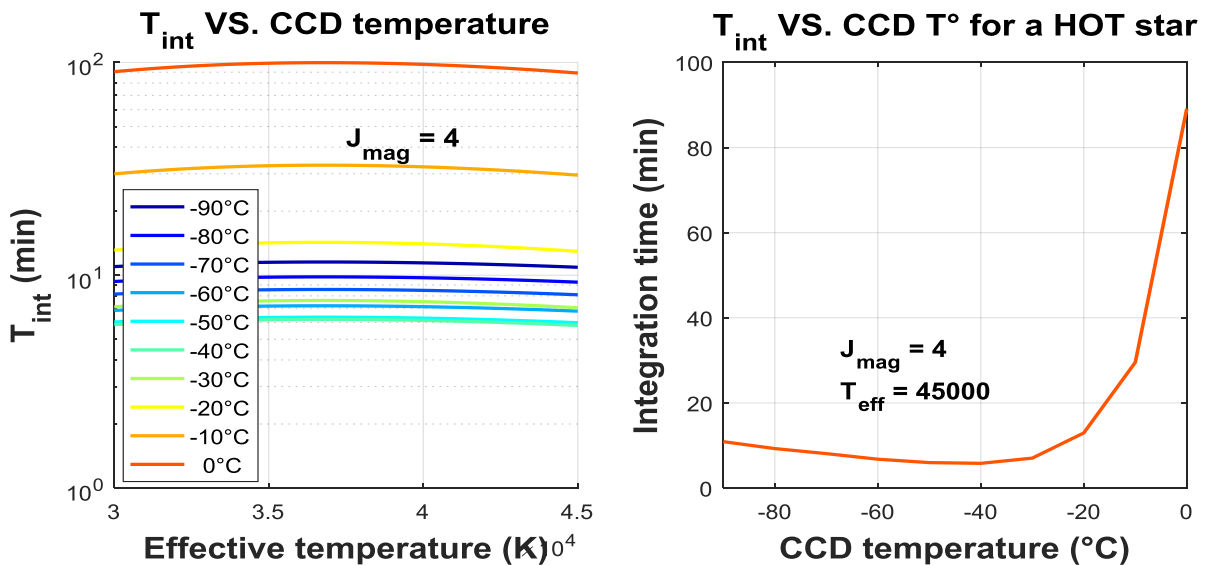


Figure 5.22 - Evolution of integration time wrt. effective temperature for stars of magnitude 4 at different CCD temperatures (left) and integration time as a function of CCD temperature for a given HOT star.

Second case: effect of A_V

As for cool stars, the effect of A_V is investigated when the value of this parameters differs from 0. The results from this analysis are plotted in Figure 5.23. The same conclusion as for cool stars can be drawn: as A_V increases, the required observation time increases and the limiting temperatures shift to hotter values. Stars that are observable at some absorption levels do not fulfill the requirements at higher levels of absorption.

Upper wavelength limit

Due to the large decrease in quantum efficiency at longer wavelengths (around $1 \mu m$) of CCDs, an upper wavelength limit appears above which it is not possible to reach a signal-to-noise ratio of 100 in less than 30 *min* for all potential targets. We have computed what would be the wavelength where the required integration time is equal to 30 *min* when observing stars of a given magnitude and whose effective temperature is 3000 *K* for cool stars and 30000 *K* for hot stars. The resulting upper wavelength limits are listed in Table 5.4 for both cool and hot stars. Above this wavelength, a lower temperature limit will appear and some stars will not be observable within a 30 *min* exposure.

As can be seen, the required integration time sorely increases with wavelength as the quantum efficiency of those detectors is very low in the near-infrared. The upper wavelength limit remains close to the previously considered central wavelength of 1050 *nm* until very bright stars of magnitude at least equal to 2 are considered. This highlights the fact that such detectors are unsuitable for our scientific case which requires a wavelength coverage from $1 \mu m$ to $1.1 \mu m$.

<i>J-mag</i>	Upper wavelength limit (<i>nm</i>)	
	<i>Cool stars</i>	<i>Hot stars</i>
4	1062.3	1074.5
3	1076.8	1085.5
2	1087.5	1093.3
1	1094.9	1098.2

Table 5.4 - Upper wavelength limit for different *J-mag* for both cool and hot stars

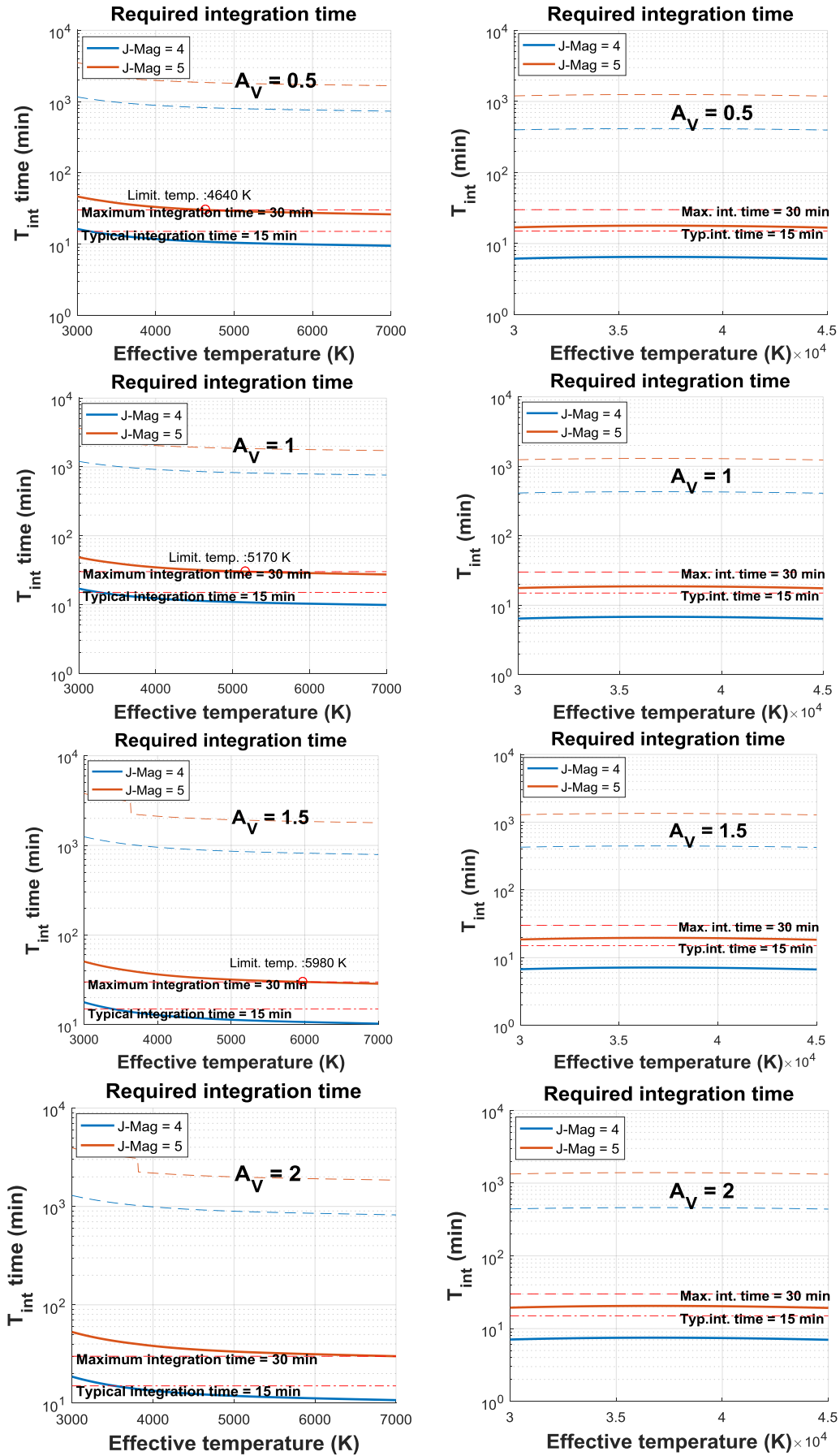


Figure 5.23 - Variation of integration time with A_V (left: COOL stars, right: HOT stars)

Temperature control strategy

The photometric analyses performed when using CCDs previously showed that the operating temperature of such detectors highly impacts on their performances. Indeed, instead of naturally cooling the sensor to its lowest working temperature, we previously showed that a tradeoff between quantum efficiency and dark current occurs. This results in the existence of optimal thermal conditions where the integration time is minimized which in addition to time saving leads to lower energy consumption.

This time, general flux values instead of stars will be considered to investigate and identify the different regimes through which the detector should be operated. All calculations are performed at the central wavelength of 1050 nm . The total flux reaching the detector dN_{foc} is considered, its expression is:

$$dN_{tot} = dN_{foc} Q_{det} f_{\lambda} \epsilon$$

$$\Leftrightarrow dN_{foc} = dN_{\lambda} d\lambda T_{atm} A_{tel} \frac{\eta_{\lambda}}{Q_{det}} [ph/sec]$$

No spectral binning is considered ($f_{\lambda} = 1$) and all the stellar flux is taken into account ($\epsilon = 1$). The left panel in Figure 5.24 illustrates the relationship between dN_{foc} and dN_{tot} when considering the CCD quantum efficiency after optimization of its operating temperature. On the other hand, the right panel illustrates the required integration time to fulfill the scientific requirements.

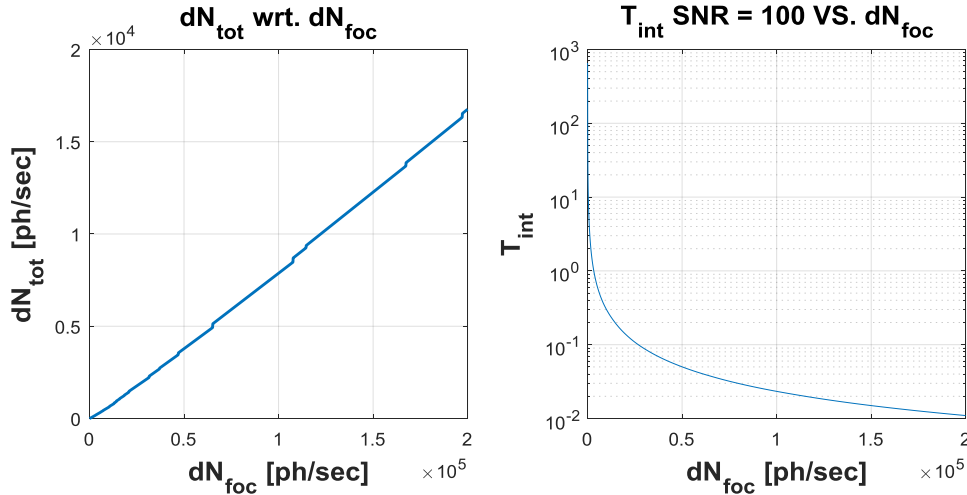


Figure 5.24 – Relationship between dN_{tot} and dN_{foc} (left) and evolution of required integration time as dN_{foc} varies

Figure 5.25 illustrates the different regimes the CCD can be operated at. This figure represents the evolution of the required integration time as dN_{foc} varies for different CCD temperatures, the redder the curve the hotter the temperature (from 0°C to -90°C). We can see that low fluxes lead to the need for low operating temperatures of the CCD to minimize the required integration time. In this regime, a better strategy is preferring a low dark current over a high quantum efficiency. At some boundary flux (7310 ph/sec , see left panel in Figure 5.25); the required integration time is the same for both the lowest and the highest working temperatures.

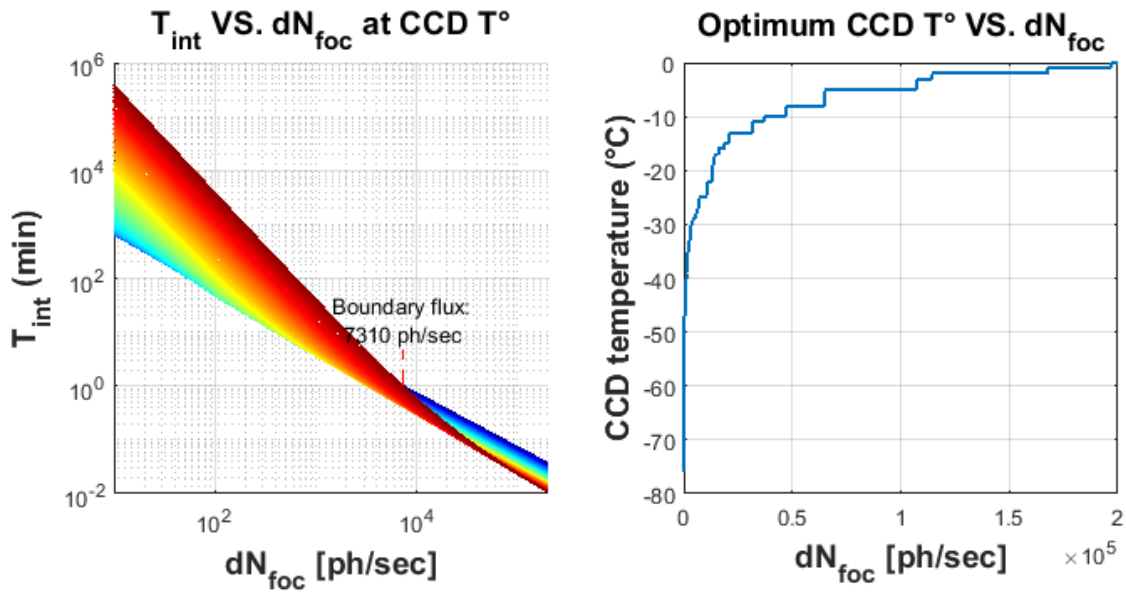


Figure 5.25 – Evolution of integration time wrt. dN_{foc} as a function of CCD temperature (left) and optimum CCD temperature as a function of dN_{foc} .

This interesting situation occurs when it is as efficient to operate the CCD at 0°C or at -90°C. After this point, higher fluxes are characterized by the fact that the minimization of the observation time now occurs with higher sensor temperatures and therefore, higher quantum efficiencies. The balance between quantum efficiency and dark current depends on the incoming flux and fixing the preferred parameter to favor depends on the amount of the target photon flux. Eventually, the preference inverts at the identified boundary flux. The left panel of Figure 5.26 confirms that low fluxes, which required cooler sensor conditions, lead to situations where the integration time reduction decreases as the lowest cooling temperature is approached. Three different fluxes (lower than, equal to and higher than the boundary one) are plotted in the right panel to illustrate the corresponding integration time variation accordingly.

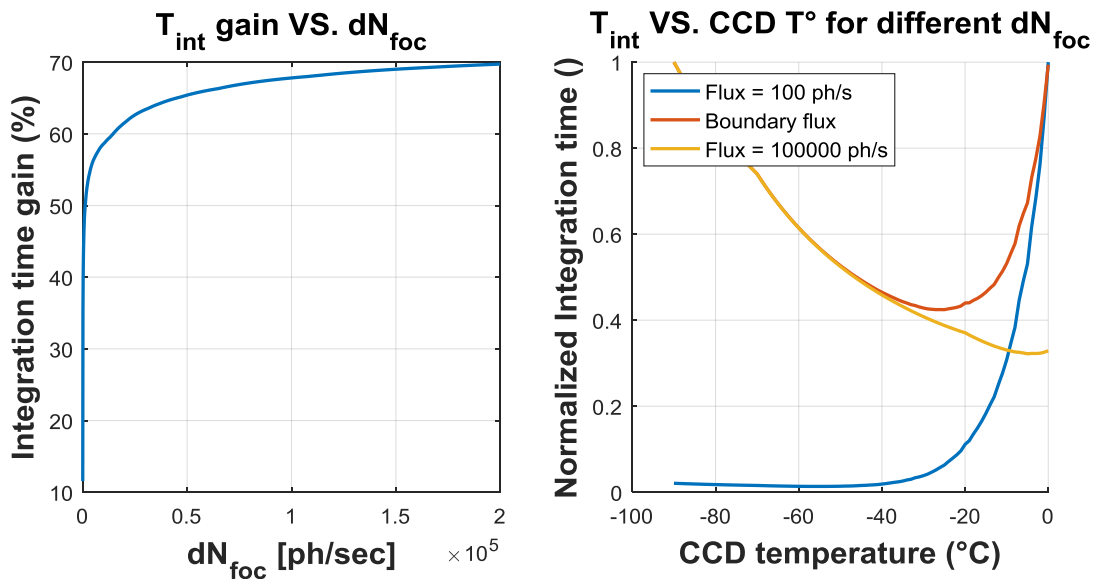


Figure 5.26 – Relative integration time reduction by optimizing the CCD sensor temperature as a function of dN_{foc} (left) and normalized integration time as a function of CCD temperature for low, boundary and high photon fluxes (right).

All previous calculations were performed at the central wavelength of 1050 nm . When going further in the near-infrared, the quantum efficiency of the CCD decreases and a weaker signal is recorded. A deeper cooling of the detector is therefore required and the boundary flux value increases.

In practice, the fact that the operating temperature of the CCD would depend on the source flux, the low quantum efficiency of these detectors in the near-IR and the steep decreasing slope of their sensitivity with wavelength render CCDs impracticable for the purpose of our spectrograph here.

5.9.2 Reducing integration time

The previous analyses considered worst cases in terms of efficiency for different parameters such as FRD properties of fibers. This section intends to identify better observing conditions and the associated integration time saving when some of those characteristics inherit from less pessimistic values. Only NIR-specific detectors are studied as CCDs were shown to be unsuitable in this wavelength range for their highly wavelength-dependent sensitivity, especially in the targeted part of the spectrum.

Better seeing conditions

A typical seeing of 2 arcsec was previously considered. However, better seeing conditions may appear at La Luz observatory and reach the value of 1 arcsec . It may therefore be worth simulating these observing conditions and calculating the required integration time in this situation. Figure 5.27 introduces the results of the radiometric budget when using an InGaAs detector under good seeing conditions to observe both cool (left panel) and hot stars (right panel). We can see that magnitudes up to 6 in J -band can be observed when considering cool stars while stars as faint as magnitude 7 fulfill the requirements when targeting hot stars.

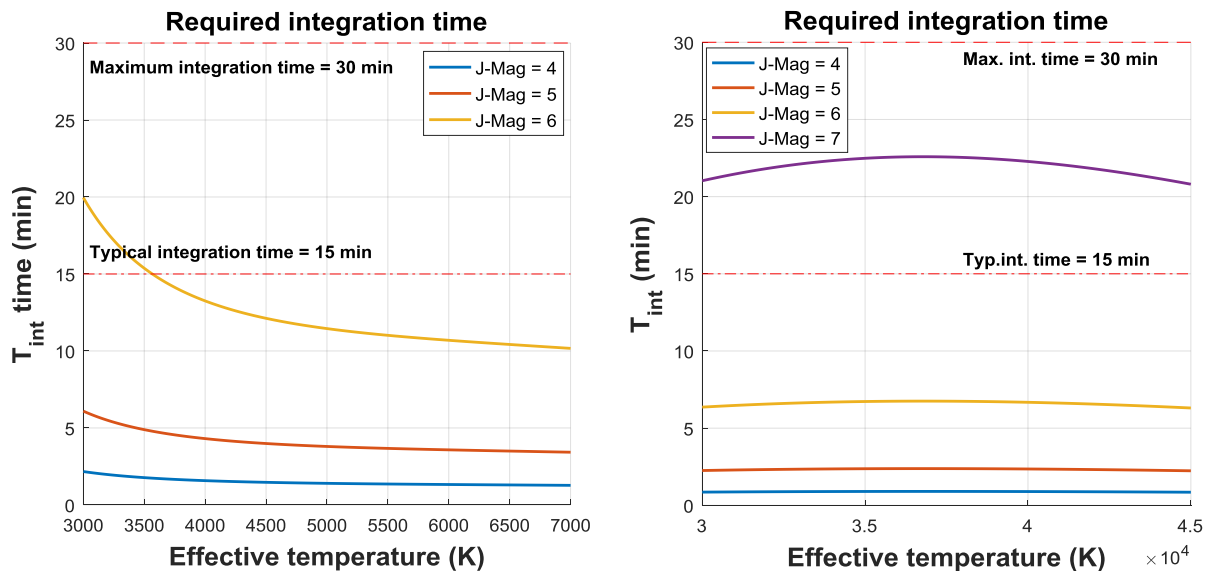


Figure 5.27 – Required integration time under better seeing conditions for cool (left) and hot stars (right).

Lower FRD losses from fibers

As for the seeing parameter, lower FRD fibers are tested according to Barden’s measurements [41]. Less light will then be lost at the collimator and the photometric budget improved. The simulation results are depicted in Figure 5.28. The integration time is effectively decreased as hot stars of magnitude 6 are now observable within an integration shorter than 30 min. The previously observed limit on cool stars’ effective temperature eventually vanishes.

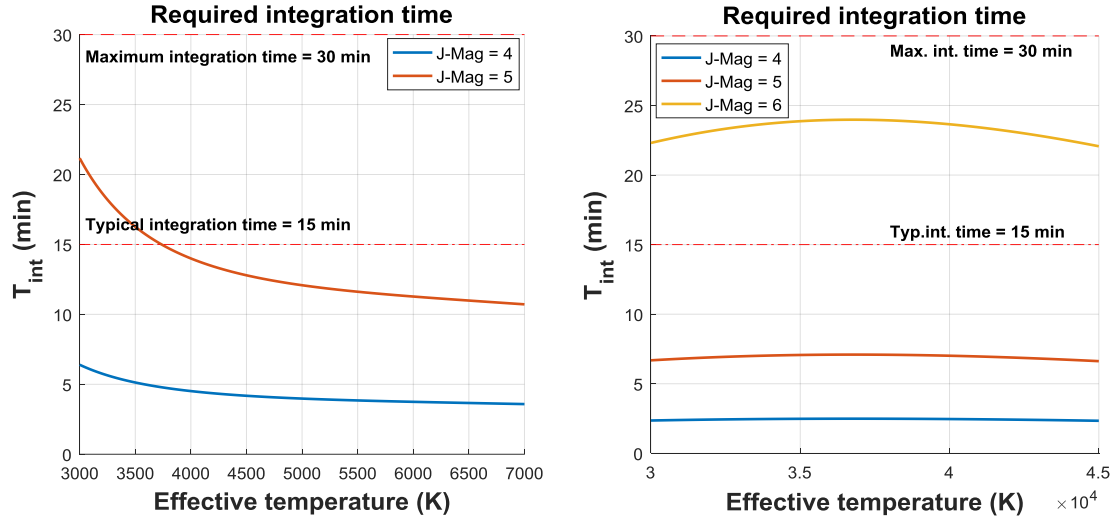


Figure 5.28 - Required integration time with lower FRD fibers for cool (left) and hot stars (right).

Use of micro-lenses

The goal of this analysis is to explore the possibilities of reducing the needed integration time by improving the performances of the telescope-spectrograph association. Indeed, a large vignetting effect is induced by the fact that the fibers do not accept the entire light received from the star under typical seeing conditions. On the other hand, the instrument suffers from the FRD losses of the fiber which enlarge the angular cone of light from the telescope and overfill the collimator. The table below illustrates the individual vignetting factors and FRD properties of the fibers as well as their cumulative effect:

Parameter		Transmission
<i>Fibers (core)</i>		$(50/93.08)^2 \approx 28.85 \%$
<i>Fiber FRD losses</i>	<i>Bad fibers.</i>	71.26 %
	<i>Good fibers</i>	94.37 %
<i>Cumulative effect</i>	<i>Bad fibers.</i>	$0.2885 * 0.7126 \approx 20.56 \%$
	<i>Good fibers</i>	$0.2885 * 0.9437 \approx 27.23 \%$

Table 5.5 - Transmission factors of fibers

From this table we can conclude that approximately only 20 % of the incoming light from the telescope is injected to the spectrograph. Therefore, improving these transmission factors would drastically reduce the required integration time. Two solutions may therefore be investigated:

increasing the fiber core diameter and/or decreasing the collimator's $F\#$. Figure 5.29 below illustrates these potential improvements on the required integration time for a star whose effective temperature and J -magnitude are 35000 K and 6 respectively.

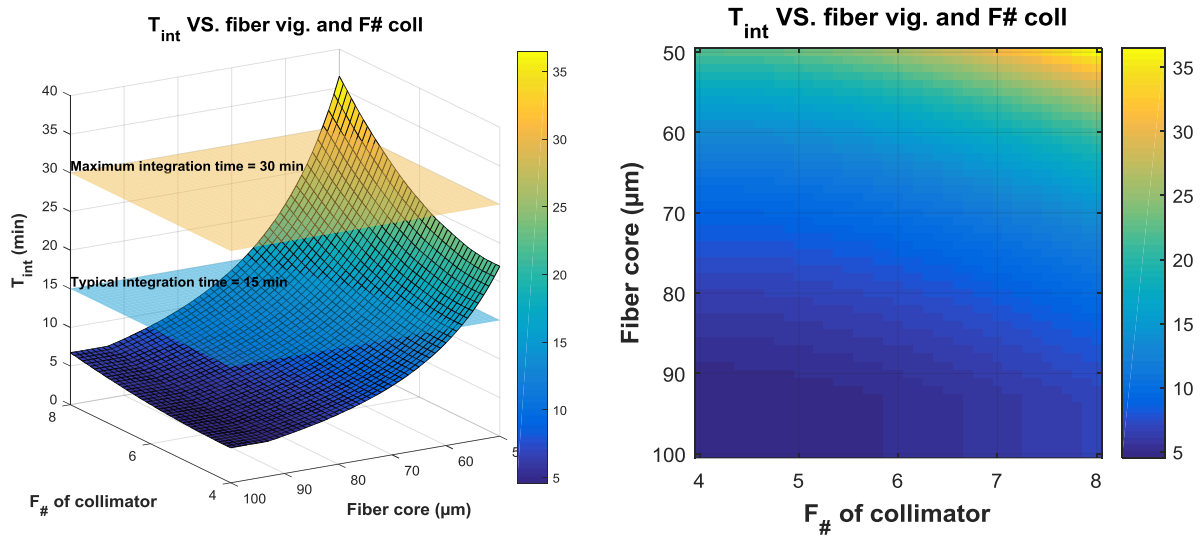


Figure 5.29 - Vignetting effect of fibers and instrument' collimator on integration time

We can clearly see that increasing the fibers' core diameter and reducing the $F\#$ of the collimator lead to a large reduction in the observation time. From nearly 37 minutes, the integration time drops to less than 5 minutes in the optimal case.

Figure 5.30 then illustrates two particular cases: the evolution of the required integration time when the fiber core is equal to 100 μm (left panel) and when the collimator's $F\#$ is equal to 4 (right panel). We notice that increasing the fiber core size leads to shorter integration times much faster than a decrease of the instrument's $F\#$ according to the foreseen FRD losses. This may be the first parameter to act on in the future in order to improve the instrument's radiometric performances. However, this observation time saving will be obtained to the detriment of the resolving power of the instrument.

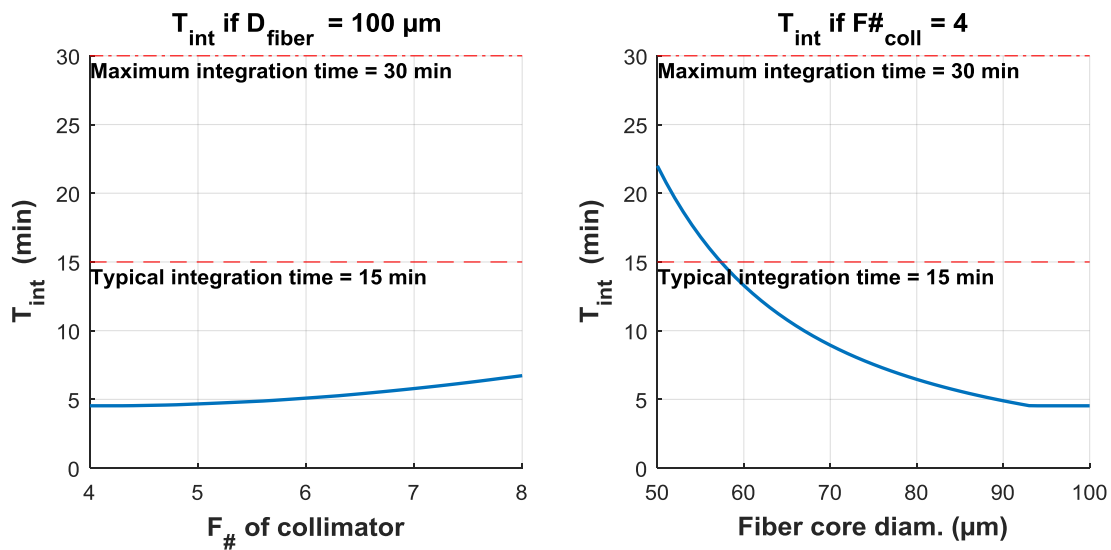


Figure 5.30 – Evolution of integration time at optimal fiber core size (left) and when the collimator's f-ratio is equal to 4

As suggested earlier, using micro-lenses at both fiber ends to collect all the flux from the star image and inject it into $50\ \mu\text{m}$ fibers could lead to increased light collection. Indeed, both vignetting of the fiber core and the FRD losses would be decreased as the injected $F\#$ into the fiber entrance would be close to 4. This solution has to be investigated since it would induce huge benefits concerning the radiometric budget of the instrument. Using such a technique would potentially mimic the use of larger fiber cores with the exception that FRD losses would be highly mitigated since the transported $F\#$ through the fiber is this time equal to 4. The pictures below eventually show the required integration time we may obtain by implementing micro-lenses at both ends of the fiber bundle when considering cool and hot stars.

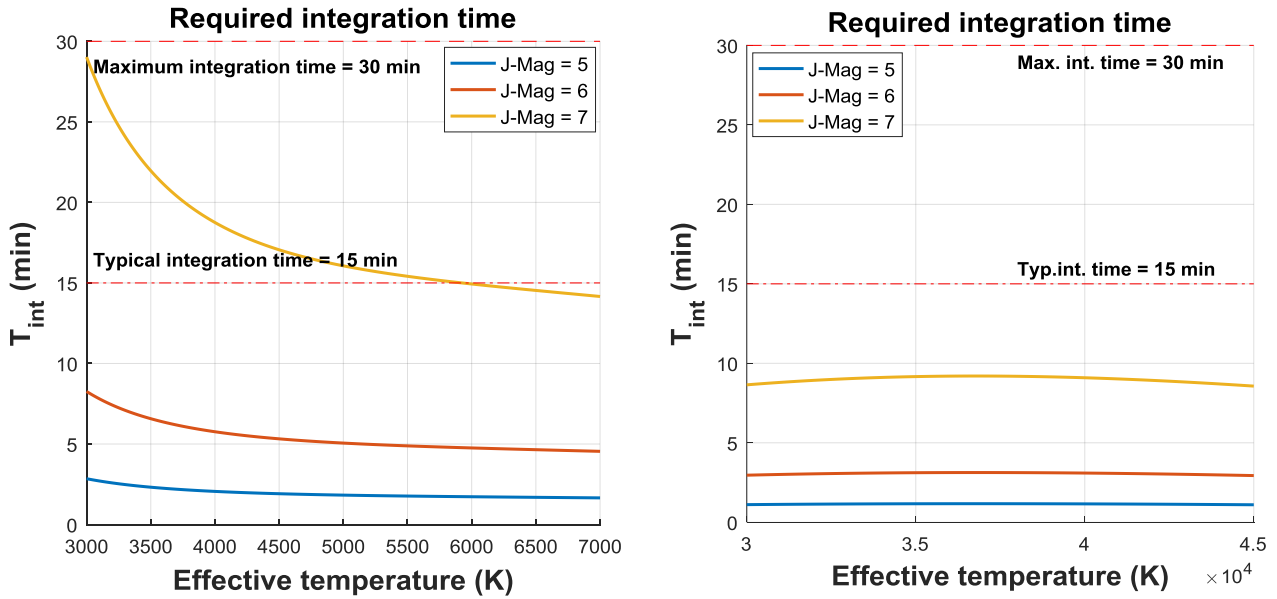


Figure 5.31 - Required integration time when implementing micro-lenses (left: cool stars, right: hot stars)

We can see that in this configuration, a signal-to-noise ratio of 100 is achieved for J -magnitudes ranging from 5 to 7 within the full range of considered effective temperatures. Such an optical design would fulfill the SNR requirement over 3 magnitudes starting from 5.

5.10 Conclusion

The photometric budget of the instrument enabled to estimate the integration time that is needed to achieve the required signal-to-noise ratio. Several parameters were taken into account such as the instrument's performances and an atmospheric transmission model. Then, a rather wide range of stellar effective temperatures was under study. The appropriate corresponding stellar parameters were employed, as well as the absorption law in the waveband of interest.

Both typical NIR detectors and CCDs were considered. The major advantage of the first category is its high quantum efficiency, which leads to suitable integration times even if light losses appear at the fiber ends. The high level of dark current of less expensive models is the main disadvantage of specific NIR detectors. CCDs on the other hand are much cheaper and avoid the use of complex cooling systems that are required for specific NIR detectors. However, their poor quantum efficiency leads to restrictions on wavelength coverage and effective temperatures. Eventually, our analyses showed that the ideal operating temperature of CCDs is usually higher than the lowest operating one that can be reached with a standard cooling system. Deep cooling conditions and the associated low dark signal are however required when targeting faint stars.

Then, more optimistic observing scenarios were simulated as well as potential sources of photometric budget improvement. Better seeing conditions and high quality fibers showed encouraging results. Naturally, adapting the collimator's $F\#$ also represents a way to collect more photons but was previously shown to be less feasible during the optical design of the instrument.

Finally, a potential suitable solution to solve the vignetting induced by small fiber cores would be to use micro-lenses at both ends of the fiber bundle. Indeed, the use of such optical devices seems to be of good practice to reduce the needed integration time. Those would entirely collect and inject the light from the stellar image into the fibers and adapt the telescope $F\#$ to lower values for better FRD attenuation. A major decrease in integration time could then be achieved while simultaneously somewhat decreasing the resolving power of the spectrograph. Indeed, this would come at the expense of a certain degradation of the spectral resolution as it is similar to a slit widening.

Following completion of the optical design and validation of its associated performances, the photometric budget of the instrument confirmed its feasibility as a new instrument for the TIGRE telescope. The estimated integration times approach the requirements even though slightly lower magnitudes need to be considered. The assembly and alignment of the instrument could then start to assess the practical performances that could be achieved and validate the previous optical calculations. Chapter 6 is dedicated to those considerations.

Chapter 6

Alignment and tests
of the instrument

6. Alignment and tests of the instrument

This chapter intends to introduce the practical alignment steps that were followed to assemble the spectrograph and assess its optical performances. The obtained experimental results are eventually compared to the simulated ones in order to verify their consistency.

6.1 Fiber illuminating setup

To align the spectrograph instrument, a fiber illumination system was first implemented (see Figure 6.1). This set-up consists in two laser sources that are coupled to the fiber bundle that will be used at the TIGRE telescope. The first light source is a visible HeNe laser which emits at 632.8 nm while the second one is a Nd:YAG whose emitted wavelength is equal to 1064 nm . Those light sources are coupled with a dichroic window which bends the laser beams to a spatial filter made of two microscope objectives that are separated by a pinhole. Two polarizers can then be rotated with respect to each other to set the illumination level to a proper value and avoid detector saturation. Eventually, another microscope objective focuses the light into a selected fiber within the bundle. This operation is performed with the help of the X - and Y -movements of the bundle mount.

This fiber illumination system features both visible and near-infrared options. This versatility is a very handy tool as it enables to first align the spectrograph in visible light and then proceed with a near-infrared wavelength that is located close to the central scientific wavelength of 1050 nm . As presented in the next section, the practical alignment was first performed in visible wavelength since only one chromatic element is contained within the spectrograph. When switching to the near-infrared waveband, only a focus correction is required to recover the best alignment position. This is the reason why the alignment of the spectrograph was first carried out in red light and then followed by a near-infrared verification which eases the laboratory operation since the near-infrared laser light is not visible, and dangerous, to the human eye.

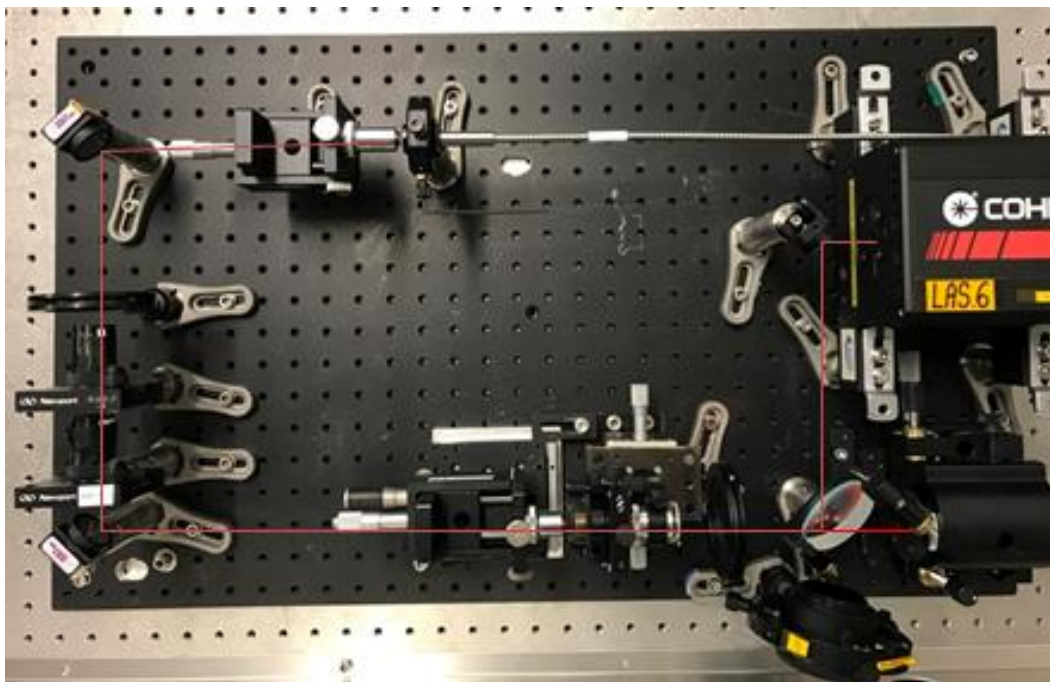


Figure 6.1 - Fiber illuminating system

6.2 Visible alignment of the spectrograph

A visible alignment of the instrument is first carried out as described further in this chapter. The reflective behavior of the instrument eases its operation at another wavelength. The only incorporated refractive element is the toroidal lens and a small refocus operation of the detector will be required when switching to near-infrared light. The dispersion of the diffraction grating however exhibits a wavelength-dependent behavior. Indeed, the Bragg relation (see Eq. (5)) writes:

$$m \lambda = 2 d \cos \gamma \sin \theta_B \cos \theta$$

The wavelength parameter λ of this equation is involved in a product whose second term is the grating order m . Therefore, changing the grating order and adapting the wavelength in such a way that their overall product remains the same keeps the spectrograph geometrical configuration unchanged. Using visible light approximately consists in dividing the design wavelength by 2 when considering the near-infrared waveband.

In other words, using the 2nd order of the diffraction grating enables the spectrograph to be used in a geometrical configuration close to its conception design. The difference in optical performances is therefore limited and is dominated by the chromaticity of the toroidal lens. This is why a HeNe laser whose emitted wavelength is equal to 632.8 nm is selected for the visible tasks. A slight grating rotation will therefore be required to center this wavelength on the detector since $1050/2 = 525 \text{ nm}$ (see Chapter 6.2.2 for the calculation of this updated incidence angle).

6.2.1 Identification of fibers

The visible alignment of the spectrograph required first to highlight the relationship between the fibers from both ends of the bundle. This enabled to identify which fiber from the entrance of the bundle lies in the middle of its exit side, i.e. the entrance slit of the spectrograph. This fiber was then used as a reference for all subsequent alignment steps.

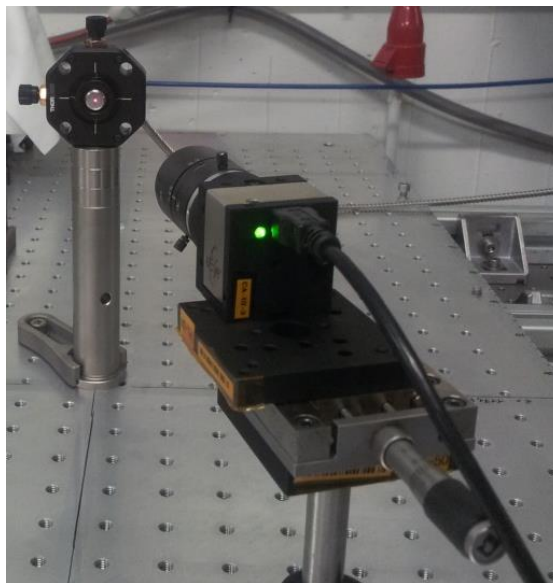


Figure 6.2 - Identification of relation between input and output fibers from the bundle

6.2.2 Installation of the collimator and grating

After having positioned the fiber bundle, the collimator was installed at its theoretical location with the help of theodolites to properly set its off-axis inclination. As a second step, the diffraction grating could be fixed on the optical bench of the spectrograph. The fiber bundle was then set in auto-collimation with the grating which means the central fiber and its associated image are co-aligned (see Figure 6.3).

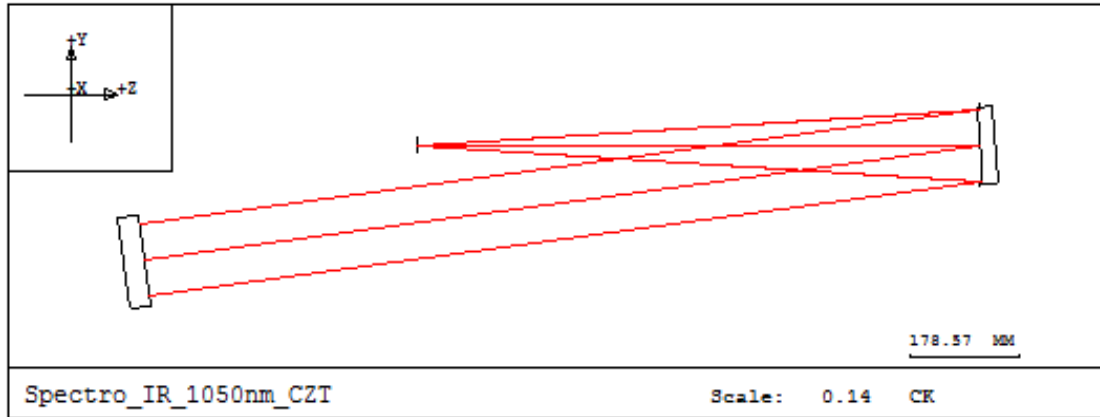


Figure 6.3 - Fiber bundle in auto-collimation with the diffraction grating. Light travels back and forth on the grating to focus at the bundle plane.

This way, the fine alignment of M_1 with respect to the grating principally consisted in adjusting the focus setting screws of the bundle mount to optimize the fiber image size. This parameter was identified as the coupled element during the tolerancing analysis which enables the correction of both radius of curvature and piston position uncertainties of M_1 .

The rotation stage was homed while performing these operations so that auto-collimation onto the grating corresponds to setting the rotation stage to 0° (see Figure 6.4). The calculation of the required angle of incidence to center a selected wavelength onto the detector then uses Bragg's relation. Since the geometrical configuration of the spectrograph does not vary while moving the grating, the collimator-grating-focusing mirror angle remains constant during this movement ($\alpha - \beta = \text{constant}$ though α and β do vary). From the Bragg relation (Eq. (5)):

$$m \lambda = 2 d \cos \gamma \sin \theta_B \cos \theta$$

we obtain if $\gamma = 0$:

$$2 \sin \left(\frac{\alpha + \beta}{2} \right) \cos \left(\frac{\alpha - \beta}{2} \right) = \frac{m \lambda}{d}$$

and we get for each wavelength the updated value for $\alpha + \beta$ with the following:

$$(\alpha + \beta)_{new} = 2 \operatorname{asin} \left(\frac{\frac{m \lambda}{d}}{2 \cos \left(\frac{(\alpha - \beta)_{const}}{2} \right)} \right)$$

where $(\alpha - \beta)_{const}$ is the constant angle between the focusing and the collimating mirrors.

The incident angle by which the rotation stage has to turn is eventually calculated as follow:

$$\alpha_{new} = \frac{(\alpha + \beta)_{new} + (\alpha - \beta)_{const}}{2} \quad (16)$$

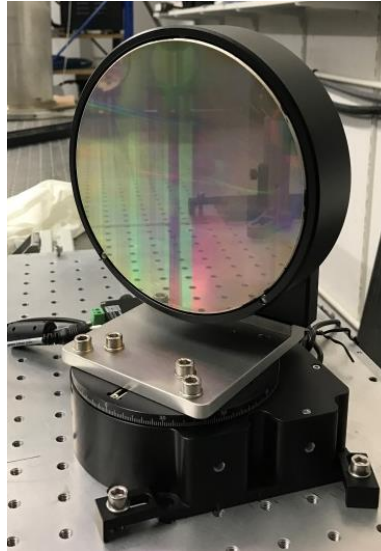


Figure 6.4 - Diffraction grating on top of its rotation stage

6.2.3 Positioning of the focusing mirror

The alignment of the focusing mirror is based on the optimization of spots on a visible camera. Though their geometrical size largely exceeds those that will be observed with the toroidal lens, their minimization leads to the best positioning of this optical element. As mentioned earlier, the visible alignment of the spectrograph requires the use of the grating's second diffraction order. This way, the visible light follows the same initial near-infrared light path. To position the focusing mirror, the grating is therefore now oriented at the right inclination to adopt the right geometrical configuration (see Figure 6.5).

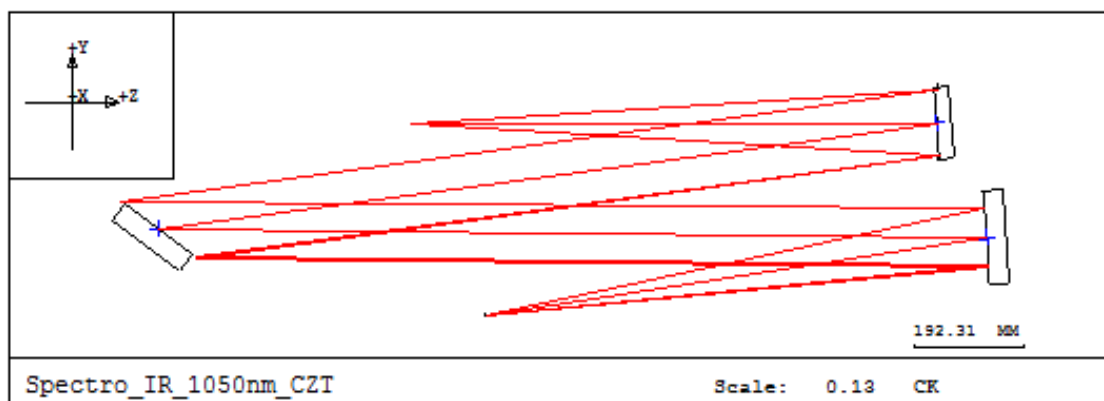


Figure 6.5 – Optical configuration that enables the alignment of the focusing mirror. The grating is positioned at the right inclination to enable the 2nd diffraction order to propagate through the system.

The observed visible image of the central fiber of the bundle at the temporary focal plane of the instrument is presented in Figure 6.6. The speckle pattern arises from the interference of the several modes running through the selected multimode fiber. The mean calculated RMS spot value from the recorded 15 fiber images is equal to $410 \mu\text{m}$. This value confirms the order of magnitude of the related simulated alignment step within the optical model of the instrument that is equal to $310 \mu\text{m}$.

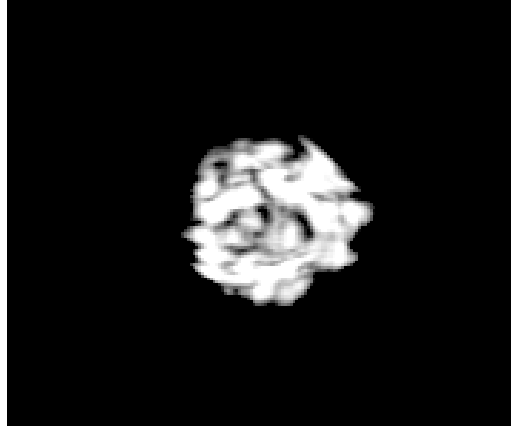


Figure 6.6 - Central fiber visible image through the imaging mirror

The difference between both simulated and measured spot sizes comes from the fact that the simulated Gaussian profile does not appear within the experiment due to the interference pattern that is observed. These energy concentration spots interfere with the RMS size calculation algorithm. A slight scrambling of the bundle might have smoothed the observed profile and led to closer results. To optimize the spot sizes, the mirror tilt was slightly tuned after having locked its position in order to benefit from the coupling relation that exists between M_1 and M_2 . Figure 6.7 illustrates both mirrors when properly aligned on the optical bench.

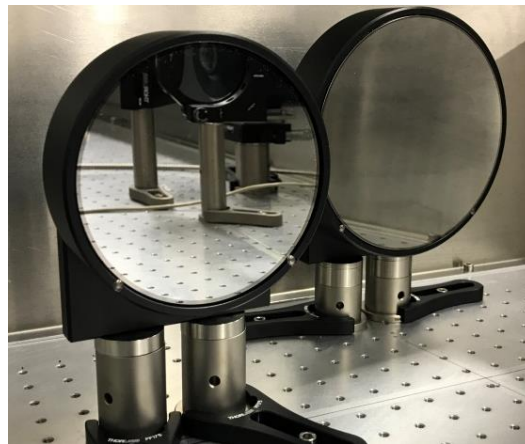


Figure 6.7 – Collimating (*left*) and focusing (*right*) mirrors

6.2.4 First spot verification with the toroidal lens

The ultimate imaging element to be settled is the toroidal lens (see Figure 6.8). The asymmetric geometry of this element intends to mitigate the astigmatic behavior of the spectrograph. The only chromatic correction to be applied to the instrument to obtain similar visible spots is a slight focus of the detector. This way, the observed spots when illuminating the bundle with the HeNe laser should closely approach their final dimension in near-infrared. The alignment of the lens is therefore not wavelength-dependent and may be carried out with the HeNe laser.

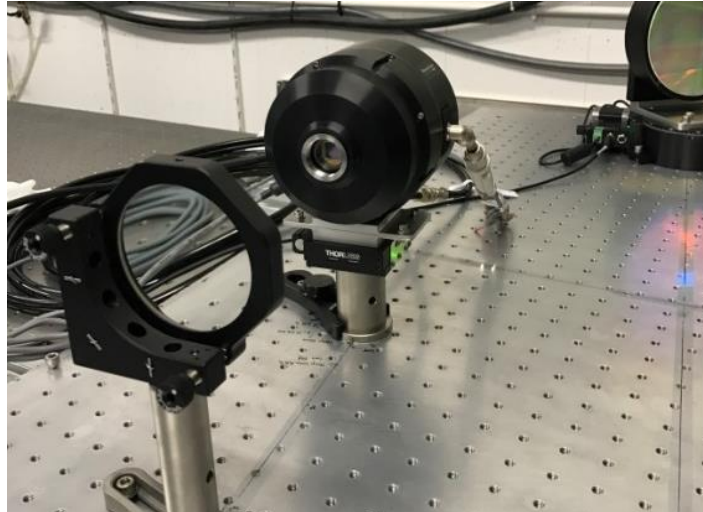


Figure 6.8 – Toroidal lens in its optical mount

The simulated and observed spots of the central fiber are shown in Figure 6.9. The foreseen horizontal asymmetry in the energy distribution within the fiber image appears and the average RMS spot dimension of $50\ \mu\text{m}$ is nearly reached as it is measured to be $62\ \mu\text{m}$. Since the observed spots in visible light converge to their simulated behavior, the visible alignment comes to a successful end. The reduced spot size with respect to the one measured previously without the toroidal lens attenuates the speckle influence on the measured spot diameter.

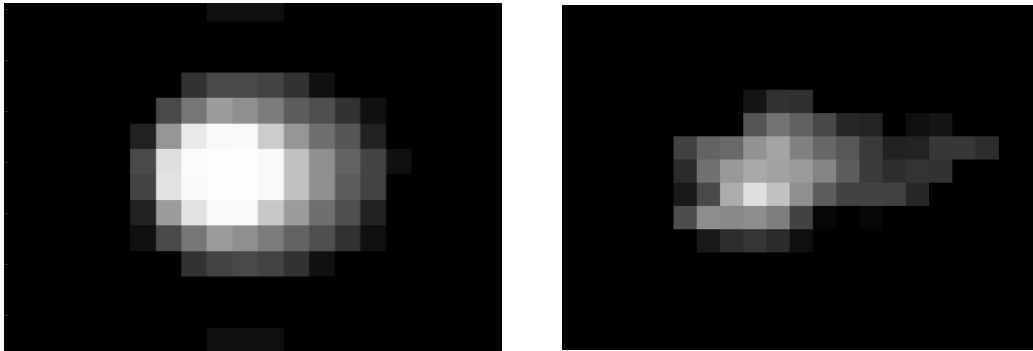


Figure 6.9 – Simulated (*left*) and observed (*right*) images of the central fiber

6.3 Going to the near-infrared

The visible alignment of the instrument ended with the recording of spots whose spatial extents are close to their simulated sizes. After validation of this initial process, the near-infrared verification of the alignment could be initiated. The Nd:YAG optical path from the fiber illumination system was then activated to propagate to the spectrograph a light beam at $1064\ \text{nm}$. This wavelength perfectly fits the requirements for the spot verification as it is right at the centre of the scientific waveband of interest.

Before evaluating the near-infrared optical performances of the instrument, the flat mirror is installed in order to fold the light beam and install the near-infrared camera at its final location on the optical bench (see Figure 6.10). At this point, the main spectrograph channel through which both observation and calibration lights propagate is operational. The near-infrared laser light may therefore be settled to investigate the optical quality of the spectrograph within its designed wavelength range.

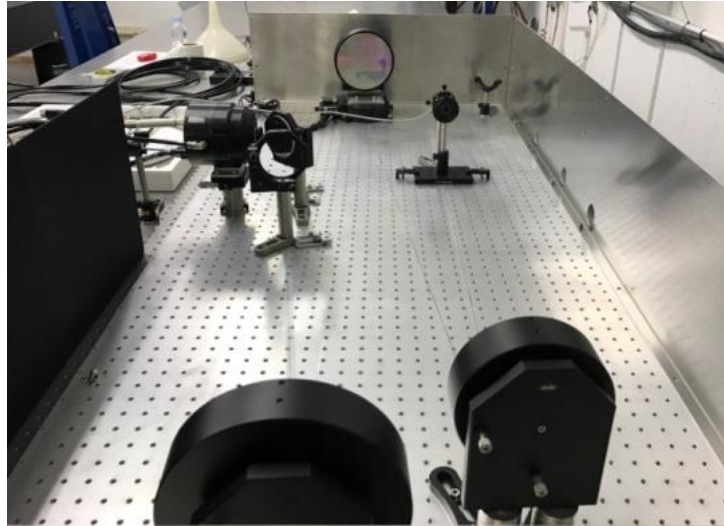


Figure 6.10 - Full spectrograph main channel assembly

Figure 6.11 introduces both simulated and observed bundle images. The experimental picture of the bundle comes from the superposition of the individual fiber images since only a single fiber can be illuminated at once with the microscope objective from the fiber illumination system. The whole bundle may be irradiated with the help of a diffuser located between the fibers and the microscope objective but this is avoided as it leads to non-uniform illumination of the fibers and poor spot size evaluation. The speckle pattern which superposes on the fiber image is still visible even though the spots are smaller than in the visible region. Due to this interference phenomenon, the fibers look like being laterally shifted from each other but they are not as will be confirmed with polychromatic light further in this chapter. The individual pictures were obtained by averaging several frames while scrambling the bundle but the effect remains visible. On the other hand, another disturbing effect comes from the vibrations induced by the camera cooler that transfer to the close spectrograph. This effect becomes more dominant as the optical quality of the spectrograph increases.

The detector position was adapted to minimize the image of all fibers. Indeed, the tolerancing analysis previously highlighted that a misalignment of the fold mirror could be corrected by repositioning the detector. The simulated average RMS spot size of $35 \mu\text{m}$ is closely approached since the experimentally measured one amounts to $45 \mu\text{m}$. Both visible and near-infrared performances are therefore validated. This precise monochromatic evaluation must then be extended to the whole spectral waveband of interest to assess the resolving power not only locally.

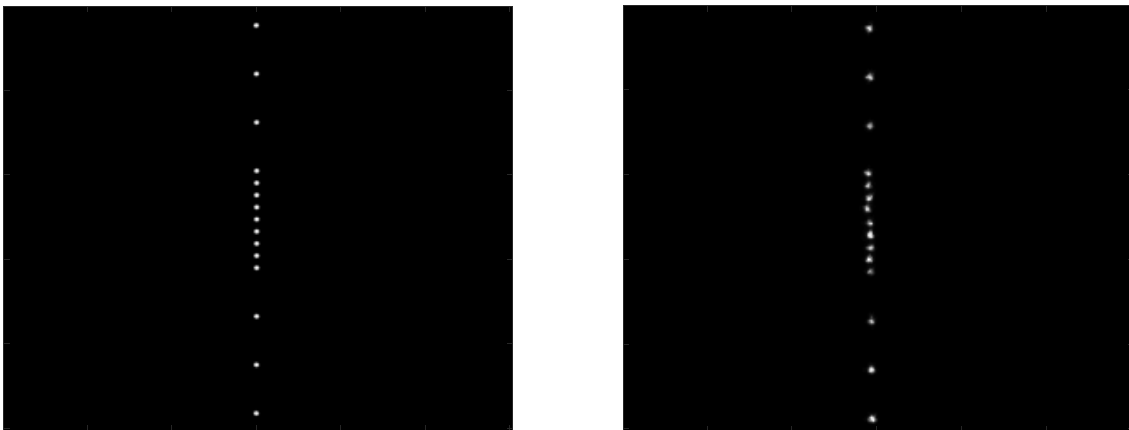


Figure 6.11 – Simulated (*left*) and measured (*right*) bundle images

6.4 Polychromatic performances

The previous section illustrated the different steps the visible and near-infrared alignments were made of. The optical performances of the instrument were evaluated with monochromatic laser light in order to measure the Point Spread Function of the spectrograph. The optical quality on the sides of the focal plane of the instrument was also sampled by rotating the grating in order to decenter the image of the bundle. The detector tilt was then optimized to obtain spot sizes whose diameters are constant from one side of the detector to the other, i.e. through the entire imaged wavelength range.

This section now introduces the polychromatic behavior of the instrument. For that purpose, the fiber injection system presented in Chapter 6.1 was modified in order to enable the fiber bundle to be lit with polychromatic light. As can be seen in Figure 6.12, a translation stage is employed to be able to either position the bundle into a path where laser light propagates or collect photons from the HCL. In order to maximize the coupling efficiency between the fiber and the lamp, a lens is used to image the cathode onto the bundle.



Figure 6.12 - Adapted fiber illuminating system incorporating a UNe hollow cathode lamp

6.4.1 UNe hollow cathode lamp spectra

The polychromatic performances of the instrument are investigated by observing *UNe* spectra generated with the help of a hollow cathode lamp from Photron. This way, the resolving power of the spectrograph can be measured by first calibrating the dispersion relation through the focal plane and then evaluating the spectral profile of selected lines. The identification of the observed spectral lines is performed by comparing the experimental spectrum with the atlas from Redman et al. that was previously presented in Chapter 4.7.1 [74]. As explained further in that section, two lamps are tested within the experimental setup. The first one is the Superlamp model, which we selected because it was presented as more luminous than the standard version. A major issue immediately appears when looking at the focal plane of the instrument and comparing with Redman's atlas: only a few lines are visible whereas the atlas indicates that a large number should appear. This situation is illustrated in Figure 6.13 where the recorded spectrum of the Superlamp centered at 1082.6898 nm is depicted. As can be seen, only two lines appear while Redman's atlas, which is shown in Figure 6.14, lists several lines which do not show up in our experimental results. Moreover, two missing lines that should appear between the ones that are recorded practically exhibit high relative intensities. Therefore, this situation does not arise from an insufficient exposure time.

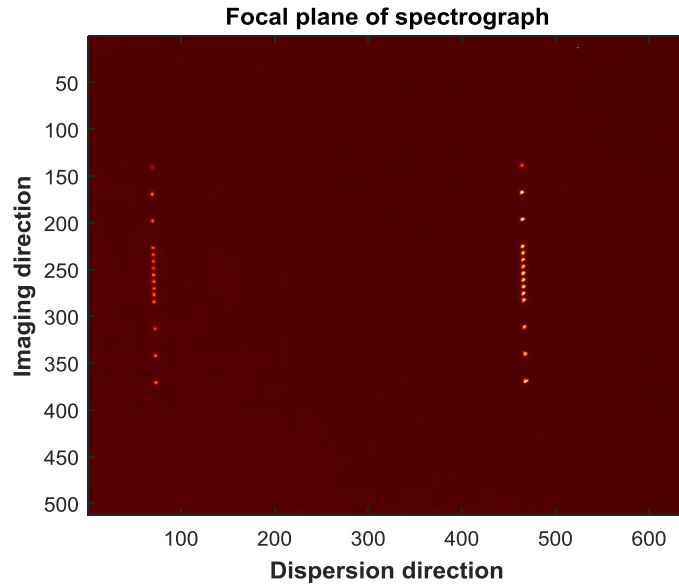


Figure 6.13 – Recorded spectrum of the Superlamp HCL centered at 1082.6898 nm

After having explored potential reasons explaining the origin of this problem, we observed that only *Ne* lines actually appear on the detector. *Ne* lines that are observable within the spectrograph focal plane are highlighted in Redman’s atlas in Figure 6.14. Explications of this phenomenon were then obtained from the manufacturer: Superlamps boost the primary emission line of the uranium cathode, which is located at 358.5 nm, but actually totally suppress all other secondary lines at the same time. This mechanism was unexpected and unforeseen from our side and a standard HCL was then ordered to replace the Superlamp as the latter is not suited for astronomical calibration purposes.

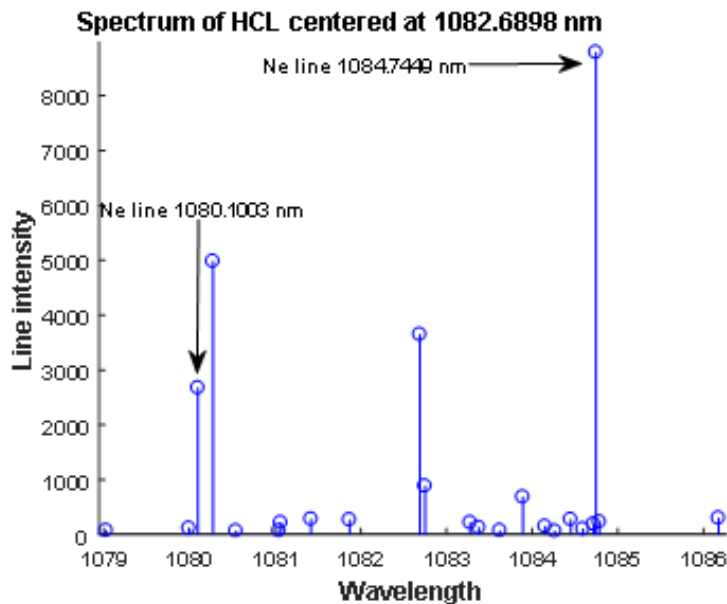


Figure 6.14 - Recorded spectrum of a *UNe* HCL by Redman et al. [74]

A new spectrum is presented in Figure 6.15 where a regular HCL is inserted in front of the fiber bundle. Uranium lines can finally be observed and confirm our previous hypothesis that only the primary emission line of uranium was observable. It might be noticed in Figure 6.15 that the recorded intensities of the *Ne* lines do not follow those given in Redman’s atlas. This is due to the fact that those gas lines suffer from pressure, temperature and Doppler effects and are not suited for spectral

calibration, as stated in Chapter 4.7.1 [70]. Their intensity may therefore vary from one HCL to another. These gas lines are expected to shine very brightly as previously stated in Chapter 4.7.1 and may lead to detector saturation problems. Figure 6.15 illustrates the difference between the observed brightness of the lines and the one expected from Figure 6.14. *Ne* lines are indeed extremely intense with respect to *U* ones and will for sure limit the integration time.

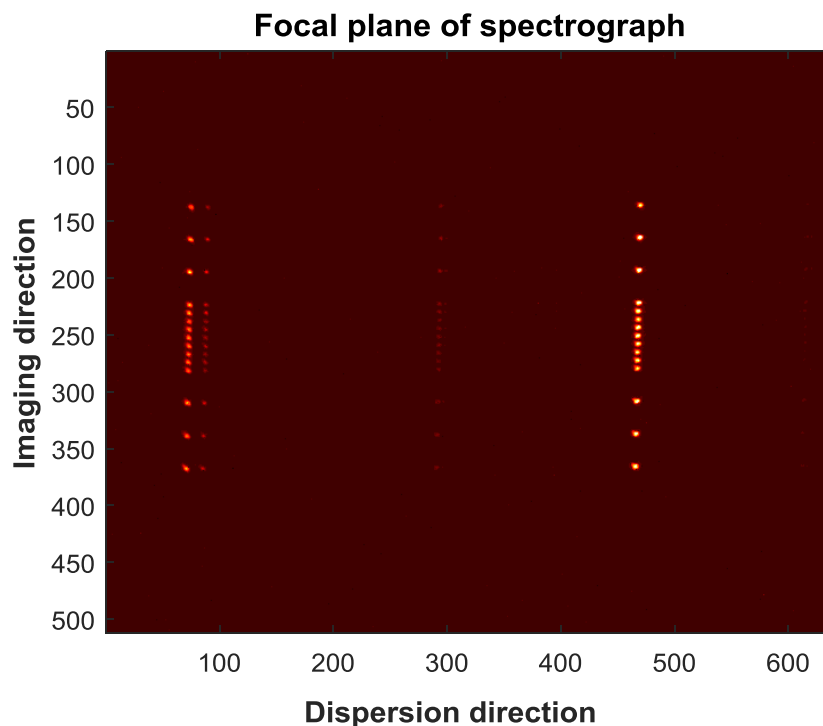


Figure 6.15 - Recorded spectrum of the regular HCL centered at 1082.6898 nm

Other example spectra are recorded at respectively central wavelengths of 945.5 nm, 994.9162 nm, 1006.1 nm, 1059.30 nm, 1071.9 nm and 1119.03 nm. These wavelengths span the whole scientific waveband of interest and investigating the spectrum quality at these locations enables exploring the instrument's global optical efficiency. On the other hand, these precise regions of the spectrum are selected for the existence of specific doublets within these ranges as explained further in this chapter. The focal plane images and the associated reduced spectra are presented in Figure 6.16 and Figure 6.17.

Figure 6.16 (a) and Figure 6.17 (a) and (c) contain at least one *Ne* line as can be noticed from the reduced spectrum which exhibits at least one pronounced intensity peak. This remarkable feature is easily noticed as it completely outshines all uranium lines. These may be used during spectral calibration to quickly recognize some spectral features and identify subsequent uranium lines. Then, the dispersion relation calculation should avoid using those lines for the reasons cited before and concentrate on uranium lines only. When a *Ne* line appears in the spectrum of Figure 6.16 and Figure 6.17, these are intentionally truncated in order to emphasize fainter *U* lines. As said earlier, these spectral regions were selected thanks to the presence of specific doublets that were identified with a dedicated algorithm in order to perform a first check of the resolving power. This latter identifies within Redman's atlas spectral lines of sufficient intensity that are close enough to be resolved only if the instrument benefits from a sufficient resolving power. The algorithm also accepts couples separated by faint intermediate lines that cannot be detected by the detector. In other words, first neighbors are not the only candidates but up to four neighbors are allowed (three intermediate faint lines).

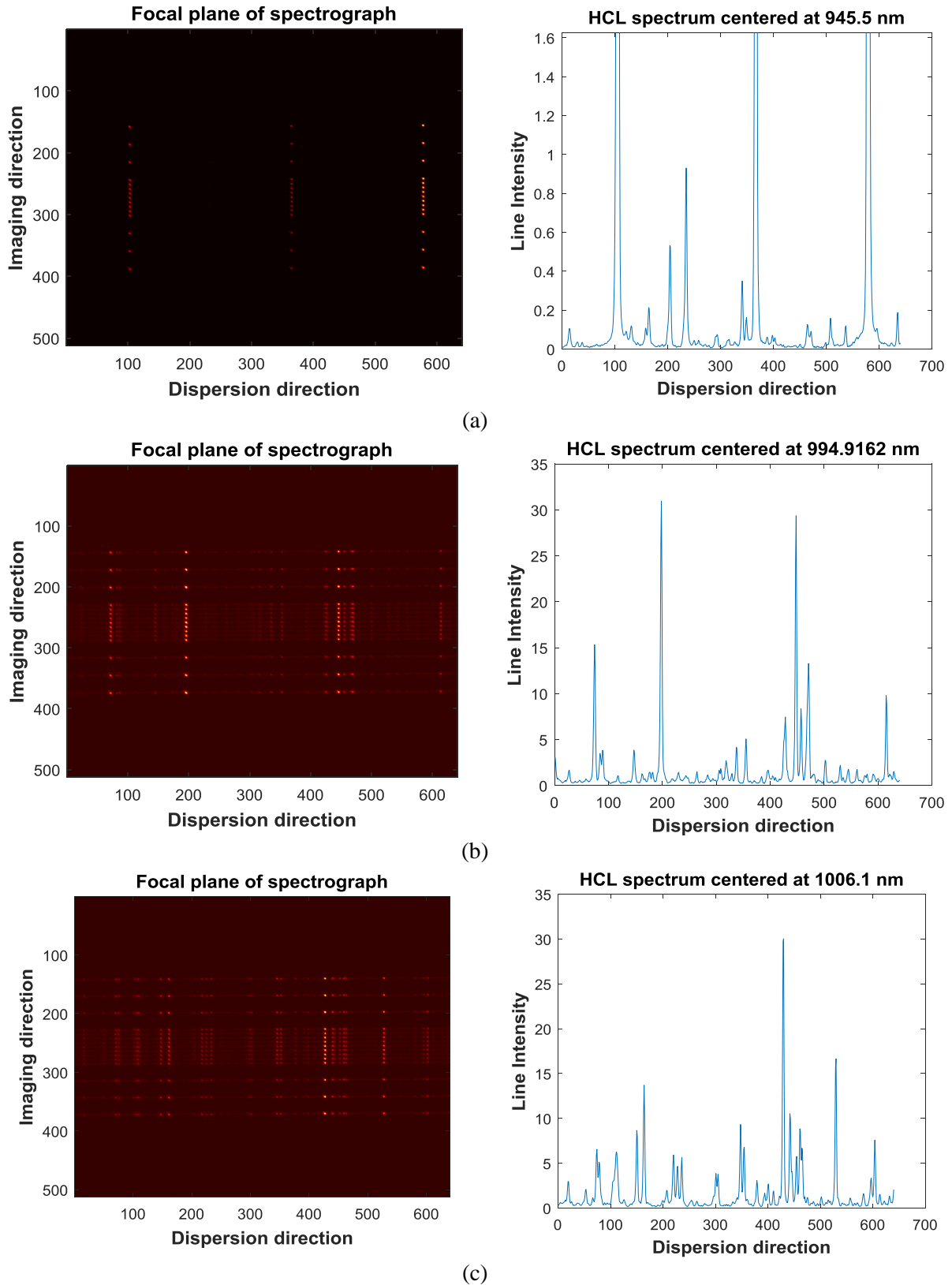


Figure 6.16 – Focal plane images (*left*) and reduced spectra (*right*) when observing the HCL spectrum centered at (a) 945.5 nm, (b) 994.9162 nm and (c) 1006.1 nm

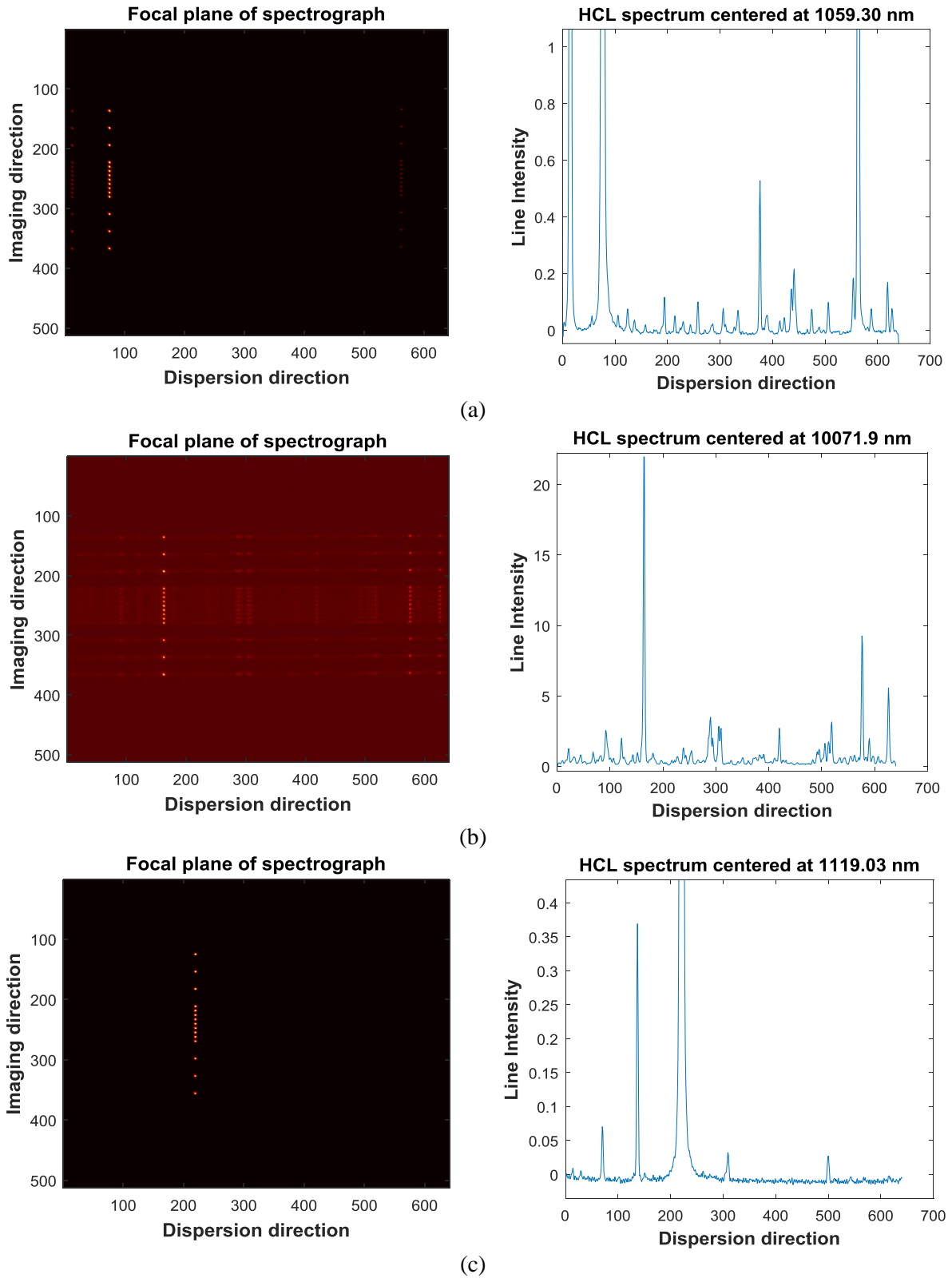


Figure 6.17 - Focal plane images (left) and reduced spectra (right) when observing the HCL spectrum centered at (a) 1059.30 nm, (b) 1071.9 nm and (c) 1119.03 nm

Observing these doublets with the instrument thus enables checking whether the required resolving power is reached or not. This assessment of the instrument optical performances is rather qualitative as it does not precisely measure the resolving power but rather investigates the identification of two adjacent spectral lines. This process is illustrated below (see left panel in Figure 6.18) when having a closer look at the two adjacent lines centered at 1006.1 nm that are images by the 9 central fibers. A zoom onto the focal plane image enables to identify to the naked eye the individual spectral features of interest within the spectrum close to the pixel column 302. These spectral lines are respectively centered at 1006.0344 nm and 1006.0827 nm and require a resolving power equal to 20899 to be distinguished on the detector.

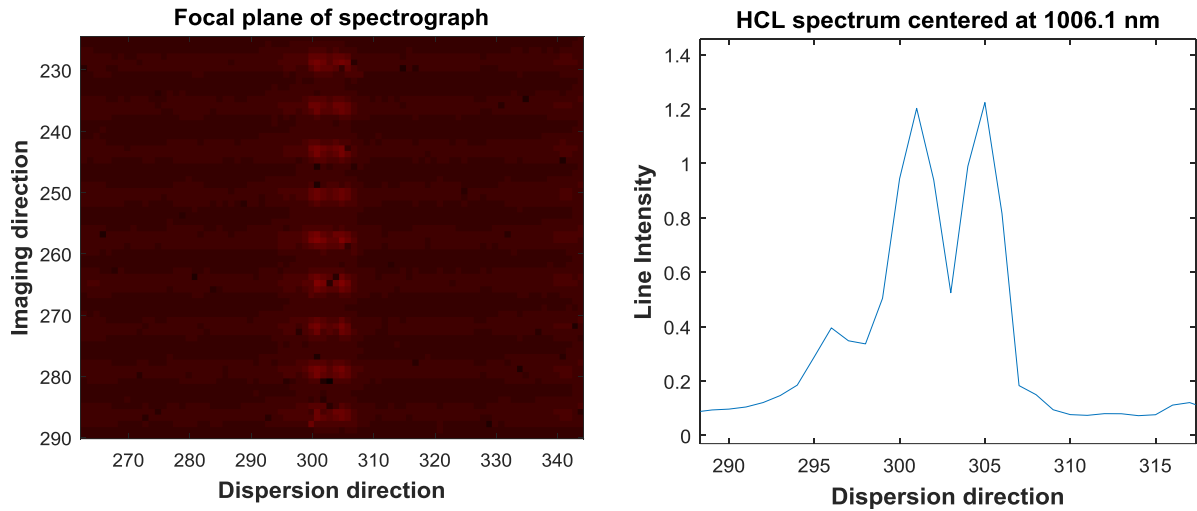


Figure 6.18 - Focal plane image (*left*) and reduced spectrum (*right*) when observing the HCL spectrum centered at 1006.1 nm

According to the Rayleigh criterion on resolving power that is depicted in Figure 6.19 (Chapter 3 employed this criterion to derive the expression of the resolving power), two sources can be resolved if the midway intensity between their two peaks is lower than 0.74 times the maximum intensity [52]. This criterion is fulfilled when looking at the right panel in Figure 6.19 since the maximum intensity is equal to 1.1 (when retrieving the continuum offset) and the midway value is 0.42 which is lower than $0.74 * 1.1 = 0.81$. The resolving power of 20899 is then largely exceeded. The analysis of the other spectral doublets presented before leads to the conclusion that the resolving power of the instrument, according to the Rayleigh criterion, is at least equal to 23246 which fulfills the goal requirement on resolving power that was specified in Table 1.1.

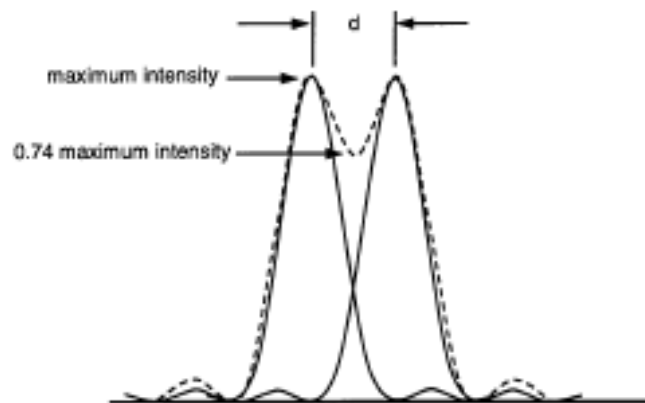


Figure 6.19 - Rayleigh criterion on resolving power [52]

6.4.2 Experimental resolving power assessment

The previous section ended with a first order resolving power evaluation. This latter is complemented by precise calculations of the focal plane dispersion and spectral line profiles. For that purpose, the *UNe* HCL spectrum centered at 1059.30 nm is used as this center wavelength lies in middle of the considered scientific waveband.

Figure 6.20 illustrates the reduced spectrum previously shown when observing the *UNe* HCL and centering the rotation stage at 1050.30 nm . Several spectral lines are identified with markers (red stars) with the help of the same portion of the HCL spectrum from Redman's atlas in Figure 6.20. The corresponding lines in Redman's atlas are highlighted with the help of red circles. *Ne* lines are intentionally truncated in order to visualize the fainter *U* lines.

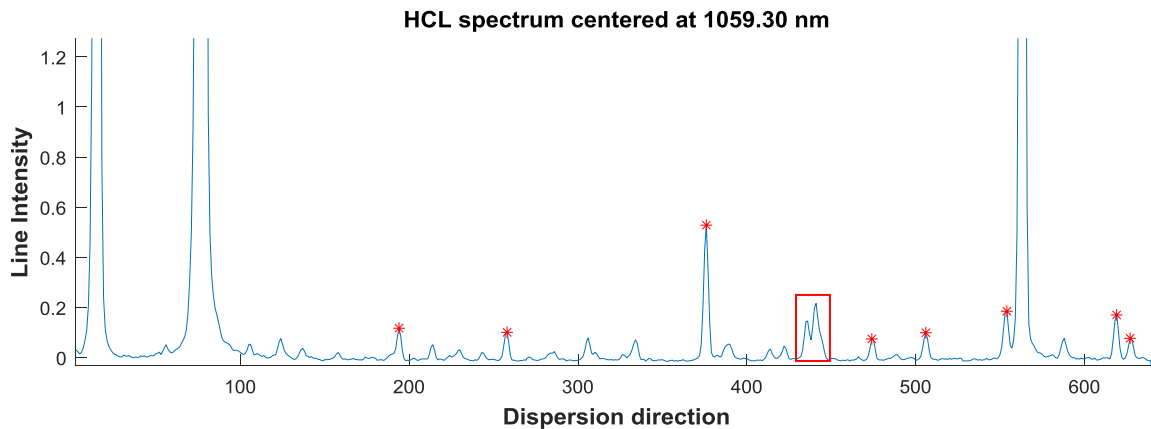


Figure 6.20 - Reduced spectrum when observing the HCL spectrum centered at 1059.30 nm , red stars indicate spectral lines used for calibration

The first high intensity line, which comes from the uranium cathode, is also truncated in the plot, but was retained to establish the dispersion relation. *Ne* lines are excluded from this calculation as explained earlier. The resolved doublet that motivated the examination of this region is represented by green and red spectral lines in Figure 6.21. The red rectangles from both figures eventually highlight another interesting doublet which can only be resolved if the resolving power exceeds 27064, which is another first order approximate lower limit.

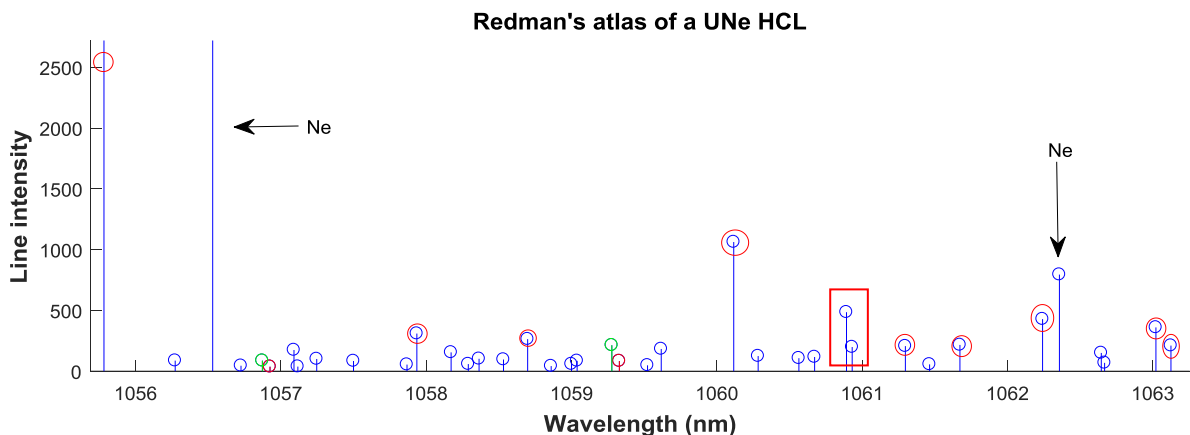


Figure 6.21 - Redman's atlas of a *UNe* HCL centered at 1059.30 nm . Red circles indicate spectral lines used for calibration.

Once the calibration lines are selected from the atlas and identified within the recorded spectrum, the dispersion relation can be established. The same process as the one followed during the resolving power analysis is then applied: a polynomial fitting is carried out between the calibration wavelengths and the detector pixels in order to obtain the calibrated spectrum. The dispersion relation when using a polynomial fitting of arbitrary order N writes as follow:

$$wav [nm] = p(1) \left[\frac{nm}{pix^N} \right] * pix^N + p(2) \left[\frac{nm}{pix^{N-1}} \right] * pix^{N-1} + \dots + p(N) \left[\frac{nm}{pix} \right] * pix + p(N + 1) [nm]$$

where the vector p contains the polynomial coefficients of the fitting. The obtained relation when fitting the selected lines from Redman's atlas with a second order polynomial is depicted in Figure 6.22.

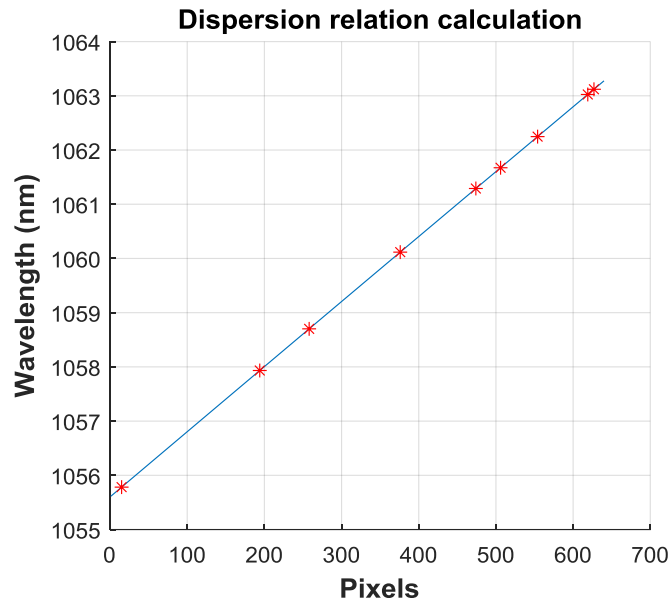


Figure 6.22 – Dispersion relation: the red stars are the spectral lines selected for calibration and the blue line is the 2nd order fitting.

The obtained values for p are the following:

$$p(1) = -6.48 e^{-8} \left[\frac{nm}{pix^2} \right], \quad p(2) = 0.012 \left[\frac{nm}{pix} \right], \quad p(3) = 1055.602 [nm]$$

They indicate a mostly linear dispersion as the 2nd order term tends to zero. The first order term, $p(2)$ in this case and $p(N)$ in general, is a direct measurement of the linear dispersion through the detector. The experimentally measured dispersion in Figure 6.22 amounts to:

$$p(2) = 0.012 \left[\frac{nm}{pix} \right] = 0.80 \left[\frac{nm}{mm} \right]$$

This result finely matches the value of 0.79 foreseen in Table 4.3 when the resolving power of the instrument was first assessed through optical simulations. Thanks to this polynomial fitting, the calibration of the measured spectrum can be processed that is presented in Figure 6.23. The abscissa that was previously measured in *pixels* is now expressed in *nm* and the spectrum is therefore wavelength calibrated.

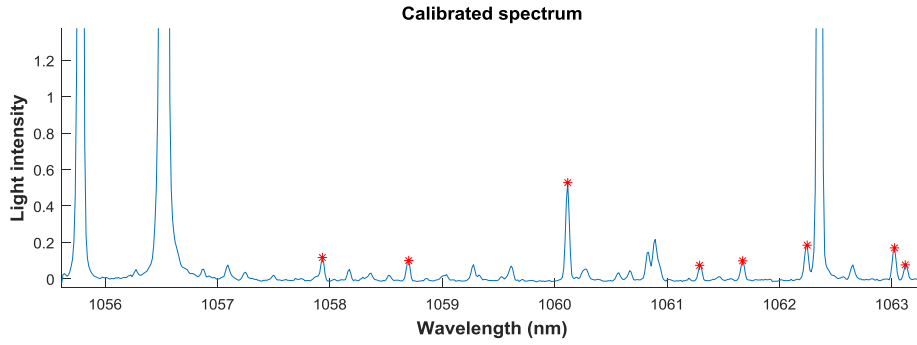


Figure 6.23 - Calibrated spectrum when observing the HCL spectrum centered at 1059.30 nm, red stars indicate spectral lines used for calibration.

Both Redman's atlas and the calibrated spectrum are superposed in Figure 6.24 to illustrate the fine matching between each other. Both spectral positions and intensities are recovered finely except for the Ne line intensities for reasons previously introduced.

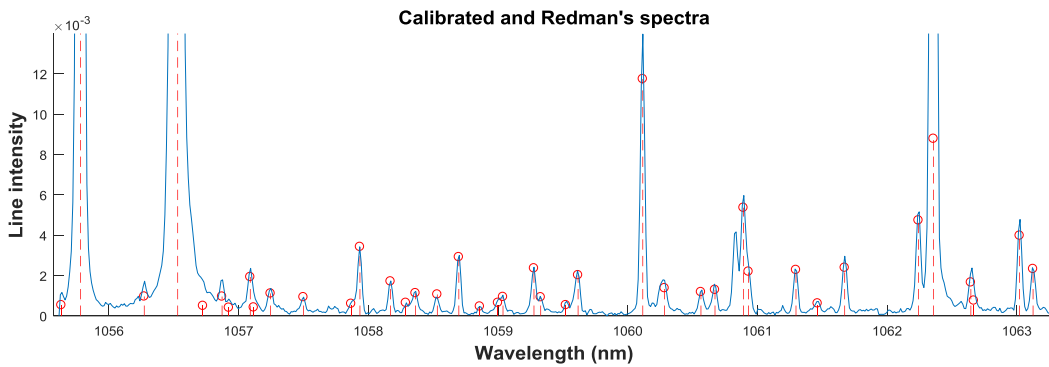


Figure 6.24 – Redman's and calibrated recorded spectra superposed on top of each other.

As a last step, the resolving power of the instrument may be measured on a selected spectral line. The brightest available *U* line is chosen, the leftmost on all spectra previously shown (this one was deliberately truncated due to its high intensity). On the other hand, this line is isolated from any neighboring spectral line and its spectral profile can be easily computed. The *FWHM* obtained from this spectral line enables then the calculation of the resolving power. This process is presented in Figure 6.25.

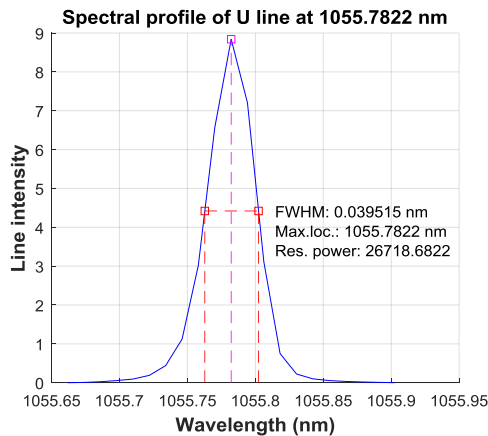


Figure 6.25 - Spectral profile of the *U* line centered at 1055.7822 nm and calculation of the associated resolving power.

The measured *FWHM* amounts to 0.039 nm and finely matches the previously deduced one during the resolving power analysis of Chapter 4.4.2 that was equal to 0.038 nm . The evaluated resolving power amounts to 26718, which is very close to the value that was deduced from the observation of a pair of very close lines in the *UNe* spectrum. The test of other lines led to the same order of magnitude and the value of approximately 27000 may be reasonably taken as a sensible baseline for the resolving power of the spectrograph. The average theoretical value of 29000 is then also nearly achieved.

6.5 Calibration box assembly and tests

This section focuses on the alignment and fine adjustment of the calibration box. This element provides the instrument with both flatfield and spectral calibrations and requires precise positioning of the mechanical slits. As presented in the Optical Design chapter, a beamsplitter is used to enable the light from both calibration sources to propagate through the instrument. On the other hand, a moving fold mirror switches between its end and home position when calibrating and observing respectively. The alignment of these optical elements is presented in the following subsections.

6.5.1 Alignment of mechanical slits and beamsplitter

The fiber bundle is first repositioned to its final location and illuminates the collimator with the help of the moving fold mirror previously introduced. For that purpose, the translation stage is installed on the optical bench and the mirror assembly fixed to the moving plate. A fine alignment of the fiber images at the detector plane is carried out with the help of both the mirror and bundle optical mount settings. The mechanical slits can then be set and their alignment started in order to co-align them with the optical fibers. The slits for spectral and flatfield calibration purposes are located within mechanical mounts which enable both *X*, *Y* and *Z* movements. Therefore, a fine adjustment of their lateral and vertical positions and a focus movement can be performed. This way, both imaging quality performances and perfect superposition of the slits on the fiber bundle at the focal plane can be obtained.

As a first step, the mechanical slits are inserted within their respective mechanical mount and their verticality ensured. Once they are correctly set within their own holder, the co-alignment of their image at the spectrograph focal plane can start. The optical elements and mechanical enclosure from the calibration box are presented in Figure 6.26.

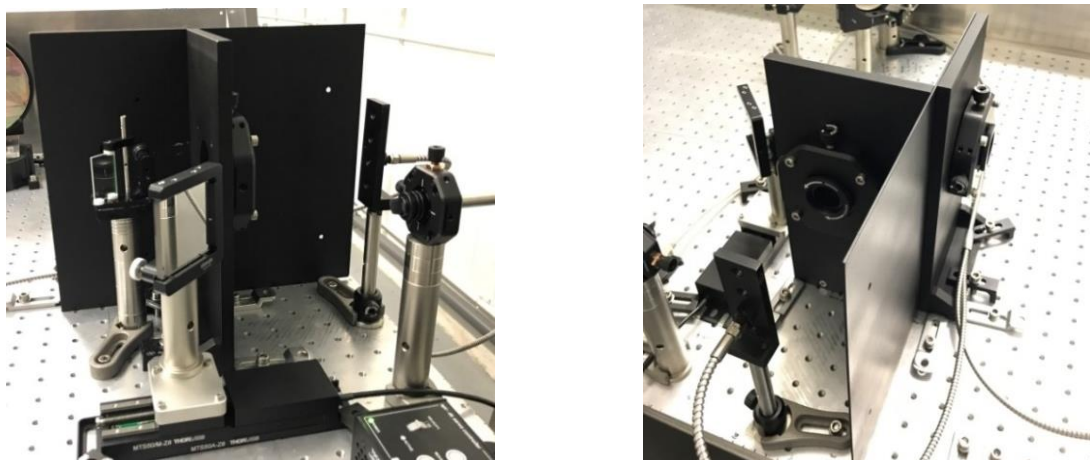


Figure 6.26 – Moving mirror (in home position), beamsplitter and scientific fiber (left) and mechanical slits (right).

The beamsplitter is first positioned to its theoretical location and fine adjustments to tip and tilt settings are carried out to bring the slit images onto the detector center. In order to co-align both mechanical slits and then superpose them on the fiber bundle, optical fibers are used to illuminate these rectangular apertures with the *Nd:YAG* laser light. The beamsplitter at this point is fixed and the fine settings are applied with the help of the micrometer actuators from the optical mounts holding the slits. The obtained data when superposing images of both slits and the fiber bundle is shown in Figure 6.27. No distinction between spectral and flatfield slit images can be made as they perfectly coincide. On the other hand, fiber images are perfectly co-aligned with the slit images which ensures a proper calibration.

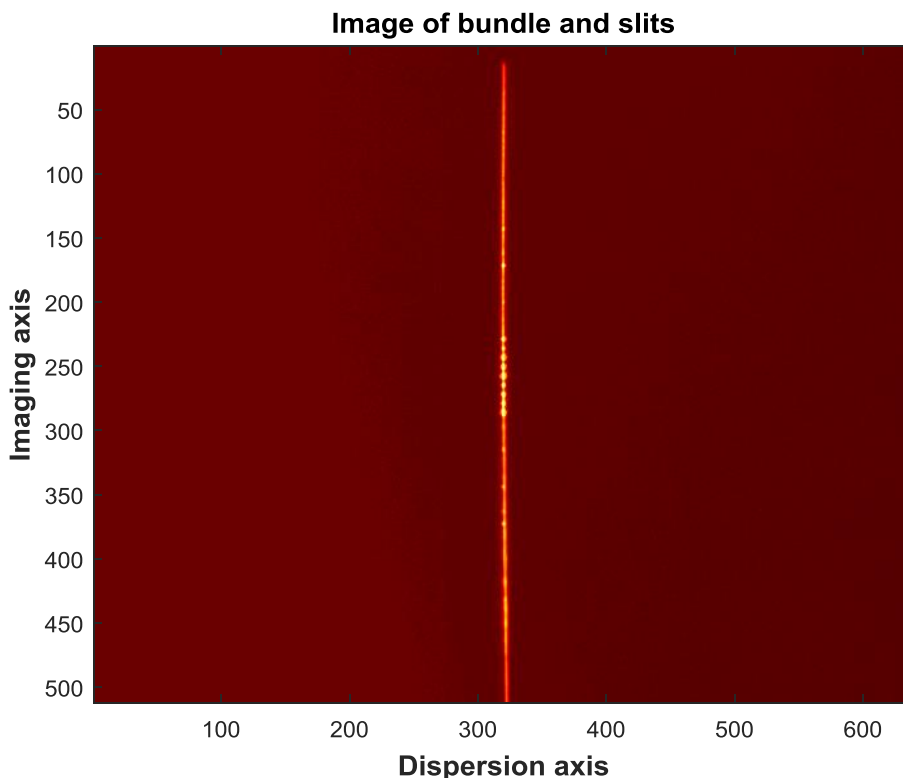


Figure 6.27 – Superposition of both slit and bundle images.

The above visual inspection is confirmed in Figure 6.28 where the horizontal, i.e. along the dispersion axis, profiles of the bundle and slits' images are depicted. Indeed, these three spectral profiles exhibit their maximum at the exact same pixel. The fact that the spectral profile from the flatfield calibration slit is affected by a larger amount of noise is due to the high reflectance of the beamsplitter which favors the hollow cathode lamp.

This reflecting ratio of 90:10 which enables only 10% of the halogen lamp to propagate through the spectrograph was selected because of the large power of the halogen lamp in comparison with that of the hollow cathode lamp. Illuminating both slits with the same laser power then requires longer integration times for the halogen lamp and this is the reason why a larger noise amount pollutes the associated profile in Figure 6.28 (blue curve). Nevertheless, the emission peak can be easily noticed and this does not affect the co-alignment of both slits with the fiber bundle.

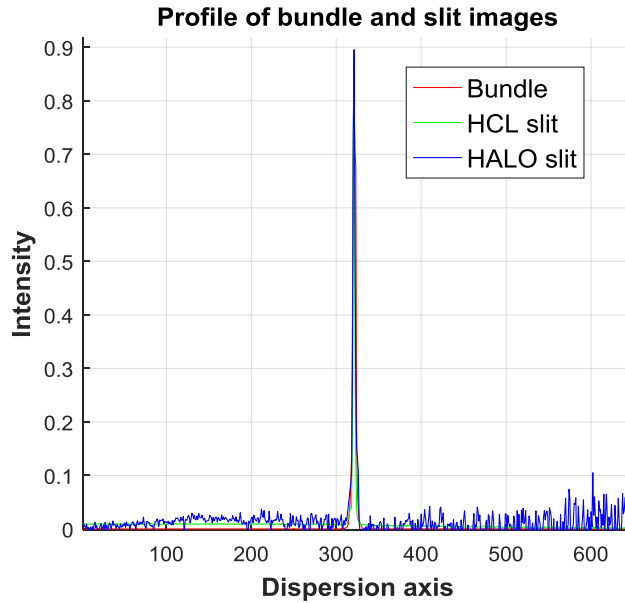


Figure 6.28 – Profiles of bundle, spectral and flatfield slits’ images

Once the mechanical slits and the fiber bundle are co-aligned, a last verification of the spectral calibration accuracy can be carried out by comparing the *UNe* HCL spectra obtained through both channels. For that purpose, a first spectrum is recorded when illuminating the front (telescope) side of the bundle with the HCL installed within the adapted fiber illuminating system (see Figure 6.12 (a)). As a second step, the hollow cathode lamp is inserted into the spectrograph calibration box to illuminate this time the appropriate mechanical slit and a new spectrum is observed at the focal plane of the instrument (see Figure 6.12 (b)). Comparing both HCL spectra enables the identification of any shift between the same identified lines and correcting for this last discrepancy. At this point, the calibration of the spectrograph must also logically produce the same polynomial coefficients at a given vertical position through the slit/bundle.

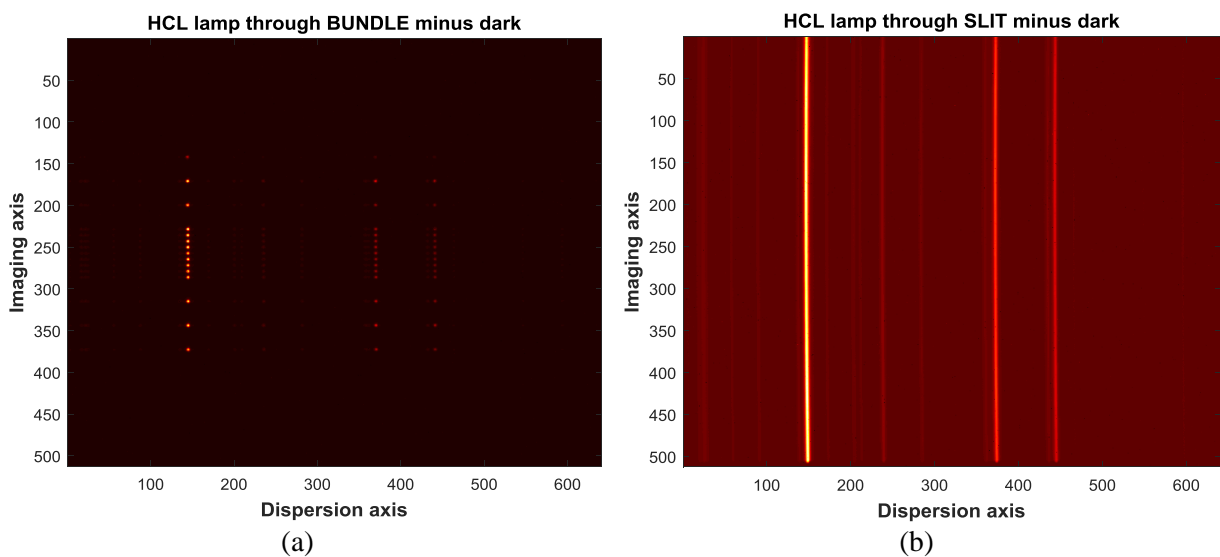


Figure 6.29 – Hollow cathode focal plane image as seen through the bundle (a) and the mechanical slit (b).

The identification of several U lines within both recorded spectra and comparing their location enables to get rid of any misalignment left between the mechanical slit and the bundle. Once both spectra coincide perfectly, the associated dispersion relations are identical and the spectrograph calibration box alignment is complete. Figure 6.30 illustrates the perfect superposition of both spectra.

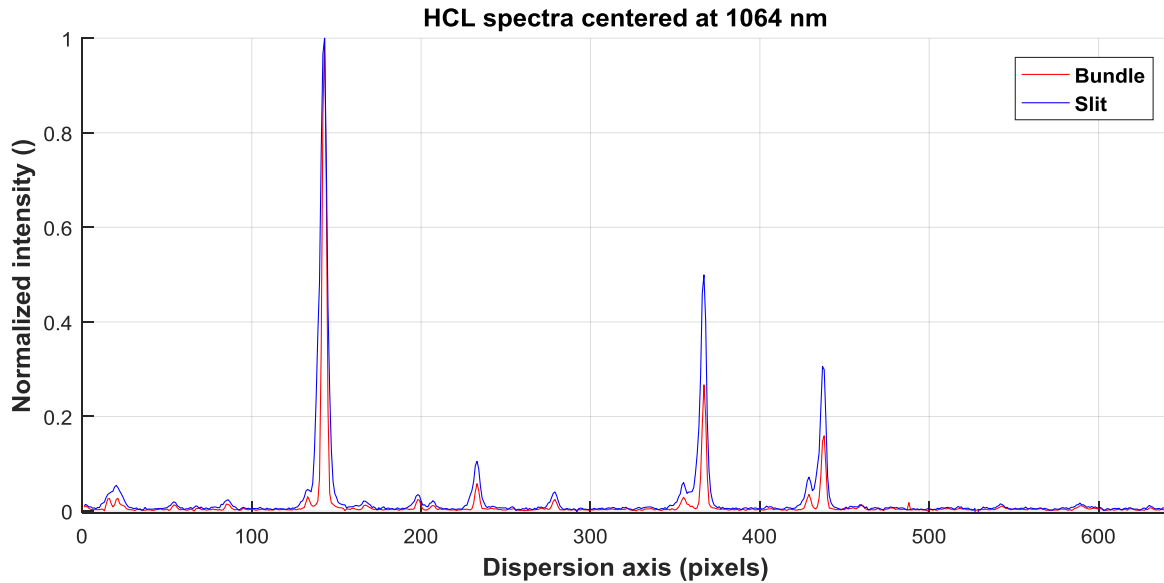


Figure 6.30 - Spectra of the UNe HCL as seen through the bundle (*red*) and the mechanical slit associated to the spectral calibration box (*blue*).

6.5.2 Calibration test

This section initiates a first calibration test before using the calibration box for observations. A $Nd:YAG$ laser was used during the near-infrared alignment of the spectrograph. The emitted light was considered to be precisely equal to 1064 nm but its experimental measurement can now be carried out with our calibrated instrument and the grating centered at 1064 nm .

The calibration of the spectrograph focal plane is first conducted by illuminating the mechanical entrance slit with the hollow cathode lamp as performed earlier. The fibers then propagate the laser light through the system after having repositioned the translation stage to its observing position. The calibration process of the spectrograph then follows the same sequence: identifying spectral lines from the atlas, establishing the dispersion relation and calibrating the spectrum. The individual fiber wavelengths can then be extracted and compared to check if they all indicate the same value within a certain tolerance which should be less than the required spectral calibration accuracy. Figure 6.32 illustrates the different steps described above starting from the calibration step to the laser wavelength measurement.

The obtained spectral profile for a single fiber is depicted in the left panel of Figure 6.31. The associated $FWHM$ and resolving power are indicated next to the obtained curve. The average resolving power that is measured from this experimentation is equal to 27414. This value approaches the one foreseen by the optical analyses presented in Chapter 4.4.2 when the precise spectral profile was sampled with the ASAP software. This last experimental assessment of the resolving power of the spectrograph closely matches the simulated behavior.

Monochromatic laser light is now used to sample the precise spectroscopic resolving power of the instrument by benefiting from the calibration box. On the other hand, the previous evaluations based on the visual inspection of close pairs of U lines represented a convenient way to obtain rough estimates of this parameter. Indeed, the collected information assigned a sensible lower limit on the resolving power of the instrument.

The individual wavelength measurements are depicted in the right panel of Figure 6.31. The limiting zone to fulfill the requirement on spectral calibration specified in Table 1.1 is delimited by two red dashed lines. Several values are located outside this allocated zone. Indeed, the speckle pattern printed over the fiber image perturbed the centroid calculation of the fiber image. The associated wavelength measurement is therefore affected by this inhomogeneity over the spot. Slight departures from the requirement, which were not foreseen by the analysis of Chapter 4.7.3, therefore appear.

In addition to that phenomenon, illuminating each fiber in identical conditions with the fiber illuminating system is rather difficult. A slight radial displacement with respect to the microscope objective impacts the output radiation pattern of the fiber (as pointed out in Chapter 2.4.2). Indeed, the scrambling properties of the bundle are not optimized with the used fiber illuminating system since the numerical aperture of the microscope objective is high. The wide input light beam is therefore not suited for high scrambling efficiency and the coupling between input and output light distribution is tight. Using a slower input light beam may lead to a reduced sensitivity of the optical setup. The scrambling efficiency of the fiber would indeed benefit from these irradiation conditions. FRD losses, on the contrary, would undergo the opposite effect as mentioned in Chapter 2.4.2.

In conclusion, this analysis cannot confirm the fulfillment of the requirement on spectral calibration accuracy as long as the fiber illuminating system is not modified. However, it is likely that the slight departures from the allowed interval decrease when suppressing the speckle effect induced by the laser. In order to avoid such an inhomogeneity and improve the measurement accuracy, monomode fibers may be used to record perfect Gaussian profiles on the detector.

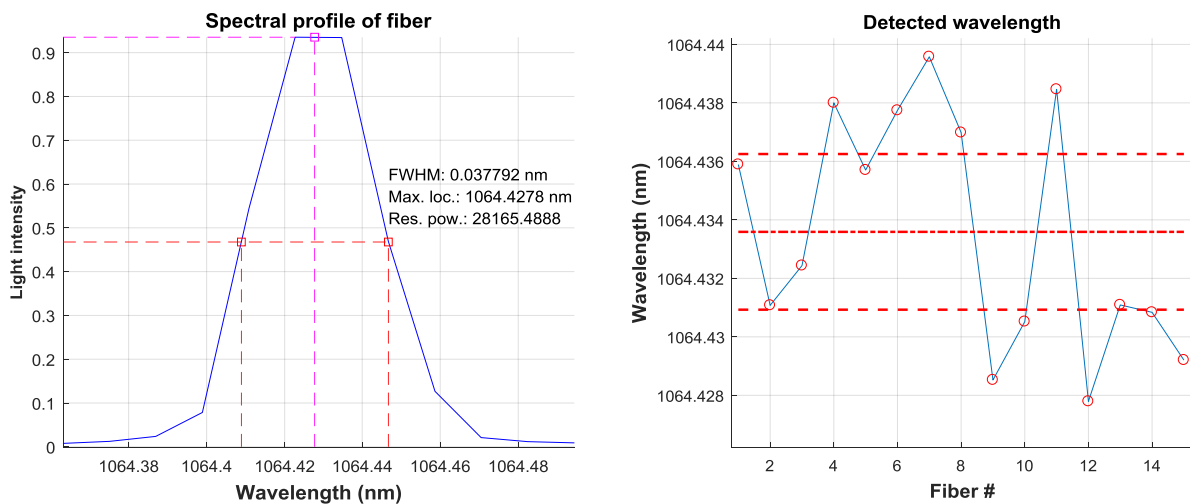


Figure 6.31 – Spectral profile of a given fiber (*left*) and detected wavelength values along with their calculated average (*right*). The upper and lower limits to fulfill the requirement on calibration accuracy are depicted by red dashed lines.

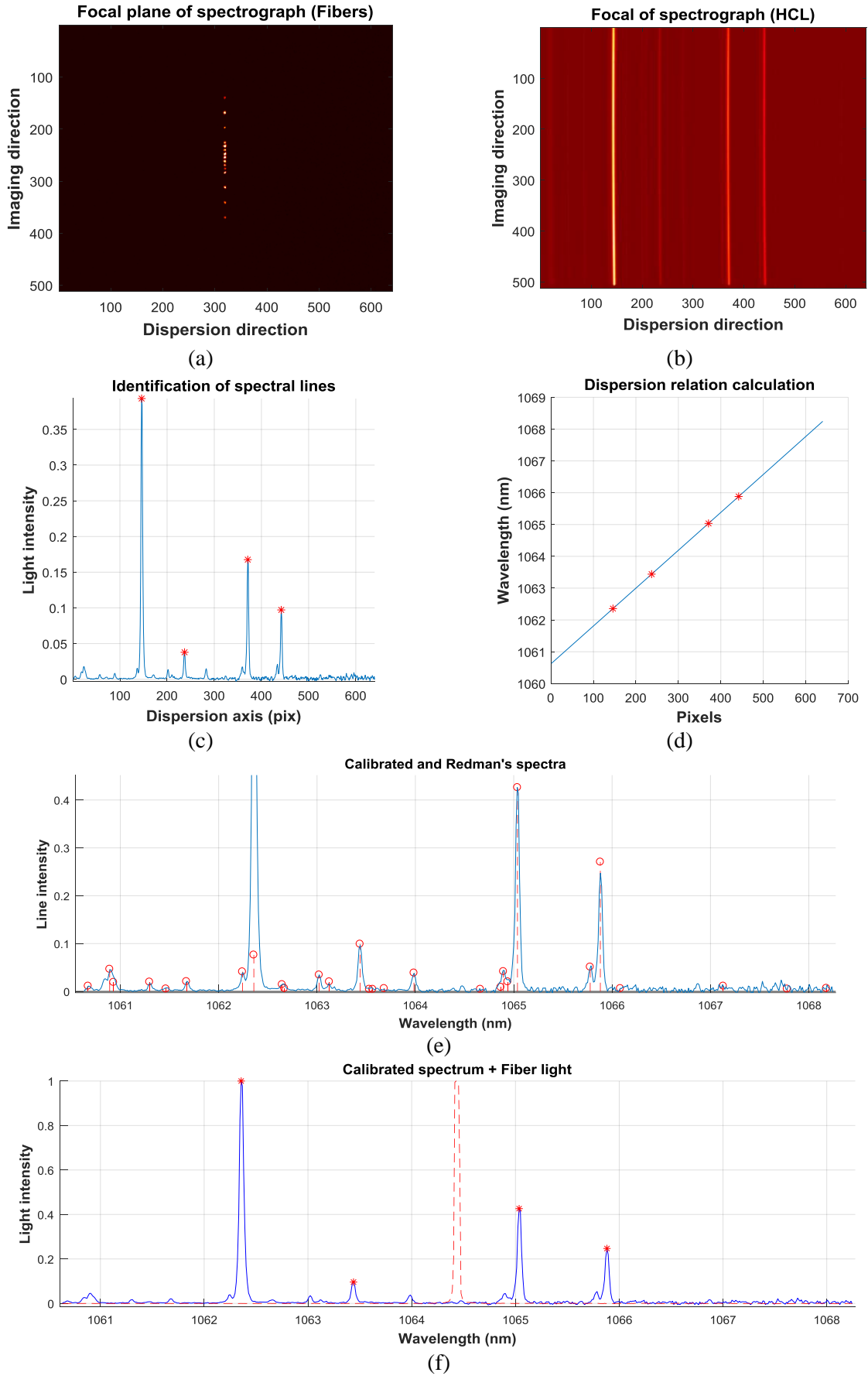


Figure 6.32 - Images of fibers (a), spectral calibration (b), identified lines (c), dispersion relation (d), calibrated and Redman's spectra (e) and fiber image along with the calibrated spectrum (f).

6.5.3 Verification of translation stage repeatability

In order to assess the translation stage repeatability and the associated calibration stability, the folding mirror is moved from its home to end positions and the spot image of a fiber is recorded. The sequence is repeated 10 times to measure the average centroid position of the fiber image within the detector. The induced spectral calibration error due to any shift along the dispersion axis is then calculated. In order to fulfill the requirement on spectral calibration accuracy specified in Table 1.1, the maximum spectral shift that can occur between two successive calibrations must be lower than $\delta\lambda/20$. This analysis intends to confirm that the translation stage enables fulfilling this latter when switching from its “calibration” to “observation” positions.

The recorded spot positions are indicated in Figure 6.33. Their horizontal, i.e. along the dispersion axis of the detector, component is represented by blue circles. The average position is depicted by a red dash-dot line while the upper and lower limits of the calibration stability interval are the red dashed lines. The centroid positions must then be included within this interval in order to properly calibrate the instrument at each observation. Indeed, the maximum distance between any two measured positions will be lower than the maximum accuracy error on spectral calibration that is allowed by the scientific requirement.

The observation of Figure 6.33 reveals that nearly all blue circles are located in this interval. A single measurement is located outside the acceptable range. This analysis therefore cannot confirm that the translation stage ensures a sufficient accuracy to certify that switching from home to end positions does not influence the calibration precision. The use of single mode fibers may also suppress this uncertainty since no speckle pattern will develop and impinge upon the results’ quality.

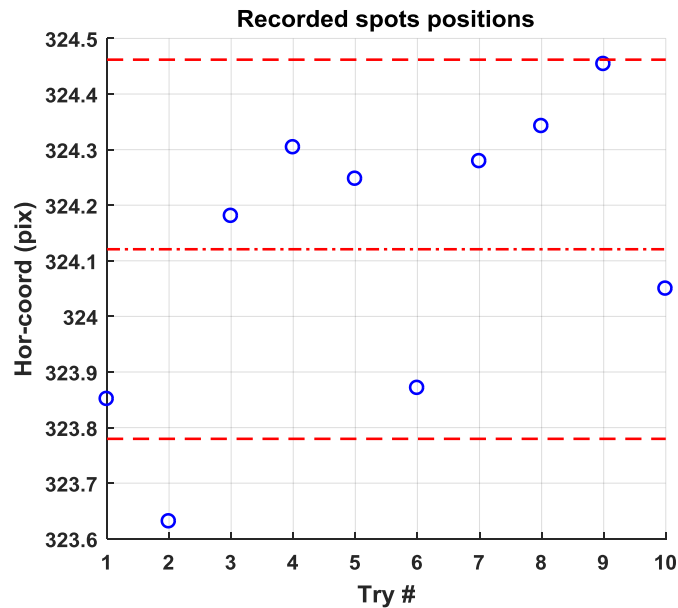


Figure 6.33 - Horizontal component of the recorded centroids (*blue circles*). The mean value is indicated as a red dash-dotted line and the upper and lower limits of the tolerance interval are the red dashed lines.

6.6 Conclusion

The alignment of the instrument required first the elaboration of an illumination system. This device intended to supply the instrument with calibrated light, either from monochromatic laser beams or hollow cathode lamps. The developed setup featured both options and enabled to perform both monochromatic visible and near-infrared alignments as well as the verification of polychromatic performances.

The visible alignment consisted in operating the spectrograph with the second order of diffraction of the grating. This way, visible light could propagate through the system and eased the practical alignment tasks of the instrument. Once the optical elements were assembled, the near-infrared verification of the performances could start and confirmed the previous visible analyses.

Light from the *UNe* hollow cathode lamp was then injected through the system. This way, a first spectrum could be imaged. The comparison of the obtained results with an atlas allowed to estimate the average resolving power of the instrument. The simulated behavior of the spectrograph could be finely approached and the alignment validated.

The alignment of the calibration box required accurately positioning both mechanical slits with respect to the fiber bundle. To do so, the translation stage that activates the fold mirror movement was first installed on the optical bench. The beamsplitter that selects both halogen and hollow cathodes photons could then be aligned. The fine alignment of the slits was eventually adjusted by comparing the hollow cathode lamp spectrum when imaged through both the mechanical slits and the fiber bundle. An experimental calibration test was performed on the Nd:YAG laser and an assessment of the translation stage repeatability concluded this chapter. This last analysis was perturbed by the speckle pattern due to the multimode fibers of the bundle but still indicated encouraging results on the translation stage repeatability.

Once the performances of the instrument were verified in comparison with the previous optical analyses, the assembly of the star positioning system could start. Chapter 7 is devoted to the conception and alignment of this component. Final observation tests of the spectrograph are explained in Chapter 8.

Chapter 7

Star positioning system

7. Star positioning system (SPS)

7.1 Purpose of the instrument

When collecting the light from a telescope and feeding a spectrographic instrument with the help of a fiber, a perfect alignment of the stellar image with the fiber core must be achieved in order to maximize the transmitted flux to the instrument. Hence, a system must be developed in order to be able to drive the telescope pointing and align the target image with the fiber core. To do so, both the star and the fiber core images may be visualized on a single camera and the alignment process consists in approaching both close together until they overlap.

7.2 Optical design

The proposed system is made up of a beamsplitter, a spherical mirror and a guiding camera (see Figure 7.1). Moreover, a back-illuminating system of the fiber is included into the spectrometer housing. This way, the fiber can be lit from its spectrograph-side outwards and inject light towards the telescope. To do so, a LED (Light-emitting diode) can be turned on and imaged onto the fiber with the help of an achromatic doublet inside the spectrograph when the fold mirror stands in its up position. The translation stage is therefore used for both calibration and star positioning processes.

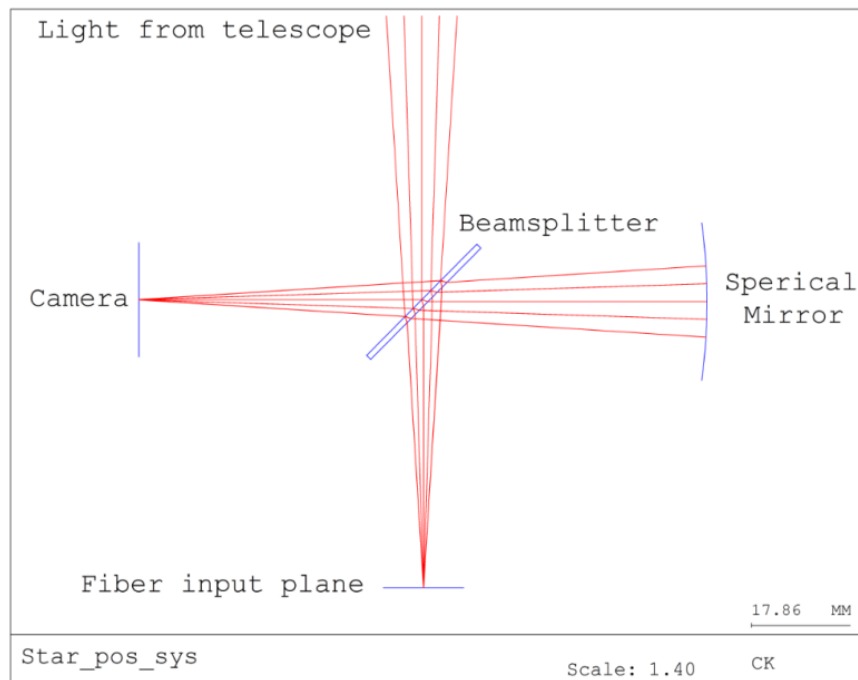


Figure 7.1 - Star positioning system. The instrument intends to align the observed target image with the fiber core to maximize the transmitted flux from the telescope to the spectrograph

The selected beam-splitting optical element is an off-the-shelf antireflective window to be used in the near-infrared waveband. This exotic choice intends to minimize the proportion of useful light, i.e. belonging to the 1 to 1.1 μm waveband, that is used for star positioning to the detriment of stellar spectra recording. This is the reason why a near-infrared antireflective window is selected: part of the

visible stellar image is reflected onto the camera while the near-infrared one goes through the window and reaches the fiber input. Indeed, the anti-reflective coating of the window works fine for near-infrared wavelengths but quickly loses those characteristics when considering visible light. This part of the spectrum is therefore prevented from propagating into the spectrograph and used for guiding purposes. Moreover, this also serves as a first “visible filter” since less visible straylight pollutes the spectrograph. Once the information about the star position is known, the fiber location has to be determined in order to co-align both. This is the utility of the LED located inside the spectrograph housing which illuminates the fiber. This way, visible light is transmitted to the telescope and reaches the antireflective window. This reflected light path is then focused with the help of a spherical mirror through the window onto the camera. The fiber is now imaged onto the camera and the star-to-fiber matching can be performed.

7.3 Atmospheric dispersion

As explained in Chapter 2.3, the atmospheric dispersion requires to be corrected by a dedicated ADC. Such a device is foreseen to be incorporated later within the enclosure of the star positioning system but will be missing at first operations. In the meantime, our star alignment strategy will focus on a narrow waveband centered at 889 nm thanks to a methane filter. This adapted plan is introduced further in this chapter.

Equation (1) of the differential refraction is used here to assess the mismatch that will occur between the near-infrared (of scientific interest) and visible (for tracking) star images. The temperature and pressure conditions are typical La Luz meteorological parameters and equal to $p = 766.9\text{ hPa}$ and $T = 275.65\text{ K}$ (2.5°C) respectively.

Two common astronomical narrowband filters are tested for guiding, these are centered at 672.4 nm (*S II*) and 889 nm (methane) to highlight the impact of the guiding wavelength λ_0 on the differential refraction. The effect of zenith distance z_a is also investigated as it highly impacts on the change in apparent object location on the sky: the larger the airmass the more atmosphere thickness the star light has to go through before reaching the telescope.

Figure 7.2 illustrates the results: figures (a) and (b) implement the sulfur filter whereas (c) and (d) simulate a methane filter. The graphs introduce the calculated differential refraction that is observed on the sky in *arcsec* as well as the induced shift at the telescope focal plane in μm , i.e. $\Delta D_{atm}\text{ at focal plane} = f_{tel} [\mu\text{m}] * \tan(\Delta D_{atm})$. As could be expected, the differential refraction effect is much more pronounced when guiding at a wavelength λ_0 that is located farther away from the scientific waveband of interest (represented on the graphs with vertical dashed red lines). Indeed, the misalignment of the SPS will be larger if the star image is observed through a sulfur filter with respect to a methane filter.

On the other hand, the larger the zenith angle, the larger the differential refraction. The $1.1\ \mu\text{m}$ near-infrared star image shift with respect to the reference one rapidly increases when observing closer to the horizon. Starting at a value of $9.56\ \mu\text{m}$ for a zenith angle of 30° in Figure 7.2 (b), the misalignment grows to $61.82\ \mu\text{m}$ as the zenith angle increases to 75° .

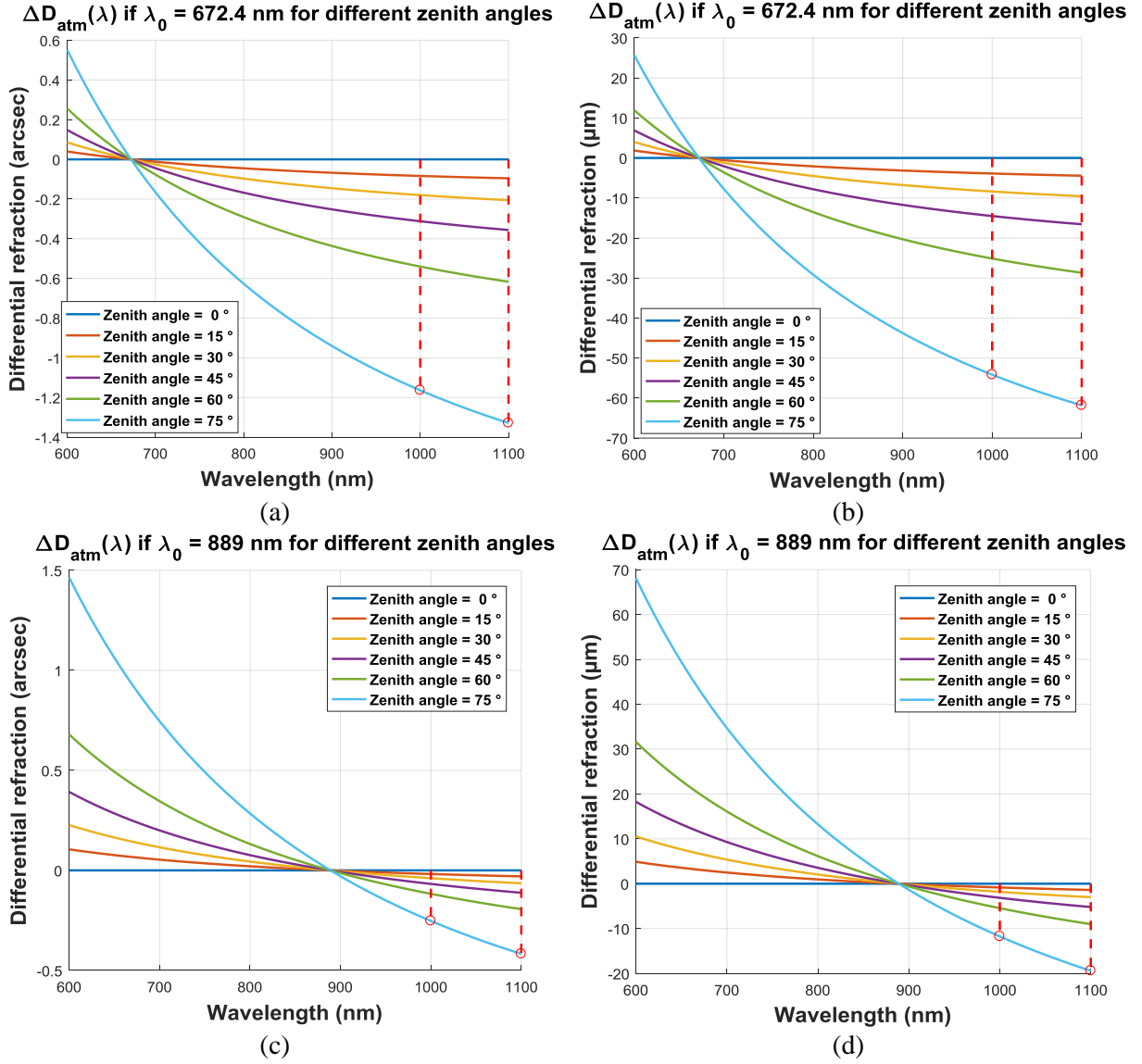


Figure 7.2 – Evolution of the differential refraction as a function of wavelength at different zeniths for two different guiding wavelengths.

Since no Amici prisms will be installed at spectrograph first light, the clear advantage in using a methane filter is the shift of the zero differential refraction point, of course located at the guiding wavelength λ_0 , to the longer wavelength side of the graphs. The induced chromatic star image shift is therefore lessened and the transmitted flux through the fiber increased. Indeed, this shift amounts to $3 \mu\text{m}$ at $1.1 \mu\text{m}$ if the zenith angle amounts to 30° and increases to $19.42 \mu\text{m}$ when setting the telescope close to the horizon at $z_a = 75^\circ$.

Moreover, the separation between the 889 nm and $1.1 \mu\text{m}$ star images remains lower than $10 \mu\text{m}$ for zenith angles as high as 60° which is in principle the largest value accepted for TIGRE observations. Considering a star image of approximately $93 \mu\text{m}$ under typical seeing conditions at La Luz of 2 arcsec and a fiber core of $50 \mu\text{m}$, the light loss due to this chromatic misalignment is highly reduced when using a methane filter rather than observing at a shorter visible wavelength.

7.4 Photometric budget

This section focuses on the photometric budget of the SPS. This intends to predict the required integration time to reach a specified signal-to-noise ratio accounting for the complete optical system performances of the SPS. This calculation takes into account several wavelength-dependent parameters. First, the target star radiometric budget is required. Then, the atmospheric transmission has to be accounted for. Eventually, the anti-reflective window reflectivity outside its design range and the methane filter transmission waveband are required, as is the detector quantum efficiency.

7.4.1 Methane filter

The selected methane filter from Custom Scientific exhibits the transmission profile that is depicted in Figure 7.3 [84]. This rectangular-shaped function is centered at 889 nm and its bandpass amounts to 18 nm.

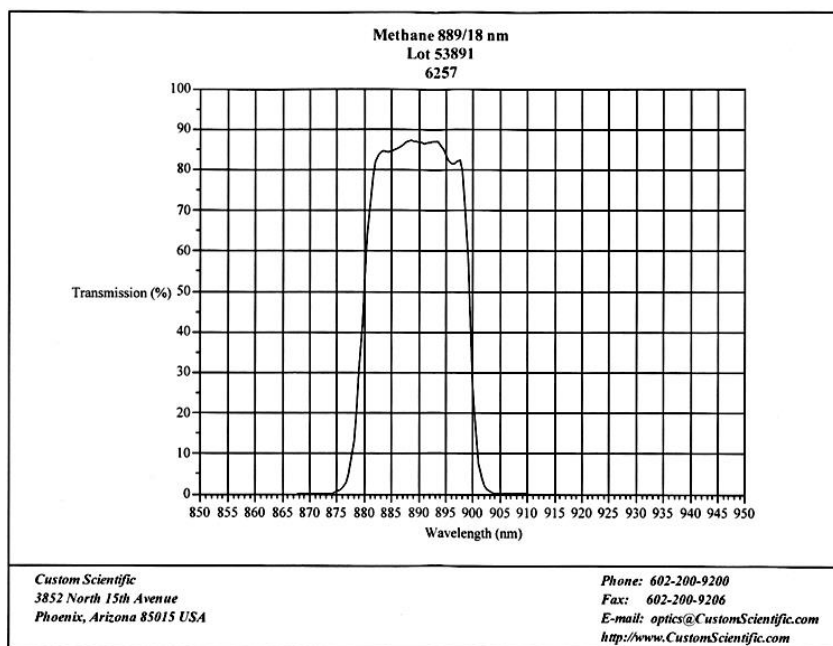


Figure 7.3 - Transmission of the standard Methane filter from Custom Scientific [84].

7.4.2 NIR Anti-reflective window

The beamsplitting optical element selected to illuminate the camera with the visible star image is an anti-reflective window optimized for the near-infrared wavelengths. As can be seen in Figure 7.4, the applied coating reflects light outside the NIR spectral region and more specifically towards shorter wavelengths [85]. This enables using part of the stellar signal outside the scientific wavelengths for acquisition and guiding while optimizing the photon flux transmission to the fiber.

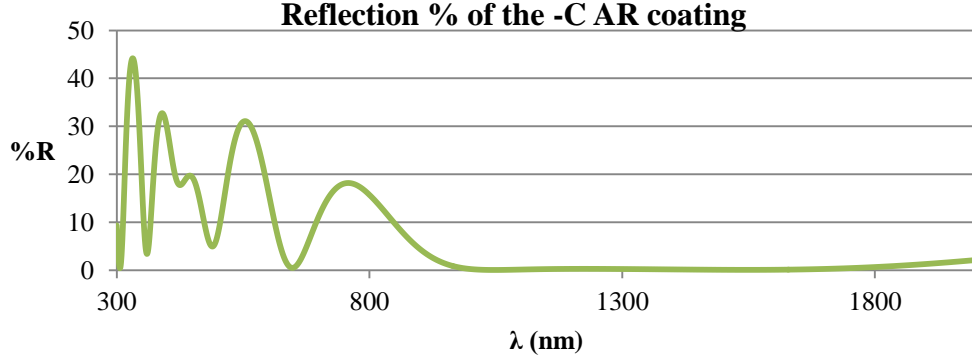


Figure 7.4 - Reflection of the near-infrared AR window down to the visible region [85].

The methane filter transmission wavelength is located in the wings of a reflection peak of the window.

7.4.3 Visible camera characteristics

The selected visible camera exhibits a sensor quantum efficiency that is shown in Figure 7.5 [86]. The methane filter waveband lies at the far end of this detector sensitivity.

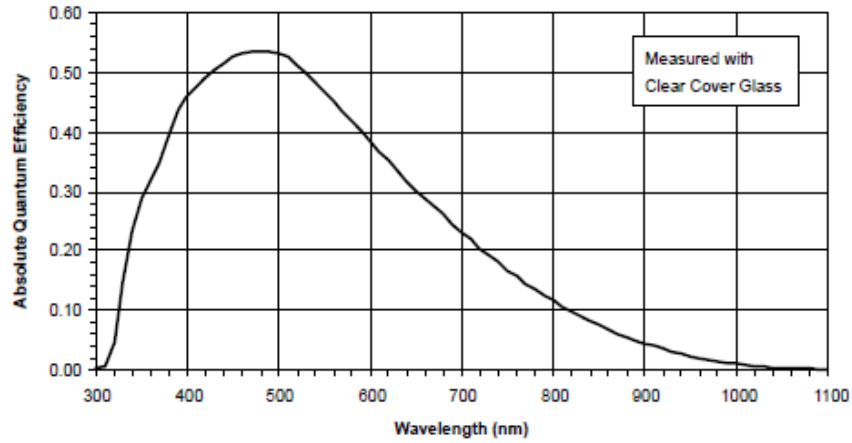


Figure 7.5 - Absolute quantum efficiency of the visible camera CCD [86].

7.4.4 Stellar radiometric budget over the selected filter waveband

A general stellar radiometric budget was introduced in Chapter 5.2 and the photon flux that reaches the primary mirror of the telescope is calculated with the help of Eq. (13)

$$dN = \frac{8.412 \cdot 10^{34} \cdot 10^{-0.4 (m_W - A_W + BC_W + A_\lambda)} d\lambda}{T_{eff}^4 \lambda^4 \left(\exp\left(\frac{1.439 \cdot 10^8}{\lambda T_{eff}}\right) - 1 \right)} \quad [ph \ s^{-1} \ cm^{-2}]$$

In contrast with the spectrograph photometric budget where that $d\lambda$ element was associated with the resolution of the instrument, this parameter is this time the sampling interval of an integration over the filter waveband. Indeed, the photon flux is now accounted for all wavelengths that are transmitted through the narrowband filter. The expression to integrate is now the photon flux per wavelength unit

$$dN_\lambda = \frac{8.412 \cdot 10^{34} \cdot 10^{-0.4 (m_W - A_W + BC_W + A_\lambda)}}{T_{eff}^4 \lambda^4 \left(\exp\left(\frac{1.439 \cdot 10^8}{\lambda T_{eff}}\right) - 1 \right)} \quad [ph \ s^{-1} \ cm^{-2} \ \text{\AA}^{-1}]$$

where $d\lambda$ has disappeared from Eq. (13). More precisely, the function to be integrated is the product of the photon flux per unit wavelength and the overall efficiency of the SPS as a function of wavelength. This latter is the combination of the atmospheric transmission T_{atm} with the “beamsplitter” reflectivity R_{BS} , the filter transmission T_{filt} and detector quantum efficiency QE_{det} . The integration of this *detected* photon flux per unit wavelength then writes

$$dN_{Meth. Filter} = \int_{\lambda_{inf}}^{\lambda_{sup}} dN_{\lambda,det}(\lambda) d\lambda$$

$$= \int_{\lambda_{inf}}^{\lambda_{sup}} dN_{\lambda}(\lambda) T_{atm}(\lambda) R_{BS}(\lambda) T_{filt}(\lambda) QE_{det}(\lambda) d\lambda \quad [ph s^{-1} cm^{-2}]$$

where λ_{inf} and λ_{sup} are the lower and upper wavelength limits of the filter waveband. The integration is calculated over the filter waveband since this latter is the limiting factor in terms of spectral selectivity. Figure 7.6 illustrates the variation of a stellar photon flux per wavelength unit as a function of wavelength when considering a “cool” star of 3000 K and a “hot” star of 30 000 K. Both calculations are performed by fixing the *J-mag* to 5 and A_V to 0. Both continuous (blue line) and sampled (red circles) curves are plotted. The sampling is deliberately exaggerated to 10 Å for proper visualization (fine sampling of 0.001 Å is needed to sample all atmospheric lines).

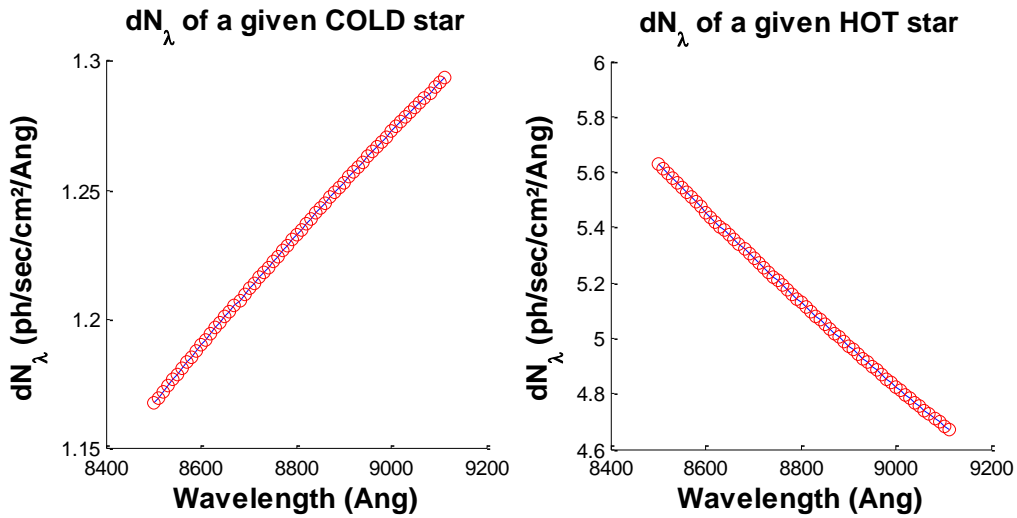


Figure 7.6 - Photon flux per wavelength unit for arbitrary COOL (3000 K) and HOT (30 000 K) stars at *J-mag* = 5 and $A_V = 0$.

Figure 7.7 introduces the variation of atmospheric transmission with wavelength as well as all contributors to the SPS chromatic efficiency. Red circles are again the sampled values of all previously introduced parameters involved in the integration. On the other hand, the coarse sampling of 10 Å clearly under-samples the atmospheric transmission as can be seen in Figure 7.7 (a) (this one only helps for graphical illustrations).

The filter waveband is located in a region where the near-infrared anti-reflective coating starts getting less efficient. The reflected portion of light varies from 9.75% to 3.55% at 8500 Å and 9100 Å respectively. The quantum efficiency of the detector in that range of wavelengths has a peak value of 7.52% while its minimum reaches 3.99 % at the end of the considered curve tail.

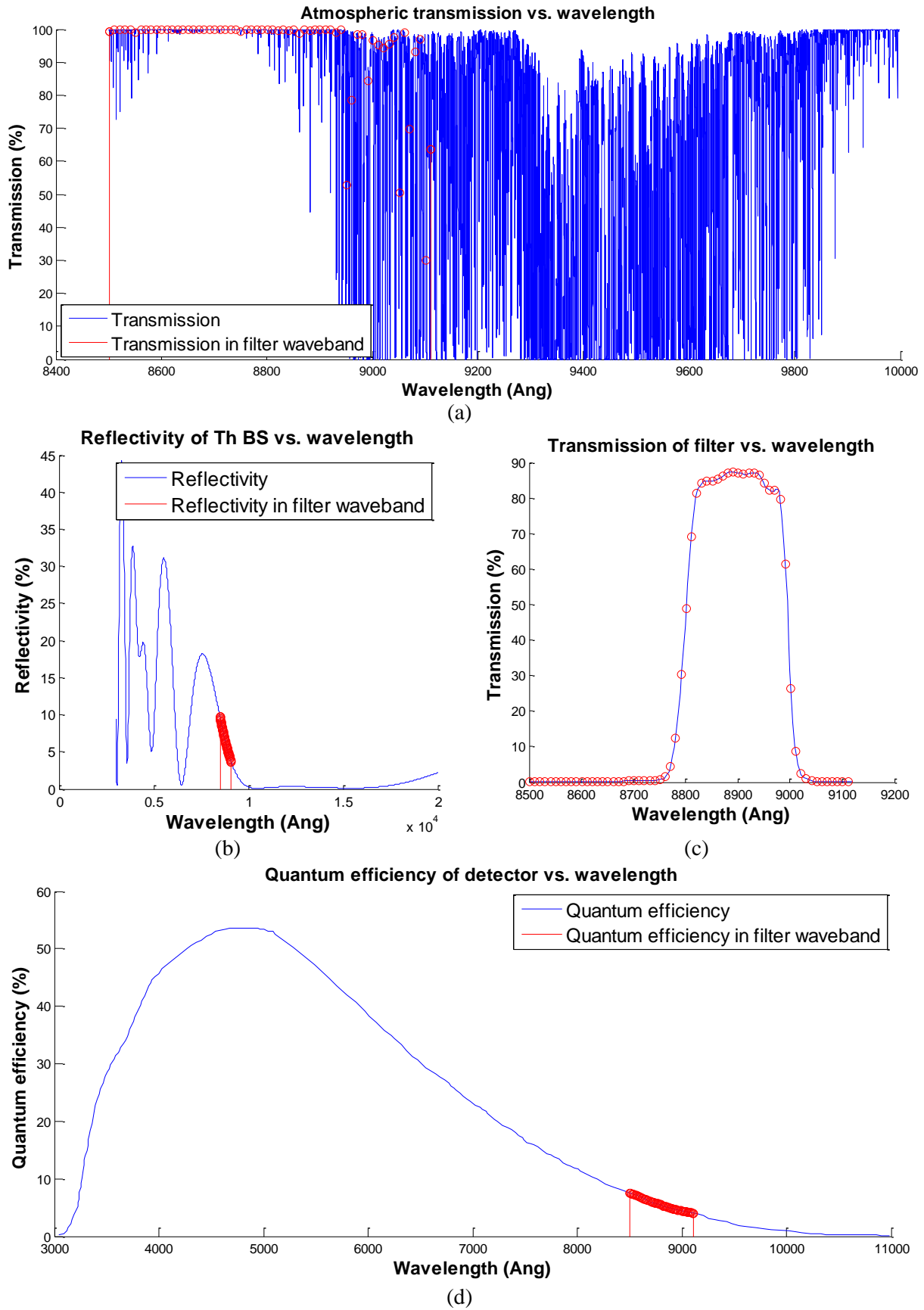


Figure 7.7 – Atmospheric transmission (a), Reflectivity of the window (b), transmission of the methane filter (c) and quantum efficiency of the detector (d).

The obtained detected photon flux profile when using a wavelength step size that is fine enough to sample accurately the atmospheric transmission is presented in Figure 7.8.

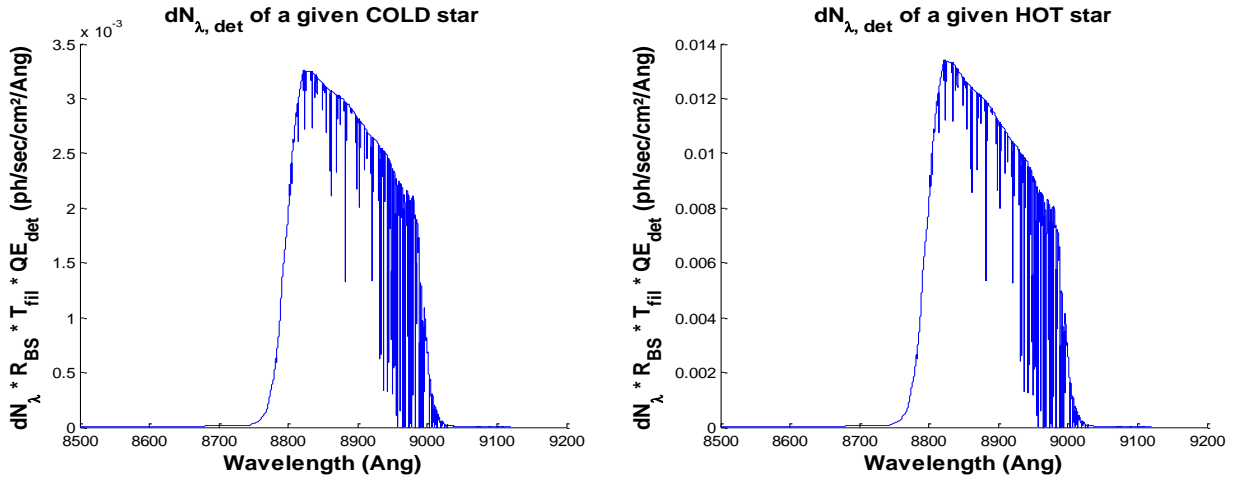


Figure 7.8 – Detected star photon flux per wavelength unit $dN_{\lambda, det}$

The integration process of $dN_{\lambda, det}$, which leads to the evaluation of the detected photon flux over the filter waveband $dN_{Meth. Filter}$, is depicted in Figure 7.9 (coarse sampling). The total area of the red rectangles evaluates $dN_{Meth. Filter}$ for a given star. This process is shown for the typical cool and hot stars previously introduced but is actually carried out for a bunch of stars which differ in magnitudes and effective temperatures.

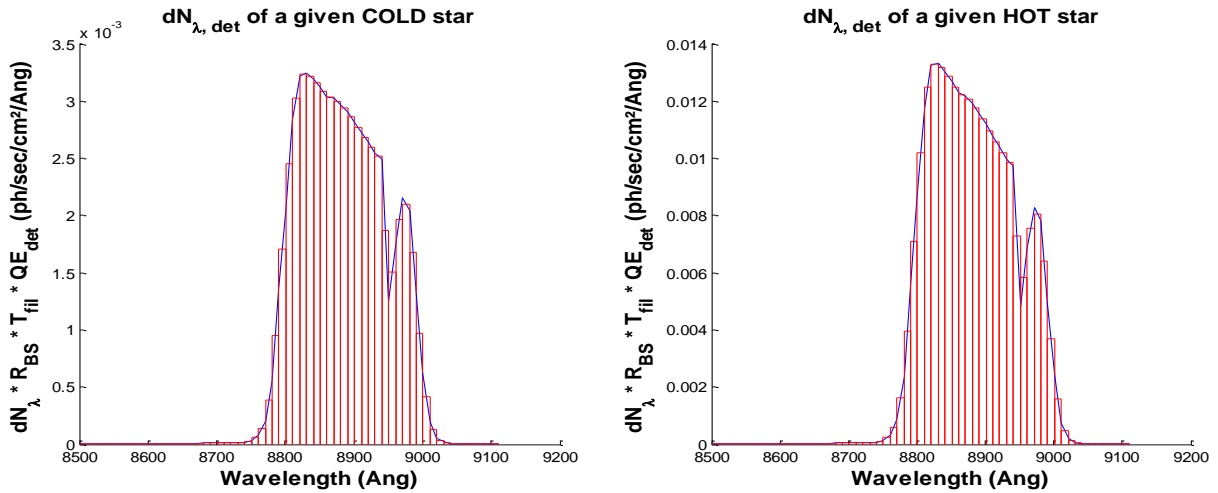


Figure 7.9 - Integration process of the detected star photon flux per wavelength unit $dN_{\lambda, det}$.

Once the integration is complete, the resulting value of $dN_{Meth. Filter}$ can be injected into Eq. (15) and the required integration time calculated by reversing this equation. The results are shown in Figure 7.10. Figures (a) and (b) illustrate the resulting photon flux $dN_{Meth. Filter}$ that is calculated after the integration process for different cool and hot stars respectively. When multiplied by the telescope aperture, the number of photons arriving at the focal plane per second $N_{Meth. Filter}$ is evaluated (see Figures (c) and (d)). Eventually, the required integration time to reach a signal-to-noise ratio of 100 is depicted in Figures (e) and (f). This one amounts to approximately 2 seconds over the entire range of considered hot stars whereas less than 5 seconds are needed to perform the observation of cool stars.

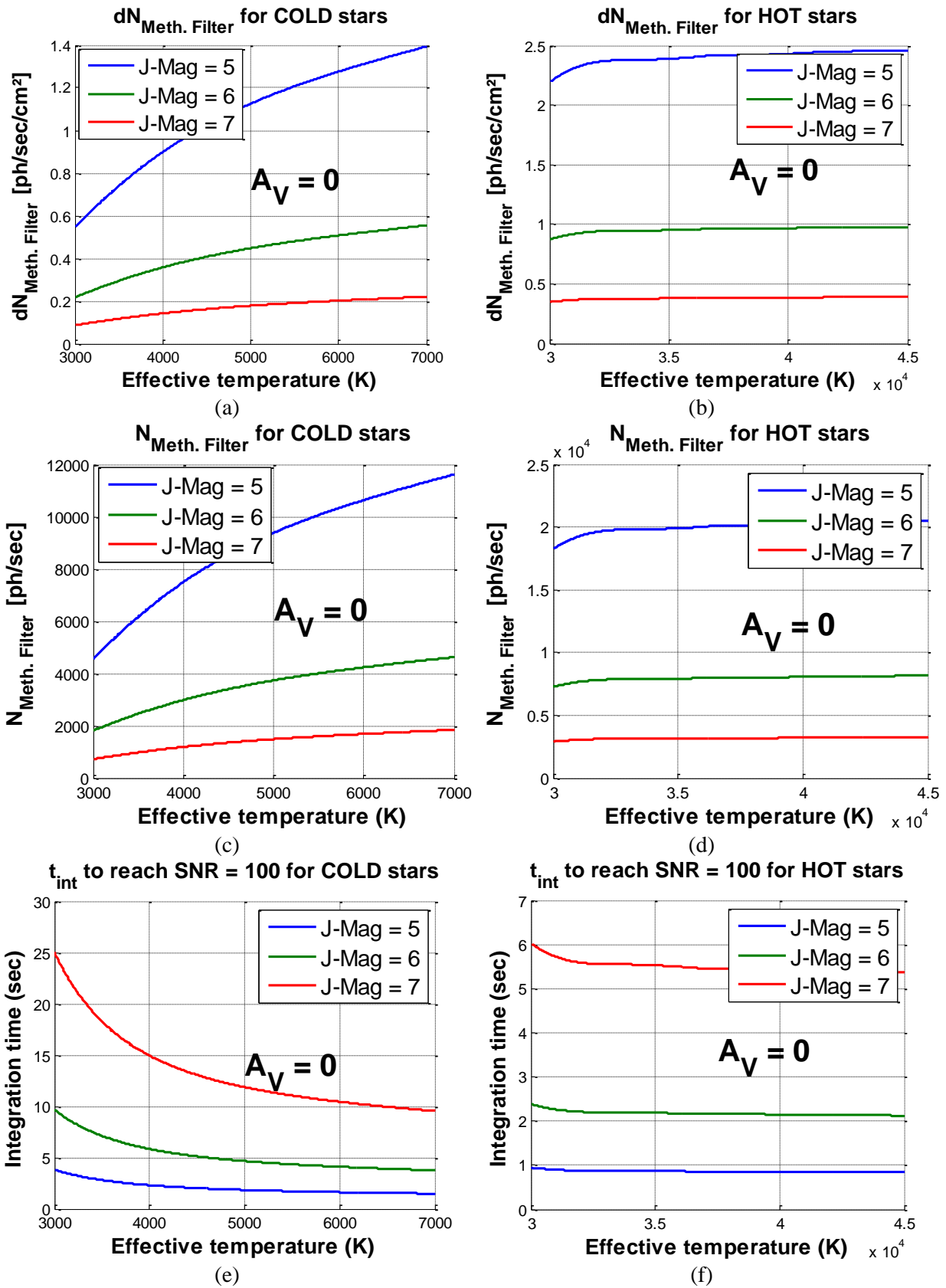


Figure 7.10 - Photometric budget results

7.5 Assembly and alignment

The assembly and alignment of the SPS was eventually carried out to conclude the overall construction of the instrument. The ultimate fine settings must however be carried out when associating the SPS with the telescope. Indeed, mechanical tolerances on the coupling flange and uncertainties on the telescope focal plane must be accounted for [49]. This operation was conducted with the help of the fiber illuminating system. A folding mirror was used to bend the beam before the microscope objective and illuminate the SPS enclosure (see Figure 7.11).

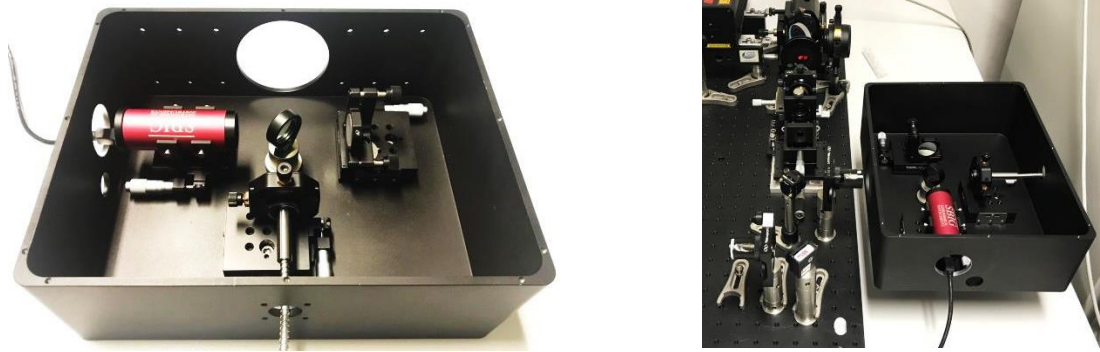


Figure 7.11 – Alignment setup of the SPS: the *HeNe* laser is used to illuminate the SPS optical elements

A diaphragm reduced the beam aperture as much as possible before the beam was launched onto the fiber bundle. The optical axis of the SPS was oriented along the incoming laser beam by sending back this latter onto itself with the help of a planar mirror positioned on the enclosure inner wall. Once its position was locked, the small laser beam could be positioned on the central fiber by maximizing the output flux onto the spectrograph detector (for that purpose the *Nd:YAG* laser was switched on). This illumination scheme mimics the stellar image projection onto the bundle with the telescope. Once the laser centered onto the fiber, the image of the fiber bundle could be optimized onto the SBIG camera by illuminating this time the other side of the bundle with the incorporated LED. Figure 7.12 illustrates the image of the bundle that is captured by the guiding camera. By tuning the mirror orientation, the centroid location of the central fiber was eventually brought to the same location as the one of the laser beam that reaches the camera after being reflected by the window. Co-aligning both therefore maximizes the stellar flux transmission through the fiber. The ghost image that appears on Figure 7.12 does not compromise the alignment strategy as it falls next to the bundle and is out of focus.

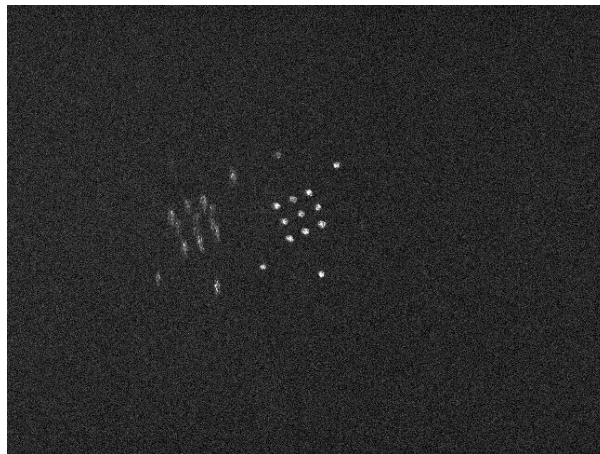


Figure 7.12 – Image of the fiber bundle onto the guiding camera.

Star positioning system (SPS)

Once the optical alignment of the SPS was complete, the final mechanical assembly could be achieved by fixing the coupling flange to the enclosure. This latter will connect the SPS to the TIGRE telescope Nasmyth focus interface.

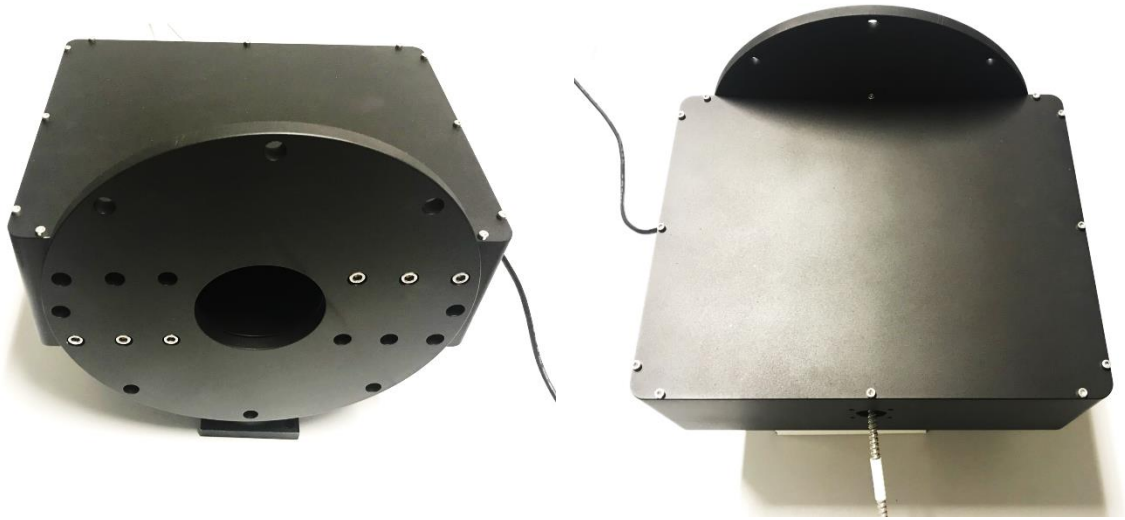


Figure 7.13 - Complete SPS assembly with the coupling flange attached

7.6 Conclusion

The star positioning system purpose is to provide the observer with a device able to accurately align the star image onto the selected fiber. Indeed, a perfect alignment of the star image onto the fiber core highly conditions the flux transmission to the spectrograph. The photometric budget of the instrument therefore directly depends on the proper operation of this equipment.

The optical conception of the instrument was first introduced. The alignment strategy proposed to use the visible stellar light for the purpose of telescope guiding. The near-infrared flux would therefore only be devoted to scientific data recording. The atmospheric dispersion however appears to be a showstopper to that approach. Indeed, this upstream dispersion effect produces a first very low resolution stellar spectrum at the focal plane of the telescope. The induced separation between the visible and near-infrared images was therefore reduced by using a methane filter. In this way, the tracking wavelength is closer to the near-infrared region leading to a better correspondence between the position of the stellar image as used for guiding and the image used for feeding the spectrograph.

A photometric budget eventually estimated the required integration time to reach a proper signal-to-noise ratio with that equipment. The conclusion was that only a few seconds are needed and the design was validated. The assembly and alignment of the star positioning system concluded this chapter.

Once the overall instrument was aligned and ready to be operated, the first observations could be initiated. These are discussed in Chapter 8 that just follows.

Star positioning system (SPS)

Chapter 8

On sky observations
from Liège

8. On sky observations from Liège

8.1 Introduction

Before shipping the instrument to the TIGRE telescope, tests are performed on the Belgian sky from the Centre Spatial de Liège. These intend to assess the instrument performances by observing bright stars with a small telescope. On the other hand, this will procure some hands on experience and enable debugging the spectrograph manipulation before using it on site.

8.2 Adapted photometric budget

As a first step, this section intends to investigate whether enough photons can be collected with the selected telescope to obtain useful scientific data. The photometric budget previously performed for the TIGRE telescope is thus adapted to simulate the observation of bright stars with a small telescope, a Celestron NexStar 8 SE. The aperture of this telescope is 8 *in* and its focal length is equal to 2 *m*. Several bright targets were identified and their characteristics are plotted in Figure 8.1.

The choice of the target for our test observations was guided by several constraints. These include the fact that the telescope had a rather limited aperture and the foreseen difficulties to guide the telescope in such a way that the stellar flux enters the fiber. Therefore, in order to maximize our chances to collect a useful spectrum, we decided to restrict our list of possible targets to the very brightest stars of the Northern autumn sky. Moreover, we wanted to make sure that the star would remain observable over a large fraction of the night. This condition excludes stars with too low a declination (e.g. Antares, $J = -2.73$, $RA = 16h\ 29min\ 24sec$, $DEC = -26^{\circ}25'55''$), as well as objects which were in the Western half of the sky at the beginning of the night (e.g. Arcturus, $J = -2.25$, $RA = 14h\ 15min\ 40sec$, $DEC = +19^{\circ}10'57''$).

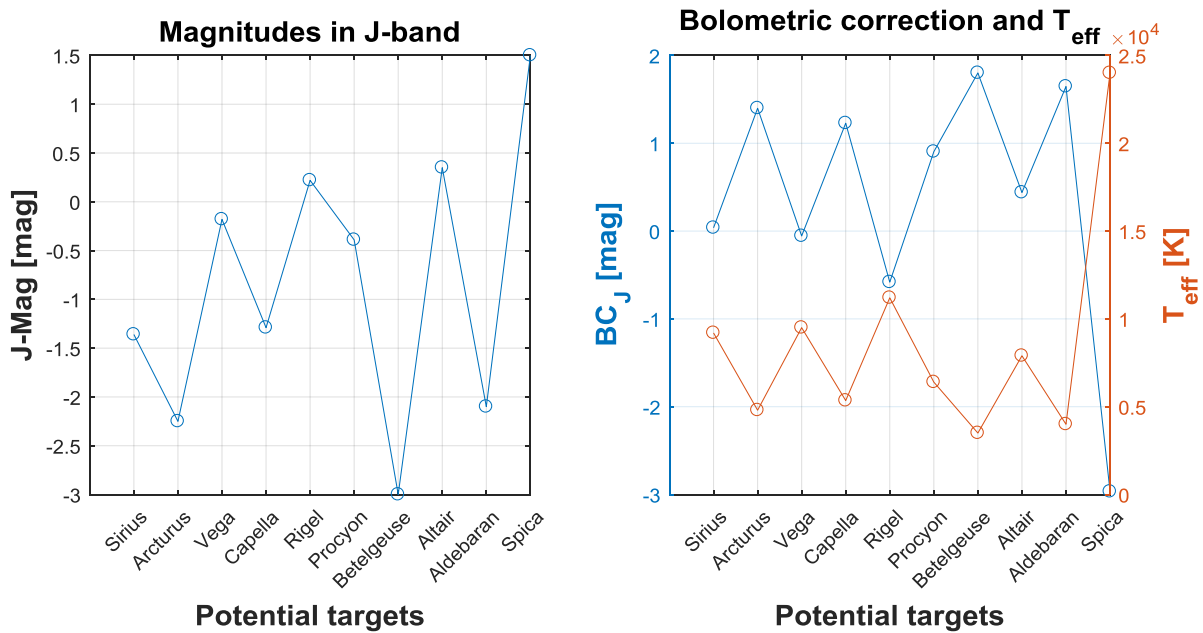


Figure 8.1 – *J*-mag, bolometric corrections and effective temperatures of identified potential targets

Their bolometric correction in the J -band is interpolated from Figure 5.2 as depicted in the figure below where the different stars are sorted according to their effective temperature.

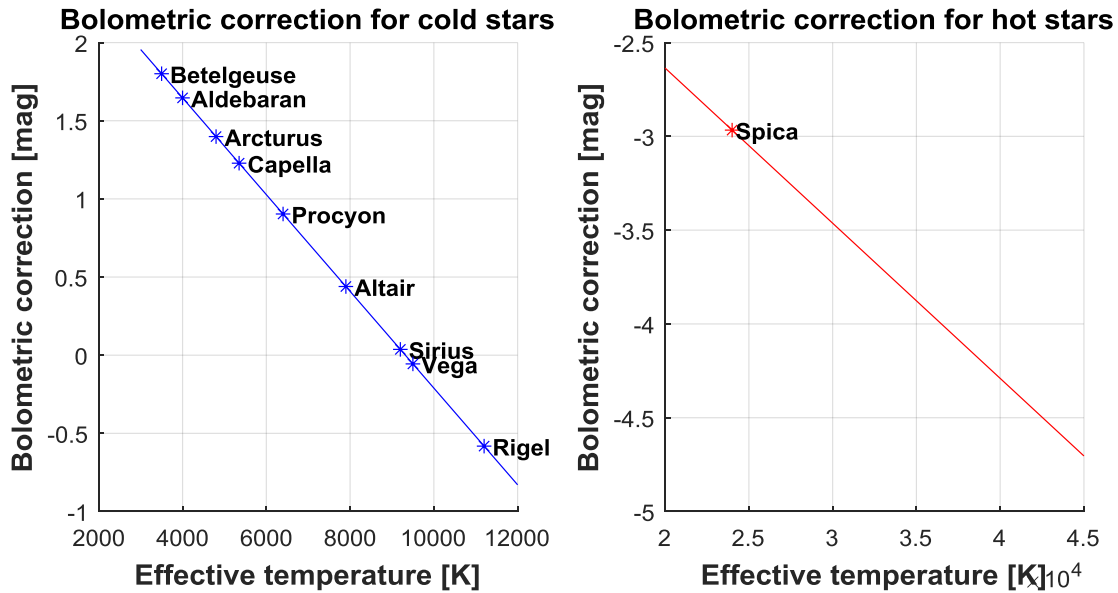


Figure 8.2 – Bolometric corrections of identified targets sorted according to their temperature.

The evolution of the star image diameter and the related vignetting factor previously introduced as a function of seeing with this telescope are depicted in Figure 8.3. We notice that the light injection through the fiber is perfectly performed until a seeing value of 5.08 arcsec . Therefore, no vignetting should be observed during the observations if we consider a typical value of 3 arcsec and a perfect positioning through the focal plane of the telescope.

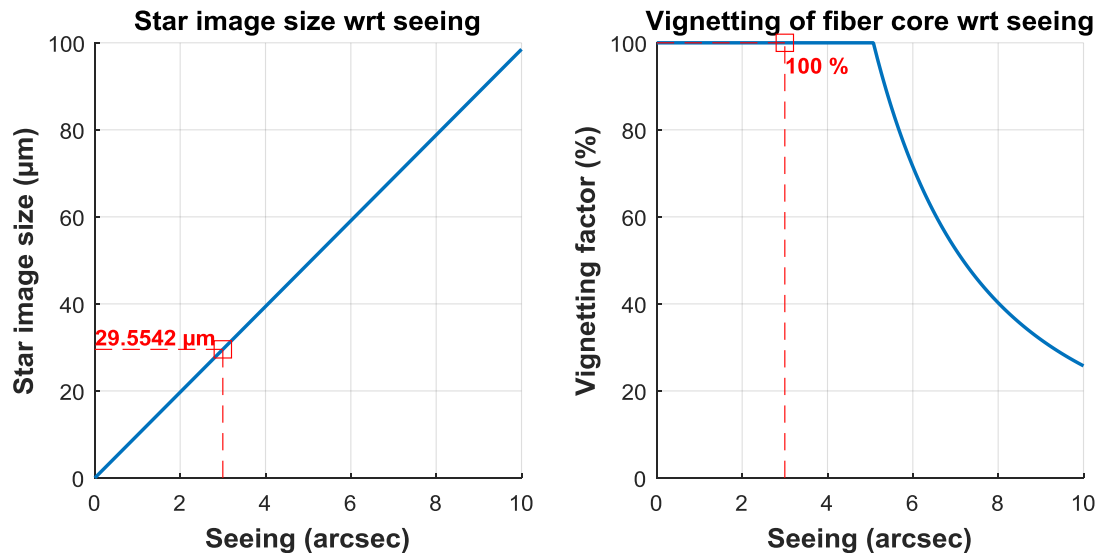


Figure 8.3 - Evolution of star image size and fiber core vignetting factor as a function of seeing with the selected small telescope. Sampled values for a typical seeing of 3 arcsec are also represented.

The calculated received (dN_λ) and detected (dN_{tot}) fluxes are then illustrated in Figure 8.4. These are much larger than the previously observed predictions of Chapter 5 due to the brightness of the considered targets and their perfect transmission into the fiber core for seeing conditions better than 5 arcsec .

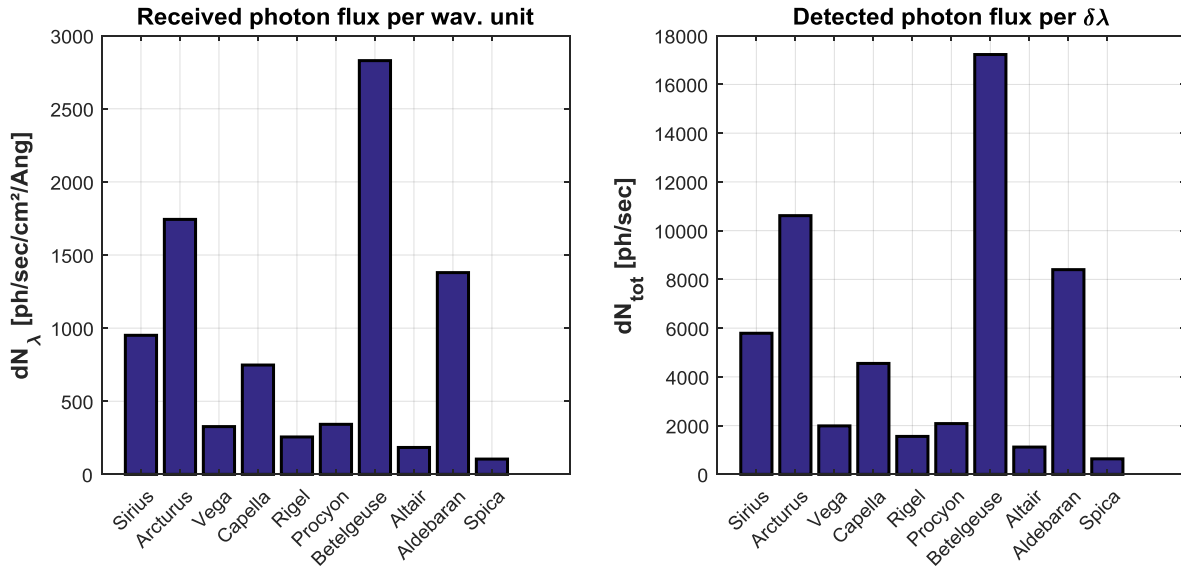


Figure 8.4 - Flux of photons received and detected at 1050 nm for the identified targets

The required integration time is calculated in the same conditions as presented in Table 5.3 except for the change in the telescope parameters, observing site typical seeing and restriction in targets. The calculated observing times are shown in Figure 8.5. These amount to a few minutes which should limit the required tracking period of the small telescope.

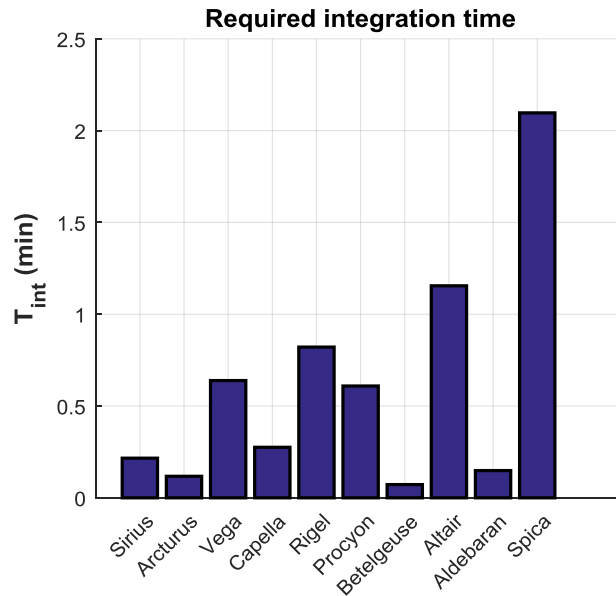


Figure 8.5 - Required integration time at 1050 nm for the identified targets

The possibility of using a CCD is also studied to illustrate their potential utility even if this option will not be implemented practically. The results are plotted in Figure 8.6 for both the central wavelength of 1050 nm (left panel) and 1100 nm (right panel). While the whole list of targets fulfill the requirements at the shorter wavelength, the CCDs are again pointed out as a non-suitable technology for our scientific case as the majority of these bright sources require hours of observation at 1.1 μm . Some of them could however be studied in approximately half an hour such as Arcturus (36 min), Betelgeuse (19 min) and Aldebaran (47 min). Only for those specific cases would CCDs be suitable. The next following graphical results will only concern the central wavelength.

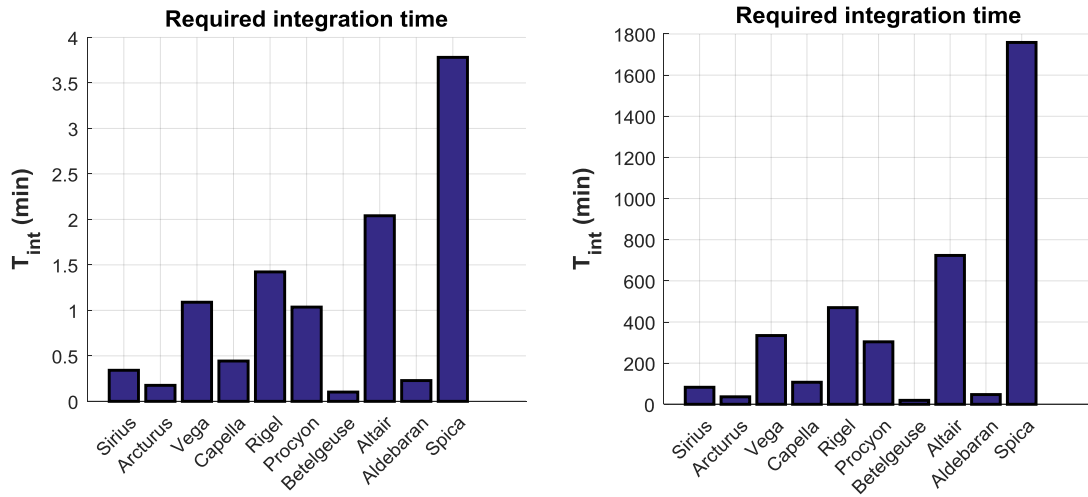


Figure 8.6 - Required integration time for the identified targets when using a CCD at the central wavelength of 1050 nm (left) and 1100 nm (right).

The optimum CCD temperature to observe the identified targets within a minimum observing time as well as the associated time reduction are depicted in Figure 8.7. Since the analyses are focused on bright stars whose fluxes are entirely falling within one fiber core, the best CCD working temperature is much higher than the lowest one the cooling unit may achieve. These high intensity illumination conditions lead to remarkable decreases in integration time.

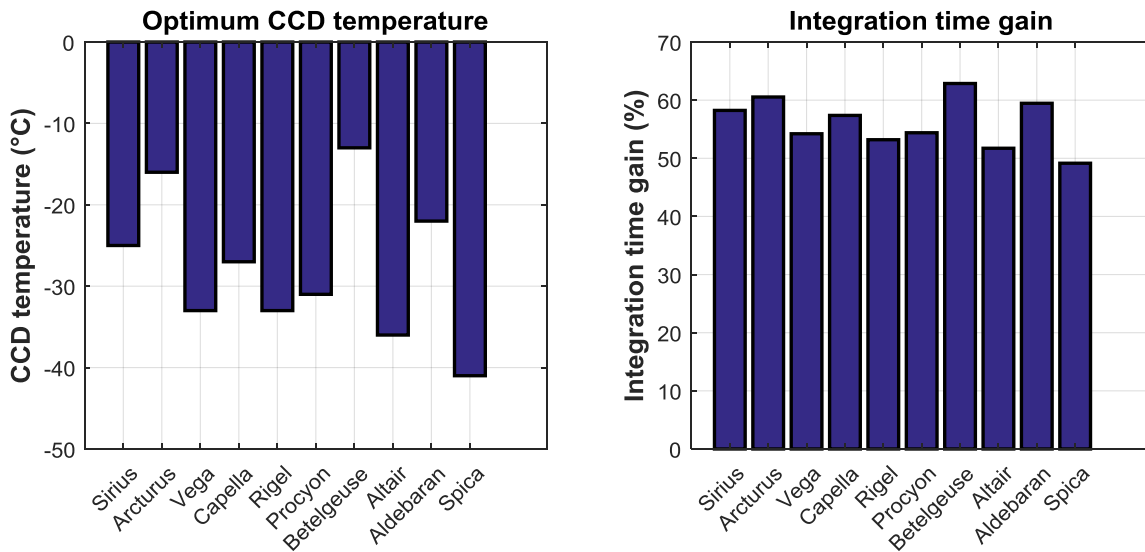


Figure 8.7 - Optimal CCD temperature and integration time gain for the identified targets

The temperature optimization process can be observed in Figure 8.8. As previously observed during the radiometric study of the instrument at the TIGRE telescope and especially within the developed temperature control strategy, the optimization process highly depends on the incoming light flux. While the observation of some stars requires low temperatures (Spica for example), the observation of others such as Betelgeuse is carried out in a shorter period of time under warmer conditions (see right panel of Figure 8.9).

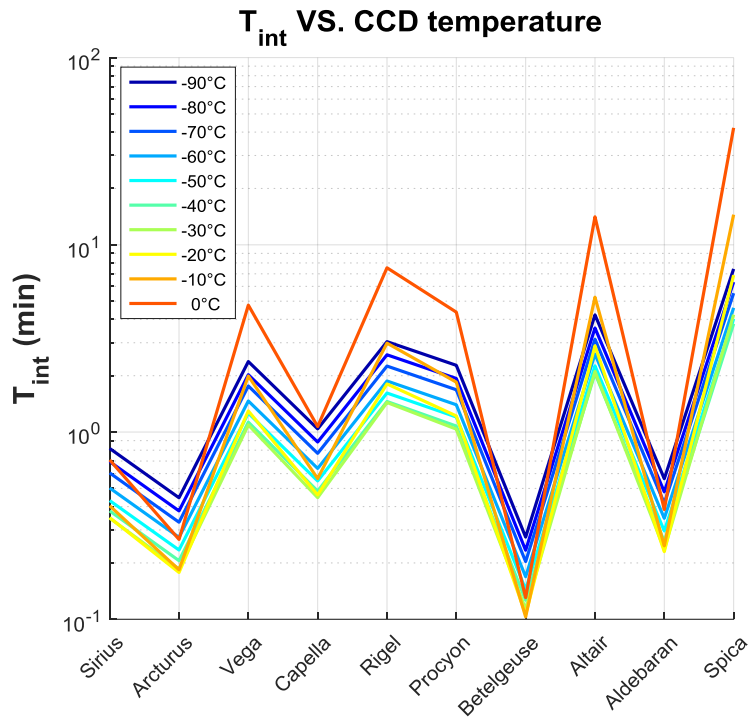


Figure 8.8 - Evolution of integration time as a function of different CCD temperatures for the identified targets

The conclusion that can be drawn is that lower CCD temperatures should be chosen when observing low flux stars. Luminous targets on the other hand may be observed under weak cooling conditions, which leads to time and energy saving. The left panel of Figure 8.9 depicts the distribution of the stars' photon fluxes with respect to the boundary flux that was previously identified (see *Temperature control strategy* of Chapter 5). The corresponding operating temperatures follow the same increasing trend from left to right: from Spica to Betelgeuse, the advised CCD temperature varies from -41°C to -13°C . One should therefore favor higher quantum efficiencies when observing luminous targets rather than reduced dark currents.

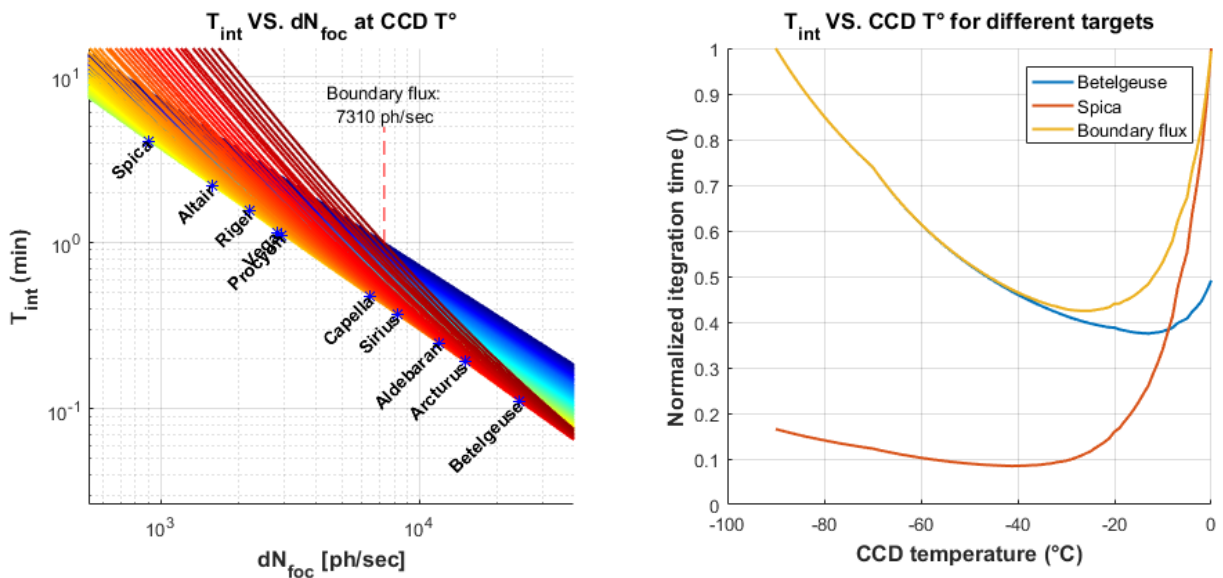


Figure 8.9 - Evolution of integration time wrt. dN_{foc} as a function of CCD temperature with targets depicted on top (left) and normalized integration time as a function of CCD temperature for Betelgeuse, Spica and the boundary flux (right).

8.3 First light in Liège

The photometric budget highlighted the possibility to observe the identified luminous targets with a small telescope located in Liège. This section then intends to introduce the successive practical steps that led to the instrument Belgian first light. Indeed, several technical issues were faced during the first observations and the photon transmission chain from the telescope down to the instrument was established after several iterations. These steps and the associated solutions are described within the upcoming sections.

8.3.1 Preparation of spectrograph for observation

Once the instrument alignment was completed, blackout material was applied on its internal panels to attenuate reflections of light within the instrument enclosure. These absorbing sheets attenuate the straylight generated by light leakages from the regular light path of the instrument. These latter come from the different straylight sources highlighted in Chapter 4.9 such as divergent calibration lamps or the large fiber numerical aperture. Figure 8.10 introduces the instrument final configuration.

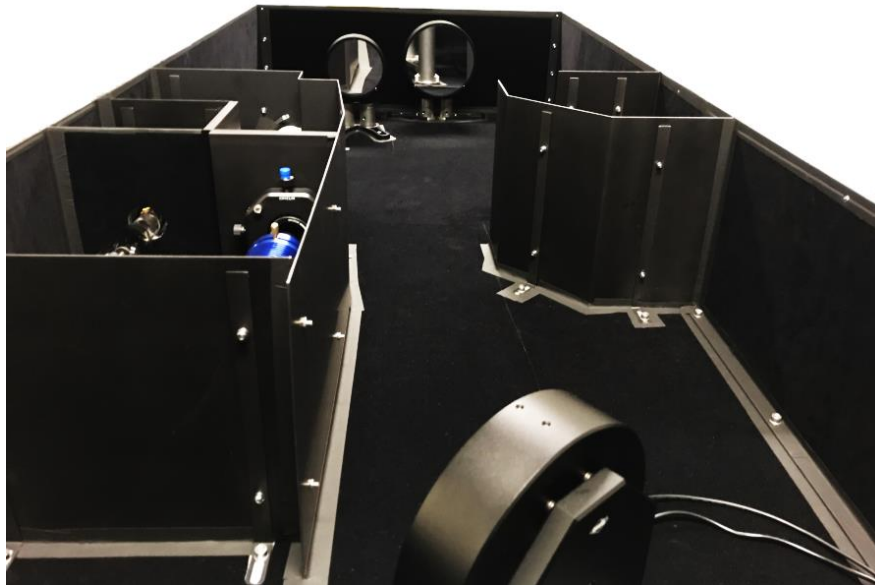


Figure 8.10 - Final configuration of the instrument with black flocked paper

Other complementary equipment was then added to the spectrograph. The fiber bundle and the HCL mechanical slit are equipped with mechanical shutters. These enable to record dark frames during the observation and calibration operations. After the observation of the target, the telescope pointing may then remain locked on the target during the acquisition of dark frames. Indeed, the associated shutter closes and no stellar flux escapes from the bundle. The same advantage occurs when considering the spectral calibration. The hollow cathode lamp requires to be turned on at least 10 minutes before running the spectral calibration process. A mechanical shutter is therefore located on the optical mount holding the calibration slit to control the HCL flux. This avoids turning on and off the hollow cathode lamp and getting rid of the associated warming periods. The Halogen lamp does not require any external mechanical shutter as it is equipped with an internal one. Figure 8.11 illustrates both shutters. They are located as far as possible from the detector as advised by Dallier et al. [26]. This way, the entire spectrograph environment is captured when recording dark frames. It may be possible in the future to re-locate the bundle shutter within the SPS for better results.



Figure 8.11 - Shutters that equip the spectral calibration mechanical slit and the fiber bundle

The LED which intends to back-illuminate the fiber bundle when performing the tracking alignment was eventually positioned (see Figure 8.12). The achromatic doublet that images the LED onto the fibers by reflection through the folding mirror was also aligned.

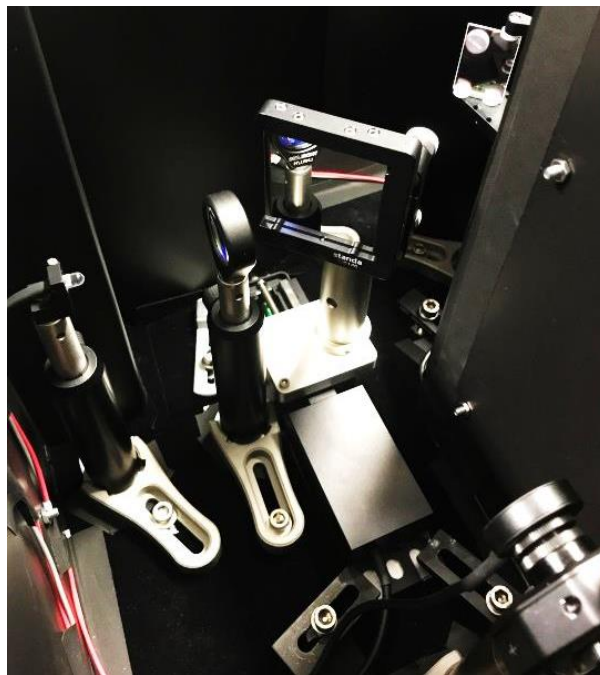


Figure 8.12 - Fiber back-illuminating system that incorporates the LED

The control of these shutters and the LED incorporated inside the spectrograph assembly is performed with the help of a dedicated controller. This small programmable electronic platform establishes the connection with the control computer of the spectrograph. The general control unit of the instrument is supplied with a custom software that was elaborated by two successive students (see Annex B). This latter enables several operations to be carried out such as the calibration or the scientific observation. Both manual and automatic modes were implemented. This enables to either manually control each component separately or run automatic sequences with no required external action. The general aspect of the control software is depicted in Figure B.1 in Annex B.

The spectrograph was then moved from the laboratory to another room suited for night astronomical observations. This room is located a few meters below from the flat roof and has a direct access to the roof. This enables the spectrograph to be connected to the telescope with the selected 15 m fiber bundle. This laboratory was equipped with the fiber illuminating system in order to allow further realignment procedures. The observation room is depicted in the left panel of Figure 8.13 where the instrument, its control computer and the fiber illuminating system can be seen. Figure 8.13 (b) illustrates the removable cover plates which were manufactured within the instrument enclosure. These latter can be rotated in order to provide an easy access to specific optical elements while keeping the instrument cover plate in place. This way, a realignment of the instrument is enabled by finely tuning the position of specific optical elements.



Figure 8.13 – Observing control room (a) and final instrument configuration with removable cover plates (b).

On the other hand, a network connection was installed up to the roof in order to be able to remotely drive the spectrograph from a laptop. The operations of the telescope and the instrument are therefore both carried out from the observation site, which largely eases their synchronization. Figure 8.14 illustrates the observation setup that was installed on top of CSL facilities for the first observation trials: the telescope, equipped with the fiber bundle, and the remote laptop.



Figure 8.14 - Telescope initialization and remote control computer

8.3.2 Coupling with the telescope and first tests

The telescope that was used for the observations on the roof of CSL facilities was equipped with a flipping mirror accessory located close to its focal plane (see Figure 8.15). The initial purpose of this component is to enable pointing at the target star with an eyepiece by reflection with the incorporated mirror and then take an exposure with a camera by flipping this latter out of the field of view. This convenient device was used in a first stage to position the fiber bundle onto the star image and transmit the light to the spectrograph. The bundle mount thus takes the place of the camera within the flipping mirror assembly for our purpose.



Figure 8.15 - Flipping mirror device: the upper flange connects to the telescope, the left connecting tube intends to hold an eyepiece and the lower hidden aperture incorporates a standard thread for cameras. The small turning button activates the flipping mechanism.

In order to connect the telescope to the spectrograph, an adapted fiber holding system must therefore be designed and manufactured. This latter must account for the telescope optical design and position the fiber at its focal plane while using the flipping mirror device. For that purpose, on sky observations of bright stars were conducted to accurately identify the focal plane position of the telescope with respect to the coupling flange with the flipping mirror mechanism. This way, the required mechanical piece could be manufactured to properly position the fiber optical mount at the correct location. The connecting mechanical piece and the overall adapted assembly are respectively shown in Figure 8.16 (a) and Figure 8.16 (b).



Figure 8.16 - Connecting mechanical piece using the standard camera thread (a) and adapted fiber positioning system (b)

First observations were conducted with this setup on June 22nd 2017 by pointing Arcturus. As a complement to the telescope guiding, micrometer setting screws onto the fiber optical mount were used to finely align the star image onto a selected fiber. In order to identify the best flux transmission condition, the spectrograph was set at the zeroth order in order to maximize the light visualization as no dispersion occurs in those conditions. The best transmission situation was therefore examined at the spectrograph detector. It must be noticed that doing so does not logically enable both tracking and recording tasks since the grating inclination angle changes from one operation to the other. A first issue directly appeared: several fibers were illuminated instead of only one. Accounting for the approximate seeing, the telescope focal length and the fiber core diameter leads to the conclusion that only a severe defocus of the telescope may explain these conditions.

Another problem was that fibers were twinkling until the moment they turned off one after the other. The guiding of the telescope was this time the source of perturbation. A drift in the guiding mechanism actually continuously shifts the star image across the focal plane leading to a variable illumination of the fibers. This explains the fact that fibers were transmitting the photon flux in turn and the difficulty to align the star image onto a fixed selected zone of the bundle. Moreover, the defocus of the Schmidt-Cassegrain telescope induced another artifact: the observed star image pattern exhibited a dark hole in its center. Indeed, when defocusing such a telescope, the secondary mirror obstruction appears and the circular pattern starts looking like a donut. When centering the star image onto the fiber bundle, only the “satellite” fibers were therefore illuminated and this falsely appeared as a misalignment.

Without a direct view at the scene in the bundle plane, obtaining proper scientific observations was extremely difficult. The conditions were not suitable neither to establish nor to maintain a proper light transmission chain and record the stellar spectrum. However, an average frame of a hundred 3 sec exposures is depicted in Figure 8.17. To obtain this focal plane image, the camera was therefore setup in a way to record a hundred images and then compute their average. This way, the several exposures can be combined to reach a higher signal-to-noise ratio when the observing time of the camera is limited by the dark noise.

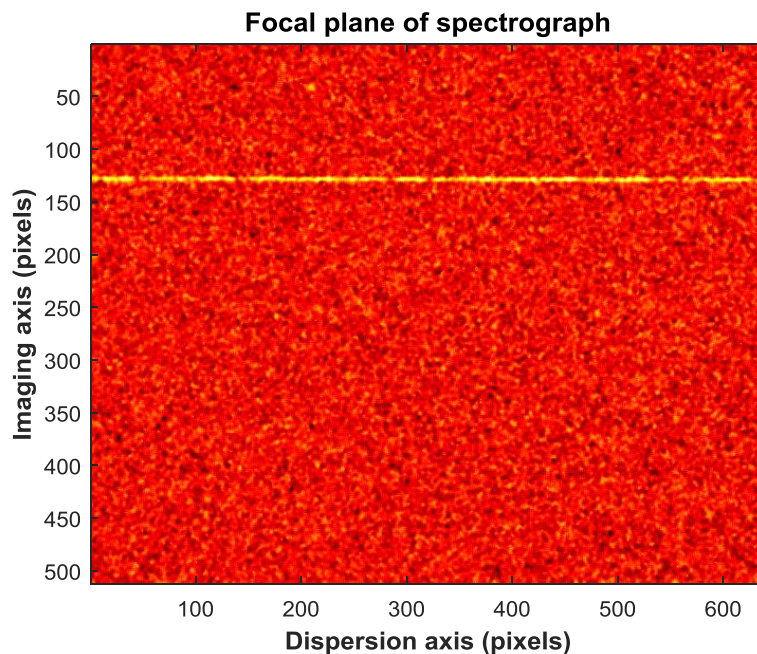


Figure 8.17 - Focal plane image when pointing at Arcturus with the initial observing setup

Figure 8.18 illustrates the reduced spectrum from this observation. Due to the weakness of the recorded spectrum, it appears rather difficult to isolate the scientific signal from the inherent noise of the detector. Some features in the obtained curve may be associated to genuine absorption features but the obtained signal-to-noise ratio is insufficient to certify they do not originate from noise.

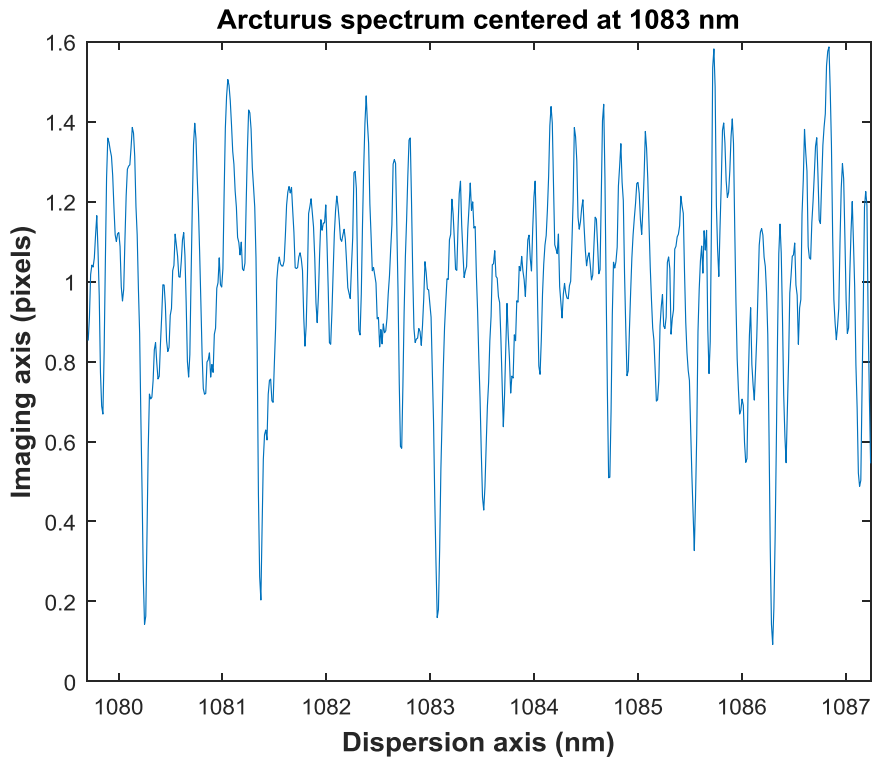


Figure 8.18 - Arcturus spectrum centered at 1083 nm from our first observation on the 22nd of June

Improvements in the observing equipment were therefore required to obtain useful data. The first correction we applied on the next observation night was to refocus the telescope. The obtained result was an increased difficulty to center the star image onto the fiber. Indeed, the previous situation, i.e. featuring a large blurred image, eased the superposition of part of the light from the star onto the fibers. This led to a few photons to propagate to the focal plane of the spectrograph.

Once the telescope was refocused, superposing the tiny star image onto the small fiber core became a lot more challenging. Indeed, the tracking drift did not help in bringing the star light onto the fiber and locking that situation. Moreover, we discovered the stability of the floor to be an issue. The flat roof of CSL facilities is indeed made of a membrane covered by gravels. In addition to the poor telescope-ground contact conferred by the gravels, the soft membrane changed in shape as we were moving on it. Any movement while observing therefore modified the telescope pointing accuracy and the observation suffered from those perturbations.

Eventually, we also noticed the flipping mirror repeatability was not sufficient to ensure the perfect superposition between the star and the fiber. These complications made it difficult to perform good quality observations. A few nights were dedicated to try to achieve that goal but no satisfying result was obtained with that strategy anymore. A revised plan was therefore required to achieve the first light and obtain a decent spectrum.

8.3.3 Advanced tracking device

Initial prototype

In order to overcome the tracking issues we were facing, we developed a better-suited star positioning system. Our previous tests clearly pointed out the need of having a direct view onto the bundle surface. This way, we would be able to observe the actual star image position and superpose it onto a selected fiber. To identify the fiber position, we can benefit from the available lightning solution that is already incorporated inside the instrument. Indeed, the designed star positioning system that will be used at TIGRE requires the bundle to be retro-illuminated with the help of a LED. This LED could therefore be used for the same purpose: observing the fiber onto a camera positioned at the telescope side of the bundle. The adapted visualization system could therefore mimic the methodology of the star positioning system designed for TIGRE.

The required modification to be applied on our system was therefore to incorporate a small camera and replace the flipping mirror by a beamsplitter. Indeed, both the star image and the fibers must be observed simultaneously. The technique that was considered is not exactly the same as the one employed for the real star positioning system. As a reminder, this latter incorporates an antireflective window, namely the beamsplitting element, which selects the light both from the telescope and the fibers. To do so, fibers are projected onto the SBIG camera with the help of a small mirror. In the present case, for simplicity, compactness reasons and availability of the equipment, another strategy is adopted. The camera features an objective which focuses directly onto the bundle plane. This way, the fiber locations can be identified when the fibers are lit from the spectrograph. On the other hand, since the bundle end is planar and metallic, the induced reflectivity can be used as a mirror to visualize the star by reflection as long as it remains away from a fiber. As soon as the star flux is transmitted through a selected fiber, the image disappears from the camera focal plane and the transmission occurs. The optical design of the modified tracking device is depicted in Figure 8.19.

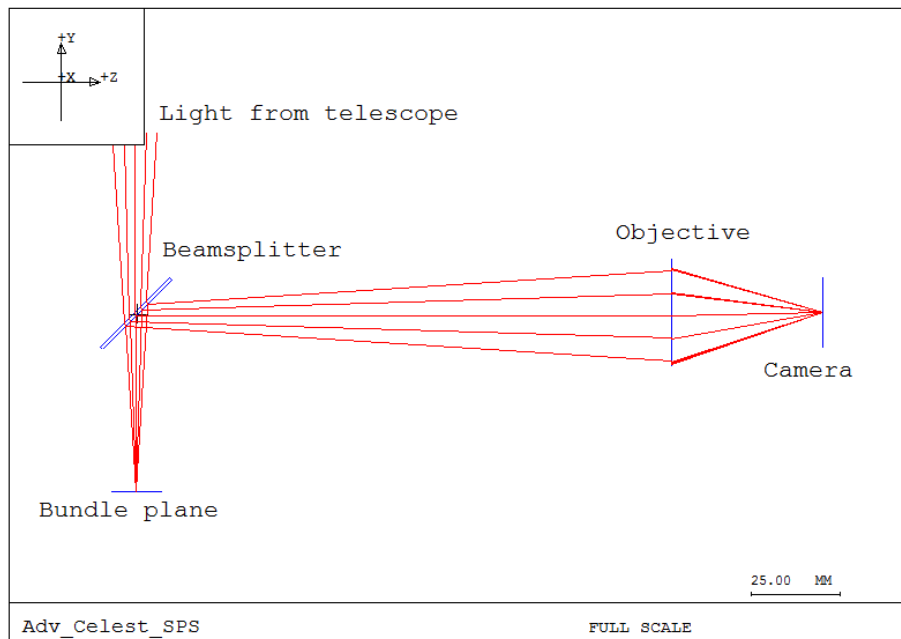


Figure 8.19 - Advanced tracking device optical design. Light propagates from the telescope down to the bundle plane. The reflected beam onto the metallic ferrule then goes back to the beamsplitter along with the light from the fibers and reaches the camera.

The first version of this updated device featured an available spare beamsplitter whose splitting ratio is 70:30, i.e. 70% of the light is reflected. Moreover, the optimized waveband for this element is 700-1100 *nm* within the near-infrared. Both the splitting and anti-reflective (applied on the other side of the element) coatings are therefore designed to efficiently work in that region of the spectrum. The camera we used for the visible alignment of the spectrograph was chosen to integrate the new tracking instrument. Both its interface and compactness eased its integration. In order to insert the beamsplitter within the flipping mirror containing box, the mechanism of this latter was replaced by a threaded shaft holding a U-shaped metallic mount. This latter intended to support the beamsplitter which replaced the flipping mirror. Teflon plates are used to sustain the beamsplitter within this custom optical mount. The beamsplitter mount and its modified assembly are presented in Figure 8.20.

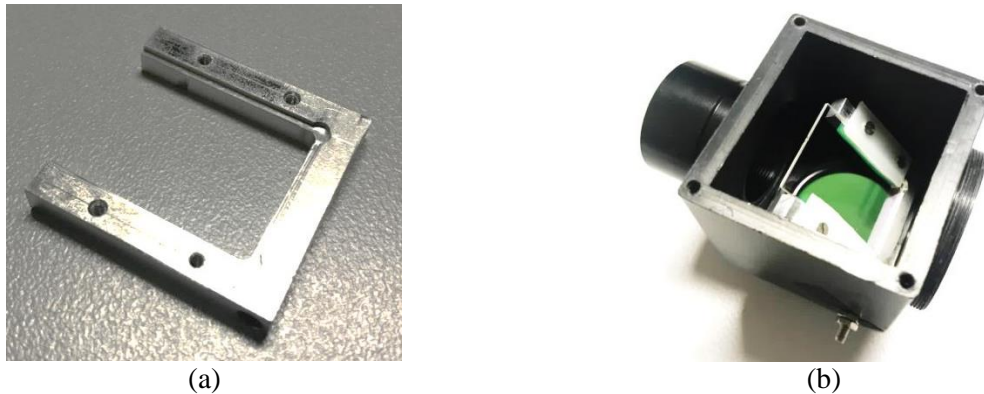


Figure 8.20 - Beamsplitter mount (a) and modified flipping mirror box (b).

In order to position the camera the correct distance away from the fiber bundle, a circular tube with setting grooves was manufactured. The latter enable the camera piston to be adjusted to finely focus onto the bundle and clearly distinguish the different fibers. The camera holding system and the obtained visualizing apparatus are depicted in Figure 8.21.



Figure 8.21 – Camera holder (a) and adapted tracking device (b).

The next observing night was conducted with the help of the updated tracking system. A second display screen was added to our observation setup on CSL facilities roof to perform the live tracking (see Figure 8.22). Indeed, this adapted system enables a real live tracking of the target and a simultaneous recording of the spectrum. The previous device did not allow both operations to be carried out at the same time since the star alignment was performed using the grating zeroth order. Therefore, switching between the tracking and recording activities required the spectrograph configuration to be modified. Due to guiding uncertainties, the alignment condition had deteriorated while modifying the setting configuration and the recorded frames were therefore of poor quality. The

advanced tracking system enables to follow the target position within the bundle plane and correct for any misalignment in real time. The added display was thus dedicated to following the target position with respect to the fiber while the laptop was devoted to the spectrograph control.



Figure 8.22 - Observation setup installed on CSL facilities roof. A second display devoted to the tracking operation was added. The laptop was dedicated to the spectrograph control.

Visualizing both the fibers and the star image was a success. An unexpected behavior however appeared: both the fiber bundle and the star image were polluted by multiple ghosts. These are created by multiple internal reflections within the beamsplitter. Indeed, the beamsplitting side faces an anti-reflective coating that maximizes the transmission of light through this part of the beamsplitter. The use of a visible camera however motivated the choice of a visible LED to illuminate the bundle. The spare beamsplitter, as previously stated, is optimized to perform in the near-infrared part of the spectrum. Both its beamsplitting and anti-reflective properties are specified within this waveband and fail outside this region. Multiple reflections are therefore induced within the piece of glass and create numerous image copies of the observed object. These internal reflections are depicted in Figure 8.23 with the help of optical simulations with ASAP.

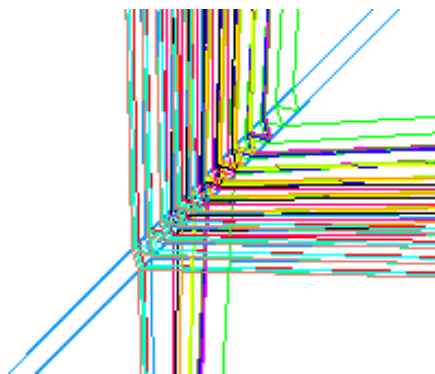


Figure 8.23 - Internal reflections that occur within the beamsplitting glass plate.

Ghosts of the fiber bundle and the star image slightly differ when observed on the camera. Since the fiber bundle is directly viewed in reflection through the beamsplitter (see Figure 8.24 (a)), ghosts appear as fainter copies of the initial image regularly spaced away from this latter (see Figure 8.24 (b)). The original image is naturally the most luminous one and is easy to locate as it lies at one extremity of the series.

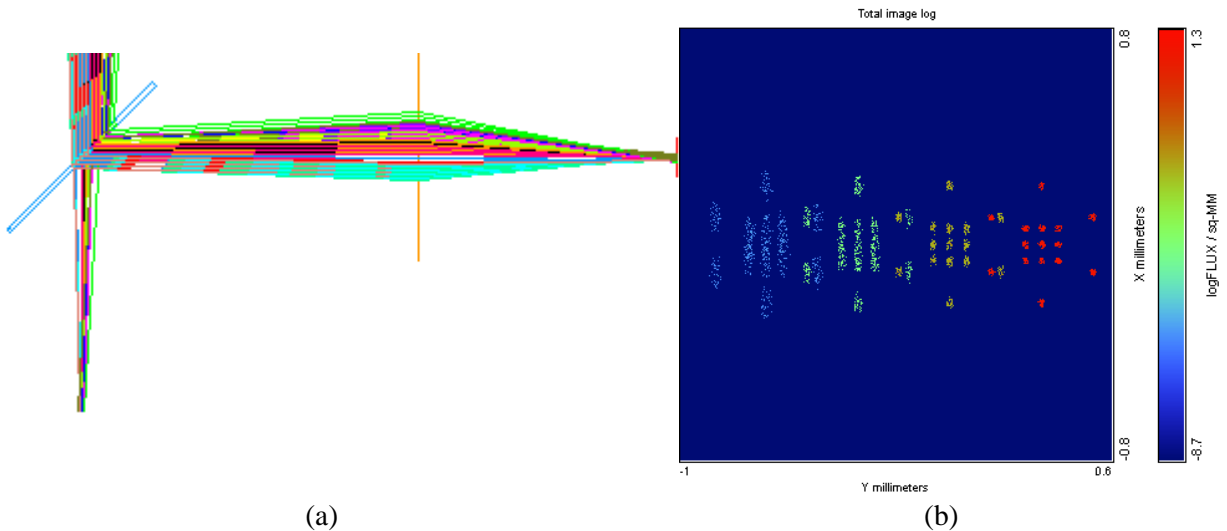


Figure 8.24 - Simulated behavior of the ghost generation associated with the fiber bundle light (b).

On the other hand, the star image reaches the camera focal plane after a transmission through the beamsplitter, a reflection onto the bundle metallic ferrule and a last reflection on the beamsplitter. The light path therefore involves two interactions with this piece of glass and thus involves two ghost productions. Ghost images are first created within the bundle plane (see Figure 8.25) and these multiple images individually induce in turn a series of second order replicas at the camera focal plane (see Figure 8.26 (a)).

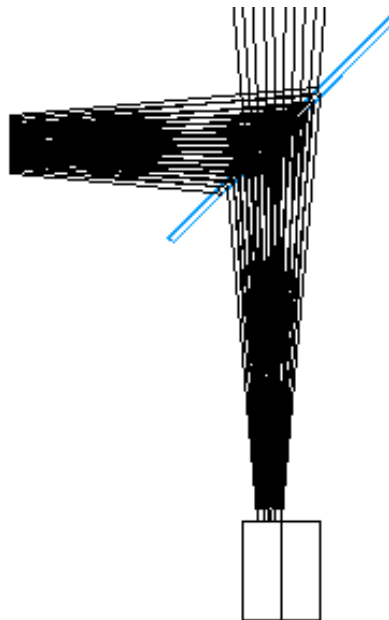


Figure 8.25 - Multiple image formation onto the bundle ferrule due to internal reflections within the beamsplitter during the transmission process of the star light.

These series are regularly spaced in the same way as the bundle images as illustrated in Figure 8.26 (b). Although there exists an offset between the successive sets of ghost images, they overlap at the camera detector and produce a complicated pattern of images of different light intensities. Indeed, the

individual ghosts from a given group fall at the same location as other ghosts of another series (the first ghost of a sequence overlaps with the second one from the second series and the third ghost from the subsequent series and so on). The original image we intend to observe to perform the tracking task therefore does not lie at an extremity of the ghost sequence anymore. An additional difficulty thus arises from the double interaction between the beamsplitter and the star light.

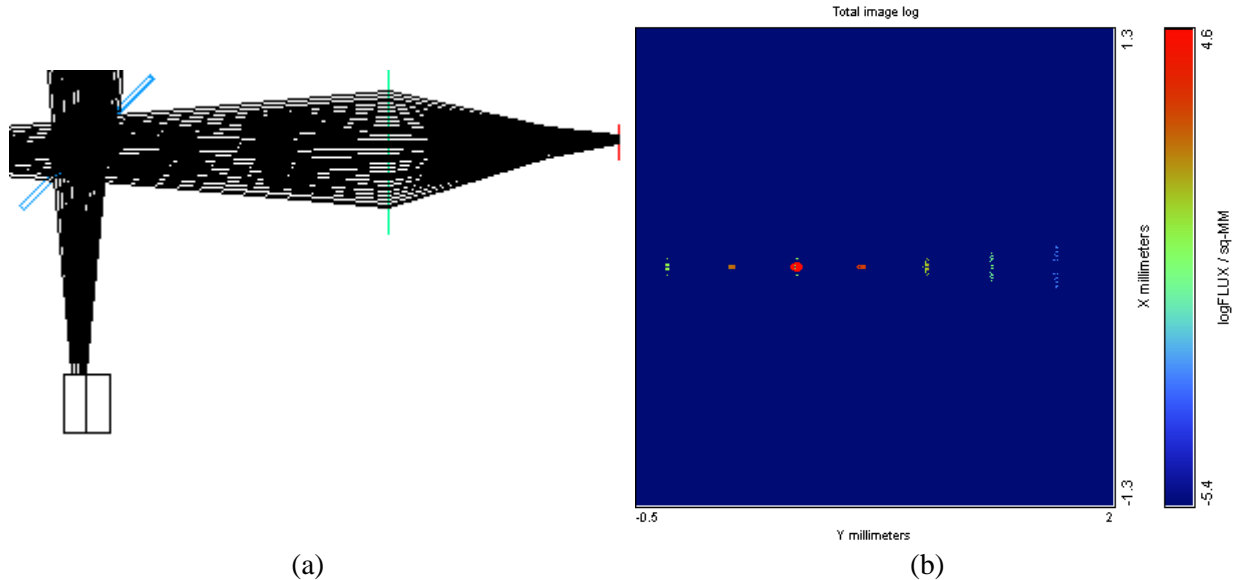


Figure 8.26 - Simulated behavior of the ghost generation issued from the star light (b).

Unfortunately, the above considerations on ghost generation appeared to us when we started the first live tracking operation. Identifying the most luminous star image was not a trivial task and the tracking operation turned out to be difficult. This first use of the adapted tracking device however confirmed the mandatory need for such equipment. Recording the live scene from the bundle plane highlighted that continuous corrections of the telescope tracking were needed. Indeed, the previously suspected drift was confirmed and a slight correction every few seconds or so was carried out to compensate for this pointing error. Manipulating the telescope during the acquisition to ensure the perfect superposition of the star and the fiber remained difficult because sometimes the guiding corrections failed and the star image was taken a large distance away. Only a few frames per night actually successfully caught the star spectrum and maximizing their number represented an arduous effort.

On the other hand, this version of the advanced tracking system did not favor a high transmission of the stellar flux through the fiber even when the fiber and star images perfectly overlap. Indeed, only approximately 30% of the photons are transmitted by the beamsplitter whereas 70% are discarded and remain unused. This is due to the selection of an available spare beamsplitter and was foreseen. A better selection would be the exact opposite beamsplitter ($R = 30\%$, $T = 70\%$) since 70% of the light would travel to the fiber whereas the exact same number of photons would be imaged onto the guiding camera. Indeed, the number of photons this guiding detector observes depends on the product of both the transmittance and reflectance of the beamsplitter, which would remain equal to 21%.

Despite these issues, a faint spectrum could be reduced from the combination of several observations of the night. The focal plane image is depicted in Figure 8.27. Once again unfortunately, the amount of remaining noise after data reduction did not enable the production of a high-quality spectrum. The tracking system therefore required additional modifications.

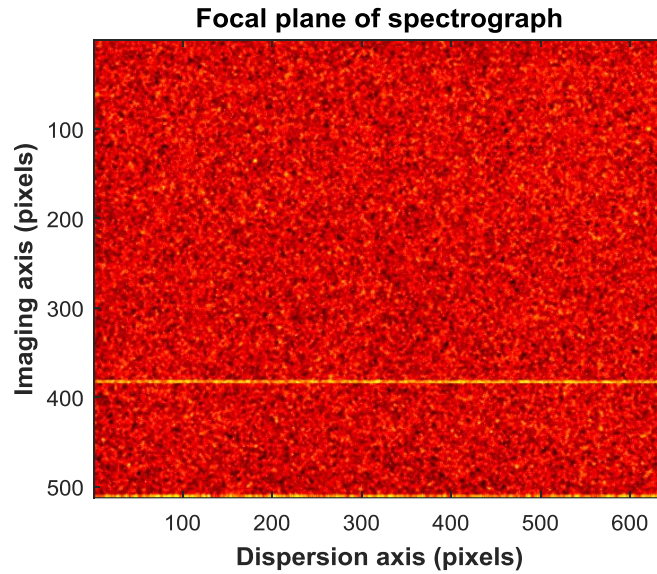


Figure 8.27 - Focal plane image when pointing at Vega with the advanced tracking device.

Suppression of ghost images

The first correction we implemented was the suppression of all ghost images to ease the star tracking process. This operation consisted in avoiding the ghost generation process from both the stellar flux coming from the telescope and the LED light from the bundle. For that purpose, the tracking device must therefore be used within the design waveband of the beamsplitter: from 700 to 1100 *nm*.

The selection of the visible LED was motivated by the use of a small visible camera. Indeed, this CMOS (Complementary metal–oxide–semiconductor) detector does not benefit from a high quantum efficiency in the near-infrared as depicted in Figure 8.28 [87]. Moreover, this detector is equipped with a near-infrared filter with a cutoff wavelength at 650 *nm* (the reddened part of Figure 8.28 is filtered out). In order to be able to run this camera in the near-infrared region of the spectrum, we first removed this filter. We could then install the near-infrared LED within the spectrograph to illuminate the fiber bundle without the production of any ghost at the camera side of the fibers. The selected near-infrared LED has an emission peak located at 870 *nm* and a bandwidth of 40 *nm*. Without the filter; this falls in a region where the camera benefits from approximately 30% of quantum efficiency and the observation of the bundle is enabled.

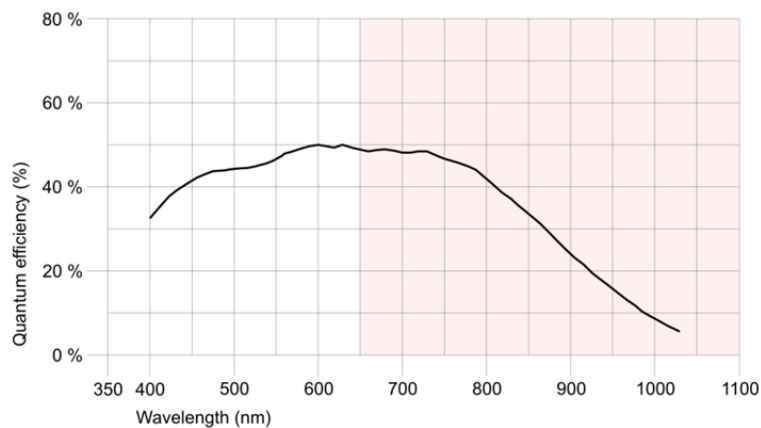


Figure 8.28 - Quantum efficiency of the tracking visible camera [87].

On the other hand, we had to discard the visible spectrum of the observed target to reach the camera to avoid any ghost image. In order to tackle with this issue, a long-pass filter was installed between the camera tube connector and the beamsplitter containing box. This colored glass filter has a lower cut-off wavelength equal to 840 nm and the visible stellar light was therefore discarded from propagating within the tracking system. No target ghost image could therefore appear at the tracking camera focal plane anymore.

The next observing night intended to test this first update of the tracking device by observing Vega a second time. Figure 8.29 is a live tracking acquisition showing the star image which lies close to the fiber bundle. As expected, no more ghost, neither from the bundle nor from the star, is polluting the camera focal plane anymore. Visualizing both the target and the bundle occurs when the stellar flux impacts on the metallic ferrule and is reflected to the camera. The fiber bundle is illuminated to be able to locate and select an acquisition fiber. As a second step, a green cross mark is positioned onto this fiber and the bundle turned off. The telescope pointing is then adapted to bring the target onto the cross mark and maximize the photon transmission to the spectrograph. When superposed to the fiber core, the stellar image disappears from the acquisition screen. The goal is then to correct the telescope tracking as soon as the star becomes visible again to avoid light leakages since the spectrograph camera is acquiring data in a continuous way.

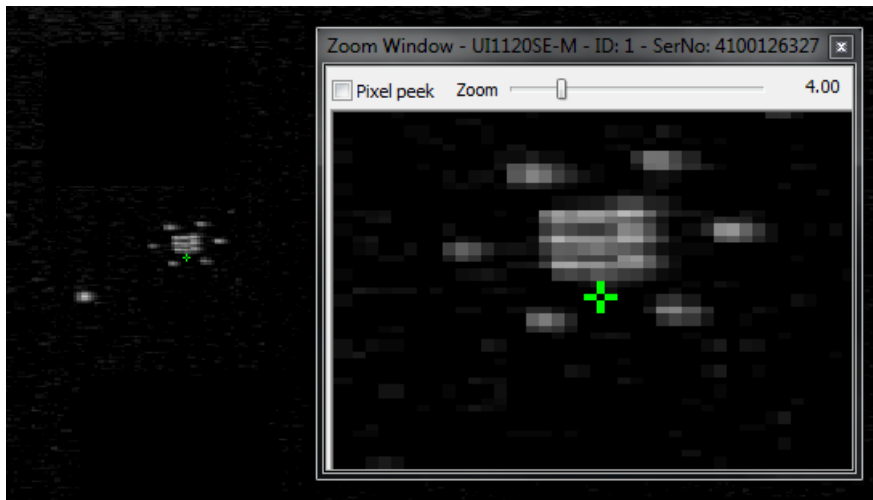


Figure 8.29 - Live tracking acquisition. The star image lies at the left side of the picture and the fiber bundle right above. A zoom onto the bundle enabled to tick a mark onto a fiber to lock its position after having turned off the LED.

This first improvement of the tracking device eased the superposition of the stellar image and the fiber bundle. The continuous correction of the telescope guiding remained a difficult task as previously noticed but more acquisitions incorporated scientific signal. The data reduction however revealed that the poor beamsplitter transmission remained a showstopper to acquire high quality spectra. Indeed, more than half of the photons (70%) are rejected by this piece of glass and directed onto a wall of the enclosure. Figure 8.30 illustrates the resulting focal plane image combining those observations from this night which contained some stellar flux. More photons were collected and a larger signal detected but this did not enable recording a proper spectrum.

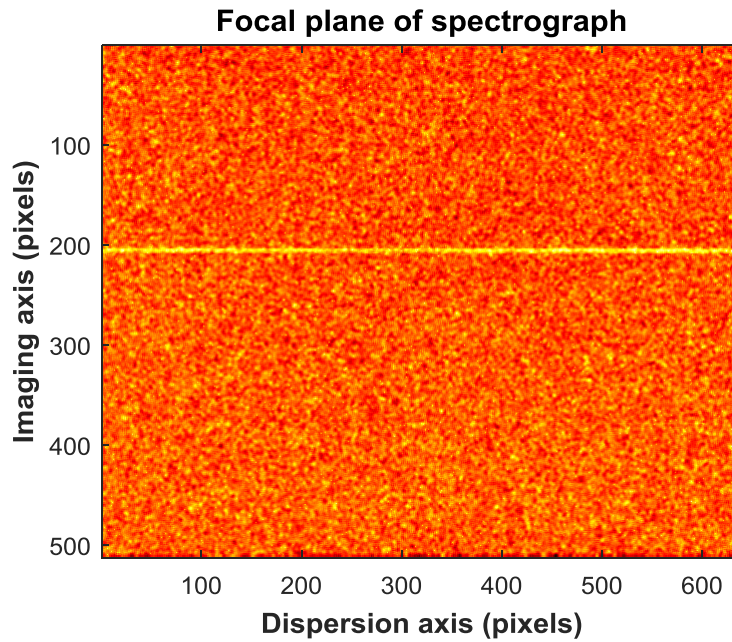


Figure 8.30 - Focal plane image when pointing at Vega with the first update version of the advanced tracking device.

This observation night therefore confirmed the operational state of the tracking device but also highlighted the need for a higher flux transmission within the system. We eventually concluded we needed a more appropriate beamsplitting ratio that favors transmission rather than reflection. This spare beamsplitter must therefore be replaced by another one that features a higher transmission percentage. We selected two other ratios: 30:70 ($R:T$), which is the opposite version of the first one, and 10:90. The first version ensured a workable tracking operation since the same amount of light reaches the guiding camera in that case (21 % as explained before). With such a component, more than twice the amount of light however is transmitted through the fiber. The second one features a higher transmission ratio and enables more photons to be collected by the fiber when the alignment succeeds. However, only 9% of light is sent to the tracking camera and observing the star light may be less convenient in that configuration.

Increased flux transmission

The two subsequent and last nights were dedicated to the observation of Capella. Indeed, because of its brightness in the near-IR, Capella ($\alpha Aur = HD 34029, J = -1.29, RA = 05h 16min 41sec, DEC = +45^{\circ}59'53''$) turned out to be the best candidate to receive a maximum of photons.

In order to maximize the chance of obtaining suitable scientific data, we decided to first implement the 10:90 beamsplitter into our tracking device. In case of unsuccessful tracking, we would have switched the beamsplitters but 9% of the stellar light turned out to be sufficient to perform an accurate tracking on that target. Indeed, Capella is 1.11 *mag* brighter than Vega which benefits both our tracking and recording operations⁶. The telescope guiding ability during those nights was also troubled by heavy winds.

⁶ Capella is 1.11 *mag* brighter than Vega in the J -band which corresponds to an increased near-IR flux by approximately a factor 13. Since we nearly divided by two the amount of stellar light used for tracking (21% vs. 9%), there must be no problem to use the new beamsplitter to guide the telescope on Capella. The second night however, we noticed a decrease in both tracking and recorded signals. This was due to the Ophelia hurricane that brought Sahara sand and smoke from Portugal forest fires that polluted the Belgian sky.

After having reduced the data from the previous nights, we identified the best recorded frames and their associated conditions. Indeed, the first nights, even though the received stellar flux was low, enabled to test different observing schemes. Several integration times and acquisition options were therefore assessed and the best observing strategy was established as the nights succeeded. For example, we investigated the most appropriate integration time and observed that 15 *sec* appeared to be the best value. The camera must indeed integrate several seconds to catch enough light to enable the detection. On the other hand, the star image did not lie onto the fiber core more than a few seconds before a readjustment of the telescope was required. Integrating during a long period would therefore imply many intervals when the telescope is not well pointed and no light enters the spectrograph. On the other hand, the observing time was also limited by the high dark signal of the InGaAs detector we selected.

The camera settings were also optimized. We used the Medium Gain to enable integrations of a few seconds while not saturating the detector. During the first nights, we also tried to average many frames within the hardware as it is enabled by the camera. This way, a limited amount of data is produced per observation as only one light image file is generated: the mean image of the programmed frame sequence. This technique first appeared as a clever method for both limiting the amount of data to process and increase the signal-to-noise ratio of the acquired image. However, due to the limited telescope pointing accuracy, many dark sessions were involved in this averaging process which totally ruined the observations. This approach is closely related to the above conclusion on the upper limit on integration time. A preferred approach was to take a large number of similar frames and record all of them. This way, the selection of the best ones, i.e. those which contain scientific information, was enabled during the data reduction. Only the camera integrations that occurred during a proper synchronization with the telescope guiding were therefore kept for the calculation of the star spectrum.

The amount of recorded images where the stellar flux was detected largely increased in comparison to the previous observations after this second update of the advanced tracking device. Moreover, the intensity of the signal surpassed all previous measurements. The combination of data acquired from both nights enabled to largely improve the quality of the reduced spectrum and confirm the instrument's first light on 16 October 2017. The reduced image after combining the observations from both nights is depicted in Figure 8.31. The illumination of a fiber located close to the 350th line of the detector is clearly noticeable. Several absorption features appear to the naked eye when scanning the spectrum from one side to the other. They appear as dark intervals within the detector band illuminated by the target spectrum.

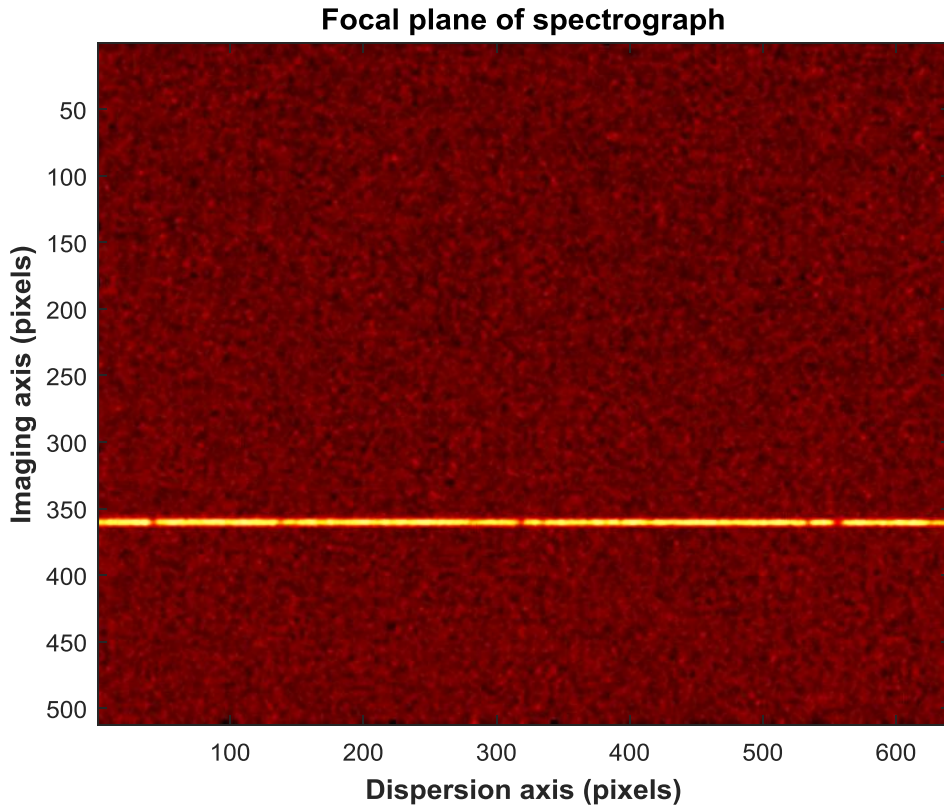


Figure 8.31 - Focal plane image when pointing at Capella with the second update version of the advanced tracking device.

The reduced spectrum from Figure 8.31 is illustrated in Figure 8.32. The absorption features appear as sharp decrease in the recorded light intensity. The amount of noise is significantly decreased in comparison with the previous results.

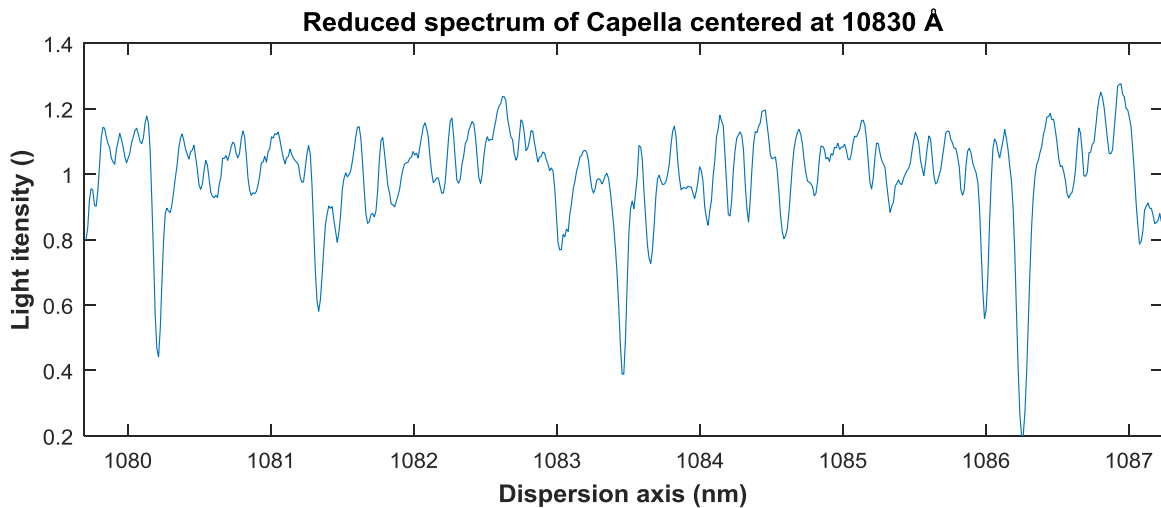


Figure 8.32 - Reduced spectrum of Capella centered at 10830 Å after combining the different observations from the last two nights.

It may appear contradictory that several 15 sec acquisitions were required to obtain a satisfying result. Indeed, the previous photometric budget roughly indicated a similar integration time to reach a signal-to-noise ratio equal to 100. However, the pointing accuracy and the associated corrections led to

acquisitions during which the star light was not continuously transmitted to the spectrograph. Therefore, dark integrations were mixed to signal recording and the photometric budget did not foresee such complications.

On the other hand, a close look at Figure 8.29 reveals that the star image is larger than the one considered during the photometric analysis. Indeed, the stellar image onto the bundle plane is poorer than the illuminated fiber core. According to Figure 8.3, this would require a typical seeing of 5 arcsec if the fiber bundle is located at the best telescope focus position. This may be another source of image blurring even if we practically optimized the telescope focus by visually minimizing the stellar image onto the camera detector.

On the other hand, atmospheric turbulence was probably important because of the strong winds. Moreover, atmospheric diffraction was probably high as a result of the large airmass during our observations. It might also be noticed that the diffraction limited performances of small telescopes at long wavelengths quickly degrade. Indeed, this small telescope when observing at $1.1 \mu\text{m}$ exhibits a PSF (Point Spread Function) of approximately $30 \mu\text{m}$. The previous geometrical considerations on the foreseen star image size and associated vignetting thus become valid around 3 arcsec . This contributor to light losses might therefore have been slightly underestimated too. Whatever the reason explaining an increased star image diameter, the consequence is a longer integration time to reach the same signal-to-noise ratio. Finally we note that the stellar image was disappearing from the tracking screen when it reached the fiber cladding, not the fiber core in reality. In that condition, light is not transmitted and the fine alignment is not complete.

8.3.4 Verification of performances

By the time of our observations (15 and 16 October 2017), Capella was still relatively low on the Eastern horizon at the beginning of the night and was then progressively rising to its near zenith position. Since we performed our observations during the first halves of the two nights, the airmass of the target was relatively high. On the first night, the first and last spectra were taken at airmasses of 3.06 and 1.50, respectively. For the second night, the corresponding range of airmasses was between 3.64 and 1.43. Therefore, one expects the presence of relatively strong telluric features in the spectrum (see below).

Capella is a so-called *RS CVn* binary system with an orbital period of 104.02 days ([88], and references therein). *RS CVn* binaries consist of two late-type subgiants or giants, with (at least) one of them displaying a strong magnetic activity. The magnetically active stars display giant stellar spots which modulate the light curve of these objects as they rotate around their axis and around their common center of gravity [89] [90]. Moreover, large magnetic loops may connect spots on both components of the binary system, hence leading to complex field entangling and producing a strong X-ray emission with frequent and substantial flaring [91].

Mekkaden (1985) reported the detection of a strong dependency between the X-ray luminosity of long-period *RS CVn* stars and the strength of their *He I* λ 10830 absorption line [92]. Therefore, this kind of objects could be scientifically rewarding targets for NÉSIE, and we have chosen a central wavelength of 10830 \AA for our observation. Nevertheless, let us remind here that the goal of the present observations is not to perform any scientific study, but rather to test the performances of our instrument.

The spectrum of Capella around the He I λ 10830 line

An important aspect to keep in mind here is the fact that Capella is a spectroscopic binary consisting of a slow rotating ($v \sin i = 4 \text{ km/s}$) G8 III primary and a rapidly rotating ($v \sin i = 35 \text{ km/s}$) G0 III secondary [88]. When interpreting the spectra, we thus need to account for the orbital Doppler shift of the two stars. Our NÉSIE observations of Capella were taken between JD2 458 042.321 and JD2 458 042.426 (first night), and JD2 458 043.305 and JD2 458 043.439 (second night). According to the ephemerides of Torres et al. [88], these dates correspond to orbital phases 0.122–0.133. For the primary star, the expected radial velocity (RV) is $52.8 \pm 0.5 \text{ km/s}$ where the quoted uncertainty corresponds to half the RV range covered between phases 0.122 and 0.133. The corresponding value for the secondary star is $6.4 \pm 0.5 \text{ km/s}$.

Figure 8.33 illustrates a comparison between our NÉSIE spectrum of Capella and the ‘summer’ atmospheric transmission spectrum of Hinkle et al. [93]. We clearly see that the strongest absorption features in the spectrum (near 10802, 10813, 10835, 10837, 10860 and 10862 Å) are due to telluric lines. A good understanding of these lines is important since the He λ 10830 line is one of the main drivers behind the NÉSIE spectrograph. A close comparison reveals that the telluric reference spectrum is shifted with respect to the NÉSIE spectrum. This shift was corrected before we compared our spectrum with the theoretically expected spectrum of Capella. For this latter exercise, we also had to account for the heliocentric correction of $+23.6 \text{ km/s}$ of Capella at the time of our observations.

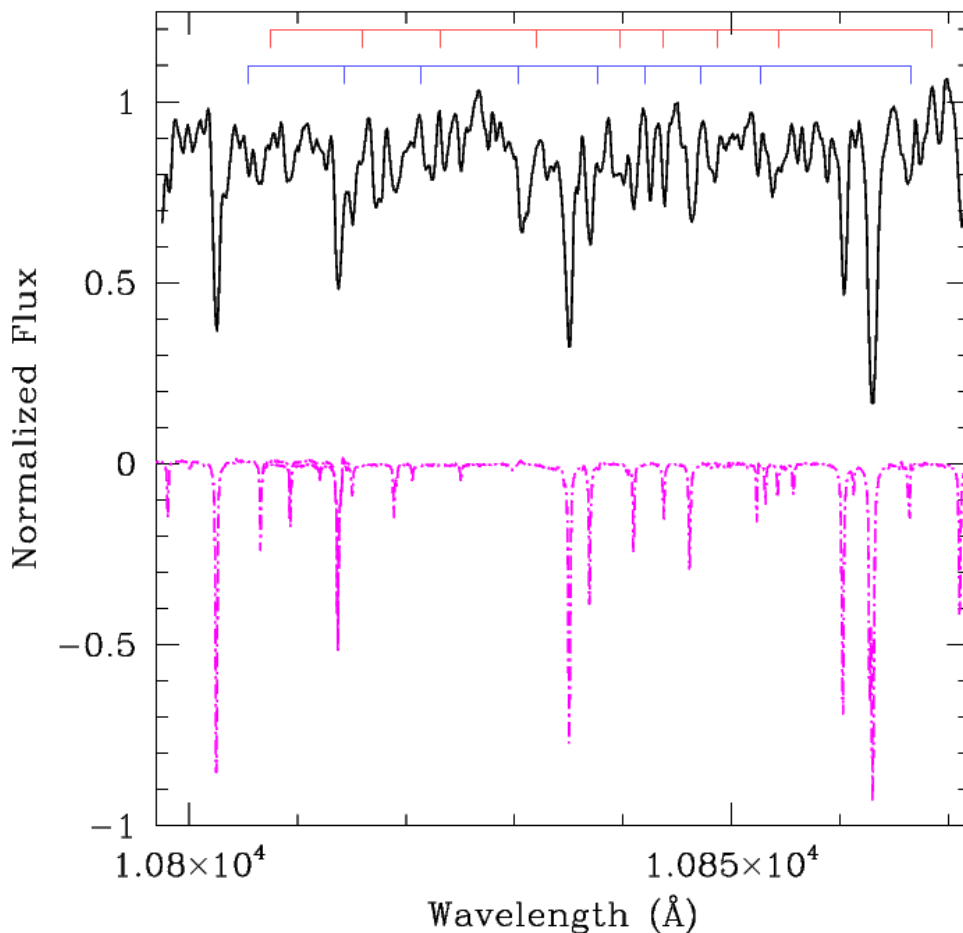


Figure 8.33 - NÉSIE spectrum of Capella (*black solid line*). The magenta spectrum corresponds to the atmospheric transmission tabulated by Hinkle et al. [93] and shifted for clarity by -1.0 . The red and blue tags indicate the expected wavelengths respectively of the most prominent primary and secondary spectral features.

Moreover, the telluric lines are much broader in the NÉSIE spectrum than in the atmospheric transmission spectrum. This is due to the much higher spectral resolving power (100 000) of the atmospheric transmission spectrum [93]. The atmospheric transmission spectrum thus needs to be broadened to match NÉSIE's spectral resolution. For the present case, we did not correct the spectrum for atmospheric transmission. Indeed, attempts to do so failed. This is most likely because of the high average airmass and the rather wide range of airmasses during our observations. Such a situation probably emphasizes the non-linear behavior with airmass of the intensity of the telluric lines.

To identify the stellar lines, we have retrieved synthetic spectra computed with the PHOENIX model atmosphere code and tabulated by Husser et al. [94]. To match as closely as possible the actual spectra of the primary and secondary star, we have extracted synthetic spectra with $T_{eff} = 5000\text{ K}$ and $\log g = 2.50$ for the primary and $T_{eff} = 5700\text{ K}$ and $\log g = 3.00$ for the secondary star. Following the results of Torres et al. [88], we have adopted solar abundances for both models. These spectra were then shifted in wavelength, according to the orbital solution of Torres et al. [88], and were broadened to account for the stellar rotational velocity (of the secondary) and the spectral resolution. These synthetic spectra then allowed us to attribute the strongest non-telluric absorptions in the spectrum to the binary components (see Figure 8.33). In particular, we found a prominent *He* λ 10830 line, mostly associated with the active secondary star (see Figure 8.34).

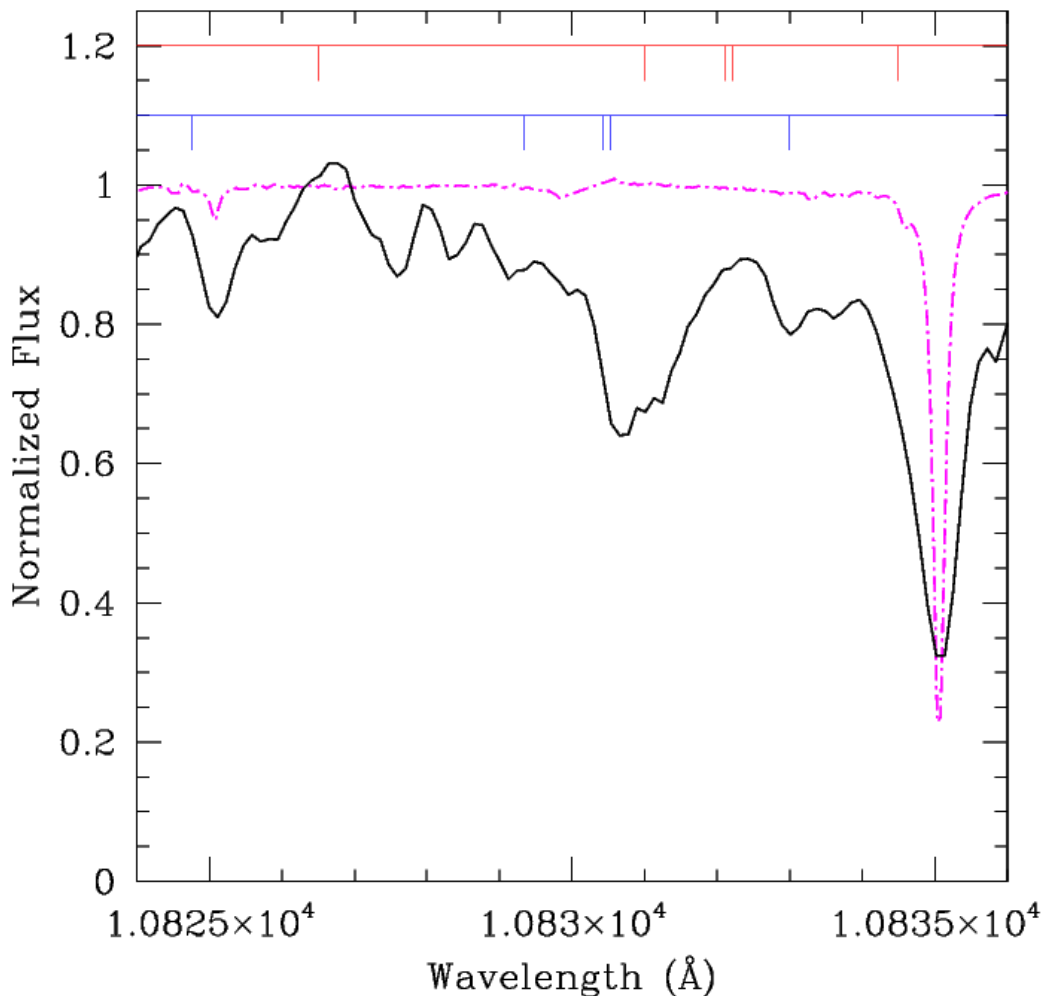


Figure 8.34 - Zoom on the spectral region around the *He* λ 10830 triplet. The atmospheric transmission is now overplotted on the NÉSIE spectrum. The other symbols are as in Figure 8.33.

8.4 Conclusion

The first observation tests of the spectrograph from Liège were motivated by an optimistic photometric budget. This latter indicated that the identified targets required observation times of a few minutes at maximum to reach a suitable signal-to-noise ratio. The potential use of a small telescope to assess the instrument performances was therefore confirmed. On the other hand, the observation strategy when using CCDs that was developed in Chapter 5.9.1 was confirmed with the selected targets: brighter stars enable operating the detector at warmer temperatures.

The practical observations at CSL facilities started with a simple tracking system made of a flipping mirror mechanism. The first results indicated that the telescope guiding was insufficient to obtain satisfying data with that set-up. Modifications were therefore required to overcome this issue. The telescope was thus equipped with a guiding camera to enable a live tracking of the star position with respect to the fiber bundle. A ghost issue then appeared due to the improper use of the selected beamsplitter. Adaptations were conferred to the system to overcome this problem and the tracking device was then operational. An increase in the captured stellar flux was eventually enabled through the replacement of the beamsplitter by a more convenient version. The target spectrum could finally be observed with the final version of this advanced tracking device.

The various improvements of the tracking equipment and the revised observing strategy led to the achievement of the instrument's first light. Several issues needed to be solved following the first observation that featured the initial tracking device. The amount of collected light increased at each modification until enough light was collected to provide a useful target spectrum.

The discussion of the spectrum accounted for the atmospheric absorption and the orbital parameters of the target. After a proper calibration of the spectrum and its comparison with the one derived by Hinkle et al. [93], strong telluric lines could be identified. These were expected due to the large airmass of the target during our observations. Synthetic spectra generated by the PHOENIX code then enabled the differentiation between the individual lines from both components of the binary target. Eventually, we were able to observe a prominent feature within the region of the *He I* 10830 triplet associated with the active secondary star.

Chapter 9

Conclusion and
perspectives

9. Conclusion and perspectives

9.1 Overall conclusion on the conception of NÉSIE

The manuscript detailed every elementary step of the conception of NÉSIE: from the early derivation of instrumental parameters to the record of first light stellar spectra on the Belgian sky. The purpose of this instrument is to observe (massive) stars in the near-infrared domain. This niche indeed suffers from a lack of dedicated instrumentation, probably due to the weak sensitivity of typical CCDs in that part of the spectrum. The collaboration between several research groups from the University of Liège aims at filling this gap. The collected data by NÉSIE will help the involved scientists to improve their models and reach a better understanding of the tremendous objects that represent massive stars.

The first chapter introduced the ARC project which intends to explain poorly understood phenomena that occur in massive stars. The association of both technical and scientific expertise is the cornerstone of a prolific collaboration that will grow and be a life-long process for NÉSIE. The scientific program of the instrument and the associated scientific requirements were developed and the host telescope presented. A macroscopic view onto the history of near-infrared fiber-fed spectroscopy then highlighted several important characteristics of similar instruments. Indeed, useful heritage could be obtained from these projects such as the identification of proper detector and fiber technologies or the requirement on potential cooling of the instrument.

Chapter 2 investigated several observation strategies and technical aspects related to the near-infrared domain. The *J*-band belongs to the observational windows accessible from the ground. These latter are spectral slots through which astronomical observations can be carried out by benefiting of the local transmission of the atmosphere. The atmospheric dispersion issue was also highlighted as it transforms the stellar image into a spectrum at the focal plane of the telescope. This problem was assessed when designing the SPS. Properties of fibers were also deeply studied as a proper manipulation of these light connectors is required to maximize the instrument efficiency. Micro-lenses were identified as suitable telescope-to-fiber couplers. Suitable coatings, filters and glasses were proposed to improve the instrument throughput. Eventually, the best available detector technologies were presented as well as the chosen sensor for our application.

The theoretical relations that govern the general behavior of a spectrographic instrument were established in Chapter 3. A proper understanding of these equations was mandatory to derive the instrument specifications starting from the scientific requirements. Several conclusions could already be drawn and gave indications on the suitable way to improve a spectrograph's figure of merit. We showed that this operation consists in maximizing both the resolving power and the throughput of the instrument. Several parameters have a strong impact on these two functions but some were advised as first elements to act on. It was for example advised by several authors to maximize the blaze angle to limit the overall size of the instrument while maintaining a high resolving power.

The optical design and the associated analyses were introduced in Chapter 4. The scientific requirements were first translated into instrumental specifications. This process involved Bingham's methodology which helps in fixing the right parameters to derive the others. Indeed, a spectrograph instrument is described by 16 parameters and establishing the most appropriate deducting path is not trivial. The optimization process then started and implemented specific solutions to deal with the selected configuration. A toroidal lens was incorporated close to the focal plane to tackle with the inherent astigmatism aberration of Czerny-Turner spectrographs. The tolerancing analysis assessed the

robustness of the optical design with respect to manufacturing and alignment uncertainties. Suitable compensators were identified in order to ensure the alignment feasibility and the recovering of the initial performances. This analysis also provided convenient indications on the alignment scheme to follow. The alignment simulation was therefore closely related to the tolerancing analysis and its development was based on these previous results. The need for a polychromatic function of merit underlined the fact that optimizing the optical quality over the entire focal plane was mandatory. This means obtaining the expected imaging quality at each side of the spectrum and both at the top and bottom parts of the entrance slit. Once the alignment scheme was established, the calibration unit of the spectrograph could be elaborated. For that purpose, two mechanical slits are located at image locations of the fiber bundle. Suitable hollow cathode and halogen lamps were selected to respectively carry out spectral and flatfield calibration tasks. An elaborated illuminating setup was also developed to optimize the spectral calibration, more specifically to favor metallic lines over unstable gas lines. The crosstalk analysis quickly checked the maximum number of fibers that could be accommodated with the selected detector. This also fixed the minimum distance between two subsequent fiber cores to avoid any interference between spectra. In order to avoid any light artifact at the focal plane and maximize the useful throughput of the instrument, a straylight analysis was eventually conducted. The design of suitable separation panels was conducted to avoid any unwanted path of light to reach the detector. This also benefits to the overall signal-to-noise ratio of the instrument since these background photons are prevented from reaching the sensor.

The Chapter 5 was devoted to the calculation of the photometric budget of the spectrograph. This estimation of the overall optical chain throughput therefore accounted for all involved elements. The radiometric budget of the typical targets first assessed the number of photons that were emitted from the source. Both interstellar and atmospheric absorptions were then included to evaluate the photon flux that reaches the telescope pupil. Next, the instrumental overall efficiency was evaluated. Fiber losses (absorption, FRD), coating reflectivity, grating efficiency and detector quantum efficiency were therefore combined for that purpose. The dominating noise sources and in particular the detector dark noise were accounted for to eventually determine the instrument signal-to-noise ratio. The integration time needed to fulfill the scientific requirements could then be extracted and several cases were investigated: different targets, specific NIR detectors and CCD, varying absorptions and foreseen parameters to improve the results.

The practical alignment of the instrument could then be initiated after the previous simulated verifications. A specific optical setup was first developed to illuminate the fiber bundle with laser light. Both optical and near-infrared possibilities were offered by this system. Indeed, the alignment of the instrument was first performed with visible light since only a slight refocus is required to correct for the chromaticity of the toroidal lens. Once the monochromatic performances were checked with NIR wavelength, the polychromatic imaging quality was assessed. For that purpose, the HCL was incorporated in the fiber illuminating system and the first spectra were observed. The resolving power was both verified by a qualitative observation of close lines and a quantitative measurement of spectral profiles. A calibration test of the instrument was also initiated and the translation stage repeatability verified to conclude the alignment.

The SPS conception was illustrated in Chapter 7. The purpose of this instrument is to align the star image onto a selected fiber core and maximize the transmission throughput from the telescope to the spectrograph. The atmospheric dispersion that is usually tackled with a dedicated ADC was also accounted for in the design. For that purpose a methane filter was fitted to the camera to drive the tracking at a wavelength located closer to the NIR domain. Otherwise, the simulations showed that the NIR stellar image could be located outside the fiber core and the associated light losses would be

dramatic. The optical design of the instrument was based on the experience acquired in the field of amateur astronomy. Several techniques have been developed by professional astronomers and have been adopted by amateurs with time being. Using a fiber bundle also limited the choice of the most suitable approach. The adopted methodology is based on the superposition of both stellar and fiber core images on a guiding camera. A radiometric budget also evaluated the integration time needed to reach the required signal-to-noise ratio. The assembly and alignment of this subsystem concluded the chapter.

The practical observations and on-the-sky tests of the instrument concluded this manuscript. These were carried out with a small telescope at CSL facilities in Liège, Belgium. In order to assess the feasibility of these observations, an adapted photometric budget was first established. The encouraging results of this analysis motivated the practical realization of the observations. The instrument was therefore prepared for those by covering the enclosure with black flocked paper to minimize straylight reflections. The shutters and LED were installed to enable the dark frame subtraction and the tracking of the telescope. An observation room was prepared to install the spectrograph with the fiber illuminating system. A control computer with a dedicated software was also installed to enable the remote control of the instrument from the observation site. Both the telescope and spectrograph control operations were therefore accomplished from the same location. The first observing nights identified several issues principally related to tracking difficulties. The obtained throughput was not sufficient therefore clearly highlighting the requirement for a better tracking system. A similar technique to the one derived for TIGRE was therefore imagined. A guiding camera was selected to image the sky scene that falls onto the bundle reflective surface. This reflected image was eventually captured by the camera with the help of a beamsplitter that promotes the transmission to maximize the photon fluxes down to the spectrograph focal plane. The optimization of this system enabled to record NÉSIE's first light. The spectrum of Capella was obtained by combining several observations over two nights. The high dark current of the detector required to perform several binning operations during the data reduction which directly decreased the resolving power. Several telluric lines could be clearly identified and the use of PHOENIX enabled the identification of the lines from both components of the target binary. Finally, we found a prominent *He* λ 10830 line, mostly associated with the active secondary stars and were therefore able to isolate stellar features from the recorded data.

9.2 Perspectives and suggested improvements

NÉSIE's first light achievement is the first step in the recording of stellar spectra with a brand new fiber-fed instrument. This newborn spectrograph must now be deeply experimented to optimize its performances and tackle with the issues it may still suffer from. This work indeed gave the life to a spectrograph whose behavior was deeply investigated through optical analyses. However, its complete and proper handling will require more experience with real observations at TIGRE.

A last look at Table 1.1 is useful to conclude on the overall success of the conception of NÉSIE. The goal waveband of interest can easily be scanned by rotating the grating. For example, Figure 6.16 and Figure 6.17 illustrated the observation of spectra from 940 to 1120 *nm* approximately. The measured resolving power through this spectral region was evaluated to 27 414, which is above the goal requirement of 20 000. The photometric budget highlighted that slightly more luminous targets should be observed to fulfill the requirement on maximum observation time. The calculation was however performed by considering pessimistic hypotheses on transmission efficiencies of the involved optical elements. The more optimistic cases showed that the requirement should be fulfilled quite easily. The sky background measurement is enabled through the use of a fiber bundle. Satellite fibers sample this background at a few arcsec from the target as it is the case in large professional observatories.

Eventually, the calibration accuracy was assessed by repeatedly moving back and forward the translation stage and recording the central fiber centroid. The maximum wavelength measurement error was then evaluated. The speckle pattern that appears at the entrance slit of the instrument impinged upon the accuracy of the measurements. The repeatability of this mechanical element could not be attested as high enough to ensure the fulfillment of the associated requirement as one recorded value was located outside the allowed interval. The perturbation of the speckle aspect of the fiber intensity distribution is however suspected to be the cause of this departure from the simulation results. The use of monomode fibers is advised to perform more precise measurements.

The overall fulfillment of the requirements is therefore achieved with great satisfaction. This achievement occurs at the end of an extraordinary adventure where multiple obstacles had to be overcome. The observation of N3SIE's first light is a clear example of the learning process that must be followed to obtain good quality results. The record of Capella's spectrum with a small 20 cm telescope was not trivial as previously explained. The recorded signal-to-noise ratio was not sufficient to perform a data reduction without impacting on the resolving power of the instrument. It is therefore difficult to assess its performances in fine details although these first data hint at an excellent scientific potential of the instrument. This scientific return within a period of only 8 nights spread over a period of 4 months already testifies of the potential of this instrument. The observations at TIGRE will help in experimentally confirming the numerous simulations from the previous chapters. The increased photon flux will provide a much stronger signal and the performances of the instrument will be checked. The better tracking will also provide more stability to the recorded spectrum as the dark periods that occurred in Belgium will not dominate. Only under such conditions can the radiometric budget be checked.

In order to further improve the instrument performances, several suggested improvements are already foreseen. These are listed below with a view from top of the optical chain down to the detector level:

- In order to overcome any atmospheric dispersion issue, a specific ADC can be implemented into the SPS, or a revised version of this latter. Amici prisms may be used to finely compensate the stellar light dispersion as the pointing of the telescope changes during the observation. The implementation of the methane filter would not be necessary anymore. A better throughput efficiency would therefore result from this implementation since the stellar image alignment onto the fiber core would be improved.
- Micro-lenses should be engraved onto the fiber core at both sides of the bundle. This would lead to a tremendous decrease of FRD fiber losses. Indeed, the injected focal ratio of the telescope would be converted to $f/4$ approximately under typical seeing conditions which benefits to the conservation of the beam numerical aperture through the fiber. Both stellar light injection and collection by the collimator would be improved with such connectors. On the other hand, the resizing of the stellar image would increase the number of photons captured by the fiber core and the telescope f-ratio would also be adapted to the collimator's one. Moreover this would lead to worse scrambling properties but does not appear as a major inconvenient at first sight. The major inconvenient induced by micro-lenses is the direct decrease of resolving power. Since the addition of micro-lenses was foreseen early in the design, the resolving power of the instrument was slightly increased over the goal requirement ($29\ 000 > 20\ 000$). This way, when micro-lenses will be added, the resolving power will still remain between the required and goal resolving powers. Additional budget needs to be awarded to the project for that purpose because of the significant cost of the implementation of micro-lenses on all the fibers of the bundle.

- As advised by Dallier et al., we may re-locate the bundle shutter within the SPS to improve the quality of dark frames [26]. However, the only part of the scene that is not captured in the actual configuration is the bundle housing.
- The overall optical performances of the instrument have been optimized thanks to Bingham's methodology. The thermo-mechanical behavior of the instrument may however be investigated to improve the stability of the instrument. The instrument was designed as a breadboard spectrograph that was aligned on a drilled optical bench. Specific optimized instrument bench and enclosure could be designed and manufactured with high precision if more budget is allocated to the project. This might be the case after the first verification of N3SIE's performances at TIGRE telescope.
- Last but not least, the detector should be changed as soon as possible as it largely dominates the limiting factors to the overall performance of N3SIE. The huge dark noise it suffers from naturally limits the target magnitude we are able to observe within an allocated period of time. Saturation rapidly occurs and long integration times are prohibited. These limitations therefore impact on the radiometric budget of the instrument. On the other hand, N3SIE's first light when observing Capella also underlined that low signal-to-noise ratio requires degrading the resolving power to decrease the overall noise amount. As a reminder, the expression of the signal-to-noise ratio (Eq. (15)) involved both the spectral resolution $d\lambda$ and the integration time d_{int} . Increasing one of these, which means degrading the spectral resolution when considering $d\lambda$, leads to a better signal-to-noise ratio. The binning operation that was performed to extract the scientific spectrum intended to do so. This detector therefore also influences the spectral resolution that may be achieved on a given target. Suitable detectors were presented in Chapter 2 and these should be considered as prior targets. These are cryogenic sensors that exhibit extremely low dark currents. Their size also largely overpasses the one of our detector and more waveband coverage will be enabled. Again, more funds must be granted to the project since the price of such detectors approximately amounts to three times the actual hardware budget of the instrument. The management of liquid nitrogen at the observation site, which requires budget and scheduling, is a direct inconvenient foreseen with such technologies. One must also pay attention on the selected technology and the potential cold filter it may require as inferred by Dallier et al (Chapter 1) [26].

Implementing those modifications to the actual design of the spectrograph will lead to both higher throughput and reachable resolving power. In any case, the instrument function of merit will benefit from these improvements.

Bibliography

- [1] Eversberg, T.; Vollmann, K. "Spectroscopic Instrumentation: Fundamentals and Guidelines for Astronomers," Springer, Berlin (2014)
- [2] Massey, P. "Massive Stars in the Local Group: Implications for Stellar Evolution and Star Formation," *Annu. Rev. Astron. Astrophys.* 41, 15-56 (2003)
- [3] Langer, N. "Presupernova Evolution of Massive Single and Binary Stars," *Annu. Rev. Astron. Astrophys.* 50, 107-164 (2012)
- [4] Zinnecker, H.; Yorke, H. W. "Toward Understanding Massive Star Formation," *Annu. Rev. Astron. Astrophys.* 45, 481-563 (2007)
- [5] Andriillat, Y.; Vreux, J.-M. "O Stars He II and H lines in the 1 μ Region," *Astronomy & Astrophysics* 75, 93-96 (1979)
- [6] Vreux, J.-M.; Andriillat, Y.; Biémont, E. "Near-infrared observations of galactic northern Wolf Rayet stars," *Astronomy & Astrophysics* 238, 207-220 (1990)
- [7] Groh, J. H.; Daminieli, A.; Jablonski, F. "Spectral atlas of massive stars around He I 10830 Å," *Astronomy & Astrophysics* 465, 993-1002 (2007)
- [8] Stevens, I. R.; Howarth, I. D. "Infrared line-profile variability in Wolf-Rayet binary systems," *Monthly Notices of the Royal Astronomical Society* 302, 549-560 (1999)
- [9] Short, C. I.; Doyle, J. G. "Pa-beta as a chromospheric diagnostic in M dwarfs," *Astronomy and Astrophysics* 331, L5-L8 (1998)
- [10] Liefke, C.; Reiners, A.; Schmitt, J. H. M. M. "Magnetic field variations and a giant flare: Multiwavelength observations of CN Leo," *MmSAI* 78, 258-260 (2007)
- [11] Schmidt, S. J.; Hilton, E. J.; Tofflemire, B.; Wisniewski, J. P.; Kowalski, A. F.; Hotzman, J.; Hawley, S. L. "The First Detection of Time-Variable Infrared Line Emission During M Dwarf Flares," *American Astronomical Society* 43, 21832604 (2011)
- [12] Choudhary, D.; Tejomoortula, U.; Penn, M. J. "Dynamics of Quiet Solar Chromosphere at the Limb," *American Geophysical Union Fall Meeting*, SH23A-1622 (2008)
- [13] Cuntz, M.; Luttermoser, D. G. "Stochastic shock waves as a candidate mechanism for the formation of the He I 10830-Å line in cool giant stars," *The Astrophysical Journal* 353, L39-L43 (1990)
- [14] Dupree, A. K.; Sasselov, D. D.; Lester, J. B. "Discovery of a fast wind from a field population II giant star," *The Astrophysical Journal* 387, L85-L88 (1992)
- [15] Kwan, J.; Edwards, S.; Fischer, W. "Modeling T Tauri Winds from He I λ 10830 Profiles," *ApJ* 657, 897-915 (2007)

Bibliography

- [16] Podio, L.; Garcia, P. J. V.; Bacciotti, F. "HeI lambda 10830 line: a probe of the accretion/ejection activity in RU Lupi," *MmSAI* 78, 693 (2007)
- [17] Schmitt, J. H. M. M.; Schröder, K.-P.; Rauw, G.; Hempelmann, A.; Mittag, M.; González-Perez, J. N.; Czesla, S.; Wolter, U.; Jack, D.; Eenens, P.; Trinidad, M. A. "TIGRE: A new robotic spectroscopy telescope at Guanajuato," *Astronomische Nachrichten* 335(8), 787-796 (2014)
- [18] Hempelmann, A. "TIGRE Telescope – General Information (Online)," http://www.hs.uni-hamburg.de/EN/Ins/HRT/hrt_general_info.html (2013)
- [19] Sagar, R. "A modern 3.6 m meter new technology optical telescope as a major national initiative in astrophysics," *National Academy Science Letters* 30, 209-212 (2007)
- [20] Sagar, R.; Kumar, B.; Omar, A.; Pandey, A. K. "New optical telescopes projects at devasthal Observatory," *Proc. of SPIE* 8444, 84441T-1 (2012)
- [21] Parry, I. R. "Multi-Object Spectroscopy with Optical Fibres," *Wide-field spectroscopy* 212, 3 (1997)
- [22] Dallier, R.; Baudrang, J.; Cuby, J. G. "Near IR Fiber Spectroscopy: First Results," *Fiber Optics in Astronomy II* 37, 310 (1993)
- [23] Dallier, R.; Cuby, J. G.; Baudrand, J. "Near Infrared Fiber Spectroscopy," *European Southern Observatory Conference and Workshop Proceedings* 42, 685 (1992)
- [24] Dallier, R.; Cuby, J. G.; Czarny, J.; Baudrand, J. "ISIS IR: the first infrared fibre-fed spectrograph for near-infrared astronomy," *Experimental Astronomy* 3(1), 183-184 (1994)
- [25] Dallier, R.; Boisson, C.; Joly, M. "A library of H band stellar spectra for stellar population analysis purposes," *Astronomy & Astrophysics Supplement Series* 116(2), 239-248 (1996)
- [26] Dallier, R.; Cuby, J. G. "Noncooled near-infrared spectroscopy," *SPIE Proceedings in Astronomical Telescopes & Instrumentation* 3354, 833-844 (1998)
- [27] Cirasuolo, M.; Afonso, J.; Bonifacio, P.; Evans, C.; Kaper, L.; Oliva, E.; Vanzi, L. "MOONS: The Multi-Object Optical and Near-infrared Spectrograph," *The Messenger* 145, 11-13 (2011)
- [28] Cirasuolo, M.; Afonso, J.; Bender, R.; Bonifacio, P.; Evans, C.; Kaper, I.; Oliva, E.; Vanzi, L.; Abreu, M.; Atad-Ettdgui, E.; Babusiaux, C.; Bauer, F.; Best, P.; Bezawada, N.; Bryson, I.; Cabaral, A.; Caputi, K.; Centrone, M.; Chemla, F.; Cimatti, A.; Cioni, M.-R.; Clementini, G.; Coelho, J.; Daddi, E.; Dunlop, J.; Feltzing, S.; Ferguson, A.; Flores, H.; Fontana, A.; Fynbo, J.; Garilli, B.; Glauser, A.; Guinouard, I.; Hammer, F.; Hastings, P.; Hess, A.; Ivison, R.; Jagourel, P.; Jarvis, M.; Kauffman, G.; Lawrence, A.; Lee, D.; Licausi, G.; Lilly, S.; Lorenzetti, D.; Maiolino, R.; Mannucci, F.; McLure, R.; Minniti, D.; Montgomery, D.; Muschelok, B.; Nandra, K.; Navarro, R.; Norberg, P.; Origlia, L.; Padilla, N.; Peacock, J.; Pedicini, F.; Pentericci, L.; Pragt, J.; Puech, M.; Randich, S.; Renzini, A.; Ryde, N.; Rodrigues, M.; Royer, F.; Saglia, R.; Sanchez, A.; Schnetler, H.; Sobral, D.; Speziali, R.; Todd, S.; Tolstoy, E.; Torres, M.; Venema, L.; Vitali, F.; Wegner, M.; Wells, M.; Wild, V.; Wright, G. "MOONS: a Multi-Object Optical and Near-infrared Spectrograph for the VLT," *SPIE Proceedings in Ground-based and Airborne*

Instrumentation for Astronomy IV 8446, 1-9 (2012)

- [29] Cirasuolo, M.; Afonso, J.; Carollo, M.; Flores, H.; Maiolino, R.; Oliva, E.; Paltani, S.; Vanzi, L.; Evans, C.; Abreu, M.; Atkinson, D.; Babusiaux, C.; Beard, S.; Bauer, F.; Bellazzini, M.; Bender, R.; Best, P.; Bezawada, N.; Bonifacio, P.; Bragaglia, A.; Bryson, I.; Busher, D.; Cabral, A.; Caputi, K.; Centrone, M.; Chemla, F.; Cimatti, A.; Cioni, M. R.; Clementini, G.; Coelho, J.; Cmojevic, D.; Daddi, E.; Dunlop, J.; Eales, S.; Feltzing, S.; Ferguson, A.; Fisher, M.; Fontana, A.; Fynbo, J.; Garilli, B.; Gilmore, G.; Glauser, A.; Guinouard, I.; Hammer, F.; Hastings, P.; Hess, A.; Ivison, R.; Jarvis, M.; Kaper, L.; Kauffman, G.; Kitching, A. T.; Lawrence, A.; Lee, D.; Lemasle, B.; Licausi, G.; Lilly, S.; Lorenzetti, D.; Lunney, D.; Maiolino, R.; Mannucci, F.; McLure, R.; Minniti, D.; Montgomery, D.; Muschnielok, B.; Nandra, K.; Navarro, R.; Norberg, P.; Oliver, S.; Origlia, L.; Padilla, N.; Peacock, J.; Pedicini, F.; Peng, J.; Pentericci, L.; Pragt, J.; Puech, M.; Randich, S.; Rees, P.; Renzini, A.; Ryde, N.; Rodrigues, M.; Roseboom, I.; Royer, F.; Saglia, R.; Sanchez, A.; Schiavon, R.; Schnetler, H.; Sobral, D.; Speziali, R.; Sun, D.; Stuck, R.; Taylor, A.; Taylor, W.; Todd, S.; Tolstoy, E.; Torres, M.; vanzella, E.; Vanzella, E.; Venema, L.; Vitali, F., et al. "MOONS: the Multi-Object Optical and Near-infrared Spectrograph for the VLT," *Proceedings of SPIE in Ground-based and Airborne Instrumentation for Astronomy V* 9147, 91470N (2014)
- [30] McLean, I. S. "Electronic Imaging in Astronomy: Detectors and Instrumentation," Springer Science & Business Media, Chichester (2008)
- [31] Lord, S. D. "A New Software Tool for Computing Earth's Atmospheric Transmission of Near- and Far-infrared Radiation," NASA Ames Research Center, Technical Memorandum, 103957 (1992)
- [32] Sánchez, S. F.; Thiele, U.; Aceituno, J.; Cristobal, D.; Perea, J.; Alves, J. "The Night Sky at the Calar Alto Observatory II: The Sky in the Near-Infrared," *Publications of the Astronomical Society of the Pacific* 120(873), 1244 (2008)
- [33] Kitchin, C. R. "Astrophysical Techniques," Institute of Physics Publishing, Bristol and Philadelphia (2003)
- [34] Wynne, C. G.; Worswick, S. P. "Atmospheric dispersion correctors at the Cassegrain focus," *Monthly Notices of the Royal Astronomical Society* 220, 657-670 (1986)
- [35] Szeto, K.; Morbey, C.; Crampton, D.; Fletcher, M.; Murowinski, R.; Stilburn, J.; Taylor, P.; Wooff, R. "Design and Implementation of an Atmospheric Dispersion Compensator/Corrector for the Gemini Multi-Object Spectrograph," *Astronomical Telescopes and Instrumentation. International Society for Optics and Photonics*, 1326-1336 (2003)
- [36] Kopon, D.; Close, L. M.; Gasho, V. "An Advanced Atmospheric Dispersion Corrector: The Magellan Visible AO Camera," *Proceedings of the SPIE Instrumentation and Methods for Astrophysics* 7015, 70156M (2008)
- [37] Szokoly, G. P. "Optimal slit orientation for long multi-object spectroscopic exposures," *Astronomy & Astrophysics* 443(2), 703-707 (2005)

Bibliography

- [38] Ciddor, P. E. "Refractive index of air: new equations for the visible and the near infrared," *Applied Optics* 35(9), 1566-1573 (1996)
- [39] Hearnshaw, J. "Astronomical Spectrographs and their History," Cambridge University Press, Cambridge (2009)
- [40] Schroeder, D. J. "Astronomical Optics," Academic Press, San Diego (1999)
- [41] Barden, S. C. "Fiber Optics at Kitt Peak National Observatory," *Instrumentation for Ground-Based Optical Astronomy*, 250-255 (1988)
- [42] Barden, S. C.; Elston, R.; Armandroff, T.; Pryor, C. P. "Observational Performance of Fiber Optics-High Precision Sky Subtraction and Radial Velocities," *Fiber Optics in Astronomy II* 37, 223 (1993)
- [43] Ramsey, L. W. "Focal ratio degradation in optical fibers of astronomical interest," *Fiber optics in Astronomy* 3, 26-39 (1988)
- [44] Craig, W. W.; Hailey, C. J.; Brodie, J. P. "Measurement of fibers to be used in fiber fed spectroscopy," *Fiber optics in astronomy* 3, 41-51 (1988)
- [45] Barden, S. C. "Review of fiber-optic properties for astronomical spectroscopy," *Fiber Optics in Astronomy III*, 14 (1998)
- [46] Carrasco, E.; Parry, I. R. "A method for determining the focal ratio degradation of optical fibres for astronomy," *Mon. Not. R. Astron. Soc.* 271, 1-12 (1994)
- [47] Lu, G.; Schoetz, G. F.; Vydra, J.; Fabricant, D. G. "Optical fiber for UV-IR broadband spectroscopy," *Optical Astronomical Instrumentation* 3355, 884-891 (1998)
- [48] Heacock, W. D. "Wavelength-precise slit spectroscopy with optical fiber image scramblers," *Fiber optics in astronomy* 3, 204-235 (1988)
- [49] Kintziger, C.; Hempelmann, A. Personal communications (2015)
- [50] Spectrum Thin Films. "Metallic Coatings (Online)," <http://spectrumthinfilms.com/stf/coatings/metallic-coatings-reflective/> (2014)
- [51] Edmund Optics. "Longpass Filters (Online)," <http://www.edmundoptics.com/optics/optical-filters/longpass-edge-filters/longpass-filters/64693/> (2014)
- [52] Fischer, R. E.; Tadic-Galeb, B.; Yoder, P. R. "Optical System Design," McGraw Hill, New York (2008)
- [53] Nowicki-Bringuier, Y.-R.; Chorier, P. "Sofradir SWIR hyperspectral detectors for space applications," (2009)
- [54] AIM GmbH. "IR-Detector Technology Status at AIM," (2014)

Bibliography

- [55] Princeton Instruments. "Breakthrough Performance-Enhancing CCD and EMCCD Technology (Online)," https://www.princetoninstruments.com/userfiles/files/appnotes/eXcelon3_technote_RevA8.pdf (2015)
- [56] Andor. "Low Dark Current Deep-Depletion (LDC-DD) Technology (Online)," [http://www.andor.com/learning-academy/low-dark-current-deep-depletion-\(ldc-dd\)-technology-a-new-standard-for-low-light-nir-spectroscopy](http://www.andor.com/learning-academy/low-dark-current-deep-depletion-(ldc-dd)-technology-a-new-standard-for-low-light-nir-spectroscopy) (2015)
- [57] Kitchin, C. R. "Optical Astronomical Spectroscopy," Institute of Physics Publishing, Bristol and Philadelphia (1995)
- [58] Bingham, R. G. "Grating Spectrometers and Spectrographs Re-examined," Quarterly Journal of Royal Astronomical Society, 395-421 (1979)
- [59] Allemand, C. D. "Coma Correction in Czerny-Turner Spectrographs," Journal of the optical society of America 58(2), 159-163 (1968)
- [60] McDowell, M. W. "Design of Czerny-Turner Spectrographs Using Divergent Grating Illumination," Optica Acta: International Journal of Optics 22(5), 473-475 (1975)
- [61] Bell, R. E. "Exploiting a transmission grating spectrometer," Review of scientific instruments 75(10), 4158-4161 (2004)
- [62] Synopsys. CODE V (2016)
- [63] Xue, Q.; Wang, S.; Lu, F. "Aberration-corrected Czerny–Turner imaging spectrometer with a wide spectral region," Applied Optics 48, 11-16 (2009)
- [64] Shafer, A. B.; Megill, L. R.; Droppleman, L. "Optimization of the Czerny-Turner Spectrometer," J. Opt. Soc. Am. 54, 879-887 (1964)
- [65] Xue, Q. "Astigmatism-corrected Czerny-Turner imaging spectrometer for broadband spectral simultaneity," Applied Optics 50(10), 1338-1344 (2011)
- [66] Austin, D. R. "Broadband astigmatism-free Czerny-Turner imaging spectrometer using spherical mirrors," Appl. Opt. 48(19), 3846-3853 (2009)
- [67] Lee, K. S.; Thomson, K. P.; Rolland, J. P. "Broadband astigmatism-corrected Czerny–Turner spectrometer," Opt. Express 18, 23378-23384 (2010)
- [68] Breault Research. "Breault Research," ASAP (2016)
- [69] Yoder, P. R. "Mounting optics in optical instruments," SPIE press, Bellingham (2008)
- [70] Huke, P.; Tal-Or L.; Sarmiento, L. F.; Reiners, A. "Hollow-cathode lamps as optical frequency standards: The influence of optical imaging on the line-strength ratio," SPIE Astronomical Telescopes+ Instrumentation. International Society for Optics and Photonics, 99124K-99124K-11

(2016)

- [71] Kerber, F.; Nave, G.; Sansonetti, C. J. "The spectrum of Th-Ar hollow cathode lamps in the 691-5804 nm region: establishing wavelength standards for the calibration of infrared spectrographs," *The Astrophysical Journal Supplement Series* 178(2), 374-381 (2008)
- [72] Engleman Jr, R.; Hinkle, K. H.; Wallace, L. "The near-infrared spectrum of a Th/Ar hollow cathode lamp," *Journal of Quantitative Spectroscopy and Radiative Transfer* 78(1), 1-30 (2003)
- [73] Rossi, G.; Omenetto, N. "Feasibility of using a uranium hollow cathode lamp as primary source in atomic absorption spectroscopy," European Atomic Energy Community, Ispra (Italy). Joint Nuclear Research Center No. EUR-3558. e (1967)
- [74] Redman, S. L.; Lawler, J. E.; Nave, G.; Ramsey, L. W.; Mahadevan, S. "The infrared spectrum of uranium hollow cathode lamps from 850 nm to 4000 nm: wavenumbers and line identifications from Fourier transform spectra," *The Astrophysical Journal Supplement Series* 195(2), 24 (2011)
- [75] Redman, S. L.; Ycas, G. G.; Terrien, R.; Mahadevan, S.; Ramsey, L. W.; Bender, C. F.; Osterman, S. N.; Diddams, S. A.; Quinlan, F.; Lawler, J. E.; Nave, G. "A high-resolution atlas of uranium-neon in the h band," *The Astrophysical Journal Supplement Series* 199(1), 2 (2012)
- [76] Sarmiento, L. F.; Reiners, A.; Seemann, U.; Lemke, U.; Winkler, J.; Pluto, M.; Günther, E. W.; Quirrenbach, A.; Amado, P. J.; Ribas, I.; Caballero, J. A.; Mundt, R.; Seifert, W. "Characterizing U-Ne hollow cathode lamps at near-IR wavelengths for the CARMENES survey," *Proc. SPIE* 9147, 914754-914754 (2014)
- [77] Ramsay, S. K.; Rolt, S.; Sharples, R. M.; Davies, R. "Calibration of the KMOS multi-field imaging spectrometer," *Proc 2007 ESO Instrument Calibration Workshop*, 319-324 (2008)
- [78] Avila, G.; Singh, P.; Chazelas, B. "Results on fibre scrambling for high accuracy radial velocity measurements," *Proc. SPIE* 7735, 773588 (2010)
- [79] Cox, A. N. "Allen's Astrophysical Quantities," Springer (2000)
- [80] Pecaut, M. J. "Intrinsic colors, temperatures and bolometric corrections of the pre-main sequence stars," Draft version (2013)
- [81] Martins, F.; Plez, B. "UBVJHK synthetic photometry of Galactic O stars," *A&A* 457, 637-644 (2006)
- [82] Martins, F.; Schaerer, D.; Hillier, D. J. "A new calibration of stellar parameters of Galactic O stars," *A&A* 436(3), 1049-1065 (2008)
- [83] Richardson Gratings. "Plane Ruled Reflectance Gratings (Online)," http://www.gratinglab.com/Products/Product_Tables/Efficiency/Efficiency.aspx?catalog=53-*531R (2014)
- [84] Cidadão, A. J. "Characterization and use of two Methane-Band (889nm) filters (Online),"

Bibliography

- http://www.astrosurf.com/cidadao/methane_01.htm
- [85] Osenbach, K. "Optical Coatings (Online)," https://www.thorlabs.com/newgrouppage9.cfm?objectgroup_id=5840 (2014)
- [86] Semiconductor Components Industries. "KAI-0340: Interline Transfer CCD Image Sensor, VGA (Online)," <http://www.onsemi.com/PowerSolutions/product.do?id=KAI-0340> (2015)
- [87] IDS Imaging Development Systems GmbH. "UI-1120SE (Online)," <https://en.ids-imaging.com/store/ui-1120se.html> (2017)
- [88] Torres, G.; Claret, A.; Pavloski, K.; Dotter, A. "Capella (α Aurigae) revisited: new binary orbit, physical properties, and evolutionary state," *The Astrophysical Journal* 807(1), 26 (2015)
- [89] Eaton, J. A.; Hall, D. S. "Starspots as the cause of the intrinsic light variations in RS Canum Venaticorum type stars," *The Astrophysical Journal* 227, 907-922 (1979)
- [90] Vogt, S. S.; Penrod, G. D. "Doppler imaging of spotted stars: application of the RS Canum Venaticorum star HR 1099," *Publications of the Astronomical Society of the Pacific* 95(571), 565 (1983)
- [91] Kürster, M.; Schmitt, J. H. M. M. "The longest stellar X-ray flare observed with ROSAT," *Astronomy and Astrophysics* 311, 211-229 (1996)
- [92] Mekkadon, M. V. "The dependence of He I 10830 absorption on X-ray luminosity in RS CVn binaries and very active F and G Main-Sequence stars," *Astrophysics and space science* 110(2), 413-416 (1985)
- [93] Hinkle, K.; Wallace, L.; Livingston, W. "Infrared atlas of the Arcturus spectrum, 0.9-5.3 microns," *Publications of the Astronomical Society of the Pacific* 107(717), 1042-1046 (1995)
- [94] Husser, T. O.; Wende-von Berg, S.; Dreizler, S.; Homeier, D.; Reiners, A.; Barman, T.; Hauschildt, P. H. "A new extensive library of PHOENIX stellar atmospheres and synthetic spectra," *Astronomy & Astrophysics* 553, A6 (2013)
- [95] Wood, R. W. "On a remarkable case of uneven distribution of light in a diffraction grating spectrum," *The London, Edinburgh, and Dublin Philosophical Magazine and Journal of Science* 4(21), 396-402 (1902)

Bibliography

Appendices

A. Establishment of Bingham's equations

All notations used in this appendix are introduced in Chapter 3. First, the disperser obeys to an equation which writes as follow (here, the Bragg Equation):

$$g(\alpha, \beta, \lambda) = 0$$

Secondly, the *magnification* between the entrance and exit slit can be expressed by:

$$Mag = \frac{w'}{w} = \frac{f_{cam}}{f_{coll}} \left(\frac{\partial \beta}{\partial \alpha} \right) = \frac{f_{cam}}{f_{coll}} \frac{\left(\frac{\partial g}{\partial \alpha} \right)}{\left(\frac{\partial g}{\partial \beta} \right)} = \frac{f_{cam} \cos \alpha}{f_{coll} \cos \beta}$$

The *dispersion* is then equal to:

$$Dis = \frac{1}{P} = f_{cam} \left(\frac{\partial \beta}{\partial \lambda} \right) = f_{cam} \left(\frac{\partial g}{\partial \lambda} \right) / \left(\frac{\partial g}{\partial \beta} \right)$$

Finally, the resolving power can be written as:

$$R = \frac{\lambda}{\delta \lambda} = \frac{\lambda}{\frac{w'}{Dis}} = \frac{\lambda f_{cam} \left(\frac{\partial g}{\partial \lambda} \right)}{w' \left(\frac{\partial g}{\partial \beta} \right)} = \frac{\lambda f_{cam} \left(\frac{\partial g}{\partial \lambda} \right)}{Mag \theta_s f_{tel} \left(\frac{\partial g}{\partial \beta} \right)} = \frac{\lambda f_{cam} \left(\frac{\partial g}{\partial \lambda} \right)}{\frac{f_{cam}}{f_{coll}} \left(\frac{\partial g}{\partial \alpha} \right) \theta_s f_{tel}} = \frac{\lambda f_{coll} \left(\frac{\partial g}{\partial \lambda} \right)}{\theta_s f_{tel} \left(\frac{\partial g}{\partial \alpha} \right)}$$

Several expressions involving the resolution are now derived, each involving different basic parameters of the spectrometer. Those equations are used in the recipe designed by Bingham to derive the instrument specifications.

The first relation follows the evaluation of $R \theta_s A_{tel}$:

$$\begin{aligned} R \theta_s A_{tel} &= R \frac{w'}{Mag f_{tel}} A_{tel} = R \frac{w'}{\frac{f_{cam} \cos \alpha}{f_{coll} \cos \beta} f_{tel}} A_{tel} \\ &= R \frac{w'}{\frac{f_{cam}}{f_{coll}} \frac{A_{coll}}{L} f_{tel}} A_{tel} = R \frac{w'}{f_{cam} \frac{1}{A_{cam}}} \frac{A_{tel} f_{coll}}{f_{tel} A_{coll}} \\ &= R w' \frac{A_{cam}}{f_{cam}} \end{aligned}$$

since $A_{tel}/f_{tel} = A_{coll}/f_{coll}$. Using the definition of R , we obtain the second equation:

$$R w' \frac{A_{cam}}{f_{cam}} = \frac{\lambda}{\delta \lambda} w' \frac{A_{cam}}{f_{cam}} = \frac{\lambda}{\frac{w'}{Dis}} w' \frac{A_{cam}}{f_{cam}} = \lambda Dis \frac{A_{cam}}{f_{cam}}$$

Using the expression (6) from Hearnshaw [39] leads to the third equation:

$$\begin{aligned}
 R &= \frac{2 A_{coll}}{\theta_s A_{tel}} \frac{\tan \theta_B}{1 - \tan \theta_B \tan \theta} = \frac{2 A_{coll}}{\theta_s A_{tel}} \frac{\tan\left(\frac{\alpha + \beta}{2}\right)}{1 - \tan\left(\frac{\alpha + \beta}{2}\right) \tan\left(\frac{\alpha - \beta}{2}\right)} \\
 &= \frac{2 L \cos \alpha}{\theta_s A_{tel}} \frac{\tan\left(\frac{\alpha + \beta}{2}\right)}{1 - \tan\left(\frac{\alpha + \beta}{2}\right) \tan\left(\frac{\alpha - \beta}{2}\right)} \\
 &= \frac{2 L \cos\left(\frac{\alpha + \beta}{2} + \frac{\alpha - \beta}{2}\right)}{\theta_s A_{tel}} \frac{\tan\left(\frac{\alpha + \beta}{2}\right)}{1 - \tan\left(\frac{\alpha + \beta}{2}\right) \tan\left(\frac{\alpha - \beta}{2}\right)} \\
 &= \frac{2 L \left(\cos\left(\frac{\alpha + \beta}{2}\right) \cos\left(\frac{\alpha - \beta}{2}\right) - \sin\left(\frac{\alpha + \beta}{2}\right) \sin\left(\frac{\alpha - \beta}{2}\right) \right)}{\theta_s A_{tel}} \frac{\tan\left(\frac{\alpha + \beta}{2}\right)}{1 - \tan\left(\frac{\alpha + \beta}{2}\right) \tan\left(\frac{\alpha - \beta}{2}\right)} \\
 &= \frac{2 L \left(\cos\left(\frac{\alpha - \beta}{2}\right) - \tan\left(\frac{\alpha + \beta}{2}\right) \sin\left(\frac{\alpha - \beta}{2}\right) \right)}{\theta_s A_{tel}} \frac{\sin\left(\frac{\alpha + \beta}{2}\right)}{1 - \tan\left(\frac{\alpha + \beta}{2}\right) \tan\left(\frac{\alpha - \beta}{2}\right)} \\
 &\Leftrightarrow R \theta_s A_{tel} = 2 L \sin\left(\frac{\alpha + \beta}{2}\right) \cos\left(\frac{\alpha - \beta}{2}\right)
 \end{aligned}$$

The fourth relation is deduced from the Bragg relation (5):

$$\begin{aligned}
 m \lambda &= 2 d \sin \theta_B \cos \theta \\
 \Leftrightarrow 2 \sin \theta_B \cos \theta &= \frac{m \lambda}{d}
 \end{aligned}$$

we get:

$$2 L \sin\left(\frac{\alpha + \beta}{2}\right) \cos\left(\frac{\alpha - \beta}{2}\right) = \frac{L m \lambda}{d}$$

A last calculation leads to a simplified expression of the magnification:

$$Mag = \frac{f_{cam} \cos \alpha}{f_{coll} \cos \beta} = \frac{f_{cam} A_{coll}}{f_{coll} A_{cam}} = \frac{f_{cam} A_{tel}}{A_{cam} f_{tel}}$$

B. Control software overview

Introduction

The control of the spectrograph and the incorporated instruments requires the elaboration of a dedicated custom software. The remote control of the instrument is also required since TIGRE is a robotic telescope. This chapter is devoted to a brief description of this intrinsic control software that was elaborated by two subsequent students at CSL under the supervision of Daniel Actis: Michaël Tchado initiated this task during his Master Thesis and Florian Duchateau concluded during his summer job.

Purpose of the software and devices under control

The spectrograph control software enables the user to interact with all the electronic devices included in the instrument. These may be movable parts or detectors for example. The proper operation of the instrument requires a clear and effortless access to those devices. Table B.1 summarizes all the controlled devices by the software sorted according to their action type.

Movement	Detection	Illumination
<i>Translation stage</i>	<i>InGaAs spectrograph camera</i>	<i>UNe HCL</i>
<i>Rotation stage</i>		<i>Halogen lamp</i>
<i>Fiber shutter</i>	<i>SBIG SPS camera</i>	<i>LED</i>
<i>HCL shutter</i>		

Table B.1 - List of devices controlled by the software.

To switch between the observation and calibration phases, the translation stage position must change between its end and home positions. Homing this device is also required to illuminate the fiber bundle and carry out the tracking of the target. The rotation stage purpose is to modify the central wavelength on the detector. The grating incidence angle must be modified according to the user's selected observation wavelength (see Eq. (16) in Chapter 6.2.2). Mechanical shutters on the other hand are employed to enable recording dark frames. These are necessary to remove the instrumental/detector background from the observations. For that purpose, each observation frame the user schedules must be repeated with the respective shutter closed.

The spectrum observation at the spectrograph focal plane is carried out with the selected InGaAs camera. The star positioning system is on the other hand equipped with a CMOS sensor to visualize both star and bundle images. Both detectors incorporate settings that must be modified according to the observer's preferences.

The selected lamps must be turned off and on during the appropriate calibration phases of the spectrograph. The current intensity of the hollow cathode lamp must also be set by the user to the appropriate value. Literature and manufacturer advice drive this setting in order to obtain the appropriate spectrum stability while maximizing the life-time of the lamp. Eventually, the LED lightning must also be user-controlled to enable the tracking operation initialization and observe the bundle with the help of the SPS detector.

User interface presentation

This section intends to briefly introduce the software interface that is proposed to the observer. The software incorporates both manual and automatic modes. Their functioning is introduced below.

Manual mode

The manual mode enables the user to directly interact with all the devices presented in Table B.1. The observer is therefore able to manually change their settings and operate all related actions. This was naturally the first developed behavior of the instrument as it enables debugging each device programming. The top part of Figure B.1 illustrates the graphical interface proposed to the user when enabling the manual mode.

Each column of the graphical interface concerns the control of a single component (except the mechanical shutters that are grouped with the LED). A first connecting action to the selected hardware is required before taking its control. Then, updating the device parameters occurs either by manually changing numerical values (the central wavelength for example) or clicking on buttons which activate specific actions and change a status (open and close shutters for instance).

This way of controlling the spectrograph is particularly convenient when performing aligning actions or testing some components. Once all the verification tests were passed, the automatic drive of the instrument could be initiated.

Automatic mode

The automatic mode of operation incorporates complex sequences of actions that operate a complete plan. The various tasks required for a proper scientific observation are therefore incorporated in this automatic mode. These involve initialization, tracking, calibration and observation tasks. This functioning mode of the spectrograph benefits from the previous scripts and automates their activation in a logical order according to the user's selected operation. The bottom part of Figure B.1 illustrates the automatic interface that appears when the observer activates the associated button.

The automatic user interface proposes to the observer a series of subsequent buttons that unlock in turn as the previous actions are completed. The initialization of the spectrograph naturally appears as the first button the user can activate. The software then connects to all the devices and checks whether they react properly. Once everything answered as expected, the calibration phase can start. Both lamps turn on and a 10 *min* timer is triggered to freeze the system until the appropriate lamp temperature is reached. Once stabilized, the calibration frames can be recorded and this process can be completed. The telescope tracking can then be settled in order to maximize the stellar flux transmission down to the instrument. Eventually, the observation can start and the required scientific spectra are recorded.

All these automatic tasks are performed without any required user interaction. When installed at TIGRE, this script will therefore be available to be used in the telescope control software. The user button activations will be replaced by the telescope control algorithm messages. While actions modify the device parameters, these changes remain visible to the user while not accessible, which is very convenient for checking.

Control software overview

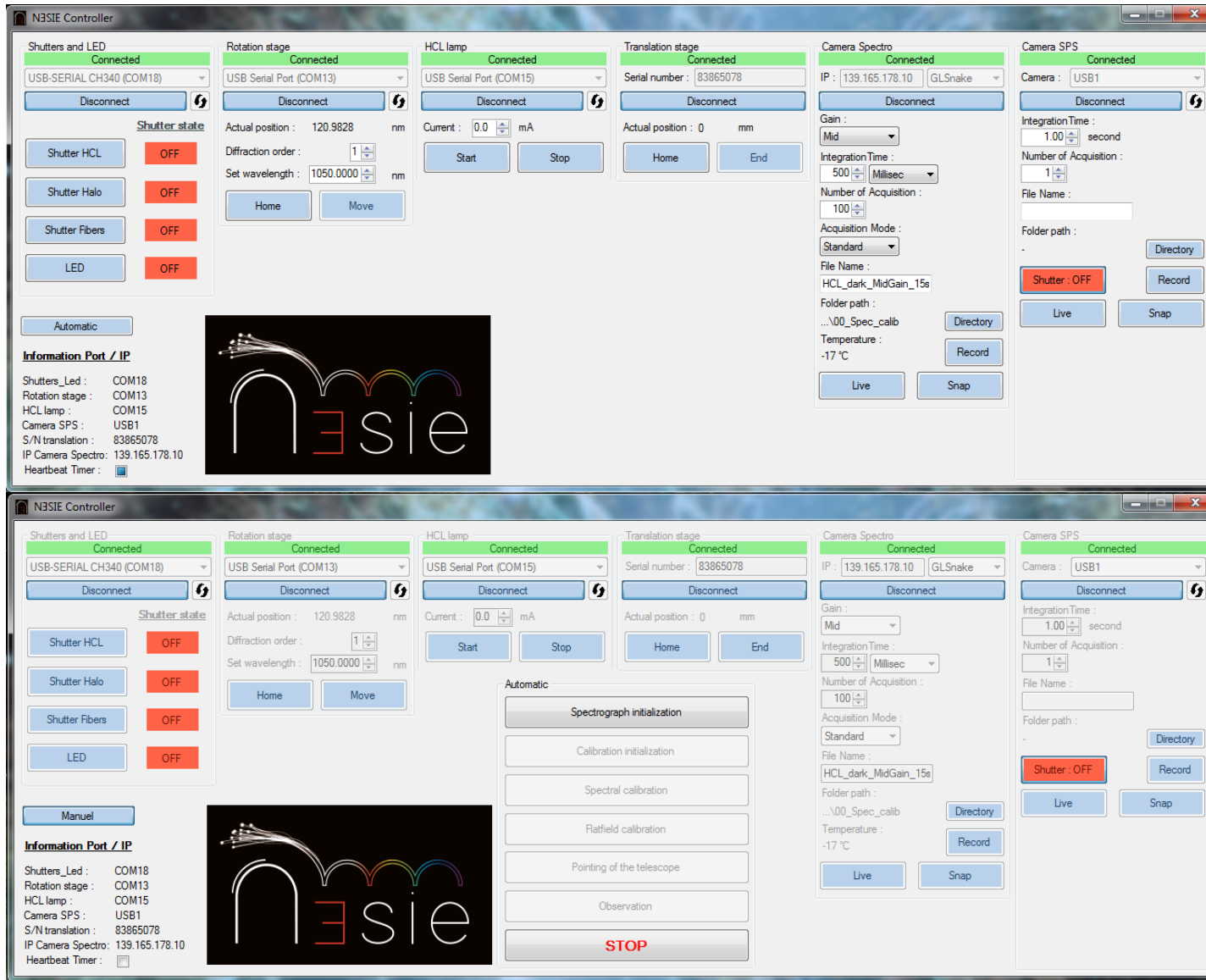


Figure B.1 – Overview of the control software manual (*top*) and automatic (*bottom*) modes

C. Associated scientific paper

Journal: Journal of Astronomical Telescopes, Instruments, and Systems (JATIS).

Peer-reviewed: Yes.

Title: *Conception of a near-infrared spectrometer for ground-based observations of massive stars.*

Authors: Christian Kintziger^{a,*}, Richard Desselle^a, Jerome Loicq^a, Gregor Rauw^b, Pierre Rochus^a.

^aCentre Spatial de Liège, Liege Science Park, 4031 Angleur, Belgium

^bUniversité de Liège, Institut d'Astrophysique et de Géophysique, Groupe d'Astrophysique des Hautes Energies, Liège, Belgium

Abstract: *In our contribution, we outline the different steps in the design of a fiber-fed spectrographic instrument for stellar astrophysics. Starting from the derivation of theoretical relationships from the scientific requirements and telescope characteristics, the entire optical design of the spectrograph is presented. Specific optical elements, such as a toroidal lens, are introduced to improve the instrument's efficiency. Then the verification of predicted optical performances is investigated through optical analyses, such as resolution checking. Eventually, the star positioning system onto the central fiber core is explained.*

Keywords: *spectroscopy; instrumentation; massive stars; TIGRE telescope; optical design.*

DOI: 10.1117/1.JATIS.3.1.015002

Journal Impact Factor: 3.5 (2016 Journal Citation Reports).

Paper 16042P received Aug. 3, 2016; accepted for publication Feb. 1, 2017; published online Feb. 21, 2017.

**Address all correspondence to: Christian Kintziger, E-mail: ckintziger@uliege.be*